PACIFIC EARTHQUAKE ENGINEERING
RESEARCH CENTER

Regionalized Ground-Motion Models for Subduction Earthquakes Based on the NGA-SUB Database

Norman Abrahamson
Department of Civil and Environmental Engineering
University of California

Zeynep Gülerce
Department of Civil Engineering
Middle East Technical University

PEER Report No. 2020/25

Pacific Earthquake Engineering Research Center
Headquarters at the University of California, Berkeley
December 2020

PEER 2020/25
December 2020

Regionalized Ground-Motion Models for Subduction Earthquakes Based on the NGA-SUB Database

Norman Abrahamson
Department of Civil and Environmental Engineering
University of California, Berkeley

Zeynep Gülerce
Department of Civil Engineering
Middle East Technical University

PEER Report No. 2020/25
Pacific Earthquake Engineering Research Center
Headquarters, University of California, Berkeley
December 2020

ABSTRACT

A set of global and region-specific ground-motion models (GMMs) for subduction zone earthquakes is developed based on the database compiled by the Pacific Earthquake Engineering Research Center (PEER) Next Generation Attenuation - Subduction (NGA-SUB) project. The subset of the NGA-SUB database used to develop the GMMs includes 3914 recordings from 113 subduction interface earthquakes with magnitudes varying between 5 and 9.2 and 4850 recordings from 89 intraslab events with magnitudes varying between 5 and 7.8. Recordings in the back-arc region are excluded, except for the Cascadia region. The functional form of the model accommodates the differences in the magnitude, distance, and depth scaling for interface and intraslab earthquakes. The magnitude scaling and geometrical spreading terms of the global model are used for all regions, with the exception of the Taiwan region which has a region-specific geometrical spreading scaling. Region-specific terms are included for the large distance (linear R) scaling, V_{S30} scaling, $Z_{2.5}$ scaling, and the constant term. The nonlinear site amplification factors used in Abrahamson et al. (2016) subduction GMM are adopted. The between-event standard deviation piece of the aleatory variability model is region and distance independent; whereas, the within-event standard deviations are both region and distance dependent. Region-specific GMMs are developed for seven regions: Alaska, Cascadia, Central America, Japan, New Zealand, South America, and Taiwan. These region-specific GMMs are judged to be applicable to sites in the fore-arc region at distances up to 500 km, magnitudes of 5.0 to 9.5, and periods from 0 to 10 sec. For the Cascadia region, the region-specific model is applicable to distances of 800 km including the back-arc region. For the sites that are not in one of the seven regions, the global GMM combined with the epistemic uncertainty computed from the range of the regional GMMs should be used.

ACKNOWLEDGMENTS

The NGA-SUB project was partially supported by both funding and in-kind support from FM Global, Pacific Gas & Electric Company, and Caltrans. The authors of the model described in this report participated without financial support from PEER, providing in-kind contributions of their expertise.

A key input to this study is the NGA-SUB ground-motion database, which is a result of several years' effort by the database team. In particular, we want to acknowledge the efforts of Tadahiro Kishida, Silvia Mazzoni, Victor Contreras, Sean Ahdi, and Robert Darragh to develop the NGA-SUB flat file that was used in this study.

We thank Henry Abrahamson for preparing the plots of the residuals.

Any opinions, findings, and conclusions or recommendations expressed in this material are those of the authors and do not necessarily reflect those of the sponsoring agencies or the Pacific Earthquake Engineering Research Center and the Regents of the University of California.

CONTENTS

LIST OF TABLES

LIST OF FIGURES

1 Introduction

Over the last decade, there has been a large increase in the number of ground-motion recordings from subduction zone earthquakes. The full dataset from the Pacific Earthquake Engineering Research Center (PEER) Next Generation Attenuation - Subduction (NGA-Sub) project includes over 71,000 recordings from 1880 earthquakes; however, the dataset remains limited for large-magnitude events (M>8 for interface and M>7 for intraslab) recorded at moderate distances (<100 km) that often control the seismic hazard in subduction zones. We have developed new ground-motion models (GMMs) for the subduction zone earthquakes based on a subset of NGA-SUB database by considering the results from finite-fault simulations to constrain the extrapolation of the model outside the range constrained by the empirical data.

Many of the GMMs that are currently used in seismic hazard studies for subduction zone earthquakes are fully ergodic GMMs that combined the data from subduction earthquakes around the world into a single model (e.g. Abrahamson et al., 2016). The ergodic approach assumes that the variability about the central model that was estimated from the combined set of world-wide data is applicable to any site in the world. As the ground-motion datasets have grown, it has become clear that the ergodic assumption does not work well due to significant systematic differences in the ground-motion scaling for different regions (Atkinson, 2006; Morikawa et al., 2008; Lin et al., 2011; Anderson and Uchiyama, 2011; Villani and Abrahamson, 2015; Lanzano et al., 2017).

There are systematic differences in the median ground motions for different regions that can vary by up to a factor of two from the global average. In the last decade, there has been a move from ergodic GMMs to partially and fully non-ergodic GMMs to address these regional differences. There are several forms of partially non-ergodic GMMs. One approach removes the systematic site-specific effects from the aleatory variability (single-station sigma) and keeps the median unchanged (Renault et al., 2010; BCHydro, 2012; Rodriguez-Marek et al., 2014; Coppersmith et al., 2014; Geopentech, 2015). The median is later adjusted to the site-specific conditions using locally recorded data or amplification factors from a site-specific site response study. Another partially non-ergodic approach accounts for some of the systematic differences in the median GMM for different broad regions. This approach was used in the NGA-West2 project for shallow crustal earthquakes by dividing the global dataset into up to 10 regions (Bozorgnia et al., 2014). Other studies have developed regional GMMs using data from a single region. This works well for regions rich in strong-motion data, such as Japan (e.g., Zhao et al., 2016b,a) or the combined region of Europe and the Middle East (e.g., Kotha et al., 2016); however, this approach can lead to unconstrained extrapolation of the models for large magnitudes in regions with limited strong-motion datasets. Another approach develops the GMM for a single region but uses global data to constrain the extrapolation to large magnitudes. For example, Phung et al. (2020) used this approach to develop a GMM for subduction earthquakes in Taiwan using a dataset of Taiwan ground motions supplemented by ground motions from larger magnitude earthquakes in Japan. Fully non-ergodic models that account for systematic differences in the source, path, and site effects are beginning to be developed and should be considered in future updates of the subduction GMMs.

For the development of our subduction GMM, we used the partially non-ergodic approach that includes region-specific terms that account for the differences in the median ground motion between broad regions. Using a global dataset allows us to take advantage of the constraints from the global data and still regionalize the site and path terms with regional coefficients. Our GMM has region-specific constant terms, linear site amplification, large distance (linear R), and basin-depth scaling for seven regions: Alaska, Cascadia, Central America (Lat 8N - 20N), Japan, New Zealand, South America (Lat 38S - 2S), and Taiwan.

A key issue for the Cascadia-specific GMM is that the limited ground-motion data from intraslab earthquakes in Cascadia are about a factor of two smaller than the ground motions from comparable intraslab events in other regions. Currently, there is not a physical explanation for this large reduction in the ground motion for Cascadia compared to other regions. Finite-fault simulations for Cascadia interface events do not show this large reduction. As discussed in Section 6.2, rather than centering the Cascadia-specific model on the available Cascadia ground-motion data from intraslab events, we apply an adjustment factor such that the Cascadia model reflects the average from other regions with similar spectral shapes. There is a similar issue of sparse data for the Alaska region, and we utilized the same approach to adjust the Alaska-specific GMM. We also provide a global version our GMM that is applicable to subduction zones around the world that are not in one of the seven regions modelled in this study.

A second key issue is the regionalization of the GMM for South America. The between-event residuals from the available data in northern Peru have large negative values, suggesting that the median ground motion in this region is much lower than other parts of South America. How should this difference in median ground motions be captured in the GMM? One option is to include a regional difference in the median with the appropriate epistemic uncertainty. A second option is to include the difference as part of the aleatory variability for the broader region. We judged that there were not enough earthquakes from northern Peru and Ecuador to have a well-constrained regional constant; therefore, we included these earthquakes as part of the South America region.

Under the fully non-ergodic GMM approach, there can be large regional differences in the ground motion. In regions with sparse data, the non-ergodic approach can still be used, but with accompanying large epistemic uncertainties in the region-specific terms. With this concept, the low ground motions observed in Cascadia, Alaska, and northern Peru may simply be regional differences that should be accepted. In the development of our GMM, we have not implemented a fully non-ergodic GMM with the appropriate epistemic uncertainties. Therefore, we choose not to center the regional models for Cascadia, Alaska, and northern Peru on the sparse available data.

2 Dataset Selection

The NGA-SUB database includes recordings from seven different regions: Alaska, Cascadia, Central America, Japan, New Zealand, South America, and Taiwan as described by Stewart (2020). The full dataset includes over 71,000 three-component recordings. The October 18, 2018, version of the NGA-SUB dataset was used for this study. The main criteria used for selecting the subset of data are discussed under two main headings: (1) selection criteria for earthquakes and (2) selection criteria for recordings.

Data selection for GMM development is an iterative process. After the initial selection is made, preliminary regression analyses are performed and, by visual inspection of the residuals, outlier data are identified and evaluated. Based on the evaluation of the outlier data, the data selection criteria are modified, and the process is repeated.

2.1 SELECTION CRITERIA FOR EARTHQUAKES

The GMM is developed for two event types: interface and intraslab earthquakes. The NGA-SUB database includes six event classifications for earthquakes in subduction zones, as shown in Table 2.1. For interface events, we selected only Class 0 events. For intraslab events, we selected both Class 1 (intraslab events) and Class 5 (intraslab events from lower part of a double seismic zone). We excluded the shallow events in the overriding plate (Class 2), mantle events (Class 3), and outer-rise events (Class 4) because these events are not representative of the sources that typically control seismic hazard in subduction zones. In addition, the events that are unclassified or classified with low confidence are considered unreliable and were removed.

To reduce the potential for errors in the identification of interface and intraslab earthquakes, unusually shallow intraslab events (depth to top of rupture, Z_{TOR}, less than 20 km) and unusually deep interface events ($Z_{TOR} >$ 50 km) were excluded.

For all regions, the minimum magnitude of 5 is used. The minimum of three recordings per event (after all of the selection criteria have been met) is applied to improve the reliability of estimates of the event terms. The Cascadia region is an exception: we included Cascadia events with less than three recordings due to the small number of earthquakes in Cascadia in the database and the importance of this region for seismic hazard applications in the Pacific Northwest.

Figure 2.1 shows the distribution of between-event residuals for PGA with Z_{TOR} from a preliminary model without basin-depth scaling. Seven intraslab events (identified by the box in

Figure 2.1) have large negative event terms and shallow hypo-central depths. At short spectral periods, the intraslab events have much larger ground motions than the interface earthquakes, so these large negative between-event residuals could be explained by these shallow earthquakes being interface events that were misclassified as intraslab events. Because it is difficult to distinguish between interface and intraslab events at these shallow depths, we consider it likely that these events were misclassified; therefore, we removed them from the selected dataset.

2.2 SELECTION CRITERIA FOR RECORDINGS

To avoid potential bias in the ground motions, the following selection criteria are applied:

1. Remove recordings with multiple event flag equal to 1 (time window of the recording includes more than one earthquake);
2. Remove recordings with late P-trigger;
3. Remove recordings that are missing key metadata (magnitude, distance, or site condition);
4. Remove stations that are not free-field (GMX first letter N, Z, and F);
5. Remove downhole recordings with instrument depth greater than 2 m;
6. Remove recordings with rupture distance (R_{RUP}) greater than R_{max} ;
7. Remove ground motions from the “TW” network for Taiwan region due to an apparent bias; and
8. Remove recordings from the Tohoku earthquake with $R_{RUP} > 200$ km

The first five criteria were included to have reliable data representative of free-field conditions. The sixth item (R_{max} limit) is included to avoid biasing the data due to censored ground motions at large distances. Censoring can occur when there are missing recordings (not triggered or not above the noise level) that would have shown lower ground motions than the recorded ground motions. The procedure for estimating R_{max} is described in the NGA-SUB database report (Stewart, 2020). The recordings with $R_{RUP} > R_{max}$ are removed to avoid a bias towards larger ground motions at large distances. This criterion has the largest effect on the Taiwan dataset.

The seventh item is related to the TW network in Taiwan, which leads to systematically lower ground motions than the other networks for the recordings from the same earthquake, suggesting that there is an issue with the gains or with the instrument responses for this network. Figure 2.2 compares the residuals for the “CWB” and “TW” networks from a preliminary regression analysis. Given the apparent bias from the TW network, all of the recordings from this network were excluded. The data from TW network represents about 10% of the recordings in Taiwan dataset.

The eighth selection criterion (200-km limit for the recordings of Tohoku earthquake) is imposed because the large-distance attenuation of short-period ground motions from the Tohoku earthquake is much steeper than the large-distance attenuation of the other M>8 Japanese subduction earthquakes in our dataset; see Figure 2.3. A potential cause of the steeper attenuation could be that the distance to the closest point on the rupture (R_{RUP}) may not reflect the distance to the asperities that generate the strong ground motion for very large earthquakes; however, using the closest distance to an asperity in place of R_{RUP} did not remove the faster attenuation observed in the Tohoku recordings. We also checked the distance dependence of the within-event residuals for PGA from the M8.8 2010 Maule, Chile, earthquake (shown in Figure 2.3) and did not observe a strong trend of the residuals with distance for this large interface event.

The difference in the large-distance attenuation is likely due to the regional differences in the path effects within the Japan region, but the functional form of our GMM does not account for event-specific large-distance scaling. Including the large-distance data from Tohoku earthquake would cause the event term for this earthquake to be much more negative to be able to match the average residual over all distances. In that case, the event term would represent the path effects, but not the source effects. The key issue is that the regression approach used in Chapter 4, with a random effect for the earthquake, assumes that the attenuation is similar for all events. If the event-specific attenuation is very different, then using an event term that is a constant shift at all distances is not an appropriate statistical approach.

In addition to the criteria listed above, recordings and earthquakes were removed if they appeared as large outliers by visual inspection. The large outliers are likely due to errors in the reported gains of the instruments or errors in the meta data (magnitude and distance). The project's budget prohibited tracking down the causes of the outliers, and they were simply removed from our subset.

For regions other than Cascadia, the rupture distance range was limited to 500 km. This range captured most of the distances that contribute to the hazard, but avoided some of the potentially strong path-specific effects at larger distances. To capture the large-distance scaling in the eastern Washington and western Idaho regions, data out to a distance of 800 km from the Cascadia region (except for two northern California earthquakes) were included. The large-distance data from the northern California events that are part of our Cascadia subset were excluded because they represent very different path effects from those in the Washington/Oregon region.

The back-arc stations were excluded because the attenuation in the back-arc varies greatly among regions. There is very strong back-arc attenuation in parts of Japan that is not seen in other regions. Within the Japan region, the back-arc effects have large variations for different areas, so the back-arc attenuation will depend on the ray path lengths within different sub-regions of Japan. The NGA-SUB dataset provided the lengths of the rays paths in the different subregions in Japan that could be used in a GMM, but the model becomes overly complex if these parameters are included. To properly model these effects, the path effects should be modelled using the method of Dawood and Rodriguez-Marek (2013). This approach can be used to adjust the region-specific GMM to include path effects as shown by Kuehn et al. (2019). For our GMM, we chose to limit the GMM applicability to fore-arc sites to avoid the complexities of the back-arc path effects.

2.3 SELECTED DATASET

The number of earthquakes and number recordings in the NGA-SUB database and in the selected subset for each region are provided in Table 2.2. A large percentage of the data in the NGA-SUB dataset were not included in our subset of data: only 11% of earthquakes and 12% of the recordings are included. The event class selection (Class 0, 1, and 5 only) had a significant effect, requiring removal of over 25,000 recordings. The 500-km upper limit on distance and the M5 lower limit on magnitude removed an additional 19,000 recordings. This left a subset of just under 34,000 recordings, Criteria 1–10 (excluding the R_{max} limit) removed about 7000 recordings, and the R_{max} limit removed an additional 12,000 recordings. Restricting the sites to the fore-arc (except for Cascadia) removed an additional 3500 recordings. For Cascadia, we excluded earthquakes that are in Northern California and which are not clearly associated with the interface or intraslab, and may be more representative of crustal earthquakes. This removed an additional 270 recordings. Of the total of 10,921 recordings that met our selection criteria, an additional 2150 did not include enough recordings per event or were identified as questionable recordings and were removed. The final selected subset consists of 8764 recordings from 202 earthquakes.

As noted above, nearly 90% of the data in the full dataset were excluded. Figures 2.4 and 2.5 compare the magnitude distance distribution of the selected data and the excluded data. The excluded data includes recordings from large magnitude events at moderate distances. While the NGA-SUB project put in considerable effort to compile the ground-motion database, there is a need for additional review and correction of the metadata and ground motions so that a larger percentage of the recordings are considered reliable and can be used in future updates of subduction GMMs.

The truncation of the data at R_{max} is a simple but severe approach to address the censoring of small ground motions. As noted, almost 12,000 recordings were removed due to the R_{max} limit. A regression approach that uses a truncated distribution should be considered in the future to allow the data beyond R_{max} to be included in the regression.

The pseudo spectral acceleration (PSA) values for the selected recordings are only used in the regression analysis for spectral frequencies greater than 1.25 times the high-pass corner frequency used in the record processing to avoid a bias in the PSA values due to the filtering (Abrahamson and Silva, 1997). This requirement produces a dataset that varies as a function of period. The period dependence of the number of earthquakes and number of recordings used in the regression analysis is shown in Figure 2.6.

The magnitude-distance distribution of the selected dataset for short periods is given in Figure 2.7. The majority of the data in our dataset are from Japan. There is good coverage for magnitudes 6.0–8.2 for interface earthquakes and for magnitudes 5.0 –7.3 for intraslab earthquakes. The distribution of the V_{S30} of the recordings by region is shown in Figure 2.8. There is good coverage of the V_{S30} between 200 m/sec and 750 m/sec with 80% of the data being in this range. The number of usable recordings drops off rapidly for rock sites: less than 5% of the data has $V_{S30} > 1000$ m/sec and less than 1% of the data has $V_{S30} > 1300$ m/sec.

The NGA-SUB dataset includes multiple alternative methods for defining Class 1 (mainshocks) and Class 2 (aftershocks) events based on the size of the separation distance between events and how the separation distance is computed. This classification is only for use with GMMs to account for potential differences in the ground motions from smaller events (aftershocks) occurring close to larger magnitude events (mainshocks) in both space and time. A detailed description of the mainshock/aftershock classification scheme is given in Stewart (2020). The classification is provided for separation distances of 10 km, 20 km, 40 km, and 80 km. We selected the classification based on closest distance from the Class 1 rupture plane to the potential Class 2 rupture plane, denoted $R_{CLOSEST\_P2P}$, being less than 20 km. That is, if $R_{CLOSEST\_P2P}$ is less than 20 km for an event that occurs close in time, then the latter event is considered a Class 2 event. We selected the 20-km distance limit based on a preliminary evaluation of the between event residuals that showed that strongest correlation using this distance limit.

2.4 BASIN DEPTH AND CORRELATION WITH V_{S30}

Two parameters have been used in the NGA-W2 GMMs to model the basin-depth effects: the depth to V_S = 1.0 km/sec, denoted by $Z_{1.0}$ and the depth to V_S = 2.5 km/sec, denoted by $Z_{2.5}$. For our subduction GMM, we selected the $Z_{2.5}$ parameter over the $Z_{1.0}$ parameter because the basins in the Seattle region are deep-rock basin, and the basin effects for these basins are not captured by the $Z_{1.0}$ parameter. The NGA-SUB database only includes $Z_{2.5}$ values for the Japan and Cascadia regions.

As is common in ground-motion datasets, the $Z_{2.5}$ values in NGA-SUB database are correlated with the V_{S30} values. Figure 2.9 shows the correlation of $Z_{2.5}$ and V_{S30} values for the Cascadia and the Japan regions. As a result of this correlation, the scaling with V_{S30} scaling will include some of the basin-depth scaling. To account for this correlation, we developed models for the median basin depth as a function of the V_{S30}. For Cascadia, the median $Z_{2.5}$ for a given V_{S30} is given by Equation 2.1:

$$ln(Z_{2.50ref\_CAS}(m)) = \begin{cases} 8.52 & \text{for } V_{S30} < 200\, m/sec \\ 8.52 - 0.88\, ln(V_{S30}/200) & \text{for } 200\, m/sec < V_{S30} < 570\, m/sec \\ 7.6 & \text{for } V_{S30} > 570\, m/sec \end{cases} \tag{2.1}$$

For Japan, the the median $Z_{2.5}$ for a given V_{S30} is given by Equation 2.2:

$$ln(Z_{2.50ref\_JP}(m)) = \begin{cases} 7.3 & \text{for } V_{S30} < 170\, m/sec \\ 7.3 - 2.066\, ln(V_{S30}/170) & \text{for } 170\, m/sec < V_{S30} <= 800\, m/sec \\ 4.1 & \text{for } V_{S30} > 800\, m/sec \end{cases} \tag{2.2}$$

Table 2.1: Event classes.

Event Class Index	Event Class Description
0	Subduction interface event
1	Subduction intraslab event
2	Shallow crustal/overriding plate event
3	Mantle event
4	Outer rise event
5	Intraslab, lower double seismc zone event
-999	Unknown
-888	Interface event with small confidence
-777	Intraslab event with small confidence
-666	Shallow crustal/overriding plte events with small confidence
-444	Outer rise event with small confidence

Table 2.2: Dataset by region for the selected subset.

		Full Dataset		Selected Dataset	
Region Number	Region Name	Number Eqk	Number Rec	Number Eqk	Number Rec
1	Alaska	142	3,026	16	257
2	Cascadia	35	2,143	6	177
3	Central America	272	2,648	14	74
4	Japan	227	40,717	72	5,053
5	New Zealand	227	4,309	30	440
6	South America	849	5,994	51	660
7	Taiwan	78	12,503	13	2,103
	Total	1880	71,340	202	8,764

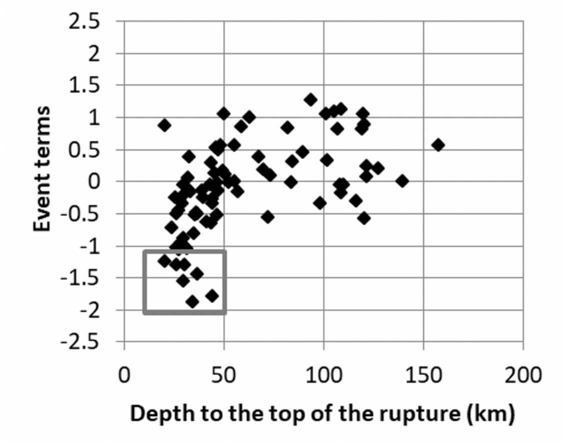

Figure 2.1: Distribution of the event terms from preliminary analysis for the intraslab events with magnitude and depth to the top of the rupture.

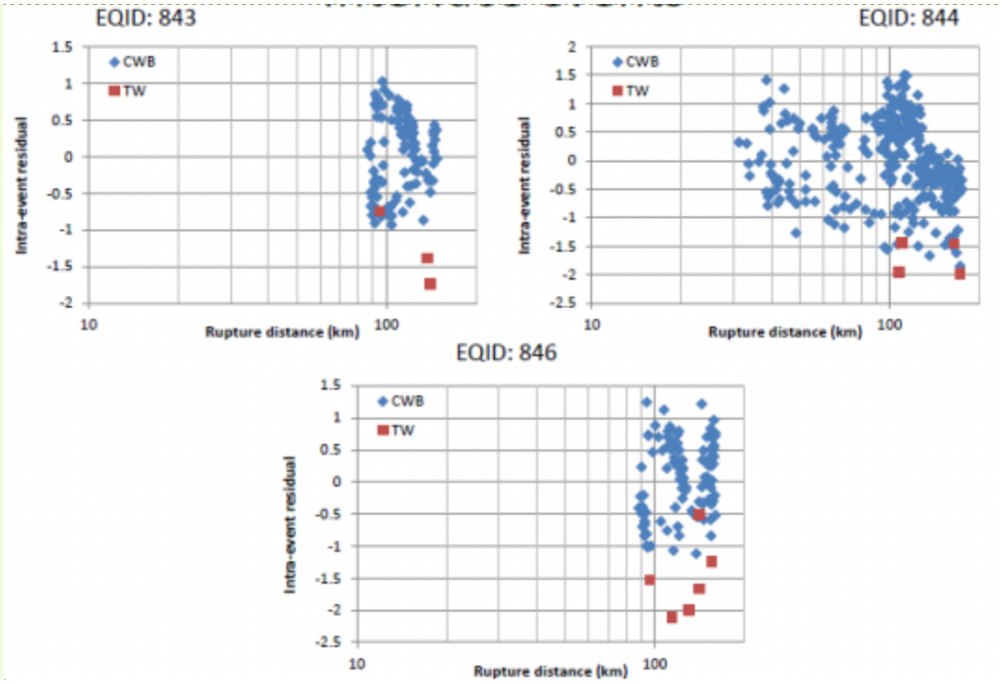

Figure 2.2: Distribution of the residuals from preliminary analysis for events in the Taiwan dataset that includes data from the TW and CWB seismic networks.

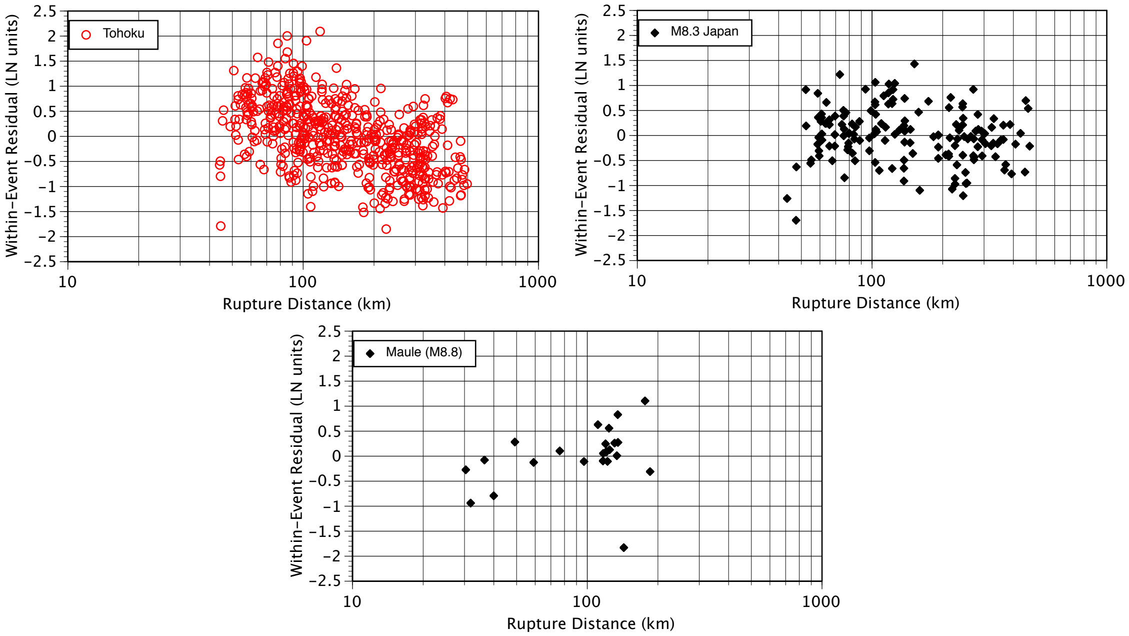

Figure 2.3: **Comparison of the distance dependence of the within-event residuals for the 2011 Tohoku earthquake with the residuals for two other large magnitude interface earthquakes.**

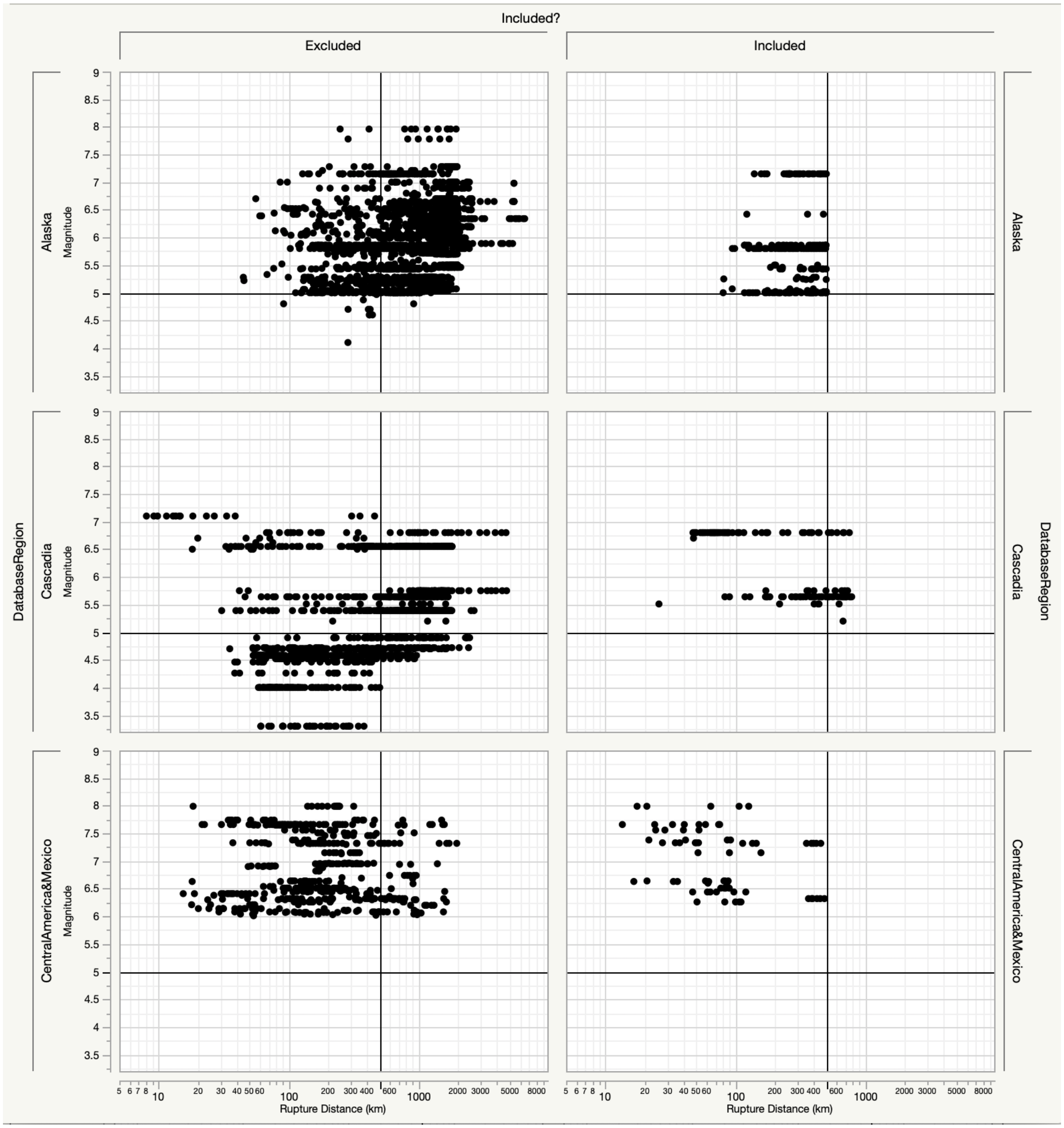

Figure 2.4: Magnitude-distance distribution for recordings in Regions 1-3 that are excluded (left panels) compared to those that are included in the selected subset (right panels).

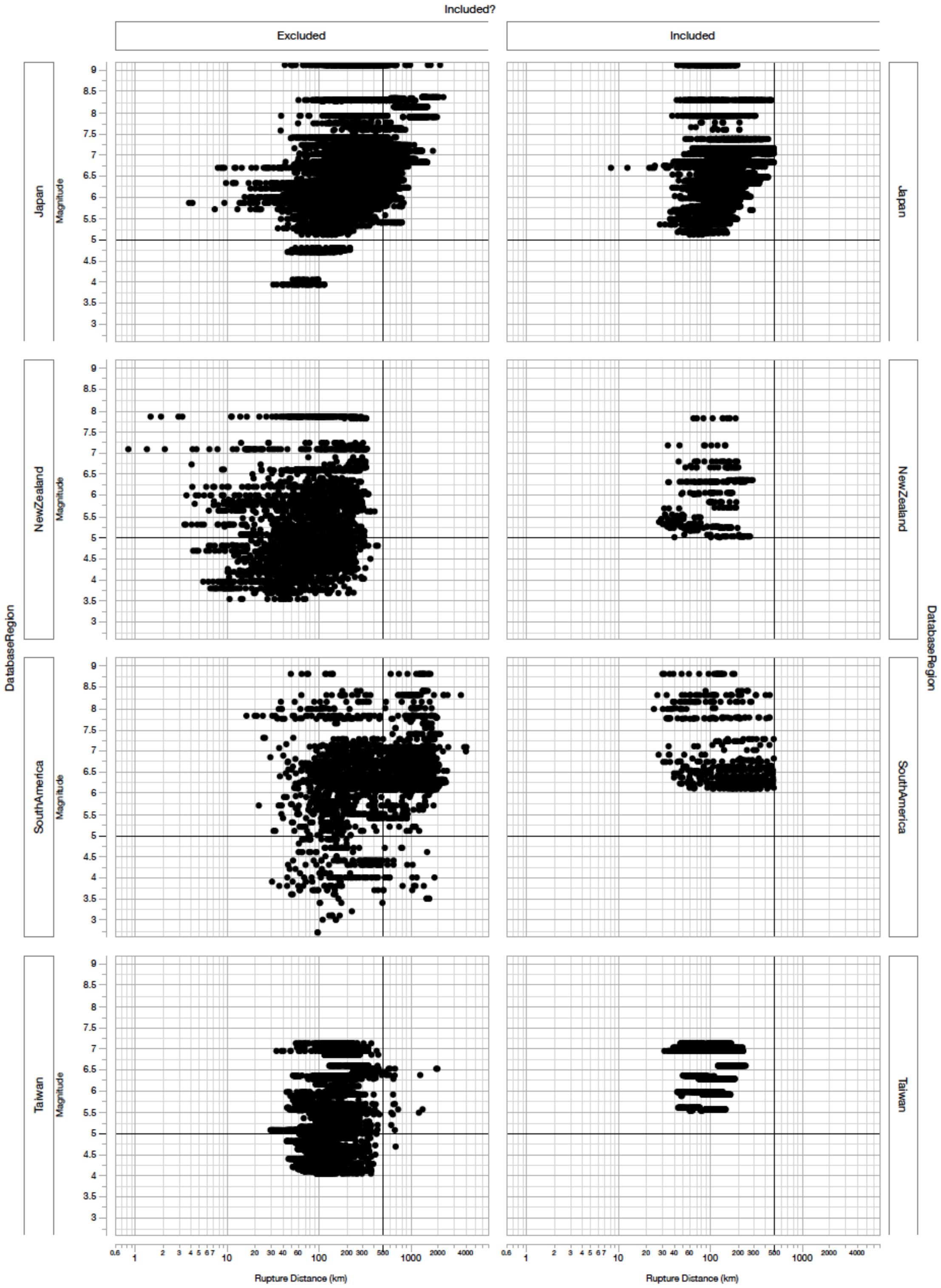

Figure 2.5: **Magnitude-distance distribution for recordings in Regions 4–7 that are excluded (left panels) compared to those that are included in the selected subset (right panels).**

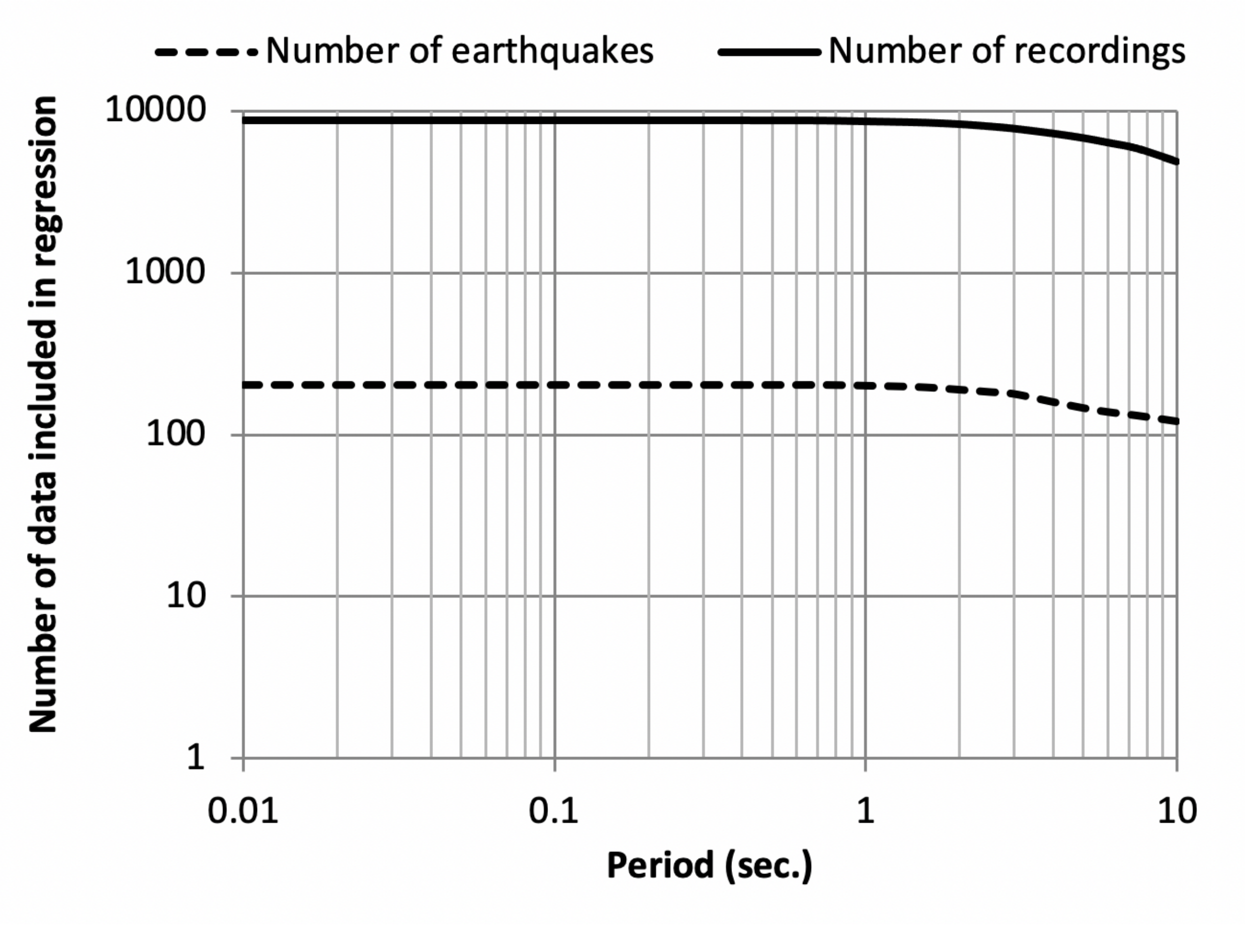

Figure 2.6: Number of earthquakes and number of recordings in the selected subset by period.

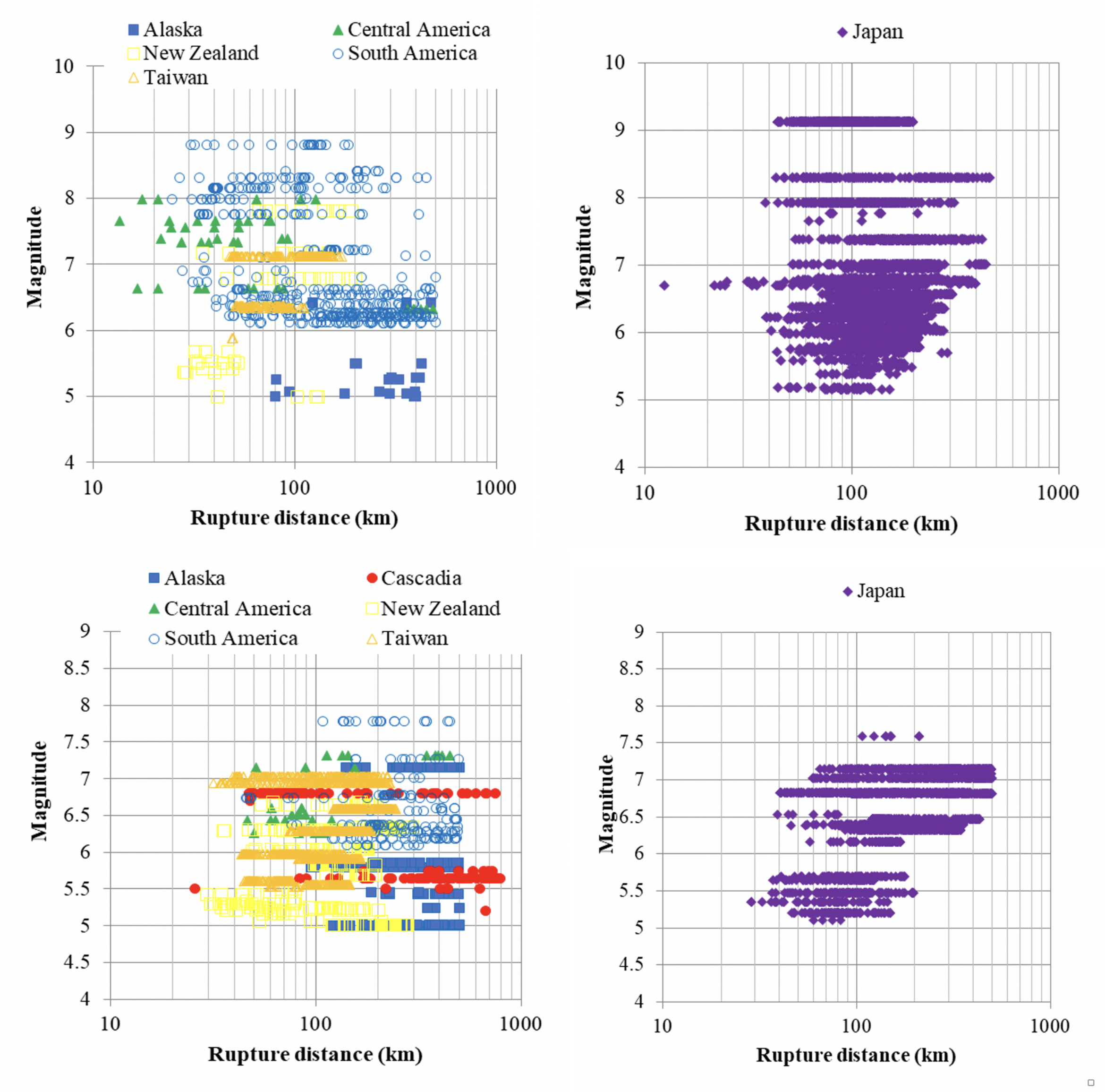

Figure 2.7: Magnitude-distance distribution for the selected subset for PGA. Top row is for interface earthquakes. Bottom row is for intraslab earthquakes.

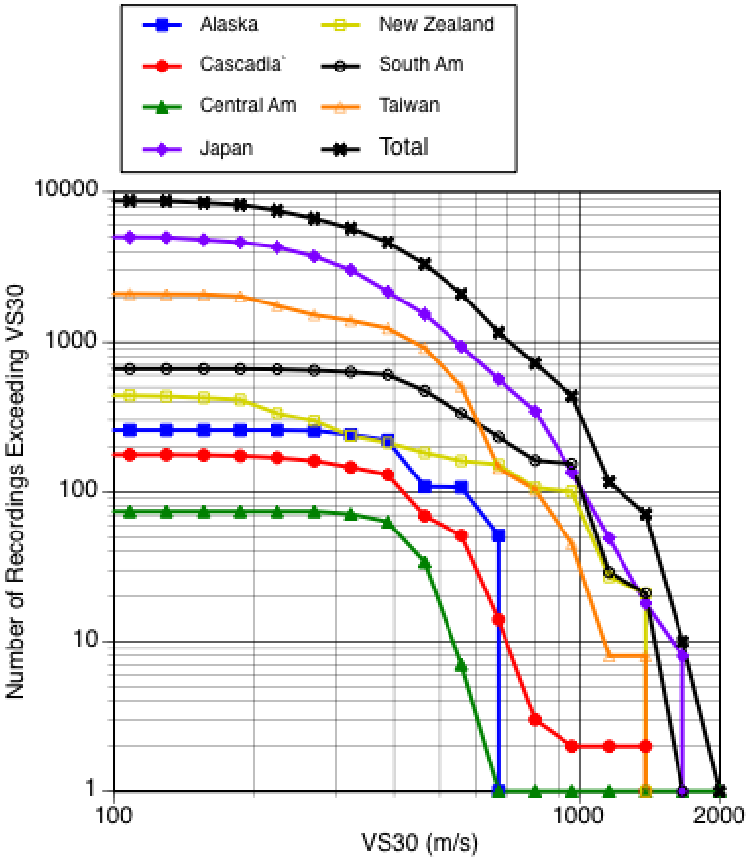

Figure 2.8: Complementary cumulative distribution of V_{S30} by region.

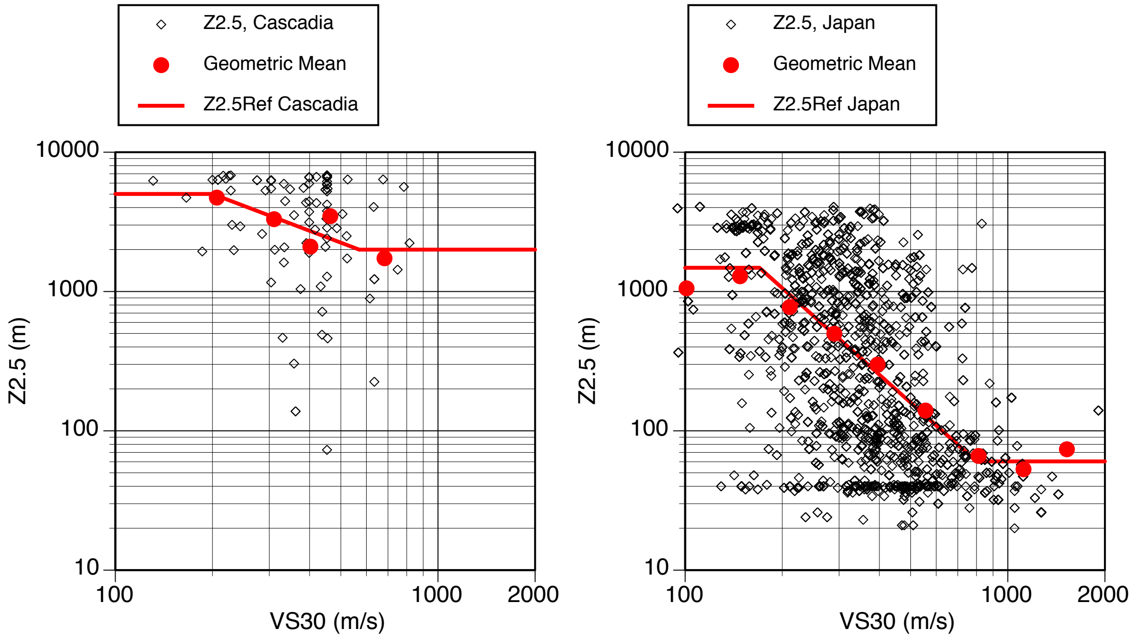

Figure 2.9: Correlation of $Z_{2.5}$ and V_{S30} for Japan and Cascadia. The geometric mean of the $Z_{2.5}$ is shown by the circles and the model used for the Z_{ref} is shown by the lines.

3 Functional Form for the Median

The functional form for the proposed model is based on the functional form used in the 2016 BCHydro GMM (Abrahamson et al., 2016) with modifications to include the regionalization for the constant, linear R scaling, V_{S30} scaling, and $Z_{2.5}$ scaling. The backarc scaling term included in the 2016 BCHydro model is removed because the selected dataset excluded the stations located in the backarc region, except for Cascadia.

The base model is given by:

$$\begin{aligned} ln\left(PSA(g)\right) = a_1 + \left(a_2 + a_3(M-7)\right) ln(R_{rup} + H_{FF}(M)) \\ + a_6 R_{RUP} + f_{mag}(M,F) + F f_{ZTOR}(Z_{TOR}) \\ + f_{site}(PGA_{1000}, V_{S30}) + F f_{slab}(R_{Rup}) \\ + f_{basin}(Z^{'}_{2.5}) + FASa_{15} \end{aligned} \tag{3.1}$$

in which:

$PSA(g)$ = RotD50 of the 5%-damped spectral acceleration

M = moment magnitude

R_{RUP} = rupture distance (km)

F = event type (0 for interface and 1 for intraslab)

Z_{TOR} = depth to top of rupture (km)

V_{S30} = time-averaged shear-wave velocity over the top 30 m (m/sec)

PGA_{1000} = median peak acceleration (g) for V_{S30} = 1000 m/sec

$Z_{2.5}$ = depth to V_S=2.5 km/sec (m)

F_{AS} = 0 for earthquake Class 1 (mainshock) and F_{AS}=1 for earthquake Class 2 (aftershock)

The finite-fault term, $H_{FF}(M)$, is adopted from the 2016 BCHydro model and is given by

$$H_{FF}(M) = C_4 exp\left((M-6)a_9\right) \tag{3.2}$$

3.1 MAGNITUDE SCALING

For shallow crustal earthquakes, there is a break in the slope of the magnitude scaling (at about M_W = 6.5 for California) due to the limits on the maximum rupture width of earthquakes resulting from the limited seismogenic thickness of the crust (about 15 km). In subduction zones, the maximum rupture width can be much larger than that for shallow crustal earthquakes; therefore, the break in the magnitude scaling is expected to occur at larger magnitudes. The 2016 BCHydro model used a period-dependent break in the scaling for large magnitudes (**M**7.6 to **M**8.0) for the interface and assumed that the break in the magnitude scaling is period-independent at M_W=7.5 for intraslab events because there was no quantitative data to constrain that value.

Archuleta and Ji (2018) conducted a suite of numerical finite-fault simulations for intraslab earthquakes to constrain the break in the magnitude scaling for intraslab events. The simulation results showed that the break in the magnitude scaling depends on the thickness of the slab. Using a relation between the thickness and the age of the slab, an estimate of the break points in the magnitude scaling for intraslab events in different subduction zones around the world was developed. We adopted the region-dependent magnitude break points for intraslab events from Archuleta and Ji (2018), which are listed in Table 3.1.

Recently, Campbell (2020) used the concept of the break in the magnitude scaling being related to the down-dip width of the subduction interface to estimate the region-specific break in the magnitude scaling for interface earthquakes. We agree with the general concept of this approach, but there are no accompanying finite-fault simulations to calibrate the break point in the magnitude scaling. Therefore, we use region-independent break points similar to those from the 2016 BCHydro GMM for interface earthquakes, which are based on numerical simulations and the ground motions from the 2010 Maule and 2011 Tohoku earthquakes.

To account for the break in the magnitude scaling, a bi-linear functional form is used with different small-to-moderate magnitude scaling for intraslab and interface events, but with the same large magnitude scaling:

$$f_{mag}(M) = \begin{cases} (a_4 + Fa_{45})(M - C_1) + a_{13}(10 - M)^2 & \text{for } M \leq C_1 \\ a_5(M - C_1) + a_{13}(10 - M)^2 & \text{for } M > C_1 \end{cases} \tag{3.3}$$

in which C_1 is the break point in the magnitude scaling. To allow the break point for the large-magnitude scaling to differ for interface and intraslab events, the C_1 term in Equation 3.1 and Equation 3.3 is given by:

$$C_1 = FC_{1s} + (1 - F)C_{1i} \tag{3.4}$$

in which C_{1s} is the break point for intraslab events, and C_{1i} is the break point for interface events.

A preliminary regression showed stronger magnitude scaling for intraslab events. Therefore, Equation 3.3 allows for a difference in the magnitude scaling between intraslab and interface events (a_{45} term) for magnitudes less than C_1. This is a major change from the 2016 BCHydro model, which had used the same magnitude scaling for intraslab and interface events. As a result of weaker magnitude scaling for interface events, the C_1 values for interface earthquakes are increased by about 0.2 magnitude units to maintain the same amplitude of the ground motion for large magnitudes to be consistent with the Tohoku and Maule data. The period-dependent magnitude break points for interface events range from 8.2 at short periods to 7.8 at long periods.

3.2 INTRASLAB SCALING

In addition to difference in the magnitude scaling shown in Equation 3.3, the model for intraslab events includes a difference in the geometrical spreading and constant terms compared with the terms for interface events:

$$f_{slab}(R_{Rup}) = a_{10} + a_4(C_{1s} - \Delta C_{1s,reg} - 7.5) + a_{14} ln(R_{rup} + H_{FF}(M)) \tag{3.5}$$

The a_{10} and a_{14} terms represent the differences in the constant term and the geometrical spreading for intraslab events and interface events, respectively. The $\Delta C_{1s,reg}$ is the difference between the region-specific C_{1s} and the global C_{1s} of 7.5. The $a_4(C_{1s} - \Delta C_{1s} - 7.5)$ term is an additional constant that leads to a continuous function above and below $M = C_1$.

3.3 DEPTH SCALING

For intraslab earthquakes, the 2016 BCHydro model used a linear scaling with Z_{TOR} without any additional depth scaling for depths greater than 120 km. As part of preliminary analysis, the Z_{TOR} dependence of the short-period event terms was evaluated for different depth limits on the scaling. This evaluation showed that there is stronger depth scaling for $Z_{TOR} < 50$ km than for $Z_{TOR} > 50$ km. The steeper magnitude scaling for intraslab events with Z_{TOR} values less than 50 km may be related to some earthquakes in the 20–50 km depth range being misclassified. As discussed earlier, the intraslab events have much larger short-period ground motions than interface events for the same magnitude and distance, so the event terms for interface events that are misclassified as intraslab events would be large negative values. With these large negative residuals, the intraslab events at depths of 20–30 km have similar ground motions as interface events, which is consistent with the interpretation that they have been misclassified.

Because the depth scaling at shallow depths may reflect the misclassification of events as well as a depth effect, we modeled the depth scaling with two slopes: one for depths less than 50 km and one for depths greater than 50 km. The depth scaling is modeled using a tri-linear model with a break in slope at Z_{TOR} = 50 km and a second break at Z_{TOR} = 200 km beyond which there is no additional depth scaling.

$$f_{Z_{TOR}}(Z_{TOR}) = \begin{cases} a_8(Z_{TOR} - 50)F & \text{for } Z_{TOR} \leq 50\, km \\ a_{11}(Z_{TOR} - 50)F & \text{for } 50 \geq Z_{TOR} \leq 200\, km \\ a_{11}(150)F & \text{for } Z_{TOR} > 200\, km \end{cases} \tag{3.6}$$

We also evaluated the case where we used 100 km for the second break point; although this option improved the fit to the event terms for $Z_{TOR} < 100$km, it resulted in larger negative event terms for depths greater than 100 km. Using the limit on the depth scaling of 200 km led to a balance of the fit to the event terms for depths less than 100 km and the event terms for depths greater than 100 km.

3.4 SITE-RESPONSE SCALING

The linear site-amplification effects were modeled using a linear dependence on the $ln(V_{S30})$ with no additional scaling for $V_{S30} > 1500$ m/sec. The 1500 m/sec limit on the linear site factor is set due to lack of data for $V_{S30} > 1500$ m/sec and possible kappa effects (i.e., reduced damping) that could change the site factor at short periods for hard-rock sites.

For the nonlinear site-response effects, we adopted the nonlinear site amplification scaling in the 2016 BCHydro model, which uses the PGA_{1000} as the strength of shaking parameter. The site-response function of the proposed model is given in Equation 3.7. The V_{lin} term denotes the shear-wave velocity above which the site response becomes linear, and the V_S^* term sets the limit of the extrapolation of the linear (V_{S30}) scaling as shown in Equation 3.8.

$$f_{site} = \begin{cases} a_{12} ln\left(\frac{V_S^*}{V_{lin}}\right) - b\, ln(PGA_{1000} + c) \; + b\, ln\left[PGA_{1000} + c\left(\frac{V_S^*}{V_{lin}}\right)^n\right] & \text{for } V_{S30} < V_{lin} \\ (a_{12} + bn)\, ln\left(\frac{V_S^*}{V_{lin}}\right) & for V_{S30} \geq V_{lin} \end{cases} \tag{3.7}$$

$$V_S^* = \begin{cases} 1500 & \text{for } V_{S30} > \text{1500 m/sec} \\ V_{S30} & \text{for } V_{S30} \leq \text{1500 m/sec} \end{cases} \tag{3.8}$$

The nonlinear site-response terms, $b(T)$, n, and c, are taken directly from the 2016 BCHydro GMM. An initial evaluation of the within-event residuals versus the PGA_{1000} showed that adopted nonlinear site-amplification scaling is consistent with the nonlinear site effects in the new dataset. The applicability of the assumed nonlinear site terms to the subduction data is further evaluated using the residuals from the final model in Section 4.3.

3.5 BASIN-DEPTH SCALING

The depth to V_S=2.5 km/sec, $Z_{2.5}$ (in m), is used for the basin-depth parameter. In the GMM, the basin-depth scaling uses the normalized basin depth parameter, $Z_{2.5}^{'}$, defined by:

$$Z_{2.5}^{'} = \frac{Z_{2.5} + 50}{Z_{2.5ref} + 50} \tag{3.9}$$

in which $Z_{2.5ref}$ (in m) is the median $Z_{2.5}$ for a given V_{S30} (Equations 2.2 and 2.1). This normalized parameter is used to account for the correlation between V_{S30} and $Z_{2.5}$. The $Z^{'}_{2.5}$ term centers the basin-depth scaling so that the basin scaling that is implicit in the V_{S30} scaling is addressed.

The basin-depth scaling is modeled as a linear function of the logarithm of the normalized basin-depth parameter with a lower limit for low values of $Z^{'}_{2.5}$. For the Japan region, the basin-depth scaling is given by:

$$f_{basin\_JP} = \begin{cases} a_{41} ln(Z^{'}_{2.5}) & \text{for } ln(Z^{'}_{2.5}) > -2 \\ 0 & \text{otherwise} \end{cases} \tag{3.10}$$

For the Cascadia region, the data show an increase in the long-period ground motion for basin depths greater than $Z_{2.5ref}$, but they do not show a decrease for basin depths less than $Z_{2.5ref}$. Therefore, the basin-depth model for Cascadia is set to zero for $Z^{'}_{2.5} < 1$.

$$f_{basin\_CAS} = \begin{cases} a_{39} ln(Z^{'}_{2.5}) & \text{for } ln(Z^{'}_{2.5}) > 1 \\ 0 & \text{otherwise} \end{cases} \tag{3.11}$$

3.6 REGIONALIZATION OF THE BASE MODEL

For each region, we allow for three region-specific terms: large distance (linear R) scaling (a_6), linear site-amplification scaling (a_{12}) and the constant term (a_1). Table 3.1 shows the region-specific coefficients associated with each region. For the distance and V_{S30} terms, the coefficients are adjustments that are added to the global coefficients. Dummy variables, F_{Ri} are used to indicate the region: $F_{Ri} = 1$ for region i and 0 otherwise. The regionalized terms are denoted with a prime:

$$a^{'}_6 = a_6 + F_{R1} a_{24} + F_{R2} a_{25} + F_{R3} a_{26} + F_{R4} a_{27} + F_{R5} a_{28} + F_{R6} a_{29} + F_{R7} a_{30} \tag{3.12}$$

$$a^{'}_{12} = a_{12} + F_{R1} a_{17} + F_{R2} a_{18} + F_{R3} a_{19} + F_{R4} a_{20} + F_{R5} a_{21} + F_{R6} a_{22} + F_{R7} a_{23} \tag{3.13}$$

Because we developed the global constant at the end of the regression, using the average of the ground motion from the region-specific models, the regional constants are not added to the global constant:

$$a^{'}_1 = F_{R1} a_{31} + F_{R2} a_{32} + F_{R3} a_{33} + F_{R4} a_{34} + F_{R5} a_{35} + F_{R6} a_{36} + F_{R7} a_{37} \tag{3.14}$$

There is an additional regional term included for the Taiwan region. The distance scaling for Taiwan region is weaker than the distance scaling for other regions. This may be related to the limited distance range in the Taiwan dataset, due in part to the small dimension of the Taiwan island that limits the sampling of the distance attenuation. It may also be related to the severe truncation of the Taiwan dataset due to the R_{max} limits. If the global geometrical-spreading term is used, then the region-specific linear R term for Taiwan becomes a positive value, which is non-physical and would lead to increasing median ground motions with distance when the GMM is extrapolated to very large distances. Therefore, we use a region-specific geometrical-spreading term combined with a small negative linear R term for Taiwan. The region-specific geometrical-spreading term is given by:

$$a_2' = a_2 + a_{16} F_{R7} \tag{3.15}$$

Table 3.1: Region-specific terms.

Region	C_{1s}	V_{S30} add to a_{12}	Linear R add to a_6	Constant replaces a_1	$Z_{2.5}$	Geometrical spreading add to a_2
Alaska	7.9	a_{17}	a_{24}	a_{31}	-	-
Cascadia	7.1	a_{18}	a_{25}	a_{32}	a_{39}	-
Central America	7.4	a_{19}	a_{26}	a_{33}	-	-
Japan	7.6	a_{20}	a_{27}	a_{38}	a_{41}	-
New Zealand	8.0	a_{21}	a_{28}	a_{35}	-	-
South America	7.5	a_{22}	a_{19}	a_{36}	-	-
Taiwan	7.7	a_{23}	a_{30}	a_{37}	-	a_{16}

4 Regression Analysis

The random-effects model was used for the regression analysis following the procedure described by Abrahamson and Youngs (1992). A single random effect for the earthquake is used:

$$ln(PSA_{es}) = \mu(M_e, R_{es}, ...) + \delta B_e + \delta W_{es} \tag{4.1}$$

in which δB_e is the between-event residual, δW_{es} is the within-event residual, and $\mu(M_e, R_{es}, ...)$ is the mean ground motion in natural log units.

The regression is performed in a number of steps to arrive at a smooth model. The coefficients are smoothed to either lead to smooth spectral shape or to constrain the model to be consistent with basic seismological constraints. Tables 4.1 and 4.2 list the parameters that were estimated by the regression in each step and those that were smoothed and then held fixed in the following step.

4.1 FIXED COEFFICIENTS

In the 2016 BCHydro model, several terms related to the scaling for large magnitudes were constrained based on analytical modeling and judgment, including the magnitude dependence of the geometrical-spreading term (a_3), the linear magnitude term for large magnitudes (a_5),and the finite-fault terms (a_9 and C_4). The NGA-SUB dataset does not include a significant increase in the large magnitude data from subduction earthquakes when compared to the dataset used to develop the 2016 BCHydro model. There is new information on ground motions from finite-fault simulations for **M**9 megathrust earthquakes along the Cascadia subduction zone from the M9 project (Frankel et al., 2018). In general, the ground motions from the M9 project are consistent with the large-magnitude scaling in the BCH2016 model. Given the consistency with M9 project results with the 2016 BCHydro GMM and the lack of new empirical data from large interface events, the constraints used in the 2016 BCHydro model are maintained in the current model. The constrained terms are listed in Table 4.3.

As noted in Section 3.4, the coefficients of nonlinear site response model $(b(T), n, c)$ are also fixed to the values from the 2016 BCHydro model.

4.2 SMOOTHING OF THE COEFFICIENTS

4.2.1 Step 1

In Step 1, the linear magnitude scaling for $M < C_1$ is evaluated. The quadratic magnitude term, a_{13}, is set to zero because the scaling for $M > 5$ should be linear for short periods that correspond to frequencies above the source corner frequency. A period-independent a_4 term is set based on the estimated values at the short periods. Figure 4.1 shows the constant value of a_4 that is set based on the estimated values for periods less than 0.15 sec. In later steps, the steeper magnitude scaling for longer periods is modeled by the quadratic term $(10 - M)^2$. This approach of separating the short-period linear magnitude term from the quadratic scaling at longer periods makes it easier to constrain the magnitude scaling to avoid oversaturation for $M < 10$ by requiring the a_{13} term to be negative. It also leads to a smoother spectral shape.

4.2.2 Step 2

In Step 2, the global additional linear magnitude scaling for intraslab events, a_{45}, is evaluated. The same approach from Step 1 is used: the a_{45} term is estimated only for the short periods. Figure 4.1 shows the smoothed combined linear magnitude term for intraslab events ($a_4 + a_{45}$).

4.2.3 Step 3

In Step 3, the global quadratic magnitude term, a_{13}, is evaluated. Figure 4.3 shows the point estimates of a_{13} and the smoothed model. As noted earlier, the a_{13} terms are constrained to be less than or equal to zero to force monotonically increasing median ground motion with magnitude (i.e., oversaturation is not allowed). In particular, the short-period values of the smoothed a_{13} are set to zero. At long periods, the quadratic term is similar to the 2016 BCHydro model.

4.2.4 Step 4

In Step 4, the global geometrical-spreading term for interface events, a_2, is evaluated. The estimated a_2 values are shown in Figure 4.4. We do not include the dip in the estimated a_2 values between 0.02 and 0.1 sec even though the amplitude of the dip is much greater than the standard error of the estimates; including it may lead to unrealistic spectral shapes at short periods if the model is extrapolated to short distances. For example, the spectral values at short periods can drop below the PGA, producing a dip in the response spectrum.

For periods up to 2 sec, the geometrical spreading for interface events is similar to the 2016 BCHydro model. At long periods (T>3 sec), the geometrical spreading is set to a constant value because there is no physical basis for the geometrical spreading becoming steeper (more negative a_2) at long periods, as shown in the estimated values. This suggests that other terms are trading off with the geometrical spreading for interface events at long periods.

4.2.5 Step 5

In Step 5, the global geometrical-spreading term for intraslab events, a_{14}, is evaluated. The a_{14} term is the difference in the geometrical-spreading terms for intraslab events and interface events. Therefore, the sum of $a_2 + a_{14}$ is used for the smoothing of the a_{14} coefficients rather than smoothing the a_{14} term by itself.

The estimated and smoothed $a_{14} + a_2$ values are shown in Figure 4.5. For intraslab events, the geometrical spreading continues to increase at long periods, which is consistent with the expected behavior. Compared to the 2016 BCHydro model, the geometrical spreading for intraslab events is much steeper at long periods. This likely reflects an improved dataset from intraslab events at long periods in terms of the amount of data and the data processing. Another difference is at very short periods (0.03 to 0.1 sec), the smoothed model follows the steeper geometrical spreading at the short periods, whereas, the 2016 BCHydro model did not allow steeper slopes at short periods.

4.2.6 Step 6

In Step 6, the global linear R term, a_6 is evaluated. To allow better constraint on the linear R term, the distance used for the regression is increased to 500 km for all regions except for Cascadia, which was increased to 800 km because of the emphasis on the applicability of the GMM to the Cascadia region. This increased distance range was used for all subsequent steps.

The estimated and smoothed a_6 values are shown in Figure 4.6. The estimated a_6 terms are very smooth, so the main smoothing applied is to the long-period values ($T > 5$ sec). As with the geometrical spreading, a reduction of the linear R term with increasing period does not make physical sense for the global model. Therefore, the smoothed a_6 model is constant for periods greater than 5 sec.

4.2.7 Step 7

In Step 7, we smoothed the two Z_{TOR} scaling terms, a_8 and a_{11}. The estimated and smoothed terms are shown in Figure 4.7. The slope for the 20–50 km range (a_8) shows a sharp drop in the 1–2 sec range. To avoid a large effect on the spectral shape with small changes in depth, we imposed a more gradual period dependence on a_8. For the 50–200 km depth range, the estimated a_{11} values are fairly smooth with period; therefore, only minor smoothing is needed.

4.2.8 Step 8

In Step 8, the regional linear R terms are evaluated. Because the regional linear R terms are modeled as an adjustment to the global linear R term, we applied the smoothing to the sum of the global and regional terms, Figure 4.8 shows the total regional R term for each region. A constraint on the GMM is that the coefficient on the linear R term is negative to avoid the model leading to increasing ground motion with distance at some very large distance range. This constraint was met for all of the regions except for Taiwan.

The large positive linear R term for Taiwan indicates that the global geometrical-spreading term is not applicable to the Taiwan region. This is likely related to the limited distance range in the Taiwan data and the severe reduction in data due to the R_{max} limit. To force a positive linear R term for Taiwan, a region-specific geometrical spreading term is needed for Taiwan.

The period dependence of the Cascadia, Japan, and South America linear R terms are similar and are close to the global model. For the New Zealand and Central America regions, the linear R terms at short periods are much larger (less negative) than the linear R terms for the global model. At intermediate periods (0.1 sec $< T <$ 1 sec), the linear R terms decrease from the values at short periods. This trend of stronger attenuation at intermediate periods compared to short periods does not make physical sense, and it indicates that the global geometrical spreading is not applicable to these two regions; however, for the distance range of interest, the current set of coefficients will lead to appropriate distance scaling and will not cause problems if extrapolated to very large distances. At long periods (T> 1 sec), the linear R terms become similar to the global model. Given the larger standard error for the coefficients for these two regions, we used the average for these two regions to develop the smoothed model of the linear R term.

4.2.9 Step 9

In Step 9, the region-specific geometrical spreading is estimated for the Taiwan region (a_{16}). The region-specific linear R term for Taiwan (a_{30}) is strongly correlated with the geometrical spreading term. Therefore, we fixed a_{30} such that the total linear R term is 0.001. That is $a_{30} = -0.001 - a6$.

With the linear R term for Taiwan held fixed, the a_{16} term is estimated and smoothed. Again, the smoothing is done on the total geometrical spreading term ($a_{16} + a2$). Figure 4.9 compares the Taiwan region-specific geometrical spreading coefficients with the global geometrical-spreading coefficients. There is a very large difference in the geometrical spreading for Taiwan and for the global model. We think that this large difference reflects a trade off between the event terms and the geometrical spreading due to the small distance ranges sampled for many of the earthquakes in Taiwan: if the data from individual earthquakes sample small distance ranges, the data can be fit equally well by different combinations of event terms and distance attenuation (i.e., both the distance slope and the intercept cannot be resolved). As discussed earlier, the higher ground motions at larger distances may also be related to the incomplete sampling of the ground motions at large distances in the Taiwan region.

4.2.10 Step 10

In Step 10, both the event-type term, a_{10}, and the global V_{S30} scaling term, a_{12}, are evaluated. The event-type term is related larger short-period ground motions from intraslab events as compared to interface events for the same magnitude and distance. Because the functional form of the model does not include a term to center it on the average distance, the a_{10} term reflects the change in the intercept at short distances and not the absolute level of the difference between the ground motion for intraslab events and interface events. That is, the value of the a_{10} coefficient by itself does not indicate the difference between the amplitude of the ground motion for intraslab and interface events.

The estimated and smoothed global V_{S30} coefficient, a_{12}, are shown in Figure 4.10. The period dependence of the a_{12} values is similar to that in the 2016 BCHydro model. As majority of the data are from Japan, this term is representative of the V_{S30} scaling in Japan. Because the dataset used to develop the 2016 BCHydro model was also dominated by Japanese data, the agreement in the V_{S30} scaling is expected.

4.2.11 Step 11

With the global V_{S30} scaling fixed, we then estimated the regional V_{S30} coefficients. As with the other regional terms, the regional coefficients were added to the global coefficient and the sum was smoothed for each region, as shown in Figure 4.11.

The V_{S30} parameter is not a fundamental parameter of the site amplification; however, in natural deposits, it is often correlated with the deeper V_S profile that does control the linear site amplification. Because the correlation between the V_{S30} and the deeper V_S profile depends on the depositional environment, there can be regional differences in the relation between the V_{S30} and the site amplification. The region-specific V_{S30} terms in the GMM are intended to capture the differences in the depositional environments for the seven regions.

For the Japan and New Zealand regions, the shape of the period dependence of V_{S30} terms are similar to the shape of the global model. Only light smoothing is applied to the V_{S30} terms for these two regions.

For the Cascadia region, the general shape of the linear V_{S30} scaling is similar to the global model, but the amplitudes are different. The Cascadia model has V_{S30} scaling similar to the global model for periods greater than 0.2 sec, but much stronger V_{S30} scaling (more negative value of $a_{12} + bn$) at periods less than 0.2 sec. The stronger scaling at short periods could indicate that there are shallow-soil sites with a strong impedance contrast that lead to site resonances at the shorter periods, which is not seen in the regions with more gradual gradients in the V_S profiles for soil sites. The standard errors of the estimates are much larger for Cascadia then for most other regions due to the smaller number of data points for this region. We smoothed the V_{S30} scaling for Cascadia so that it followed the global model for periods greater than 0.5 sec. For shorter periods, the smoothed model followed the estimated scaling.

For the Taiwan region, the general shape of the linear V_{S30} scaling is also consistent with the global model, but in the intermediate period range (0.2 - 1.0 sec), the scaling is much weaker (less negative terms). For Taiwan, there is a large number of sites to constrain the V_{S30} scaling; therefore, only minor smoothing is applied.

For Central America, the standard errors of the estimated coefficients are large, but the general shape of the linear V_{S30} scaling is consistent with the global model for periods less than 3 sec. Given the large standard errors, we assumed that the global V_{S30} scaling applies to Central

America (a_{19}=0). Given that the Alaska region has a similar issue, we assumed that the global V_{S30} scaling applies to Alaska (a_{17}=0).

For South America, the shape of the linear V_{S30} scaling is very different from the global model. It is almost flat with period, with small standard errors. If the V_{S30} values in the dataset are correct, this indicates that the softer soil sites are not associated with deeper sediment depths as seen in the other regions. The other possible explanation is that the V_{S30} values for this region are not reliable. Most of the V_{S30} values for this region were estimated from a proxy model (Stewart, 2020). We considered the nearly period-independent V_{S30} scaling to be an artifact of trade offs with other parameters. Therefore, we set the region-specific adjustment for South America (a_{22}) to be equal to the adjustment for the New Zealand region (a_{21}) based on the shape of the New Zealand V_{S30} scaling being similar to the global model but with a smaller amplitude that is closer to the South America results than the global model.

4.2.12 Step 12

The basin-scaling terms for the Cascadia region (a_{39}) and the Japan region (a_{41}) are added into the regression at this step. These terms were not included in the regression in the previous steps because they are only available for the two regions.

The estimated Cascadia basin terms are shown in the upper frame of Figure 4.12. There is increased amplification (positive values of a_{39}) at long periods as expected, but there is also increased amplification at short periods (T<0.05 sec) Without a physical reason for this behavior, we choose to set the basin term to zero for periods less than 0.2 sec and return to fit the center of the data for periods of greater than 0.75 sec. For long periods, there is a drop in the basin terms for periods of 2.5–3.0 sec. This reduction in basin amplification was not seen in the M9 simulations (discussed later in Section 6.6). We smoothed through this drop and through the peak at 5–6 sec.

The estimated Japanese basin terms are shown in the lower frame of Figure 4.12. For Japan, the basin effects are seen at both long periods (amplification with larger basin depth) and at the short period (attenuation with larger basin depth). The attenuation at short periods likely reflects additional damping for the deep-soil sites as compared to typical soil sites in Japan. The basin terms for Japan are very smooth with period, so no smoothing was applied.

4.2.13 Step 13

The Class 1 / Class 2 term for the difference in the ground motion from aftershocks and mainshocks was added to the regression in this step. The estimated (a_{15}) terms are shown in Figure 4.13. The ground motions from the Class 2 events (aftershocks) are 5–15% lower than from the Class 1 events (mainshocks). There is a trend of increasing a_{15} with period, but to keep this the model simple, we modeled a_{15} as a constant, independent of period.

4.2.14 Step 14

In Step 14, the regional constant terms ($a_{31} - a_{37}$) are evaluated. The coefficient are smoothed at long periods (T>2 sec) so that the spectral displacement varies smoothly with period without bumps in spectra. No smoothing was required for the short periods.

4.2.15 Step 15

The global constant is computed from the five regional models that were not adjusted (Central America, Japan, New Zealand, South America, and Taiwan). Specifically, the median ground motion from the five regions is computed for two events in the range well constrained by the data: a M6.5 intraslab event and a M7.0 interface event both with Z_{TOR} = 50 km, R_{RUP} = 100 km, V_{S30} = 400 m/sec, and a $Z_{2.5} = Z_{2.5ref}$. The geometric mean of the median PSA for the five regions is computed for each scenario. The constant for the global model is set based on the geometric mean ground motions for these two events:

$$a_1(T) = 0.5\,(ln(PSA_1(T) - PSA_{G1}(T)) + 0.5\,(ln(PSA_2(T) - PSA_{G2}(T)) \tag{4.2}$$

in which PSA_1 and PSA_2 are the geometric mean ground motions for the two scenarios, and PSA_{G1} and PSA_{G2} are the median ground motions from the global model for these two scenarios computed with $a_1 = 0$. Note that using the average of the regional constants will not give the same result because the magnitude and distance scaling have curvature so that the differences in the intercepts do not represent the differences at all magnitudes and distances.

The final model coefficients for the global model are listed in Tables 4.4 and 4.5. The coefficients for the regional terms are listed in Tables 4.6, 4.7, 4.8, and 4.9.

4.3 RESIDUALS

In this section, examples of the residuals are shown for T = 0.2 sec and for T = 2 sec. A full set of residuals for all 24 periods are shown in Appendix A.

4.3.1 Between-Event Residuals

The magnitude dependence of the between-event residuals for the interface and intraslab events are shown for PSA at T = 0.2 sec and T = 2 sec in Figures 4.14 and 4.15, respectively. There is no clear trend in magnitude for either the interface or the intraslab events, indicating that the magnitude scaling is consistent with the available recorded data. For the two largest interface events (**M**8.8 Maule and **M**9.1 Tohoku), the event terms are balanced around zero. The event terms at all 24 periods for these two large magnitude earthquakes are shown in Figure 4.16. The event terms are reasonably centered around zero for periods up to 2 sec. At longer periods, the event terms from the Maule earthquake are reduced, and the average of the event terms from the two earthquakes are negative, indicating that the long-period motions for these two events are overestimated by the GMM.

The depth dependence of the between-event residuals are shown in Figure 4.17. For the interface earthquakes, there is a trend of increasing δB for Z_{TOR} values of 25–50 km for the short-period ground motion, but not for the long-period ground motion. We choose not to model this trend as it could be a results of misclassification of the event types as discussed earlier. For the intraslab events, the between-event residuals do not show a trend with depth for any spectral period.

4.3.2 Within-Event Residuals

The distance scaling is evaluated by checking the distance dependence of the within-event residuals shown in Figures 4.18 and 4.19. The residuals are separated by magnitude bin to check the magnitude-dependent geometrical spreading and the magnitude-dependent finite-fault terms as well as the large-distance scaling. The within-event residuals are centered around zero for the full distance range for all of the magnitude bins.

The V_{S30} dependence of the within-event residuals is shown in Figures 4.20 and 4.21. To check the region-specific V_{S30} scaling, the residuals are separated by region. For all of the regions, there are no trends in the residuals with V_{S30}, even for the South America region, which had the V_{S30} scaling set to the V_{S30} scaling from the New Zealand region (see Step 11). This indicates that there are trade-offs between the V_{S30} scaling for South America and other parameters in the model.

The basin-depth dependence of the within-event residuals for Cascadia and Japan are shown in Figure 4.22 for T = 2 sec and T = 5 sec. For Cascadia, the data is sparse, but the residuals from the available data are centered around zero. For Cascadia, the basin scaling is only applied for the deep basins ($Z_{2.5} > Z_{2.5ref}$). The lack of a trend in the residuals for the smaller values of $Z_{2.5}$ shows that there is no basin scaling seen in the Cascadia data outside of the deep basins.

For the Japan data, the model captures the scaling for $Z_{2.5}$ values from 10 to 2000 m, which represents most of the data, but it underestimates the basin effects in Japan for deep basins with $Z_{2.5}$ greater than 2000 m. This is a result of using a simple linear scaling with $ln(Z'_{2.5})$. To fit the Japan data for $Z_{2.5}$ >2000 m, there would need to be curvature in $Z'_{2.5}$ dependence of the basin effect term.

The nonlinear site response model is evaluated by plotting the within-event residuals for short-period ground motion as a function of the PGA_{1000} value. Figure 4.23 shows the PSA(T = 0.2) within-event residuals for the softer site conditions (V_{S30} <270 m/sec). The residuals for a spectral period of T = 0.2 sec are shown because the nonlinear site effects will be stronger in the short-period range due to increased damping. The lack of trends in the residuals at the larger PGA_{1000} values indicate that the assumed nonlinear site factors, based on analytical modeling using RVT-based equivalent-linear analysis, captures the trends in this dataset in a reasonable manner.

Table 4.1: Steps for smoothing the coefficients.

		Step						
		1	2	3	4	5	6	7
a1	Global const	-	-	-	-	-	-	-
a2	Global GS interface	E	E	E	**S**	F	F	F
a3	Global mag-dep GS	F	F	F	F	F	F	F
a4	Global mag M$< C_1$ (interface)	**S**	F	F	F	F	F	F
a5	Global mag M$\geq C_1$	F	F	F	F	F	F	F
a6	Global linear R	E	E	E	E	E	**S**	F
a8	Global $ZTOR$ slope 1	E	E	E	E	E	E	**S**
a10	Global slab term	E	E	E	E	E	E	E
a11	Global Z_{TOR} slope 2	E	E	E	E	E	E	**S**
a12	Global V_{S30}	E	E	E	E	E	E	E
a13	Global quadratic mag	-	-	**S**	F	F	F	F
a14	Global slab GS	E	E	E	E	**S**	F	F
a15	Aftershock/mainshock	-	-	-	-	-	-	-
a16	Regional GS Taiwan	-	-	-	-	-	-	-
a17 - a23	Regional V_{S30}	-	-	-	-	-	-	E
a24 - a30	Regional linear R	-	-	-	-	-	-	E
a31 - a37	Regional constants	E	E	E	E	E	E	E
a39; a41	Regional $Z_{2.5}$	-	-	-	-	-	-	-
a45	Global mag M$< C_1$ (slab)	-	S	F	F	F	F	F

E = estimated, F = fixed, S=smoothed

Table 4.2: Steps for smoothing the coefficients (continued).

		Step							
		8	9	10	11	12	13	14	15
a1	Global const	-	-	-	-	-	-	-	**S**
a2	Global GS interface	F	F	F	F	F	F	F	F
a3	Global mag-dep GS	F	F	F	F	F	F	F	F
a4	Global mag M$<C_1$ (interface)	F	F	F	F	F	F	F	F
a5	Global mag M$\geq C_1$	F	F	F	F	F	F	F	F
a6	Global linear R	F	F	F	F	F	F	F	F
a8	Global Z_{TOR} slope 1	F	F	F	F	F	F	F	F
a10	Global slab term	E	E	**S**	F	F	F	F	F
a11	Global Z_{TOR} slope 2	F	F	F	F	F	F	F	F
a12	Global V_{S30}	E	E	**S**	F	F	F	F	F
a13	Global quadratic mag	F	F	F	F	F	F	F	F
a14	Global slab GS	F	F	F	F	F	F	F	F
a15	Aftershock/mainshock	-	-	-	-	-	**S**	F	F
a16	Regional GS Taiwan	-	**S**	F	F	F	F	F	F
a17 - a23	Regional V_{S30}	-	-	-	**S**	F	F	F	F
a24 - a30	Regional linear R	**S**	F	F	F	F	F	F	F
a31 - a37	Regional constants	E	E	E	E	E	E	**S**	F
a39; a41	Regional $Z_{2.5}$	-	-	-	-	**S**	F	F	F
a45	Global mag M$<C_1$ (slab)	F	F	F	F	F	F	F	F

E = estimated, F = fixed, S=smoothed

Table 4.3: Constrained coefficients for large magnitude scaling.

Coeff	Term	Value
a_3	Global magnitude-dependent geometrical spreading	0.1
a_5	Global linear magnitude for $M > C_1$	0.0
a_9	Finite-fault term magnitude scaling	0.4
C_4	Finite-fault term reference distance	10 km

Table 4.4: Coefficients for the global model.

Period (sec)	c_{1i}	a_1	a_2	a_3	a_4	a_5	a_6	a_7	a_8
0.01	8.20	4.596	-1.450	0.1	0.73	0.000	-0.0043	3.210	0.0440
0.02	8.20	4.678	-1.450	0.1	0.73	0.000	-0.0043	3.210	0.0440
0.03	8.20	4.773	-1.450	0.1	0.73	0.000	-0.0044	3.210	0.0440
0.05	8.20	5.029	-1.450	0.1	0.73	0.000	-0.0046	3.210	0.0440
0.075	8.20	5.334	-1.450	0.1	0.73	0.000	-0.0047	3.210	0.0440
0.10	8.20	5.455	-1.450	0.1	0.73	0.000	-0.0048	3.210	0.0440
0.15	8.20	5.376	-1.425	0.1	0.73	0.000	-0.0047	3.210	0.0440
0.20	8.20	4.936	-1.335	0.1	0.73	0.000	-0.0045	3.210	0.0430
0.25	8.20	4.636	-1.275	0.1	0.73	0.000	-0.0043	3.210	0.0420
0.30	8.20	4.423	-1.231	0.1	0.73	0.000	-0.0042	3.210	0.0410
0.40	8.20	4.124	-1.165	0.1	0.73	0.000	-0.0040	3.210	0.0400
0.50	8.20	3.838	-1.115	0.1	0.73	0.000	-0.0037	3.210	0.0390
0.60	8.20	3.562	-1.071	0.1	0.73	0.000	-0.0035	3.210	0.0380
0.75	8.15	3.152	-1.020	0.1	0.73	0.000	-0.0032	3.210	0.0370
1.0	8.10	2.544	-0.950	0.1	0.73	0.000	-0.0029	3.210	0.0350
1.5	8.05	1.636	-0.860	0.1	0.73	0.000	-0.0026	3.210	0.0340
2.0	8.00	1.076	-0.820	0.1	0.73	0.000	-0.0024	3.210	0.032
2.5	7.95	0.658	-0.798	0.1	0.73	0.000	-0.0022	3.210	0.031
3.0	7.90	0.424	-0.793	0.1	0.73	0.000	-0.0021	3.130	0.03
4.0	7.85	0.093	-0.793	0.1	0.73	0.000	-0.0020	2.985	0.029
5.0	7.80	-0.145	-0.793	0.1	0.73	0.000	-0.0020	2.818	0.028
6.00	7.80	-0.320	-0.793	0.1	0.73	0.000	-0.0020	2.682	0.027
7.5	7.80	-0.556	-0.793	0.1	0.73	0.000	-0.0020	2.515	0.026
10.0	7.80	-0.860	-0.793	0.1	0.73	0.000	-0.0020	2.300	0.025

Table 4.5: Coefficients for the global model (continued.)

Period (sec)	a_9	a_{10}	a_{11}	a_{12}	a_{13}	a_{14}	a_{15}	a_{45}
0.01	0.400	3.210	0.0070	0.900	0.000	-0.46	-0.1	0.34
0.02	0.400	3.210	0.0070	1.008	0.000	-0.46	-0.1	0.34
0.03	0.400	3.210	0.0070	1.127	0.000	-0.46	-0.1	0.34
0.05	0.400	3.210	0.0070	1.333	0.000	-0.46	-0.1	0.34
0.075	0.400	3.210	0.0070	1.565	0.000	-0.46	-0.1	0.34
0.1	0.400	3.210	0.0070	1.679	0.000	-0.46	-0.1	0.34
0.15	0.400	3.210	0.0070	1.853	0.000	-0.46	-0.1	0.34
0.2	0.400	3.210	0.0062	2.022	0.000	-0.46	-0.1	0.34
0.25	0.400	3.210	0.0056	2.181	0.000	-0.46	-0.1	0.34
0.3	0.400	3.210	0.0051	2.281	-0.002	-0.46	-0.1	0.34
0.4	0.400	3.210	0.0043	2.379	-0.007	-0.47	-0.1	0.34
0.5	0.400	3.210	0.0037	2.339	-0.011	-0.48	-0.1	0.34
0.6	0.400	3.210	0.0033	2.217	-0.015	-0.49	-0.1	0.34
0.75	0.400	3.210	0.0027	1.946	-0.021	-0.50	-0.1	0.34
1	0.400	3.210	0.0019	1.416	-0.028	-0.51	-0.1	0.34
1.5	0.400	3.210	0.0008	0.394	-0.041	-0.52	-0.1	0.34
2	0.400	3.210	0.0000	-0.417	-0.050	-0.53	-0.1	0.34
2.5	0.400	3.210	0.0000	-0.725	-0.057	-0.54	-0.1	0.34
3	0.400	3.130	0.0000	-0.695	-0.065	-0.54	-0.1	0.34
4	0.400	2.985	0.0000	-0.638	-0.077	-0.54	-0.1	0.34
5	0.400	2.818	0.0000	-0.597	-0.088	-0.54	-0.1	0.34
6	0.400	2.682	0.0000	-0.561	-0.098	-0.54	-0.1	0.34
7.5	0.400	2.515	0.0000	-0.530	-0.110	-0.54	-0.1	0.34
10	0.400	2.300	0.0000	-0.486	-0.127	-0.54	-0.1	0.34

Table 4.6: Coefficients for the regional linear V_{S30} scaling.

Period (sec)	a_{17}	a_{18}	a_{19}	a_{20}	a_{21}	a_{22}	a_{23}
0.01	0.000	-0.200	0.000	0.000	0.040	0.040	0.000
0.02	0.000	-0.200	0.000	0.000	0.040	0.040	0.000
0.03	0.000	-0.200	0.000	0.000	0.040	0.040	0.000
0.05	0.000	-0.200	0.000	0.000	0.040	0.040	0.000
0.075	0.000	-0.200	0.000	0.000	0.060	0.060	0.000
0.10	0.000	-0.200	0.000	0.000	0.100	0.100	0.000
0.15	0.000	-0.186	0.000	-0.055	0.135	0.135	0.069
0.20	0.000	-0.150	0.000	-0.105	0.170	0.170	0.140
0.25	0.000	-0.140	0.000	-0.134	0.170	0.170	0.164
0.30	0.000	-0.120	0.000	-0.150	0.170	0.170	0.190
0.40	0.000	-0.100	0.000	-0.150	0.170	0.170	0.206
0.50	0.000	-0.080	0.000	-0.150	0.170	0.170	0.220
0.60	0.000	-0.060	0.000	-0.150	0.170	0.170	0.225
0.75	0.000	-0.047	0.000	-0.150	0.170	0.170	0.217
1.0	0.000	-0.035	0.000	-0.150	0.170	0.170	0.185
1.5	0.000	-0.018	0.000	-0.130	0.170	0.170	0.083
2.0	0.000	-0.010	0.000	-0.110	0.170	0.170	0.045
2.5	0.000	-0.005	0.000	-0.095	0.170	0.170	0.026
3.0	0.000	0.000	0.000	-0.085	0.170	0.170	0.035
4.0	0.000	0.000	0.000	-0.073	0.170	0.170	0.053
5.0	0.000	0.000	0.000	-0.065	0.170	0.170	0.072
6.0	0.000	0.000	0.000	-0.060	0.170	0.170	0.086
7.5	0.000	0.000	0.000	-0.055	0.170	0.170	0.115
10.0	0.000	0.000	0.000	-0.045	0.170	0.170	0.151

Table 4.7: Coefficients for the regional linear Rterm.

Period (sec)	a_{24}	a_{25}	a_{26}	a_{27}	a_{28}	a_{29}	a_{30}
0.01	0.0015	0.0007	0.0036	-0.0004	0.0025	0.0006	0.0033
0.02	0.0015	0.0006	0.0036	-0.0005	0.0025	0.0005	0.0033
0.03	0.0015	0.0006	0.0037	-0.0007	0.0025	0.0005	0.0034
0.05	0.0011	0.0006	0.0039	-0.0009	0.0026	0.0004	0.0036
0.075	0.0011	0.0004	0.0039	-0.0009	0.0026	0.0003	0.0037
0.10	0.0012	0.0003	0.0039	-0.0008	0.0026	0.0003	0.0038
0.15	0.0013	-0.0002	0.0037	-0.0009	0.0022	0.0001	0.0037
0.20	0.0013	-0.0007	0.0031	-0.0010	0.0018	-0.0001	0.0035
0.25	0.0013	-0.0009	0.0027	-0.0011	0.0016	-0.0003	0.0033
0.30	0.0014	-0.0010	0.0020	-0.0009	0.0014	-0.0002	0.0032
0.40	0.0015	-0.0010	0.0013	-0.0007	0.0011	0.0000	0.0030
0.50	0.0015	-0.0011	0.0009	-0.0007	0.0008	0.0002	0.0027
0.60	0.0015	-0.0012	0.0006	-0.0007	0.0006	0.0002	0.0025
0.75	0.0014	-0.0011	0.0003	-0.0007	0.0004	0.0002	0.0022
1.0	0.0013	-0.0008	0.0001	-0.0008	0.0002	0.0001	0.0019
1.5	0.0014	-0.0004	-0.0001	-0.0008	0.0001	0.0000	0.0016
2.0	0.0015	0.0002	0.0000	-0.0007	0.0002	0.0000	0.0014
2.5	0.0014	0.0004	0.0000	-0.0007	0.0002	-0.0002	0.0012
3.0	0.0014	0.0007	0.0003	-0.0007	0.0004	-0.0002	0.0011
4.0	0.0014	0.0010	0.0007	-0.0006	0.0006	-0.0002	0.0010
5.0	0.0014	0.0013	0.0014	-0.0004	0.0008	-0.0001	0.0010
6.0	0.0014	0.0015	0.0015	-0.0003	0.0011	0.0000	0.0010
7.5	0.0014	0.0017	0.0015	-0.0002	0.0014	0.0001	0.0010
10.0	0.0014	0.0017	0.0015	-0.0001	0.0017	0.0002	0.0010

Table 4.8: Coefficients for the regional constants.

Period (sec)	a_{31}	a_{32}	a_{33}	a_{34}	a_{35}	a_{36}	a_{37}
0.01	3.7783	3.3468	3.8025	5.0361	4.6272	4.8044	3.5669
0.02	3.8281	3.4401	3.9053	5.1375	4.6958	4.8943	3.6425
0.03	3.8933	3.5087	4.0189	5.2699	4.7809	5.0028	3.7063
0.05	4.2867	3.6553	4.2952	5.6157	5.0211	5.2819	3.9184
0.075	4.5940	3.9799	4.5464	6.0204	5.3474	5.6123	4.2207
0.10	4.7077	4.1312	4.6138	6.1625	5.5065	5.7668	4.3536
0.15	4.6065	4.2737	4.5290	5.9614	5.5180	5.7313	4.3664
0.20	4.1866	3.9650	4.1656	5.3920	5.1668	5.2943	4.0169
0.25	3.8515	3.6821	3.9147	5.0117	4.8744	5.0058	3.7590
0.30	3.5783	3.5415	3.7846	4.7057	4.6544	4.7588	3.5914
0.40	3.2493	3.3256	3.5702	4.2896	4.3660	4.3789	3.3704
0.50	2.9818	3.1334	3.3552	3.9322	4.0779	4.0394	3.1564
0.60	2.7784	2.9215	3.0922	3.6149	3.8146	3.7366	2.9584
0.75	2.4780	2.5380	2.6572	3.1785	3.4391	3.2930	2.6556
1.0	1.9252	1.9626	2.1459	2.5722	2.8056	2.6475	2.0667
1.5	0.9924	1.3568	1.3499	1.6499	1.8546	1.6842	1.3316
2.0	0.4676	0.8180	0.8148	1.0658	1.3020	1.1002	0.7607
2.5	0.0579	0.4389	0.3979	0.6310	0.8017	0.6737	0.3648
3.0	-0.1391	0.1046	0.1046	0.3882	0.5958	0.4126	0.1688
4.0	-0.3030	-0.1597	-0.2324	0.0164	0.3522	0.0097	-0.0323
5.0	-0.4094	-0.2063	-0.5722	-0.2802	0.1874	-0.2715	-0.1516
6.0	-0.5010	-0.3223	-0.8631	-0.4822	-0.1243	-0.4591	-0.2217
7.5	-0.6209	-0.4223	-1.1773	-0.7566	-0.3316	-0.6822	-0.3338
10.0	-0.6221	-0.5909	-1.4070	-1.0870	-0.6783	-0.9173	-0.5441

Table 4.9: Coefficients for the regional geometrical-spreading term for Taiwan and the basin-depth scaling.

Period (sec)	a_{16}	a_{39}	a_{41}
0.01	0.090	0	-0.029
0.02	0.090	0	-0.024
0.03	0.090	0	-0.034
0.05	0.090	0	-0.061
0.075	0.090	0	-0.076
0.10	0.090	0	-0.049
0.15	0.090	0	-0.026
0.20	0.084	0	-0.011
0.25	0.080	0.101	-0.009
0.30	0.078	0.184	0.005
0.40	0.075	0.315	0.04
0.50	0.072	0.416	0.097
0.60	0.070	0.499	0.145
0.75	0.067	0.6	0.197
1.0	0.063	0.731	0.269
1.5	0.059	0.748	0.347
2.0	0.059	0.761	0.384
2.5	0.060	0.77	0.397
3.0	0.059	0.778	0.404
4.0	0.050	0.79	0.397
5.0	0.043	0.799	0.378
6.0	0.038	0.807	0.358
7.5	0.032	0.817	0.333
10.0	0.024	0.829	0.281

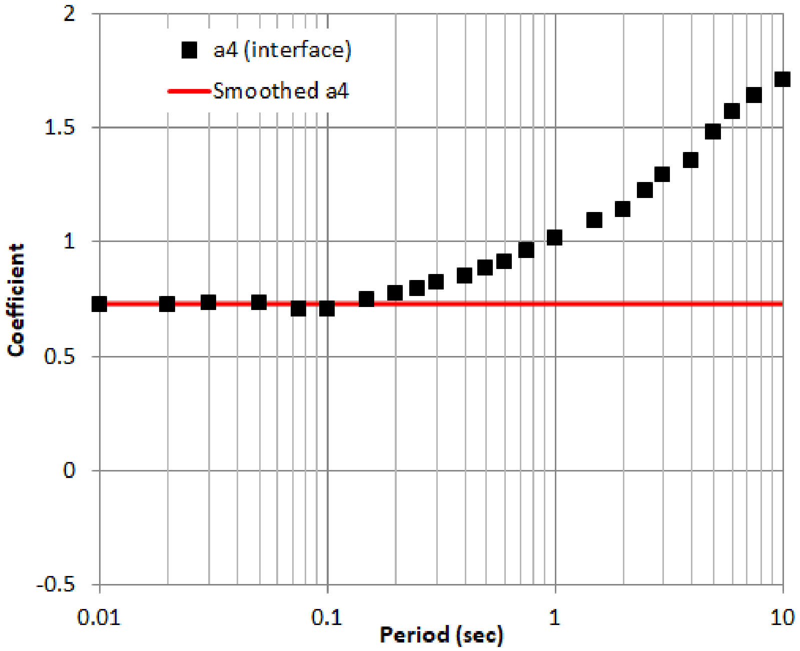

Figure 4.1: Step 1. Smoothing of linear magnitude term, coefficient a_4.

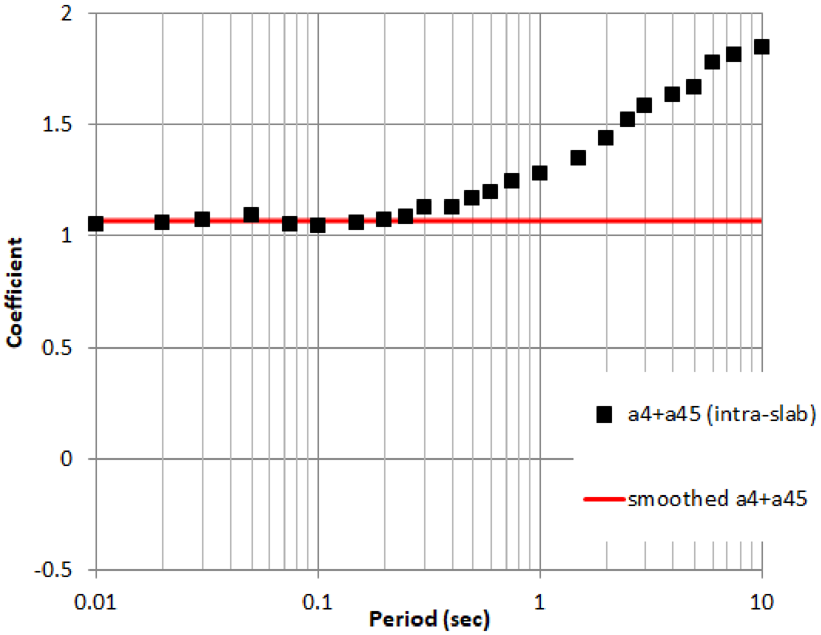

Figure 4.2: Step 2. Smoothing of linear magnitude term, coefficient a_{45}.

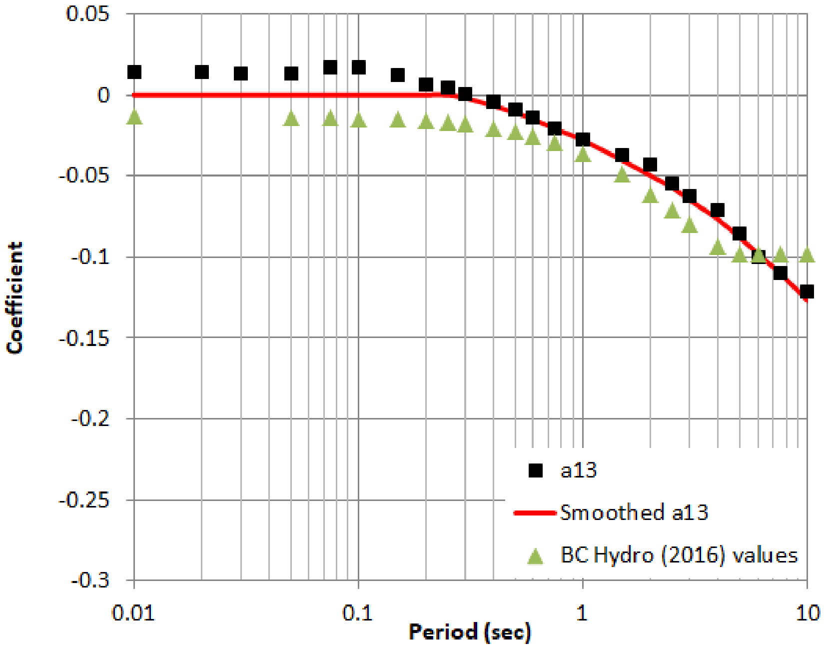

Figure 4.3: Step 3. Smoothing of quadratic magnitude term, coefficient a_{13}.

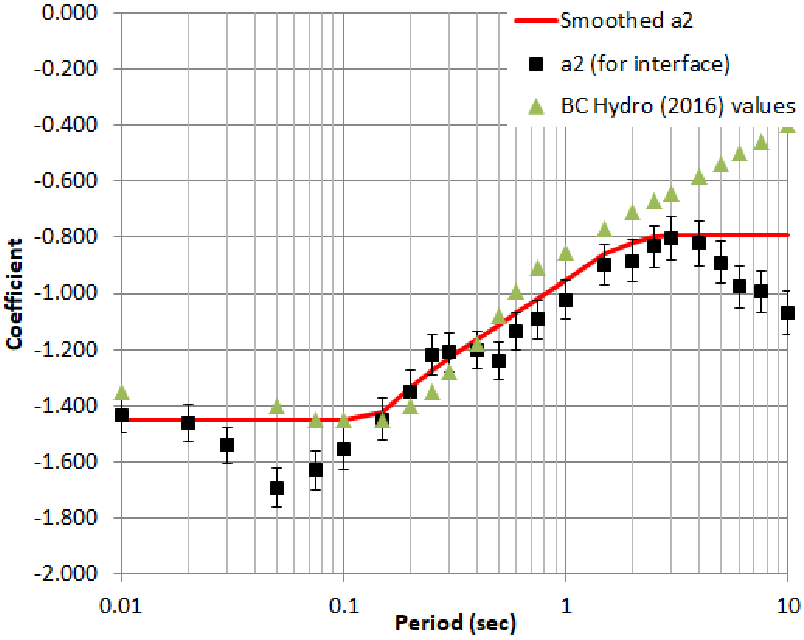

Figure 4.4: Step 4. Smoothing of the geometrical spreading term for interface events, coefficients a_2.

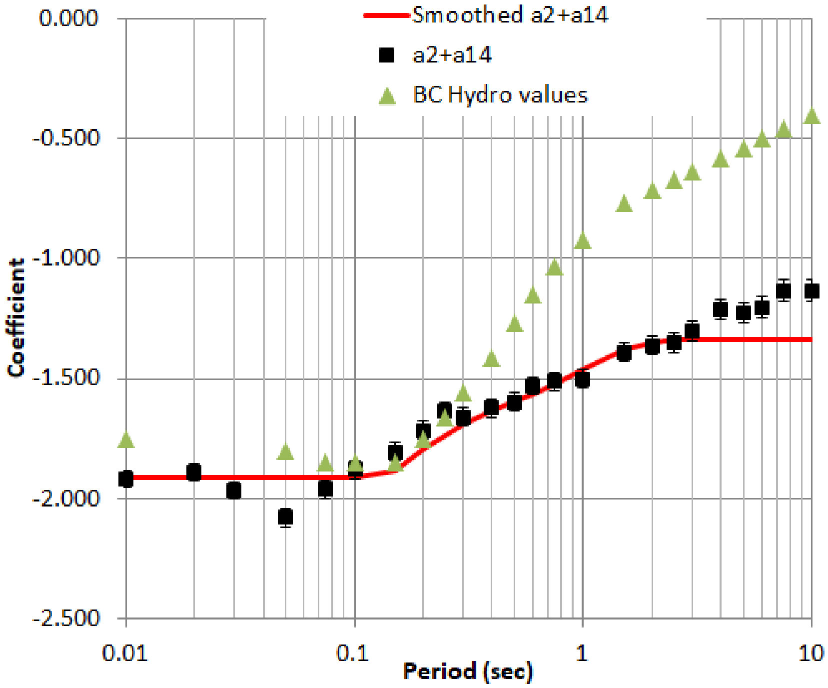

Figure 4.5: Step 5. Smoothing of the geometrical spreading term for intraslab events, coefficient $a_2 + a_{14}$.

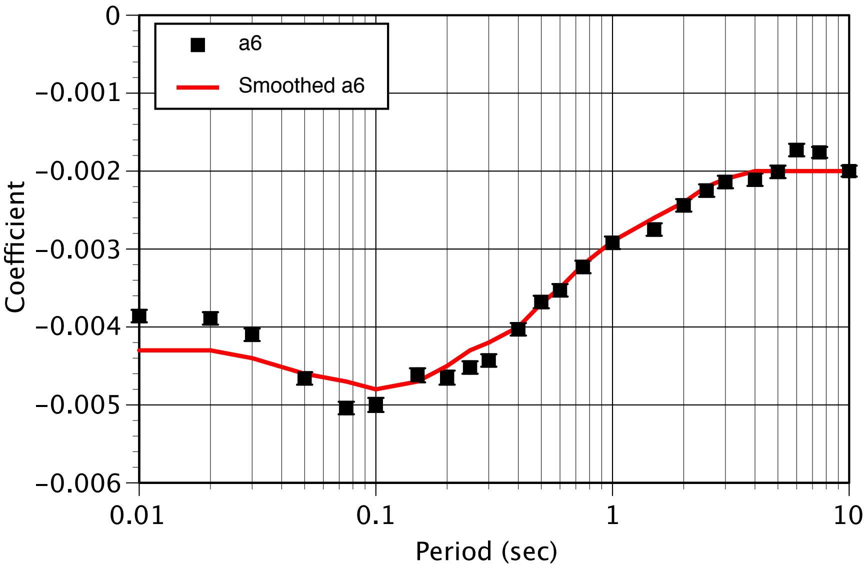

Figure 4.6: Step 6. Smoothing of the linear R term for the global model, coefficient a_6.

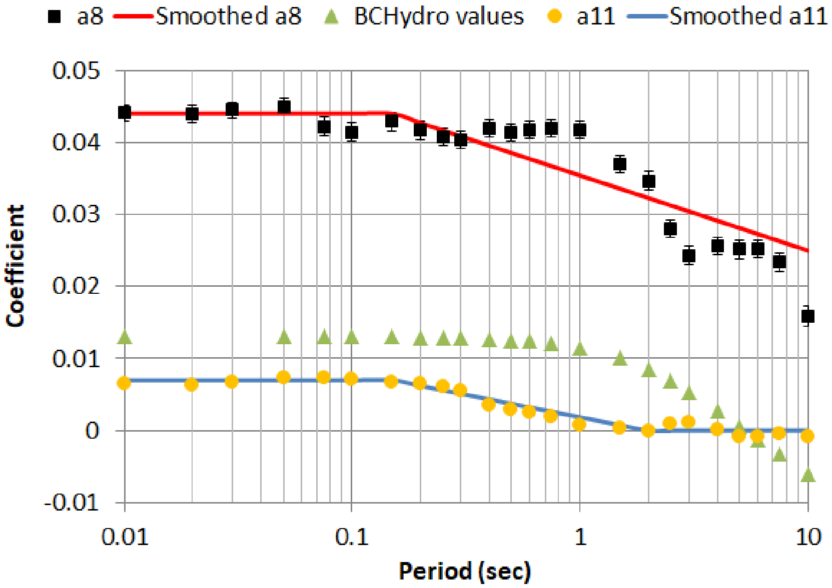

Figure 4.7: Step 7. Smoothing of the shallow (20–50 km) depth scaling term (a_8) and the deep (50–200 km) depth scaling term (a_{11}) for the global model.

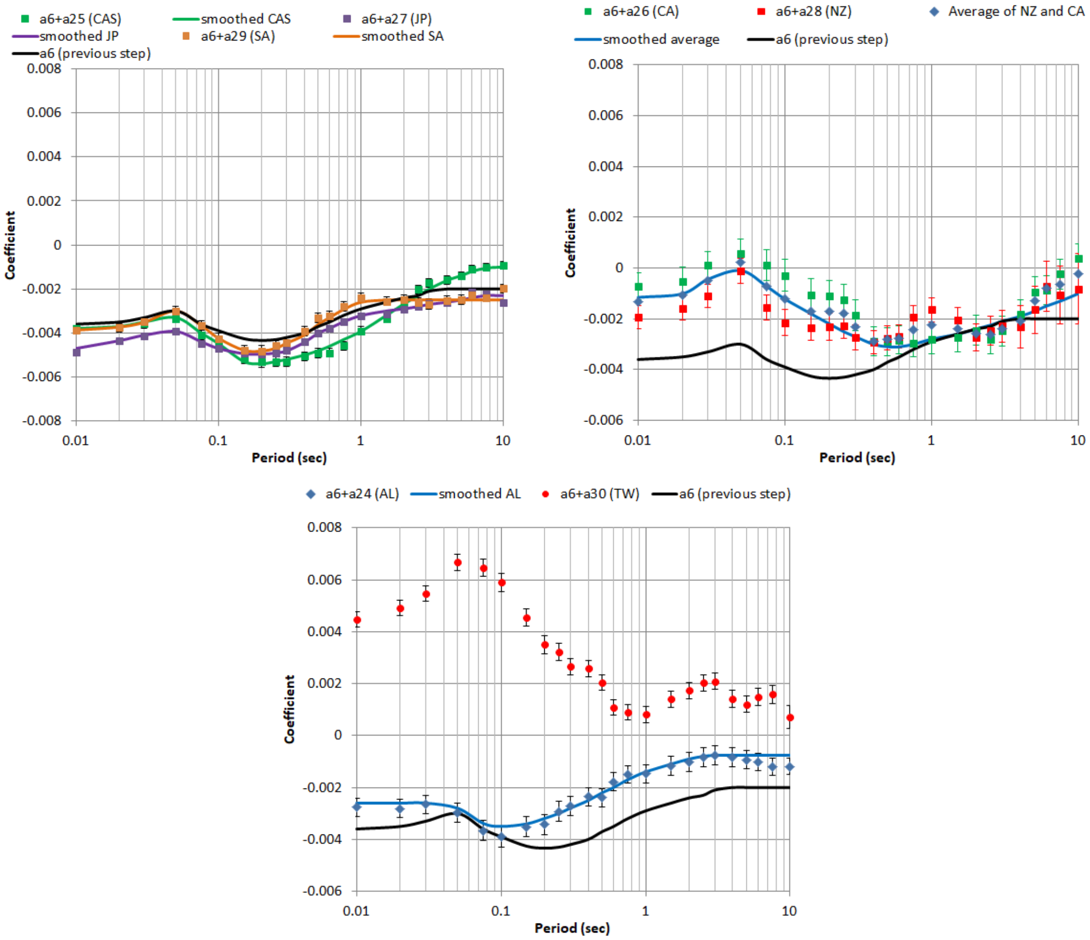

Figure 4.8: Step 8. Smoothing of the regional linear R term (a) Cascadia, Japan, and South America regions, coefficients a_{25}, a_{27}, and a_{29}; (b) Central America and New Zealand regions, coefficients a_{26} and a_{28}; and (c) Alaska and Taiwan, coefficients a_{24} and a_{30}.

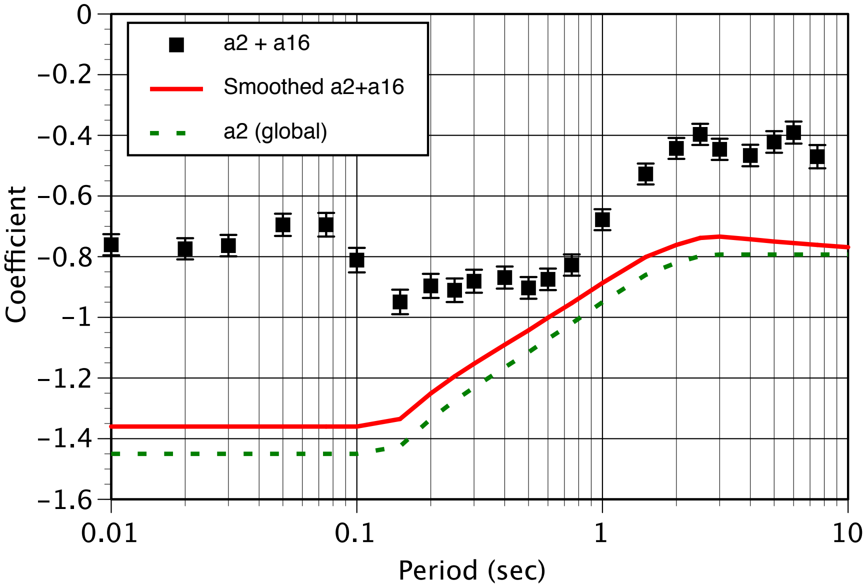

Figure 4.9: Step 9. Smoothing of the regional geometrical-spreading term for the Taiwan region, coefficient a_{16}.

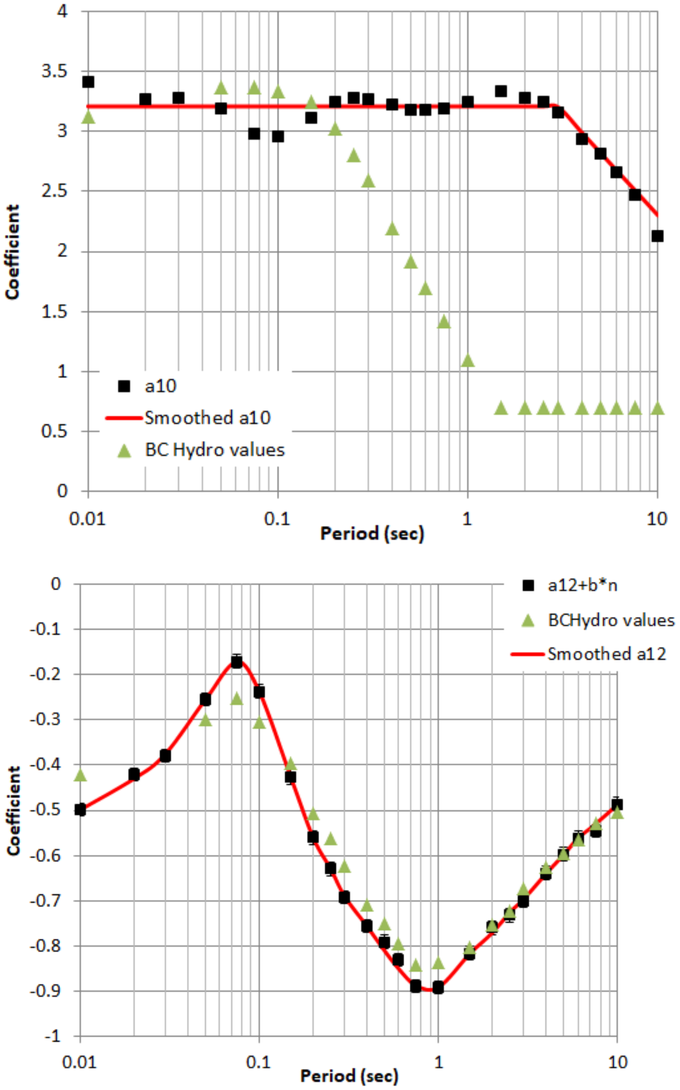

Figure 4.10: Step 10. Smoothing of global intraslab constant term, a_{10}, (top) and the global linear V_{S30} term, a_{12} (bottom).

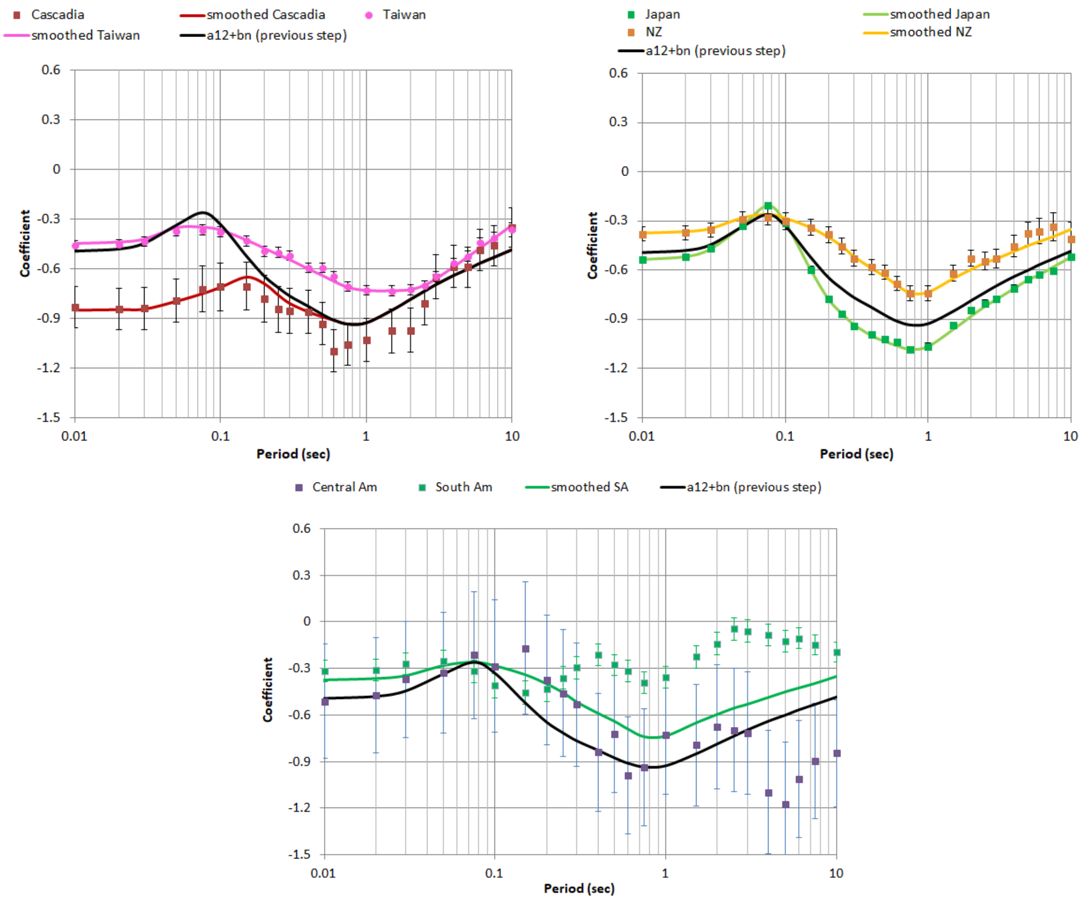

Figure 4.11: Step 11. Smoothing of regional linear V_{S30} terms (coefficients $a_{17} - a_{23}$). (a) Cascadia and Taiwan; (b) Japan and New Zealand; and (c) Central America and South America.

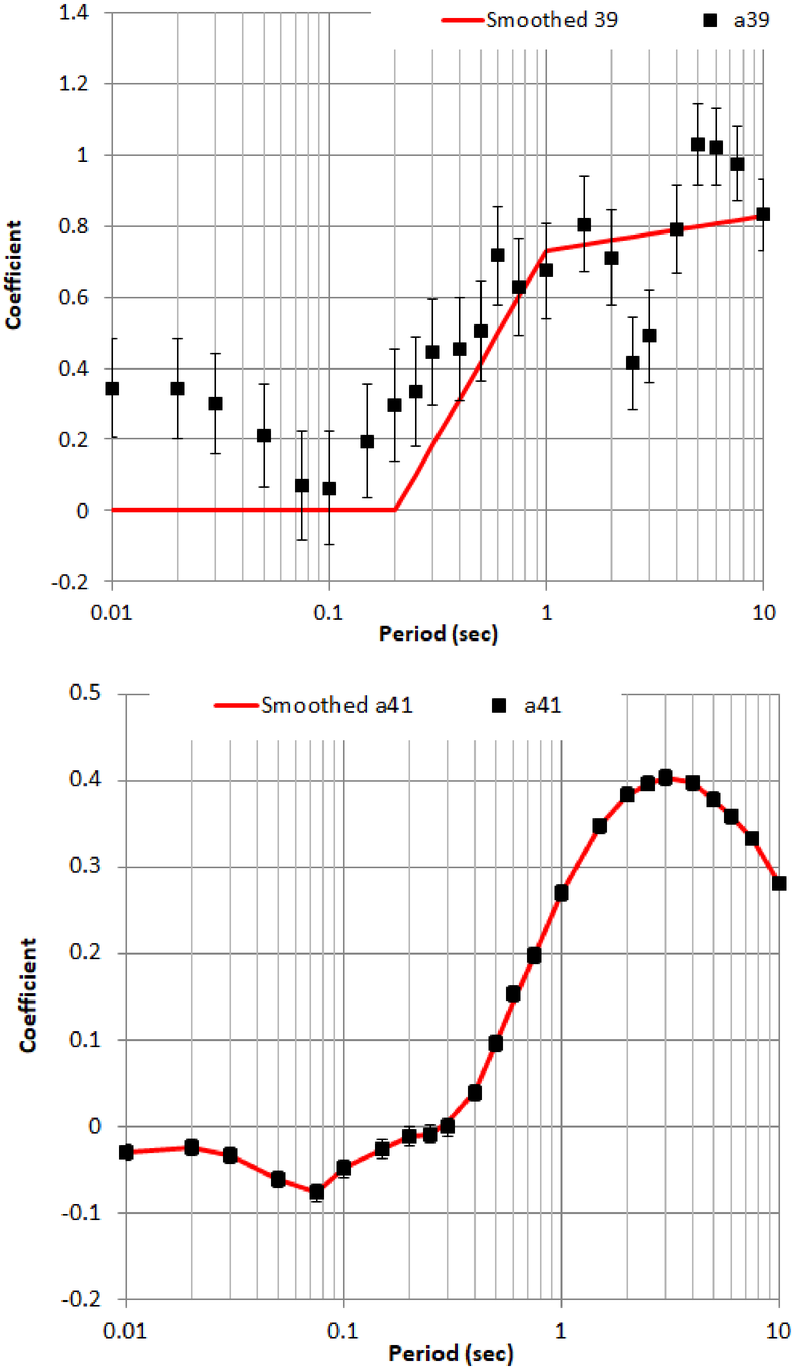

Figure 4.12: Step 12. Smoothing of basin depth terms. (a) Cascadia, coefficient a_{39}; and (b) Japan, coefficient (a_{41}).

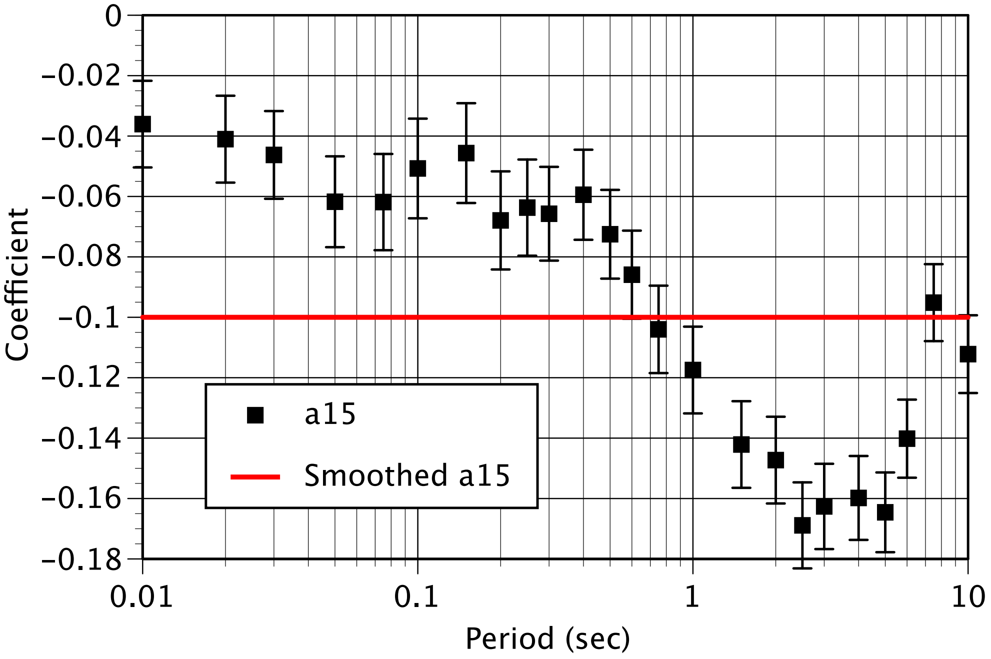

Figure 4.13: Step 13. Smoothing of aftershock/mainshock (class 1 / class 2) term (a_{15}).

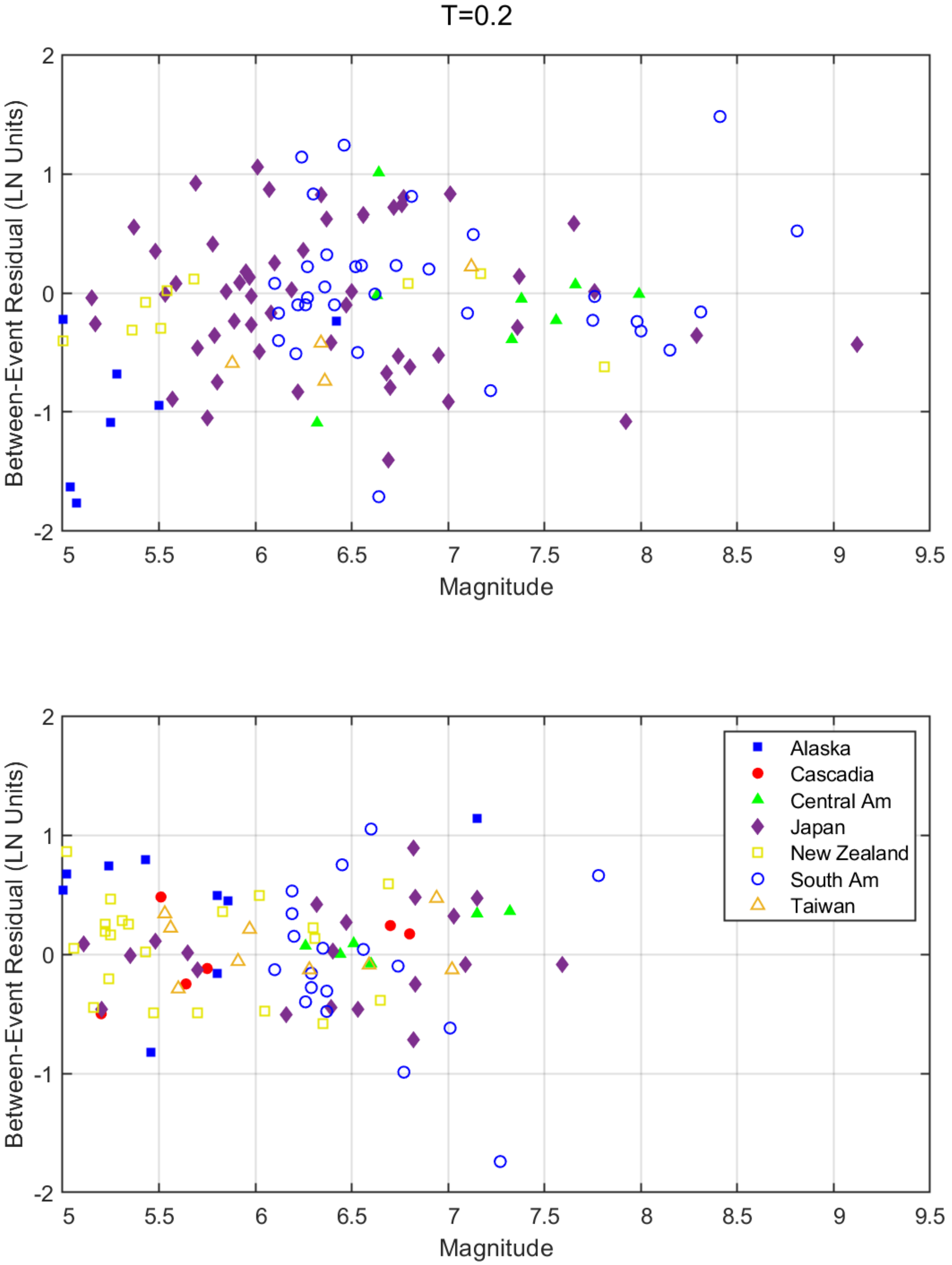

Figure 4.14: Between-event residuals versus magnitude for T = 0.2 sec. Top frame: interface earthquakes. Bottom frame: intraslab earthquakes.

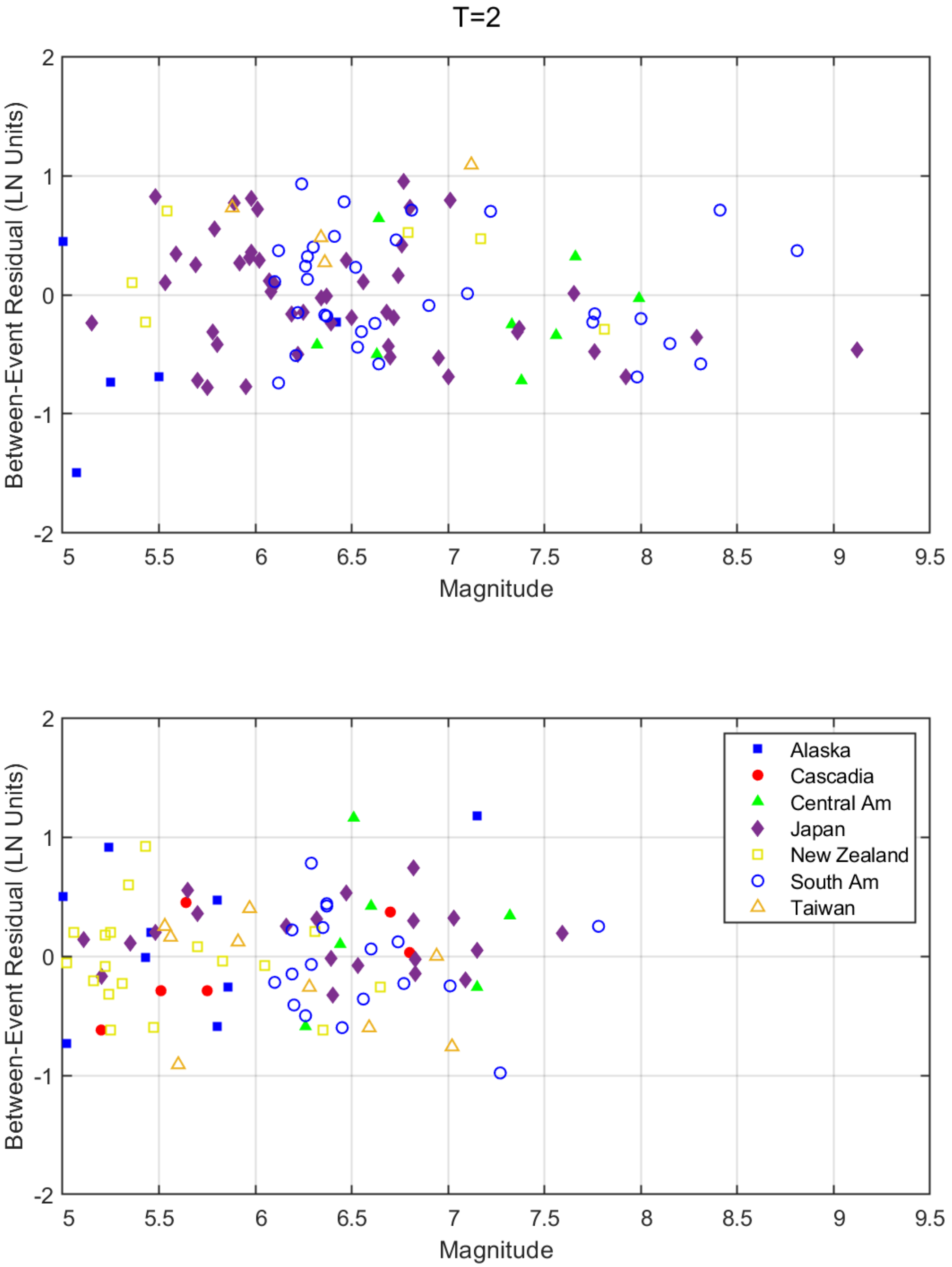

Figure 4.15: Between-event residuals versus magnitude for T = 2 sec. Top frame: interface earthquakes. Bottom frame: intraslab earthquakes

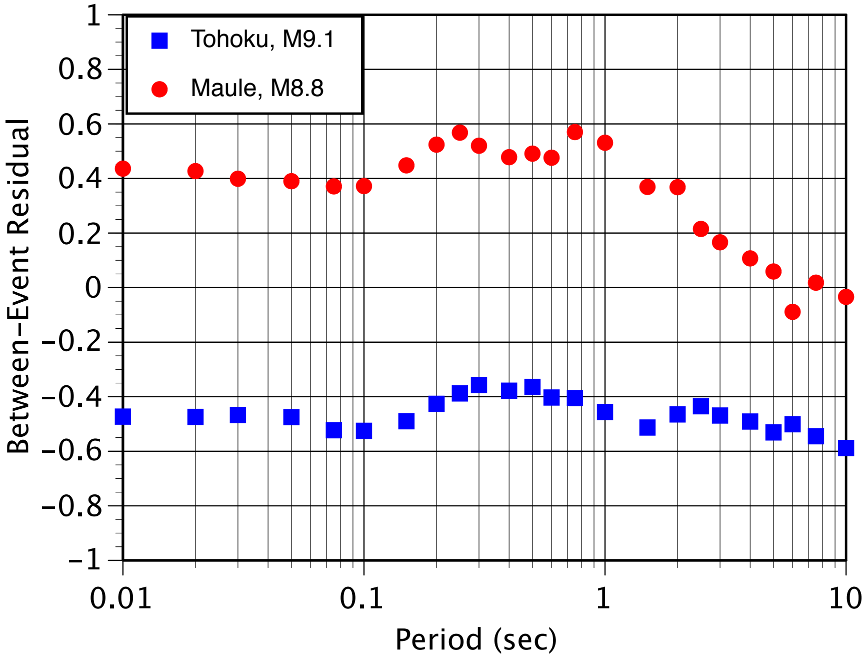

Figure 4.16: Between-event residuals for the two large interface events: Maule, Chile, and Tohoku, Japan.

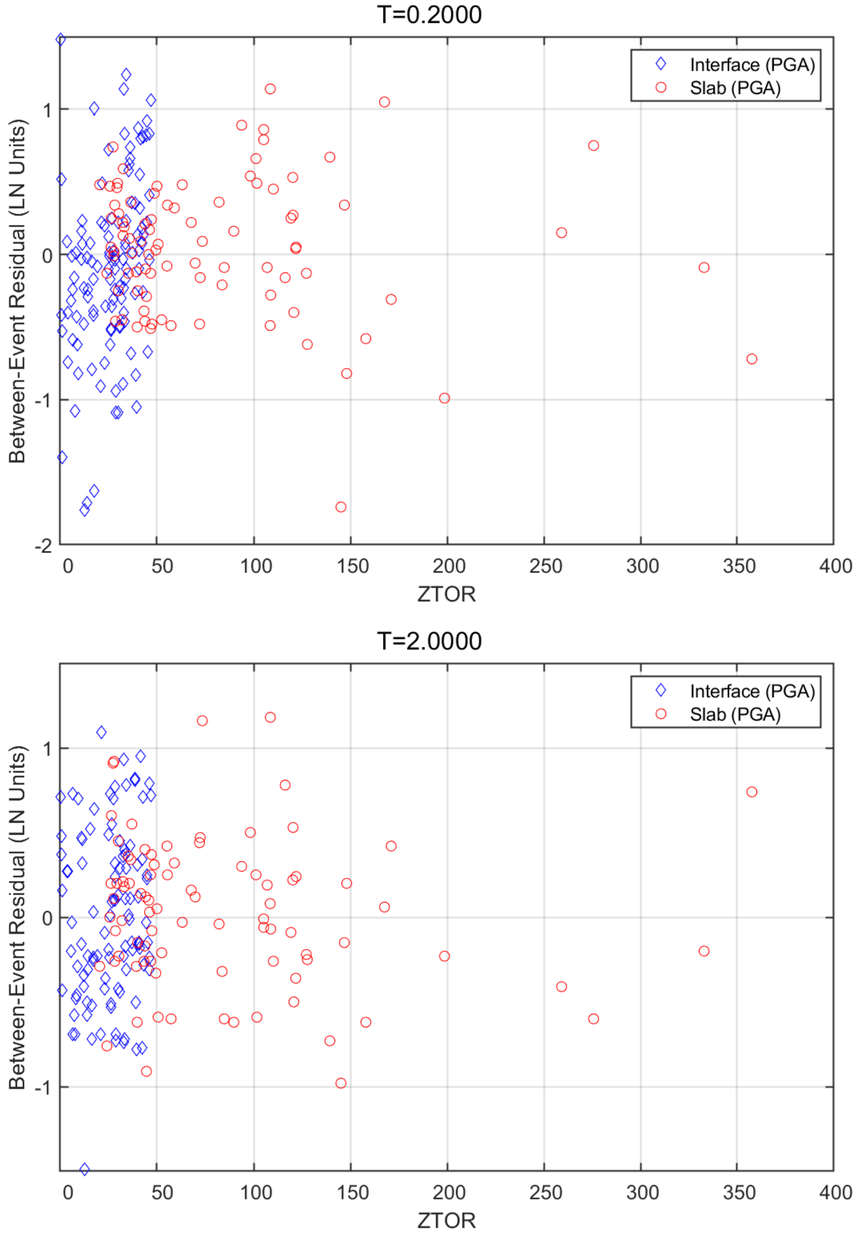

Figure 4.17: Between-event residuals versus source depth. Top frame: T = 0.2 sec. Bottom frame: T = 2 sec

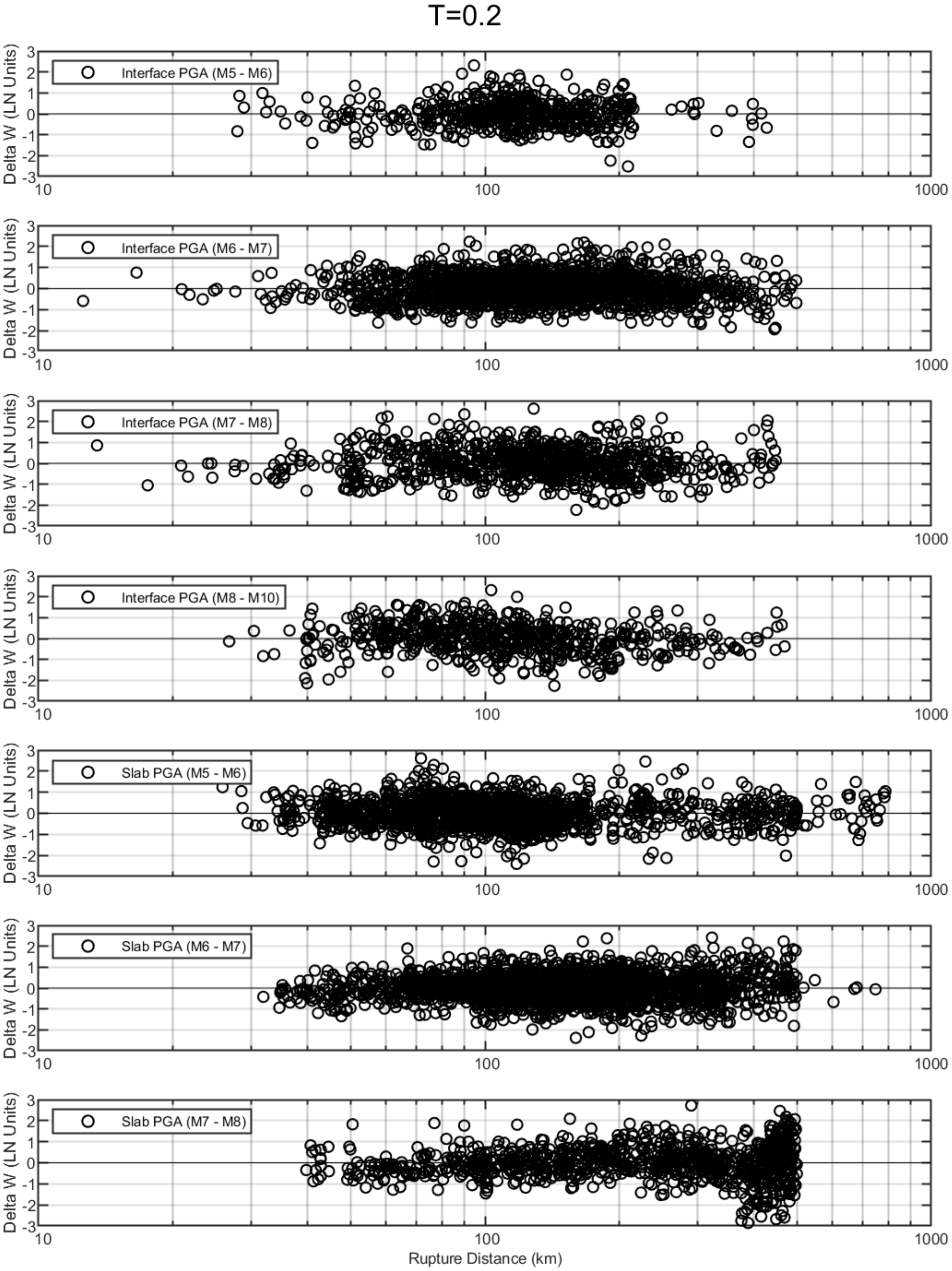

Figure 4.18: Within-event residuals versus distance for$T$ = 0.2 sec.

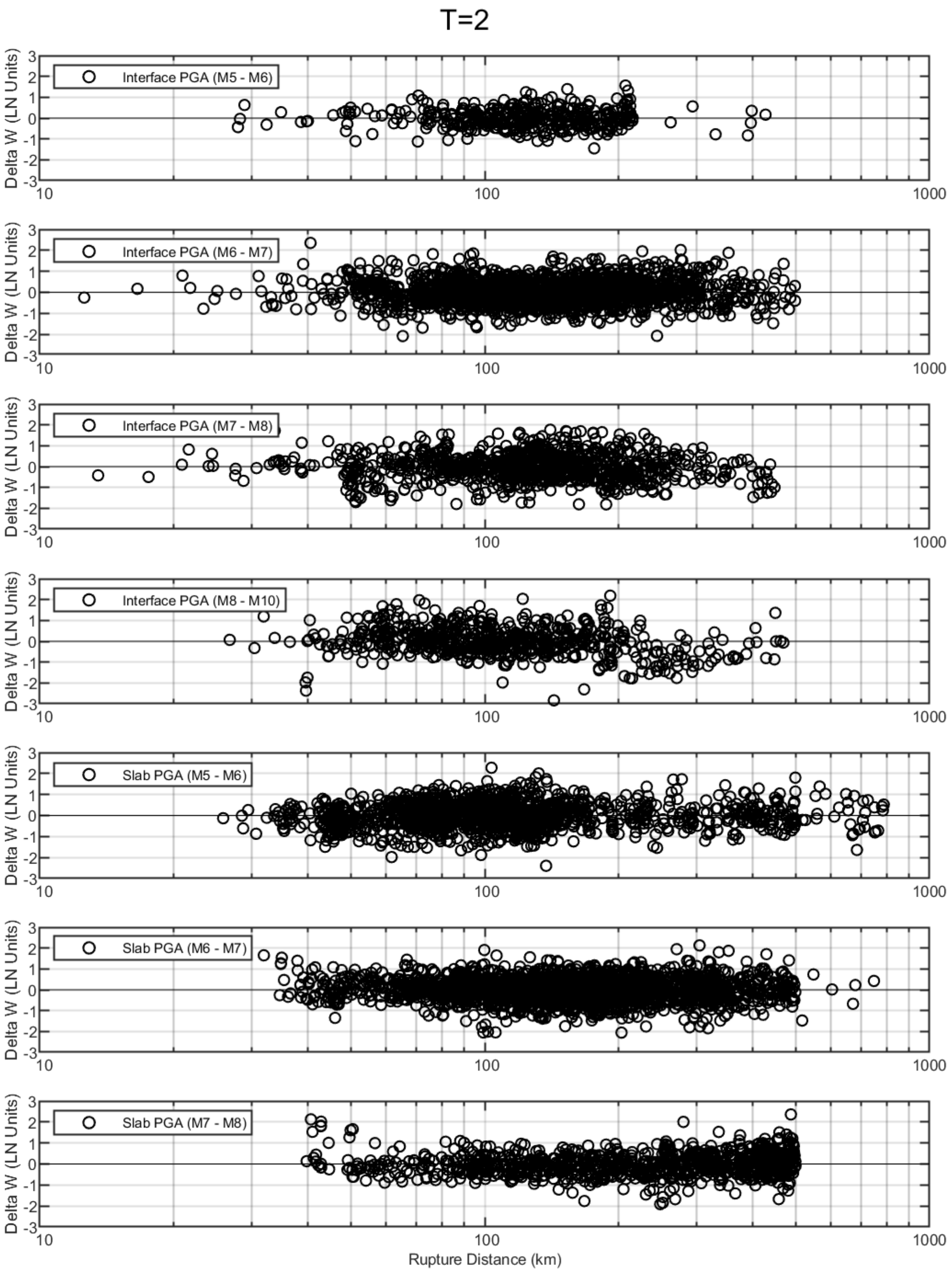

Figure 4.19: Within-event residuals versus distance for T = 2 sec.

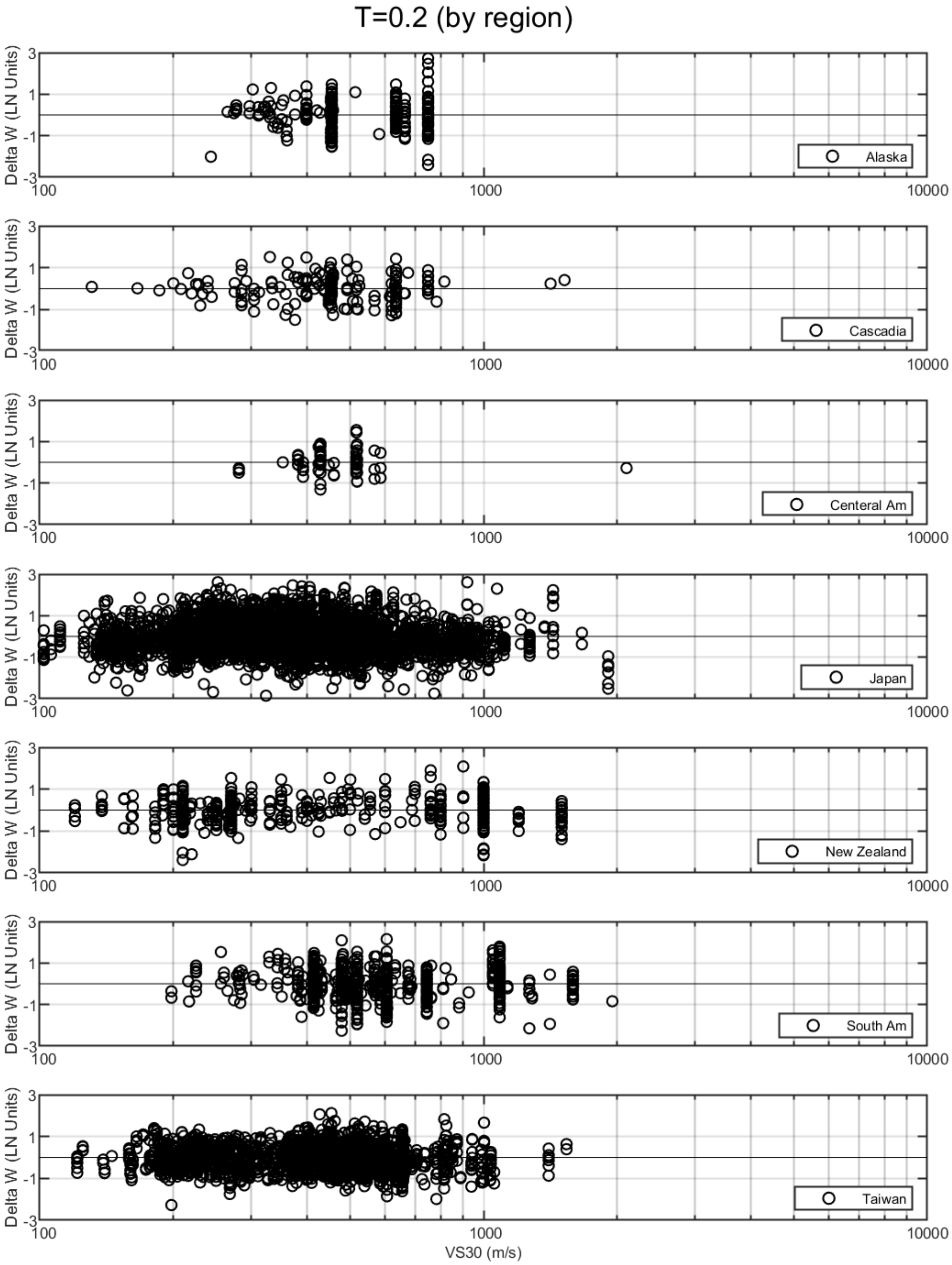

Figure 4.20: Within-event residuals versus V_{S30} for T = 0.2 sec.

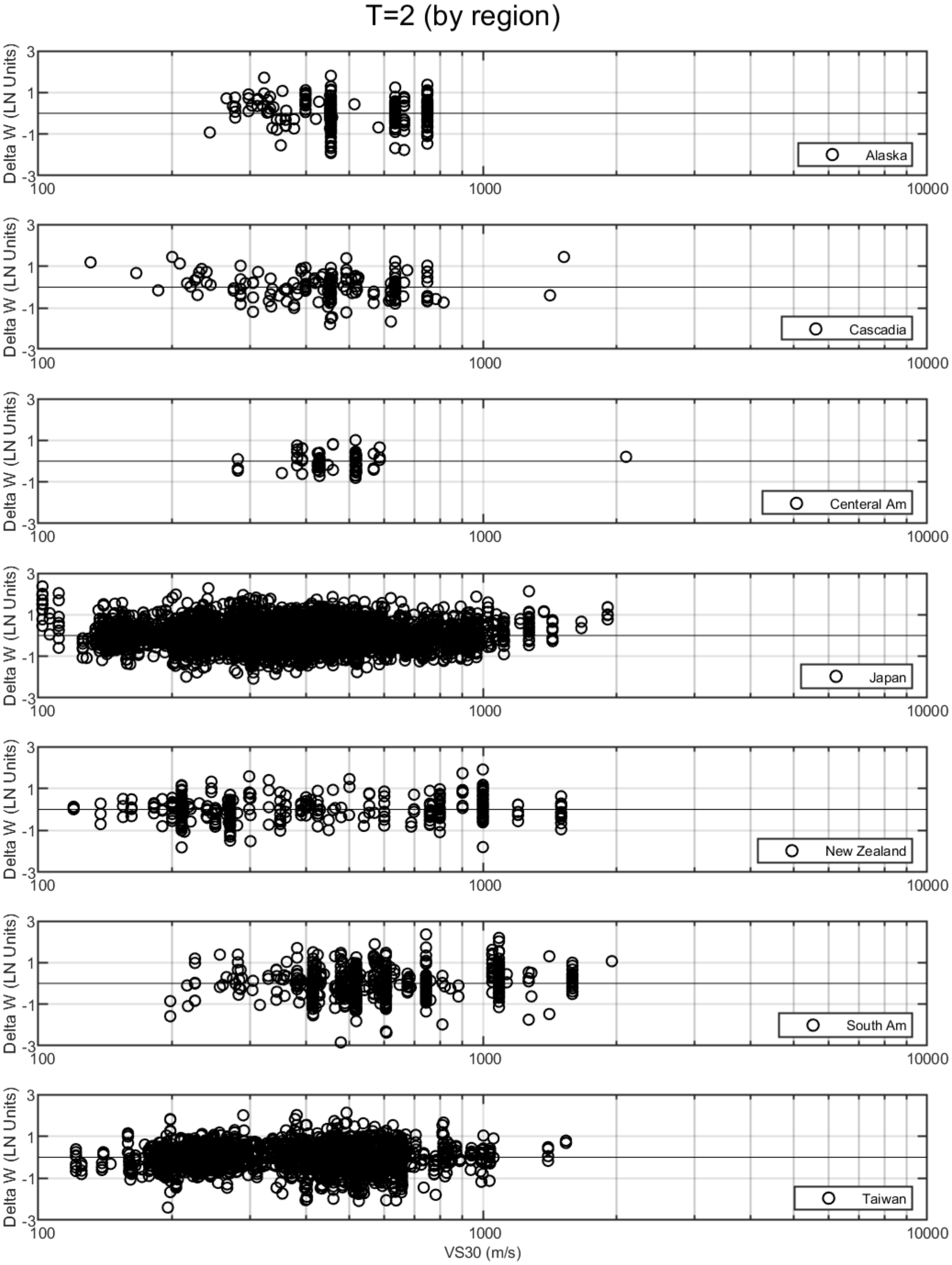

Figure 4.21: Within-event residuals versus V_{S30} for T = 2 sec.

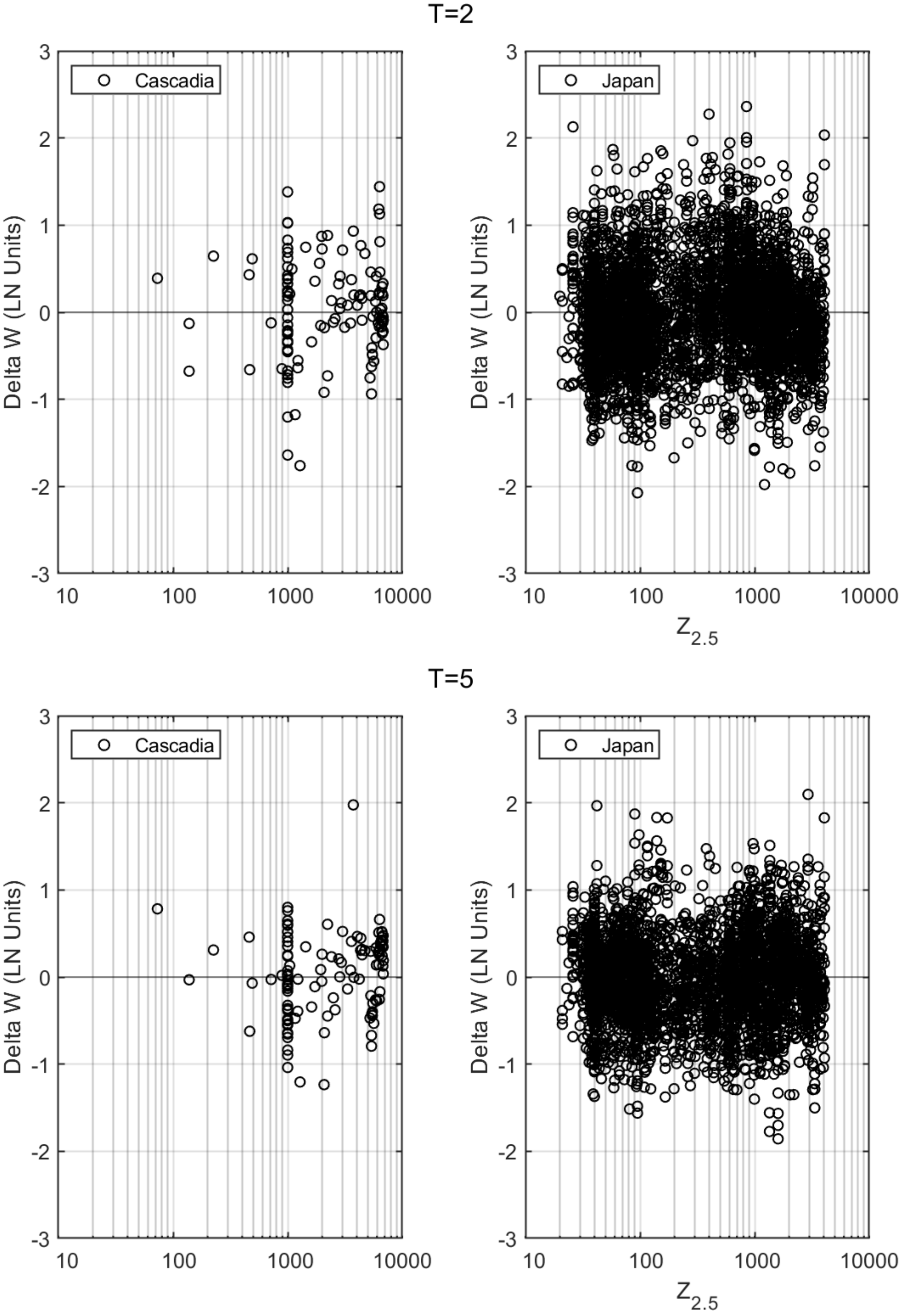

Figure 4.22: Within-event residuals versus basin depth. Top frame: T = 2 sec. Bottom Frame: T=5 sec.

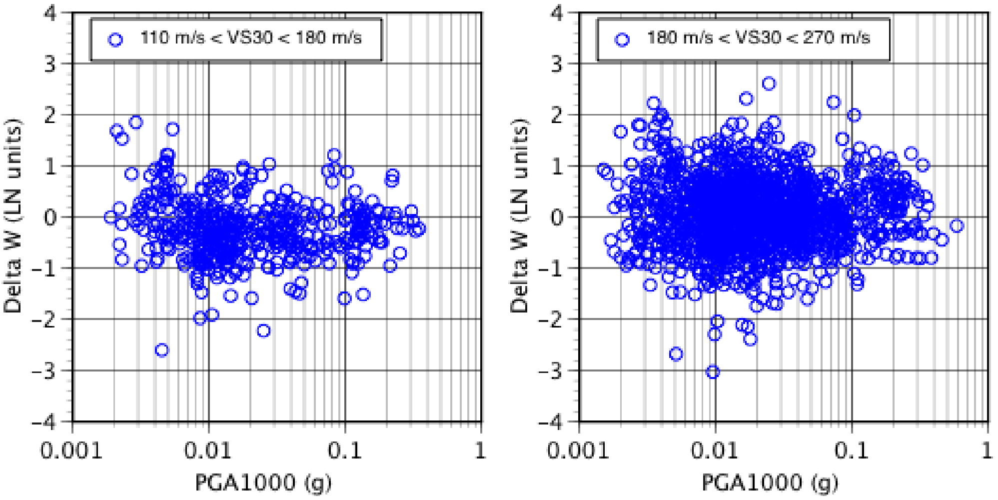

Figure 4.23: Within-event residuals for PSA (T = 0.2) as a function of PGA_{1000} for soil sites. (a) Soft-soil sites with 110 $<$ V_{S30} $<$ 180 m/sec; and (b) soil sites with 180 $<$ V_{S30} $<$ 270 m/sec

5 Aleatory Variability

The aleatory variability model is developed for the two aleatory components: between-event variability, τ, and the within-event variability, ϕ. The δB_e and the δW_{es} of Equation (4.1) can be treated as independent, and the total standard deviation, σ, is given by:

$$\sigma = \sqrt{\tau^2 + \phi^2} \tag{5.1}$$

Nearly all of the data used in the regression is in the linear range for the site response: in our subset, the median PGA_{1000} with the event term for soil sites is less than $0.1g$ for over 95% of the data and less than $0.2g$ for over 98% of the data. The effect of nonlinear site response on this small fraction of the data would change τ by less than 0.01 natural log units. Therefore, we assume that both the ϕ and the τ computed from the data apply to the weak motion. We denote this by using the subscript ”LIN” for low strain range for the ϕ and the τ computed from the regression.

5.1 ALASKA REGION DATA

In our data selection, we found the ground-motion data and meta-data from the Alaska region to be less reliable than the data from the other six regions. As part of the data selection process, large outliers were identified and removed; however, smaller errors (less than a factor of 5) were difficult to identify by visual inspection. These errors are assumed to average out for the median GMM, but they will inflate the standard deviations. We do not have the confidence in the variability of the data from Alaska region; therefore, these data were excluded from the development of the aleatory variability model.

5.2 TAU MODEL

The period dependence of τ_{LIN} for each region (except for Alaska) is presented in Figure 5.1 (left panel). For three regions (Central America, Japan, and South America), there is a large increase in τ_{LIN} in the 0.075–0.2-sec period range; he other three regions do not show this large increase in τ_{LIN} at short periods. To account for this regional difference, the τ values were averaged and smoothed as a function of period for two groups (regions with and without the increase at short periods), as shown in Figure 5.1 (right panel). The increase in the τ_{LIN} at short periods has been observed in other datasets as well and has been called the ”bump in tau.” There is no clear physical reason for the variability in the source term to have a large increase around T = 0.1 sec. It is more likely that a regional site effect (e.g., regional differences in κ) is being mapped into the source term. A regional difference in κ that affects most of the recordings in a single earthquake would manifest itself in the short-period δB_e terms. Therefore, we removed the short-period increase from the between-event variability (τ_{LIN}) and include it as part of the within-event variability (ϕ) that applies to those three regions with the observed increase in τ_{LIN} (Central America, Japan, and South America). This transfer simplified the τ term significantly: the average τ is computed for the period range of 0.3 to 10 sec, and this constant value is extended to the shorter periods as shown in Figure 5.1 (right panel). The resulting model for τ at low strains is period independent: $\tau_{LIN} = d_0$.

5.3 PHI MODEL

A common approach for developing GMMs that includes regional differences is to model the differences in the median but use the combined data to develop an aleatory variability model that is applied to all regions (e.g. Gregor et al., 2014). We followed this approach for the τ_{LIN} model, but we varied from it and incorporated regional differences into the $\phi_{LIN}(T)$ model. The variations of unsmoothed ϕ_{LIN} values for the six regions are shown in Figure 5.2. The ϕ values of Japan and South America regions show an increase at short periods (0.075 to 0.3 sec), which is similar to the increase observed in τ_{LIN} values for these two regions. This supports the interpretation that the bump in τ is due to a regional site effect. In contrast, the ϕ_{LIN} values for Cascadia, New Zealand, and Taiwan are nearly constant for T ¡ 3 sec. The ϕ_{LIN} values for Central America fall between these two groups, but it is closer to the Cascadia, New Zealand, and Taiwan group. We separated the within-event variability terms for different regions into two groups: Group 1 includes Cascadia, Central America, New Zealand, and Taiwan; Group 2 includes Japan and South America.

An initial evaluation of ϕ_{LIN} for both groups showed that there is a strong distance dependence of ϕ_{LIN} for distances greater than 200 km. Figure 5.3 shows the period dependence of ϕ_1 (average for Group 1) and ϕ_2 (average for Group 2) for four distance bins. We attribute the increase in ϕ_{LIN} at larger distances to regional path effects that are not included in our partially non-ergodic GMM. A non-ergodic GMM with path terms should remove this distance dependence of ϕ_{LIN}. There are several methods for modeling non-ergdoic path terms (Anderson and Uchiyama, 2011; Dawood and Rodriguez-Marek, 2013; Kuehn et al., 2019) that will significantly reduce the ϕ_{LIN} at large distances; note, fully non-ergodic path effects are beyond the scope of this study.

For the three regions with the short-period increase in τ_{LIN}, the difference in the computed between-event variance and the period-independent between-event variance ($\tau_{LIN}^2 = d_0^2$) is included in the ϕ_{LIN}^2 term. Therefore, the resulting ϕ_{LIN} model has three parts: ϕ_1^2 is the within-event variance for regions without increased variability at short periods (Group 1, Cascadia, New Zealand, and Taiwan); ϕ_2^2 is the additional within-event variance for regions with increased variability at short periods (Group 2, Japan and South America); and ϕ_3^2 is the additional variance from the increase in τ_{LIN} at short periods that is being included in the ϕ_{LIN} model for Central America, Japan, and South America.

The models for the within-event standard deviation for each region are given in Table 5.1. For the regions without the increase in variability at short periods (Group 1), the standard deviation of the within-event residuals is denoted as ϕ_1. To model the observed increase in ϕ_1 with distance, a simple tri-linear model for the variance, ϕ_1^2, with a constant at short and long distances, is connected by a linear function:

$$\phi_1^2(R_{Rup}, T) = \begin{cases} d_1(T) & \text{for } R_{RUP} < 150 \\ d_1(T) + d_2(T)\left(\frac{R_{Rup}-150}{300}\right) & \text{for } 150 \leq R_{RUP} \leq 450 \\ d_1(T) + d_2(T) & \text{for } R_{RUP} > 450 \end{cases} \tag{5.2}$$

The distance cutoff values of 150 km and 450 km are selected based on an evaluation of the ϕ_1 for different distance ranges. The coefficients, d_1 and d_2, are period dependent and are listed in Table 5.2.

The increase in the ϕ_{LIN} at short periods for the Japan and South America regions, shown in Figure 5.2, is limited to a narrow band of periods. This narrow-band shape is modeled as an asymmetrical trapezoid shape and peaked in the period range of 0.075–0.2 sec; it is given by the function $f_2(T)$:

$$f_2(T) = \begin{cases} 1-\alpha & \text{for } T \leq T_1 \\ 1-\alpha\frac{ln(T/T_2)}{ln(T_1/T_2)} & \text{for } T_1 < T \leq T_2 \\ 1 & \text{for for } T_2 < T \leq T_3 \\ \frac{ln(T)}{ln(T_3)} & \text{for } T_3 < T < T_4 \\ 0 & \text{for } T \geq T_4 \end{cases} \tag{5.3}$$

The α term scales the amplitude of the increased variance at short periods. An α value of unity indicates that the increase in the variance at very short periods (i.e. PGA) is zero. An example of the normalized shape of the $f_2(T)$ function is shown in Figure 5.4 .

The additional variance is modeled by scaling the normalized shape, f_2, by an amplitude, A_{phi}. Figure 5.3 shows that there is a distance dependence to the amplitude of the additional variance to be added to base model variance, ϕ_1^2. The amplitude is modeled by a simple tri-linear function of distance with a transition at a distance of 225 km:

$$A_{phi}(R_{Rup}) = \begin{cases} d_3 & \text{for } R_{RUP} < 225 \\ d_3 + d_4\left(\frac{R_{RUP}-225}{225}\right) + d_5\left(\frac{R_{RUP}-225}{225}\right)^2 & \text{for } 225 \leq R_{RUP} \leq 450 \\ d_3 + d_4 + d_5 & \text{for } R_{RUP} > 450 \end{cases} \tag{5.4}$$

The added variance, ϕ_{Add}^2, is given by

$$\phi_{Add}^2(R_{RUP}, T) = A_{phi}(R_{RUP}) f_2(T) \tag{5.5}$$

As shown in Figure 5.3, for distances less than 200 km, the ϕ_2 at the PGA does not have an increase relative to the value at T = 1 sec (Figure 5.3), so $\alpha = 1$ for this distance range. At larger distances, the ϕ_2 at the PGA is increased relative to the value at T = 1 sec, so $\alpha < 1$ for the larger distances. The α term for ϕ_2 is modeled by a distance-dependent function with smaller values at distances greater than 250 km.

$$\alpha = \begin{cases} 1 & \text{for } R_{RUP} \leq 250 \\ 1 - 0.0036(R_{RUP} - 250) & \text{for } 250 < R_{RUP} \leq 450 \\ 0.28 & \text{for } 450 < R_{RUP} \end{cases} \tag{5.6}$$

The third part of the ϕ_{LIN} model is the increase in the between-event variability at short periods seen in the τ_{LIN} values but which is modeled as within-event variability. The variance that is moved from τ_{LIN} to ϕ_{LIN} applies to a narrow period range, and the same form of the asymmetric trapezoid given in Equation 5.3 is used to model this narrow-band shape. For event terms, there is no distance dependence, so the amplitude of additional variance at short periods is modeled by a constant, d_3, with $d_4 = 0$ and $d_5 = 0$. The α term is constant for ϕ_3.

The resulting ϕ_{LIN} models are distance dependent and region dependent. The models are shown in Figure 5.5 for rupture distances of 100 km and 400 km for the three groups of regions.

5.4 NONLINEAR SITE EFFECTS ON THE ALEATORY VARIABILITY

The nonlinear response of the soil depends on amplitude of the input motion, which is affected by both the δB and δW terms. As a result, the effect of the δB term on the surface motion will be amplitude dependent, so the τ will also be amplitude dependent (Al-Atik and Abrahamson, 2010). Therefore, nonlinear site effects affect both the within-event and the between event standard deviations.

The between event residual is a constant shift that applies to all recordings in an earthquake, so some nonlinear effects could be included in τ; however, as noted earlier, the vast majority of the data used in the regression is in the linear range. In addition, we constrained the nonlinear site effect based on results from analytical site-response modeling, and we removed the median nonlinear effect from the data prior to the regression. Therefore, the event terms are for linear site response, and the τ from the regression will not be affected by nonlinear site effects.

We note others assume that nonlinear site effects only affect the ϕ term and not the τ term. For example, Stewart et al. (2017) assume that the τ from the regression includes some nonlinear effects because the event terms are computed from both soil and rock sites. Therefore, they do not modify τ for nonlinear site effects. In applications, this implies that the soil behaves differently for larger than average input motions due to a positive within-event residuals (treated as nonlinear) or due to a positive between-event residual (treated as linear). In our approach, the nonlinear soil response is based on the level of the input motion regardless of the cause of the larger input motion (within-event residual or between-event residual).

The nonlinear effects on the standard deviation are related to the variability of the input motion, but the ϕ term reflects both the variability of the input motion and the variability of the site amplification. To estimate the nonlinear effects on the standard deviation, we need to separate the ϕ into the variability of the input motion, ϕ_B^2, and the variability of the site amplification, ϕ_{amp}.

$$\phi^2_{LIN}(T) = \phi^2_B(T) + \phi^2_{amp} \tag{5.7}$$

Based on analytical site response calculations for a large number of site conditions, Abrahamson and Silva (2008) estimated ϕ_{amp} = 0.3 for all periods. We assume that this value of ϕ_{amp} applies to the subduction data.

The ϕ term with nonlinear site effects then is estimated using simple propagation of errors:

$$\begin{aligned} \phi^2_{NL}(T) =& \phi^2_{LIN}(T) + \left(\frac{\partial f_{site}(T)}{\partial lnPGA}\right)^2 \phi^2_B(PGA) \\ &+ 2\left(\frac{\partial f_{site}(T)}{\partial lnPGA}\right) \phi_B(PGA)\phi_B(T)\, \rho_W(PGA,T) \end{aligned} \tag{5.8}$$

The partial derivative term is computed from Equation 3.7 and is given by:

$$\frac{\partial f_{site}(T)}{\partial lnPGA} = \begin{cases} 0 & \text{for } V_{S30} > V_{LIN} \\ bPGA_{1000}\left(\frac{-1}{PGA_{1000}+c} + \frac{1}{PGA_{1000}+c\left(\frac{V_{S30}}{V_{LIN}}\right)^n}\right) & \text{for } V_{S30} \leq V_{LIN} \end{cases} \tag{5.9}$$

The $\rho_W(PGA,T)$ is the correlation coefficient between the normalized within-event residuals for PGA and PSA(T) for the same recording.

The τ term with nonlinear site effects has a similar form except that all of the between-event variability is associated with the input motion:

$$\begin{aligned} \tau^2_{NL}(T) =& \tau^2_{LIN}(T) + \left(\frac{\partial f_{site}(T)}{\partial lnPGA}\right)^2 \tau^2_{LIN}(PGA) \\ &+ 2\left(\frac{\partial f_{site}}{\partial lnPGA}\right) \tau_{LIN}(PGA)\tau_{LIN}(T)\, \rho_B(PGA,T) \end{aligned} \tag{5.10}$$

in which $\rho_B(PGA,T)$ is the correlation coefficient for the normalized between-event residuals. The smoothed correlation coefficients, $\rho_W(PGA,T)$ and $\rho_B(PGA,T)$ are listed in Table 5.4. Because the use of these terms are for the nonlinear site effects, the $\rho_W(PGA,T)$ is computed for rupture distances less than 200 km.

An example of the effect of the nonlinear site response on ϕ and τ is shown in Figure 5.6 for a soil site with V_{S30}=270 m/sec and PGA_{1100} = 0.15g, corresponding to a a magnitude 7 intraslab earthquake with Z_{TOR} = 60 km and R_{RUP} = 85 km based on our global model; the ϕ_1 model (e.g., Cascadia model) is used in this comparison. There is a significant reduction in both the ϕ and τ for periods less than 0.3 sec, with the largest effect at T = 0.1 sec.

5.5 SIGMA MODEL

The total σ_{LIN} for the linear range is computed using Equation 5.1. The τ_{LIN} model is a period-independent constant for all regions and all distances. The ϕ_{LIN} model is period dependent, region dependent, and distance dependent. The resulting period dependence of the σ_{LIN} model for the different regions are shown in Figure 5.7 for rupture distances of 100 km and 400 km. An example of the amplitude dependence of the effect of the nonlinear site response on the σ_{NL} is shown in Figure 5.8 for a soil site with V_{S30}=270 m/sec.

As noted in Section 5.1, we did not develop an aleatory variability model for the Alaska region. For seismic hazard applications, we recommend setting the ϕ_{LIN} for the Alaska region to the same ϕ_{LIN} category as the Cascadia region based on the spectral shapes being similar for the two regions. For applications of the global model to regions other than the seven regions listed in Table 5.1, we recommend using the ϕ_1 and ϕ_3 models with equal weight.

Table 5.1: Region-dependent within-event standard deviation models.

Region	ϕ_{LIN} Model
Alaska Cascadia New Zealand Taiwan	$\phi_1(R_{Rup}, T)$
Central America	$\sqrt{\phi_1^2(R_{Rup}, T) + \phi_3^2(R_{Rup}) f_3(T)}$
Japan South America	$\sqrt{\phi_1^2(R_{Rup}, T) + \phi_2^2(R_{Rup}) f_2(T) + \phi_3^2(R_{Rup}) f_3(T)}$

Table 5.2: **Coefficients for the ϕ_1 model.**

Period (sec)	d_1	d_2
0.01	0.325	0.137
0.02	0.325	0.137
0.03	0.325	0.137
0.05	0.325	0.137
0.075	0.325	0.137
0.10	0.325	0.137
0.15	0.325	0.137
0.20	0.325	0.137
0.25	0.325	0.137
0.30	0.325	0.137
0.40	0.325	0.137
0.50	0.325	0.137
0.60	0.325	0.137
0.75	0.325	0.137
1.0	0.325	0.137
1.5	0.312	0.113
2.0	0.302	0.096
2.5	0.295	0.082
3.0	0.289	0.072
4.0	0.280	0.055
5.0	0.273	0.041
6.0	0.267	0.030
7.5	0.259	0.017
10.0	0.250	0.000

Table 5.3: Coefficients for the τ_{LIN}, ϕ_2, and ϕ_3 models.

Coefficient	τ_{LIN} Model	ϕ_2 Model	ϕ_3 Model
d_0	0.47	-	-
T_1	-	0.03	0.03
T_2	-	0.075	0.075
T_3	-	0.2	0.1
T_4	-	1.0	0.3
d_3	-	0.109	0.242
d_4	-	0.062	0
d_5	-	0.470	0
α	-	eq (5.6)	0.42

Table 5.4: Inter-period correlation of δW and δB with PGA.

Period (sec)	ρ_W	ρ_B
0.01	1	1
0.02	0.99	0.99
0.03	0.99	0.99
0.05	0.97	0.985
0.075	0.95	0.98
0.10	0.92	0.97
0.15	0.9	0.96
0.20	0.87	0.94
0.25	0.84	0.93
0.30	0.82	0.91
0.40	0.74	0.86
0.50	0.66	0.8
0.60	0.59	0.78
0.75	0.5	0.73
1.0	0.41	0.69
1.5	0.33	0.62
2.0	0.3	0.56
2.5	0.27	0.52
3.0	0.25	0.495
4.0	0.22	0.43
5.0	0.19	0.4
6.0	0.17	0.37
7.5	0.14	0.32
10.0	0.1	0.28

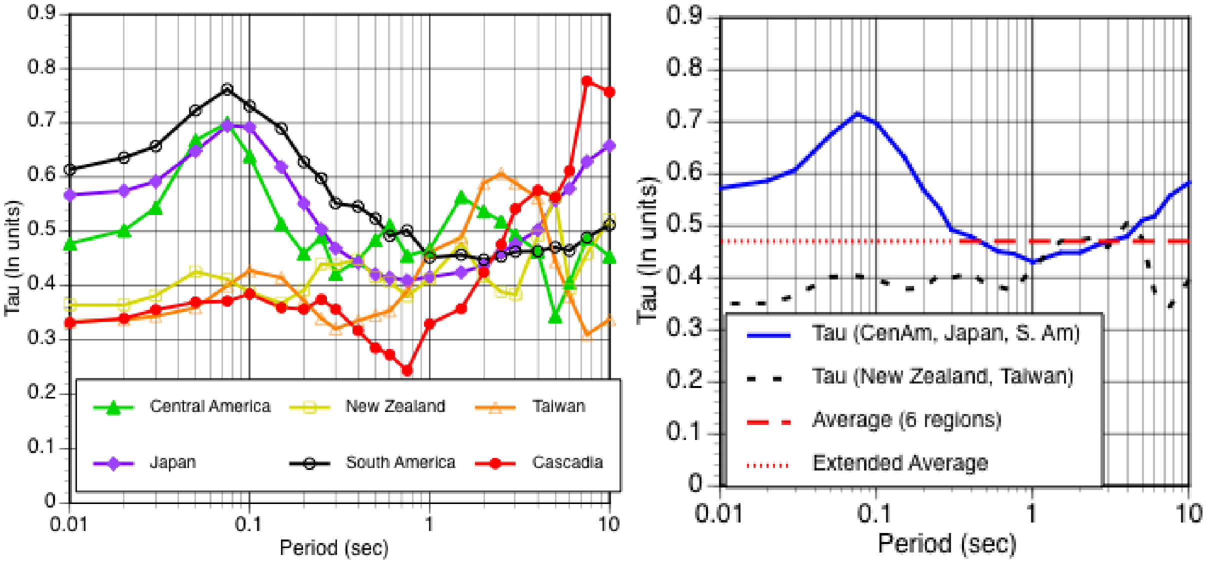

Figure 5.1: (a) Comparison of the between-event standard deviation by region; and (b) average ϕ for regions with and without the increase at short periods.

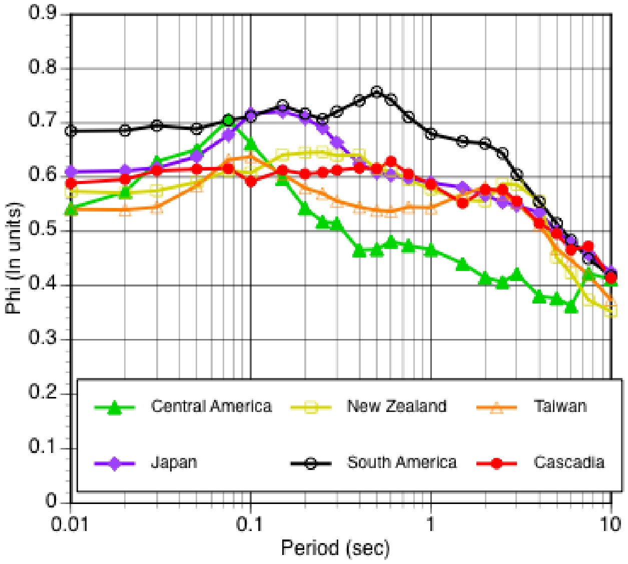

Figure 5.2: Comparison of the within-event standard deviation by region.

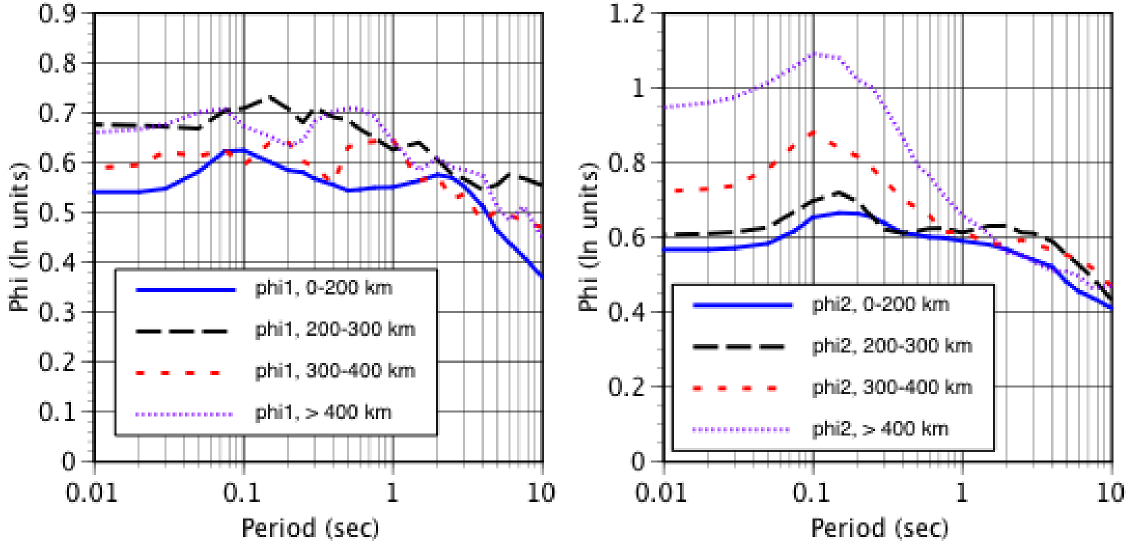

Figure 5.3: Distance dependence of the within-event standard deviation terms. (a) ϕ_1 model for Cascadia, Central America, New Zealand, and Taiwan; and (b) ϕ_2 model for Japan and South America.

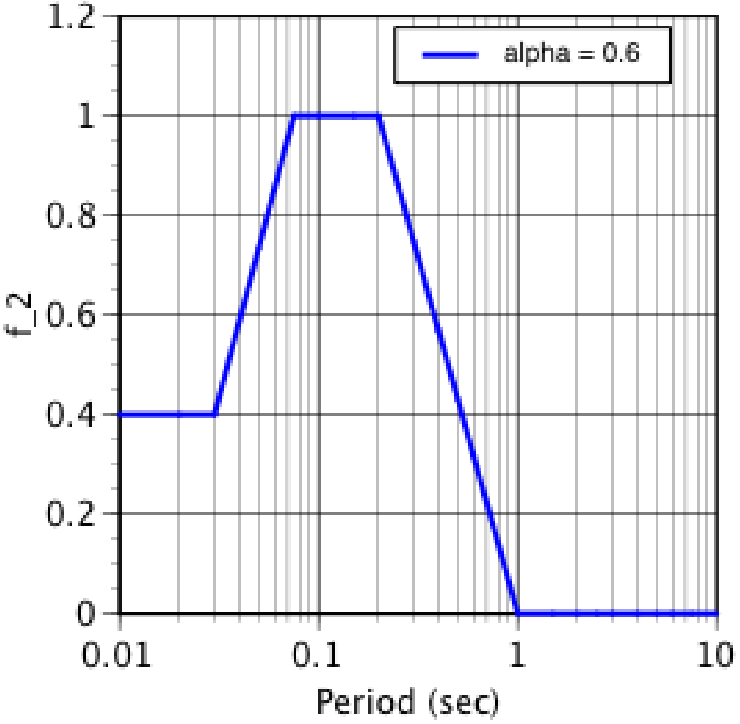

Figure 5.4: Example of the normalized narrow-band function $f_2(T)$ used for the ϕ_2^2 and ϕ_3^2 terms. T_1 = 0.03 sec, and T_2 = 0.075 sec

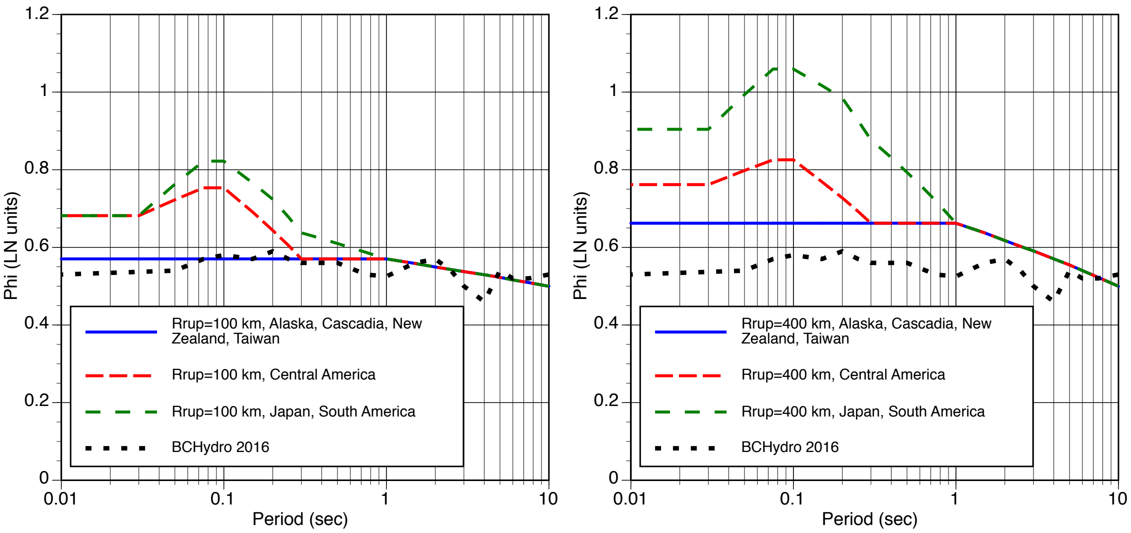

Figure 5.5: Comparison of the within-event standard deviation ϕ_{LIN} aleatory standard deviation models. (a) Distance = 100 km; and (b) Distance = 400 km.

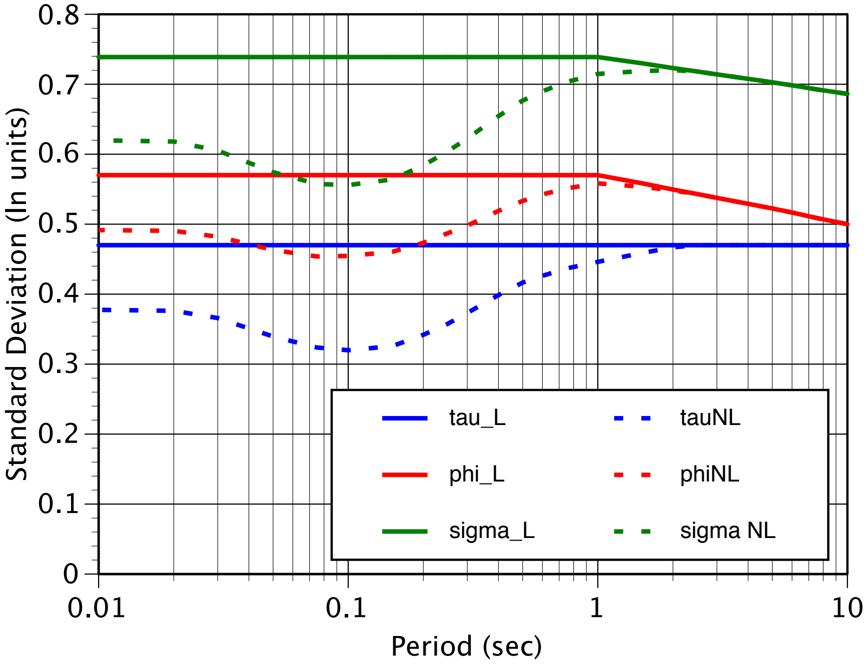

Figure 5.6: Example of the effect of the nonlinear site response on the components of the standard deviation for a soil site with V_{S30} = 270 m/sec and PGA_{1100} = 0.15g. The ϕ_{LIN} is based on the ϕ_1 model (e.g., Cascadia region).

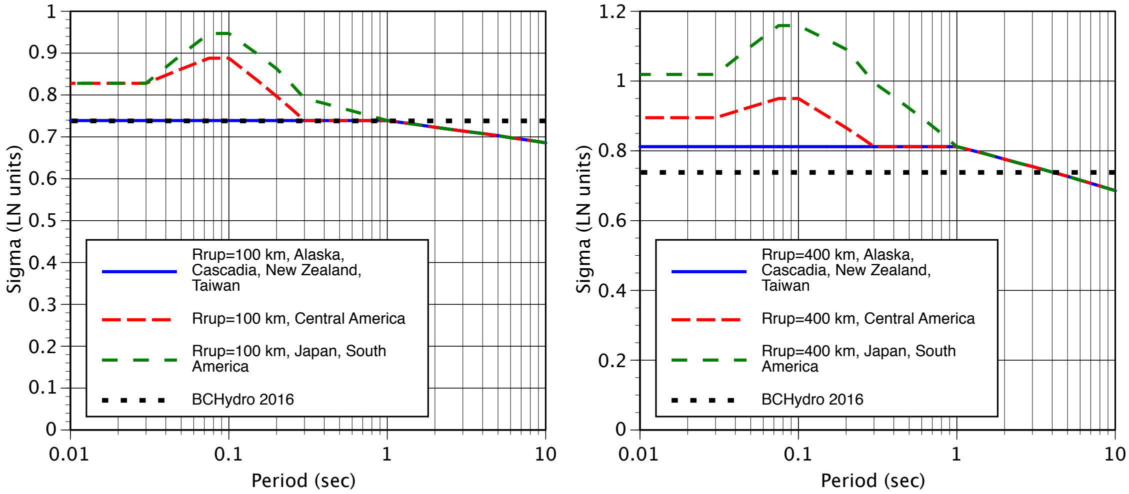

Figure 5.7: Comparison of the total σ_{LIN} aleatory standard deviation models. (a) Distance = 100 km; and (b) distance = 400 km.

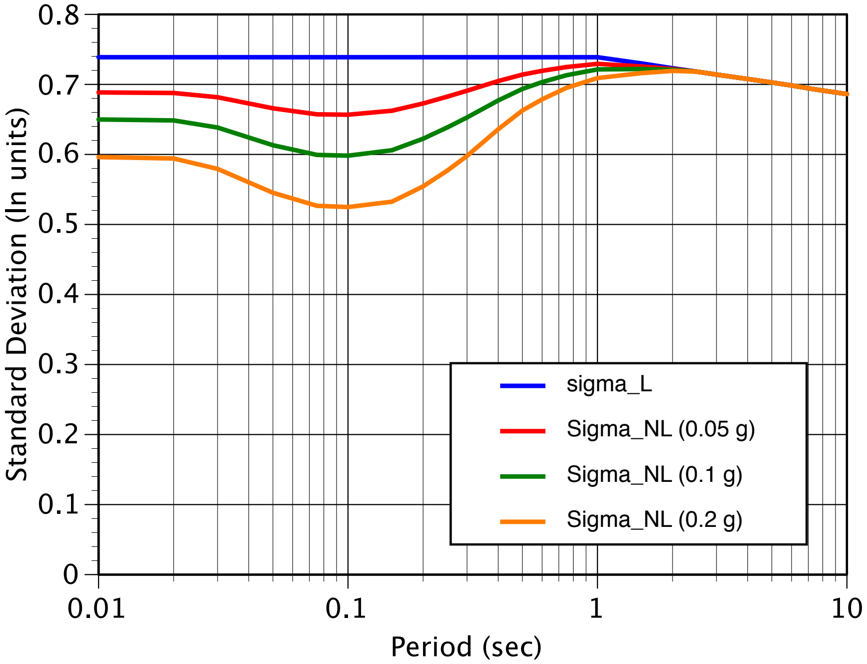

Figure 5.8: Example of the PGA_{1100} dependence of σ for a soil site with V_{S30} = 270 m/sec. The ϕ_{LIN} is based on the ϕ_1 model (e.g., Cascadia).

6 Model Results and Comparisons

6.1 COMPARISON OF REGIONAL MODELS WITH OBSERVATIONS

As a check of the regionalized coefficients, the median estimates of the region-specific GMMs are compared to the recorded ground motions at the center of the data for each region. First, the mean magnitude, mean V_{S30} and geometric mean distance were computed for each region and each event type, as shown in Table 6.1. The ranges about the central values were set at plus/minus 0.5 magnitude units and factors of 0.5 and 2 for the mean distance and V_{S30}. The geometric mean of the PSA values within the selected range were computed by giving equal weights to each data point (recording). Because the data are given equal weights, the average may be different than the regression model, which uses the weights based on the random-effects approach.

As shown in Figure 6.1, the average spectra at the center of the data for intraslab events were compared with the median spectra for the region-specific GMMs. There are too few data from Cascadia and Alaska regions in our subset for this type of comparison, so these regions were excluded from Figures 6.1 and 6.2. Overall, there is good agreement between the model for each region and the average spectrum for the center of the data for periods less than 1 sec. At long periods, the noted differences are likely the result of the reduced number of recordings that are reliable at the longer periods, which changes the sampling of magnitude and distance.

Figure 6.2 compares the average spectra at the center of the data for interface earthquakes with the median spectra for the region-specific GMMs; because there are too few interface data from Taiwan, only four regions are shown in this figure. Overall, there is good agreement between the model for each region and the spectrum for the center of the data for the full period range except for the long periods (T>2 sec) for South America.

From these comparisons, we conclude that the region-specific terms in the proposed GMM are consistent with the recordings in the center of the data.

6.2 ADJUSTMENT OF CASCADIA AND ALASKA REGION-SPECIFIC MODELS

A key issue for the Cascadia model is that the Cascadia-specific GMM estimated by the regression leads to very low ground motions at short periods compared to the global model. The Cascadia subset in our selected dataset is very sparse. There are only six earthquakes in the Cascadia region in the selected subset, two of which have only one recording. Only two of the events in the subset

(2001 M6.8 Nisqually and 1999 M5.8 Satsop earthquakes) are well-recorded. Figure 6.3 compares the median spectrum for M8 and M9 interface earthquakes at a distance of 100 km and for M7 and M8 intraslab earthquakes at a distance of 100 km and a depth of 50 km for the global and the region-specific models. The short-period ground motions for the Cascadia model from the regression are factors of 2–3 lower than the global model, and they fall below the median spectra of all the other regions. At long periods (2 to 5 sec), the Cascadia model from the regression becomes similar to the global model.

The median estimates from the Cascadia-specific model are compared with the median spectrum for three finite-fault simulations for an M9 Cascadia interface earthquake (Gregor et al., 2002, 2006; Atkinson and Macias, 2008; Frankel et al., 2018) in Figure 6.4. The comparison is made for a non-basin site at a rupture distance of 110 km. The ground motions from the finite-fault simulations vary significantly, but all of them are much larger at all period than the ground motions from the Cascadia-specific model from the regression.

The finite-fault simulations were not developed independent of the empirical ground-motion data from subduction earthquakes. There are model parameters used in the simulations that were calibrated with the available empirical ground-motion data, so having similar levels of the short-period ground motions from the Cascadia-specific simulations compared to the global empirical models is not an independent constraint on ground-motion amplitudes; however, it does show that the Cascadia-specific rupture geometry can lead to ground motions similar to the global models. That is, the narrower down-dip width of the Cascadia interface zone does not necessarily limit the amplitude of the ground motions at short periods.

With the limited empirical ground-motion data for Cascadia, and without a sound physical basis for the large reduction in the short-period ground motions in Cascadia as compared to other regions, we judged that the very low short-period ground motions given by the the Cascadia-specific model from the regression should not be used for seismic hazard studies. Therefore, we applied an adjustment to the Cascadia model so that the ground-motions for an M7 intraslab earthquake and an M8 interface earthquake—both with Z_{TOR} = 50 km, a rupture distance of 100 km, and a V_{S30} of 400 m/sec for Cascadia-specific model—are consistent with the geometric mean of the response spectra from the three regions with the lowest ground motions: Central America, New Zealand, and Taiwan. The resulting adjustment terms are listed in Table 6.2 and are shown in Figure 6.5 as a function of period. The increase corresponds to about a factor of 2 at short periods as shown in Figures 6.3 and 6.4. At short periods, the response spectrum from the adjusted Cascadia model is similar to the spectrum from the (Atkinson and Macias, 2008) simulations, but it remains lower at all periods compared to the other two finite-fault simulation results.

The Cascadia adjustment factor is applied to both intraslab events and interface events; therefore, it is applied to the predictions for the well-recorded Nisqually intraslab earthquake as well. The period dependence of the Nisqually event terms before and after the adjustment is shown in Figure 6.6. For periods less than 1 sec, the adjusted event terms are below the 16th percentile (-0.47) of the between-event residuals. Therefore, there is an implicit assumption that the Nisqually earthquake experienced short-period ground motions that were well-below average (i.e., large negative event term) for our adjusted-Cascadia model.

The Alaska-specific model from the regression also leads to very low ground motions at short periods as compared to the other regions. There are 16 earthquakes from Alaska region in our selected dataset, but only two of them have magnitudes greater than 6, and most of the data is at distances greater than 200 km. We do not have the confidence that the low ground motions from these events will be representative of the ground motions from future larger magnitude earthquakes in Alaska. Therefore, we have applied the same scaling approach used for Cascadia to the Alaska-specific model. The Alaska adjustment terms are listed in Table 6.2 and then compared to the Cascadia adjustment terms in Figure 6.5. The spectra for the adjusted Alaska-specific ground-motion predictions are compared to the spectra for other regions in Figure 6.3.

These adjustments to the Cascadia and Alaska regions are based on our subjective judgment. As more ground-motion data are collected and finite-fault simulations with thre-dimensional crustal models conducted for the these regions, these adjustment factors should be re-evaluated.

6.3 MAGNITUDE SCALING

The magnitude scaling for the global model for subduction interface and intraslab earthquakes is compared to the 2016 BCHydro model in Figure 6.7 (left panel). In the 2016 BCHydro model, the slopes of the magnitude scaling were the same for interface and intraslab events, but the current model allows for the differences in magnitude scaling for subduction interface and intraslab earthquakes. For intraslab events, the slope of the magnitude scaling of the global GMM is similar to the magnitude slope for the 2016 BCHydro model; whereas, the global model has a weaker magnitude scaling for interface events than the magnitude scaling of the 2016 BCHydro model. The slopes of the magnitude scaling are region independent, both for the interface and intraslab events, but there are region-specific magnitude break points for the large magnitude scaling for intraslab events, as shown in Figure 6.7 (right panel). The New Zealand region has the oldest slab and the largest magnitude break point (M8). The Cascadia region has the youngest slab and the smallest magnitude break point (M7.1).

Figure 6.8 compares the magnitude scaling from the Cascadia region for interface earthquakes to the magnitude scaling from the finite-fault simulations for Cascadia (Gregor et al., 2006; Atkinson and Macias, 2008). The model predictions are normalized to be equal for M7.5 to isolate the magnitude scaling of the models from other effects on the ground motion. The slope at large magnitudes (above the break point) in the 2016 BCHydro model was set using these two sets of simulations; therefore, the large-magnitude slope of the new GMM remains consistent with the slope from the two simulation-based models as expected. The magnitude scaling for Cascadia is also shown using the mean (M7.7) magnitude break point from the Campbell (2020) model compared to using the magnitude break points in the model (M8.2 for PGA and M8.0 for T = 2 sec). The M7.7 break point leads to a scaling that is similar to the Atkinson and Macias (2008) simulations; however, using the lower break point in the magnitude scaling would cause the Cascadia model to fall even further below the simulation results in terms of amplitudes. As we have adjusted the Cascadia model to increase the ground motions for large interface earthquakes, reducing it using the M7.7 break point would be counter productive.

6.4 DISTANCE SCALING

Figure 6.9 compares the short-period distance scaling for the global interface and global intraslab models to the distance scaling for 2016 BCHydro model in . At a distance of 100 km, the M7 intraslab short-period ground motions are about a factor of 3 larger than the interface ground motions. Compared with the 2016 BCHydro model, the distance attenuation in the global model is steeper for both event types.

Examples of the regional differences in the distance scaling for interface and intraslab earthquakes are shown in Figure 6.10. The geometrical-spreading term is the same for all regions except for Taiwan; therefore, the distance slopes at distances less than 150 km are similar for other six regions. The Taiwan region has weaker attenuation with distance, resulting from the inclusion of the additional geometrical spreading term (a_{16}). At large distances, the region-specific linear R terms lead to very different slopes, with the Japan and South America regions having the strongest attenuation.

6.5 DEPTH SCALING

Our GMM includes the depth scaling only for the intraslab events. The depth scaling for short periods (T = 0.2 sec) is compared with the 2016 BCHydro model in Figure 6.11. Our model has a very strong depth dependence for depths of 20–50 km: there is a factor of two increase for each 15 km increase in depth. For depths greater than 50 km, there is a more gradual depth scaling with a factor of two increase for a change in depth of 120 km. The depth-independent ground motion for the same scenario from the interface earthquakes is also shown in this figure. At a depth of 20 km, the interface ground motion is similar to the intraslab ground motion. This supports the idea that the steeper depth scaling from 20–50 is a result of misclassification of deep interface events as shallow intraslab events.

6.6 BASIN DEPTH SCALING

Basin-depth scaling for T = 3 sec for the Cascadia region is compared to the basin-depth scaling in the three-dimensional finite-fault simulations from the M9 Project in Figure 6.12. For the M9 Project results, the geometric mean of the response spectra from the simulated ground motions for sites with rupture distances between 100 and 120 km and $Z_{2.5}$ values in a specified range was computed from all 30 realizations of the rupture (Frankel et al., 2018). Due to the correlation of the V_{S30} and the $Z_{2.5}$, some of the basin scaling is captured in the V_{S30} scaling. To account for this correlation, the amplitudes were normalized by the spectral values for the $Z_{2.5ref}$ at the given V_{S30}. The normalized basin factors are shown as a function of $Z_{2.5}$ in Figure 6.12 for V_{S30} = 600 m/sec, which is the V_{S30} for the M9 Project simulations. For this V_{S30} value, $Z_{2.5ref}$ is equal to 2000 m. To be consistent with this $Z_{2.5ref}$ value, the simulations were normalized by the median response spectral values for sites with $Z_{2.5}$ between 1500 m and 2500 m. Figure 6.12 shows that basin scaling in the Cascadia-specific GMM is similar to the basin scaling from the M9 project for deep basin sites, but the simulations show a reduction for sites with $Z_{2.5} < 2000$ m that is not seen in the available empirical data.

6.7 EPISTEMIC UNCERTAINTY FOR THE GLOBAL MODEL

The global model can be used for seismic hazard applications in regions other than the seven regions included in this study. In this case, epistemic uncertainty should be added to the global model based on the range of the median ground motions from the five regions with estimated regional terms: Central America, Japan, New Zealand, South America, and Taiwan. In a site-specific application, the epistemic uncertainty in the regional constant can be developed based on the standard deviation of the median ground motion from the five regional models for the controlling source.

A generic epistemic uncertainty, representing the epistemic uncertainty due to unknown regional constants, is given below and is based on the standard deviation of the median ln(PSA) values for an M8 interface earthquake and a V_{S30} of 400 m/sec for rupture distances between 50 and 500 km.

$$C_{epistemic} = e_1 + e_2 \frac{R_{rup}}{100} + e_3 \left(\frac{R_{rup}}{100} \right)^2 \tag{6.1}$$

The coefficients for the equation 6.1 are given in Table 6.3. The $C_{epistemic}$ term represents epistemic uncertainty in the constant and should be added to the constant term for the global model. To avoid overly large uncertainty if the model is extrapolated outside the 50–500 km distance range, the R_{RUP} used in equation 6.1 should be limited to a minimum of 50 km and a maximum of 500 km. For distances less than 50 km, use the $C_{epistemic}$ value for 50 km, and for distances greater than 500 km use the $C_{epistemic}$ value for 500 km.

Table 6.1: Scenarios for the center of the data for the full dataset and for regions.

	Interface			Intraslab			
Region	Mag	R_{RUP} (km)	V_{S30} (m/sec)	Mag	R_{RUP} (km)	V_{S30} (m/sec)	Z_{TOR} (km)
Global	6.7	120	400	6.4	140	400	50
Central America	7.5	53	434	6.5	88	476	50
Japan	6.9	146	354	6.6	177	372	70
New Zealand	6.8	111	485	5.8	117	329	50
South America	6.6	137	665	6.3	291	691	150
Taiwan	6.8	87	422	6.2	120	424	45

Table 6.2: Adjustment terms for Cascadia and Alaksa.

Period (sec)	Alaska	Cascadia
0.01	0.487	0.828
0.02	0.519	0.825
0.03	0.543	0.834
0.05	0.435	0.895
0.075	0.410	0.863
0.10	0.397	0.842
0.15	0.428	0.737
0.20	0.442	0.746
0.25	0.494	0.796
0.30	0.565	0.782
0.40	0.625	0.768
0.50	0.634	0.728
0.60	0.581	0.701
0.75	0.497	0.685
1.0	0.469	0.642
1.5	0.509	0.325
2.0	0.478	0.257
2.5	0.492	0.211
3.0	0.470	0.296
4.0	0.336	0.232
5.0	0.228	0.034
6.0	0.151	-0.037
7.5	0.051	-0.178
10.0	-0.251	-0.313

Table 6.3: **Coefficients for epistemic uncertainty for the global model.**

Period (sec)	e_0	e_1	e_2
0.01	0.550	-0.270	0.050
0.02	0.550	-0.270	0.050
0.03	0.550	-0.270	0.050
0.05	0.560	-0.270	0.050
0.075	0.580	-0.270	0.050
0.1	0.590	-0.270	0.050
0.15	0.590	-0.270	0.050
0.2	0.570	-0.270	0.050
0.25	0.530	-0.224	0.043
0.3	0.490	-0.186	0.037
0.4	0.425	-0.126	0.028
0.5	0.375	-0.079	0.022
0.6	0.345	-0.041	0.016
0.75	0.300	0.005	0.009
1	0.240	0.065	0.000
1.5	0.230	0.065	0.000
2	0.230	0.065	0.000
2.5	0.230	0.065	0.000
3	0.240	0.065	0.000
4	0.270	0.065	0.000
5	0.300	0.065	0.000
6	0.320	0.065	0.000
7.5	0.350	0.065	0.000
10	0.350	0.065	0.000

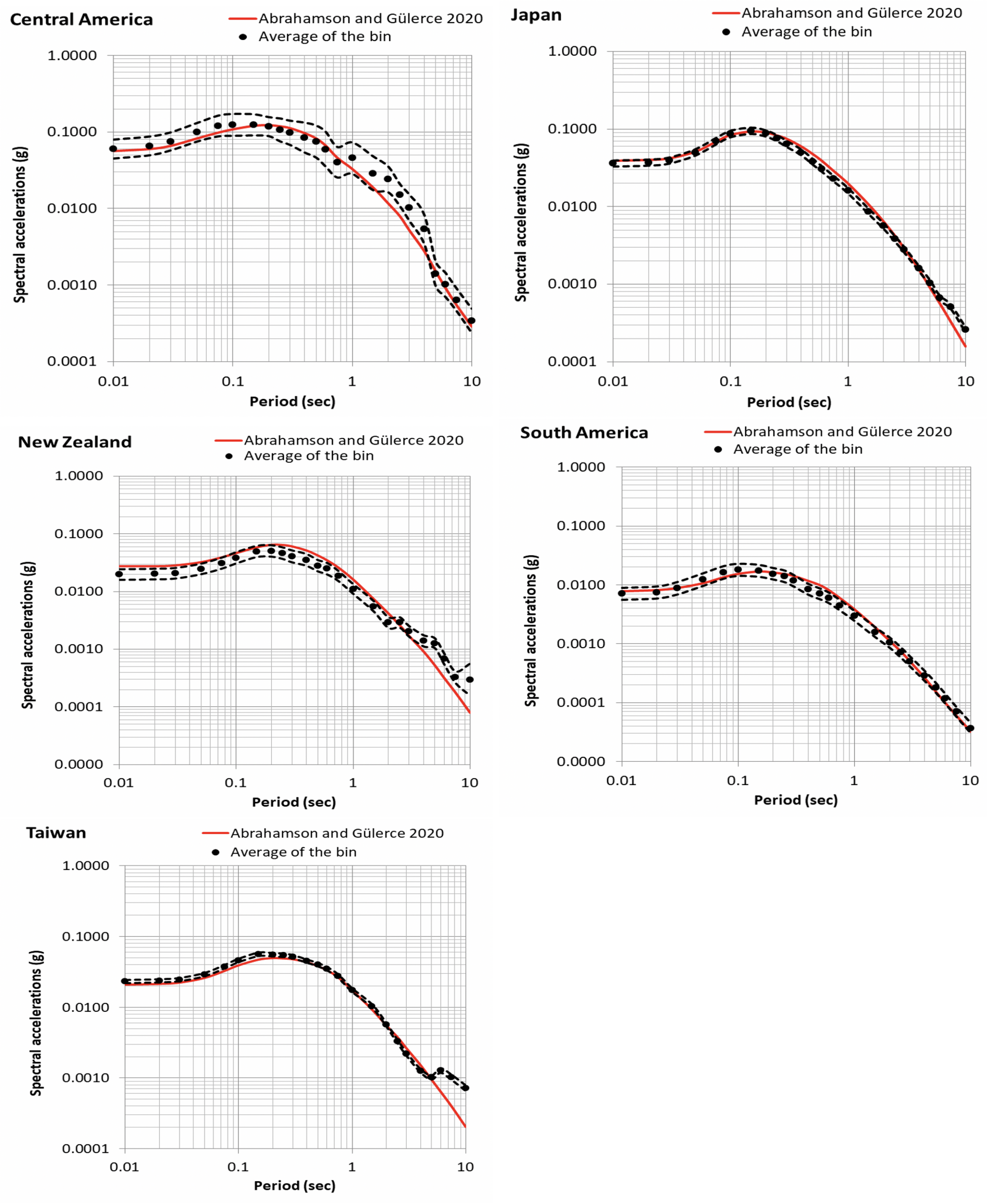

Figure 6.1: Comparison of the response spectra for intraslab events using the regionalized GMM with equally-weighted data from the center of the data for the region.

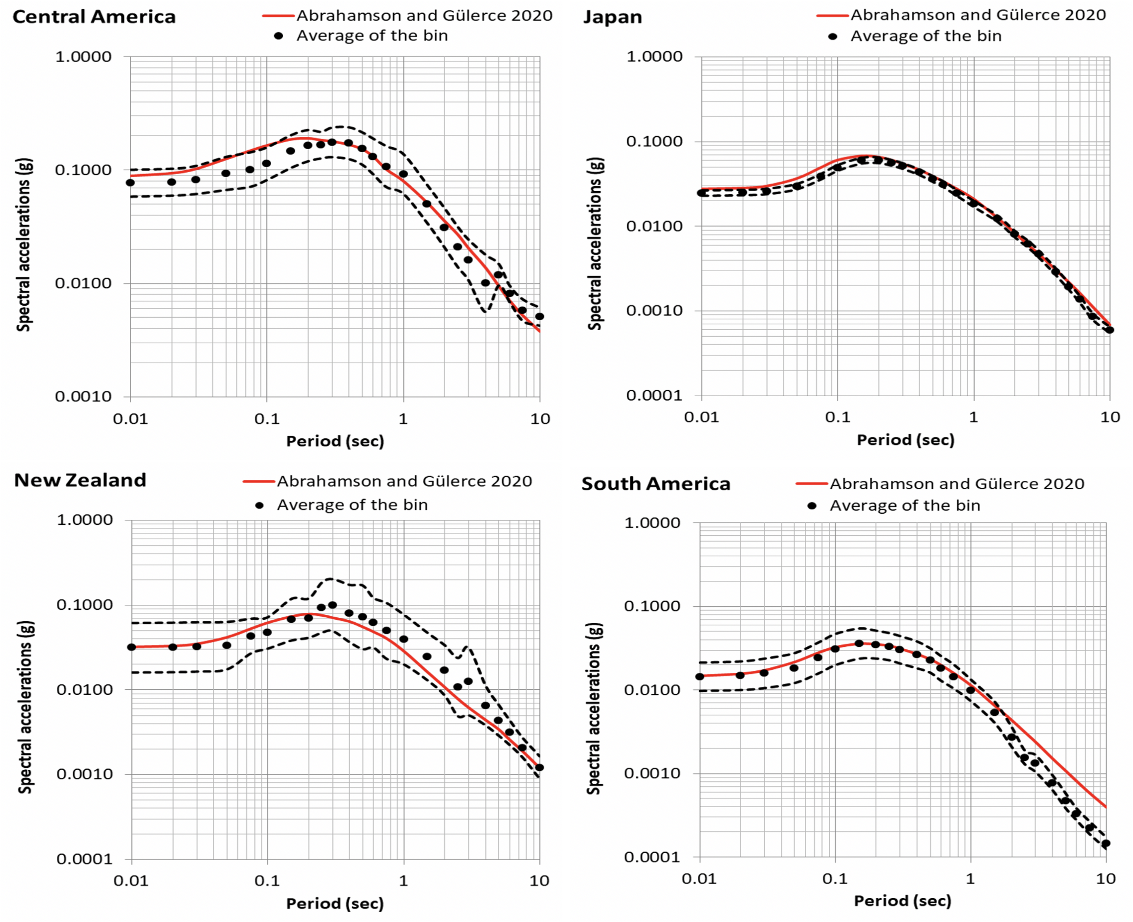

Figure 6.2: Comparison of the response spectra for interface events using the regionalized GMM with equally-weighted data from the center of the data for the region.

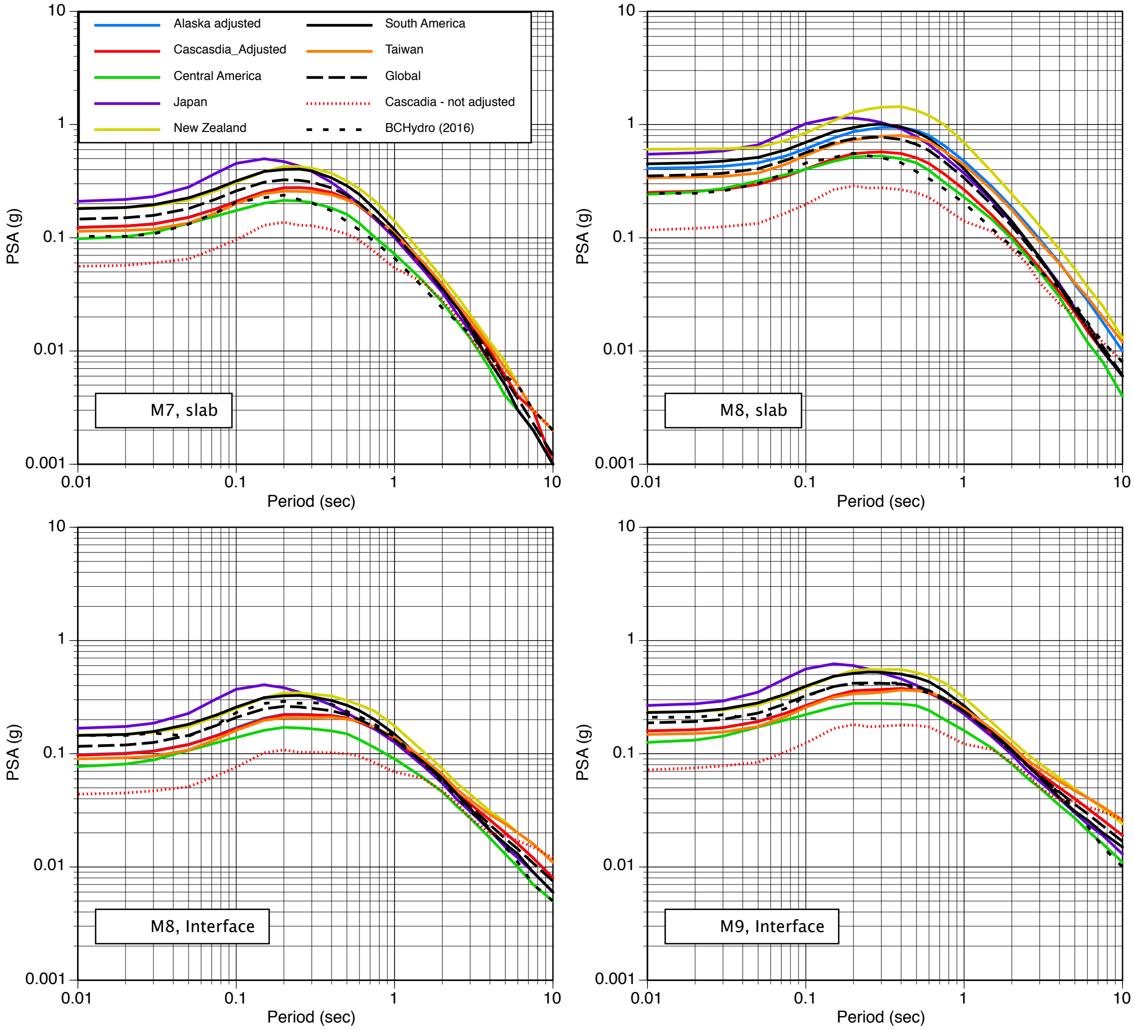

Figure 6.3: Comparison of the response spectra for seven regions.

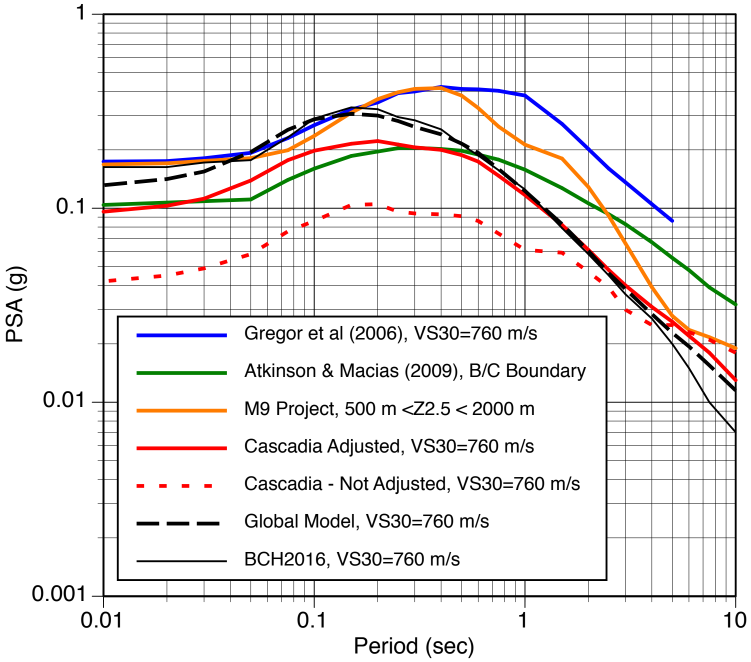

Figure 6.4: **Comparison of the response spectra for an M = 9 interface for the Cascadia model with response spectra from finite-fault simulations. The rupture distance is 110 km, V_{S30} = 760 m/sec, and $Z_{2.5}$ = 500–2000 m.**

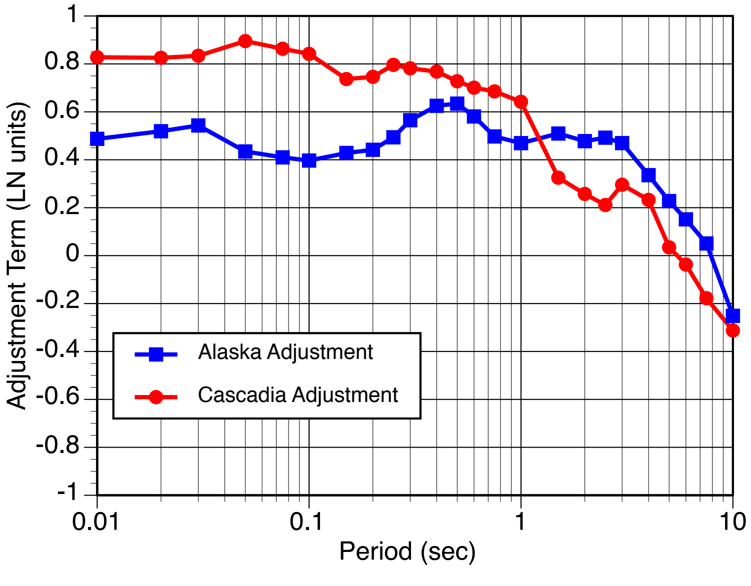

Figure 6.5: **Adjustment terms applied to the Cascadia and Alaska regions. The adjustment terms are added to the region-specific constant terms (a_{31} and a_{32}) for Alaska and Cascadia.**

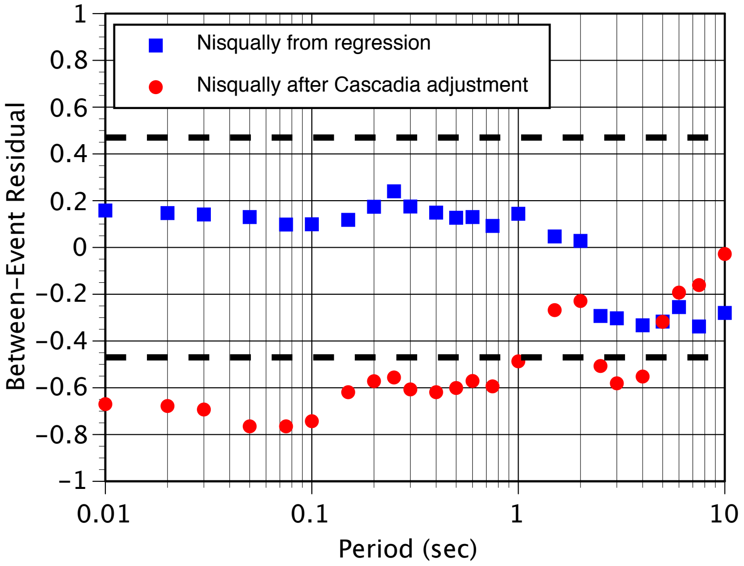

Figure 6.6: Between event residuals for the Nisqually earthquake with and without the Cascadia adjustment terms. The black dashed lines show plus/minus (one standard deviation of the between-event residuals ($\pm\tau$).

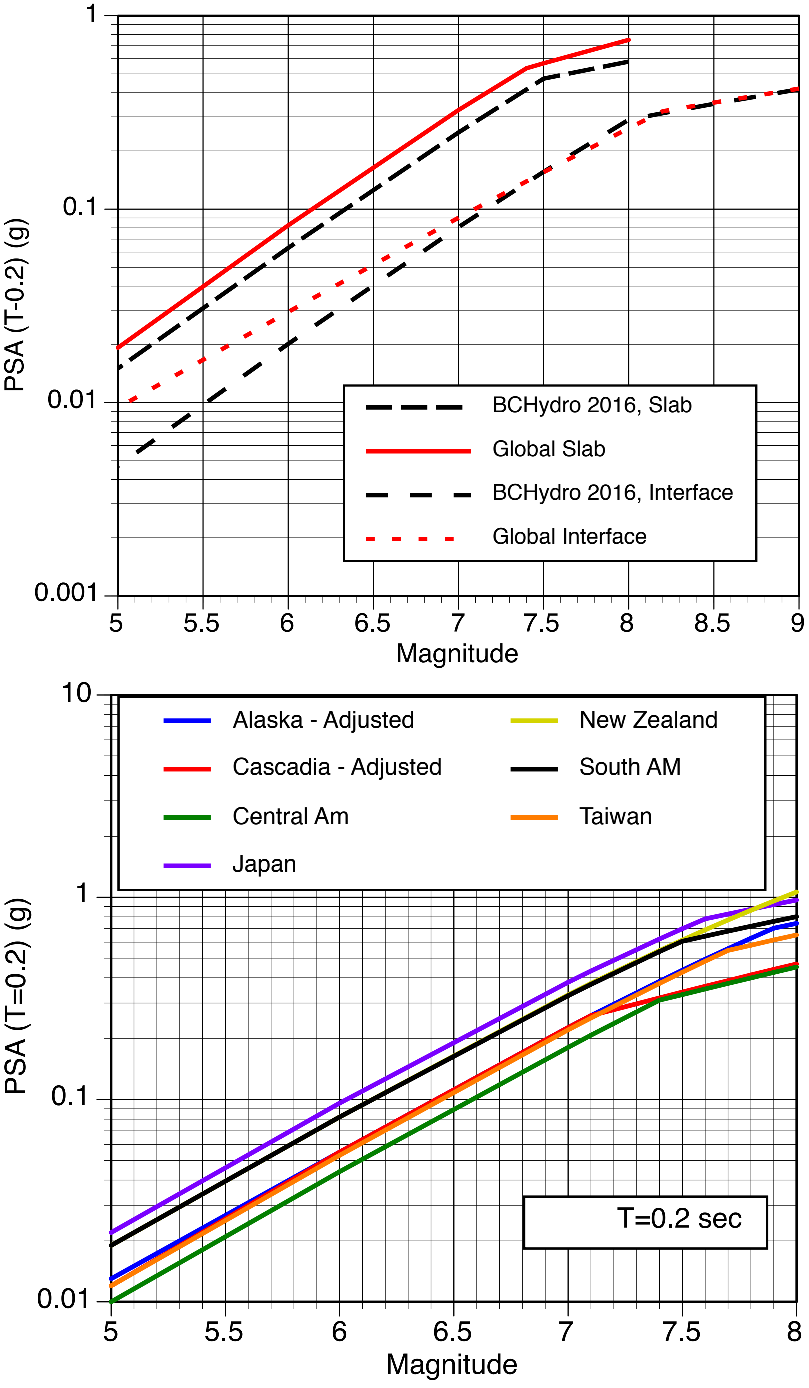

Figure 6.7: Comparison of the magnitude scaling for the final models. The top frame compares scaling for the global model with the scaling for the BCHydro2016 model. The global model has weaker magnitude scaling for interface events than for intraslab events. The bottom frame compares the magnitude scaling for intraslab earthquakes for the seven regions.

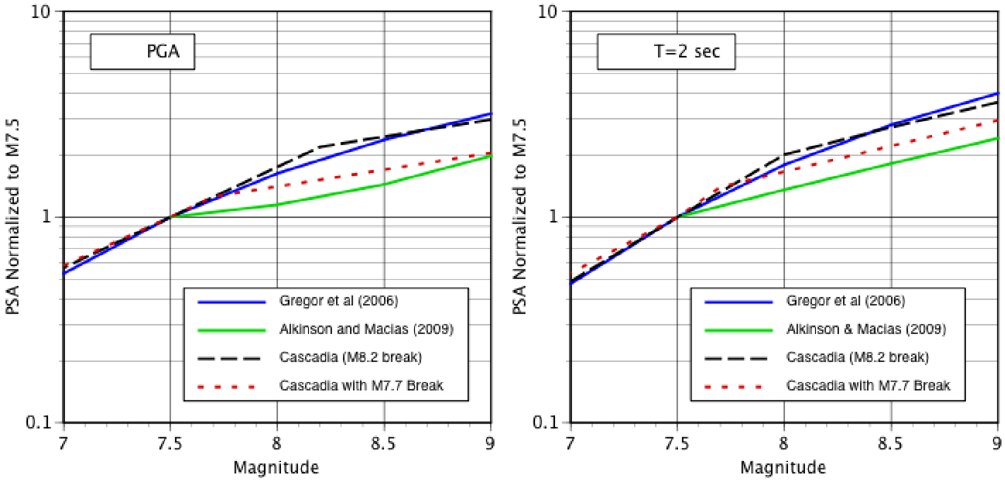

Figure 6.8: Comparison of the large-magnitude scaling for interface earthquakes for the Cascadia GMM with the scaling from finite-fault simulations for Cascadia for a rupture distance of 110 km, V_{S30} = 760 m/sec, and $Z_{2.5}$ = 500–2000 m.

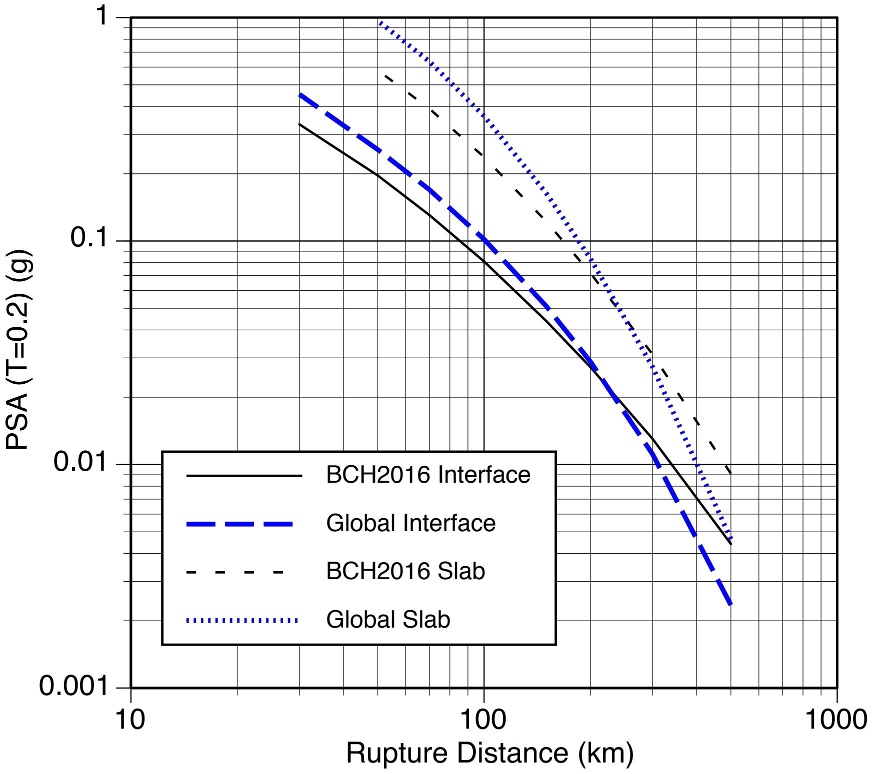

Figure 6.9: Comparison of the distance scaling for interface and intraslab events for the global model and the 2016 BCHydro model for M = 7, V_{S30} = 400 m/sec, and Z_{TOR} = 50 km.

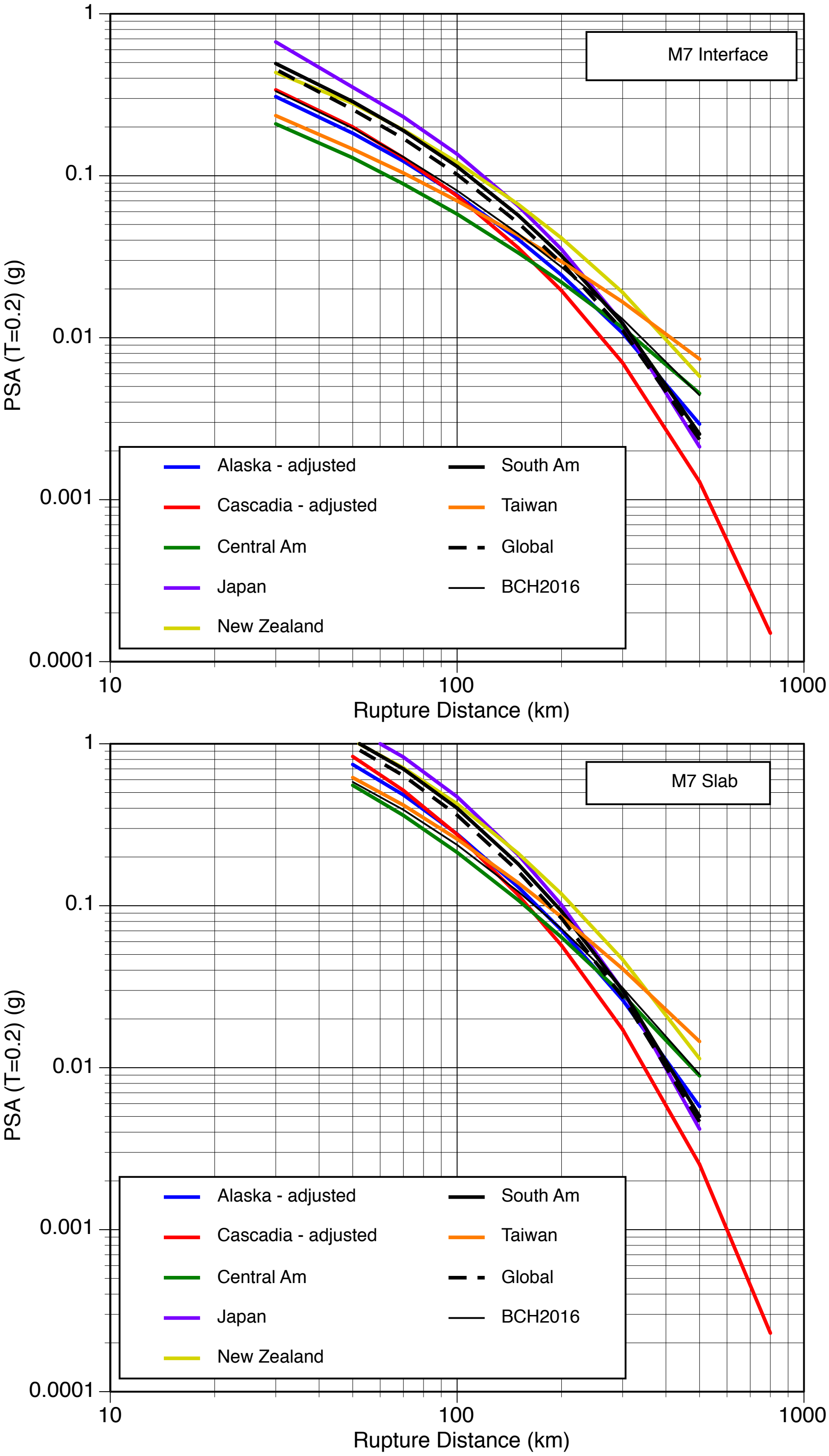

Figure 6.10: Comparison of the distance scaling for the seven regions for T = 0.2 sec. The top frame is for interface events and the bottom frame is for intraslab events.

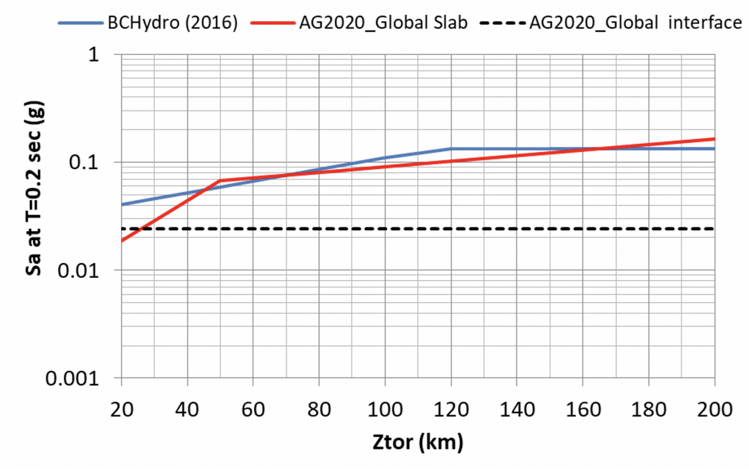

Figure 6.11: Comparison of the Z_{TOR} scaling between the global model and the 2016 BCHydro model.

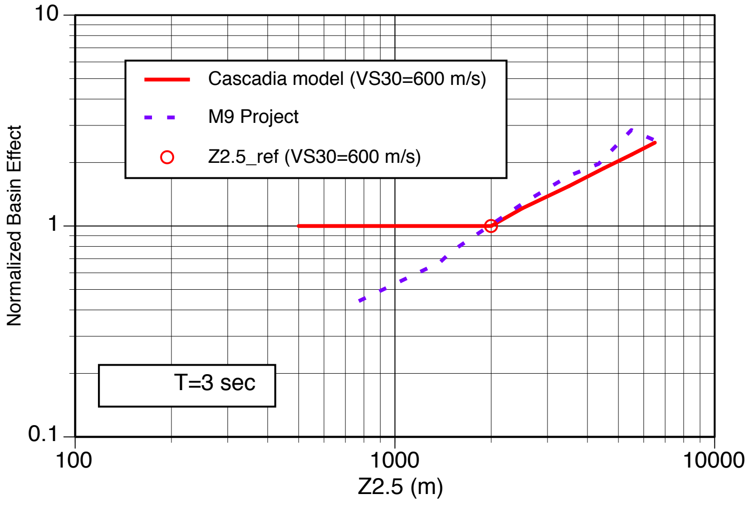

Figure 6.12: Comparison of the T = 3 sec basin scaling for the Cascadia model with the basin scaling from the M9 Project three-dimensional simulations. The normalization is for V_{S30} = 600 m/sec with $Z_{2.5ref}$ = 2000 m.

7 Model Application Guidelines

The applicability of the GMM to a specific site or a specific seismic source depends on the decisions made in the development of the GMM. The key decisions that we have made in model development and the technical basis for these decisions are summarized below. These key decisions should be considered in evaluating the applicability of our subduction GMM to a specific site for seismic hazard studies.

If local ground-motion data is used to evaluate candidate GMMs for application to a region, we recommend that the median and aleatory variability models be evaluated separately. In some cases, the median model will be consistent with the data, but the standard deviation model is not consistent (or vice versa). Treating the median and sigma separately allows for the best parts of the alternative models to be identified.

7.1 DATASET DECISIONS

The ground-motions recorded at the stations located in the back-arc region were removed from the subset of the data used in model development, except for the Cascadia region. The ground motions from back-arc stations were removed because most of the back-arc recordings are from Japan. The Japanese ground-motion dataset has a strong back-arc effect that attenuates the short-period ground motions, but this effect is much weaker in the available back-arc data from other subduction zones. In addition, the Japanese data show that there are large differences in the amount of the additional back-arc attenuation for different parts of Japan. For seismic hazard applications in which the site is located in the back-arc region, available local back-arc ground-motion data should be evaluated to determine if there is high back-arc attenuation in the region as observed in the strong motions from Japan. Our GMM is not applicable for sites located in the back-arc of regions with strong back-arc attenuation.

The large-distance attenuation of the M9.1 Tohoku earthquake is very different from the large-distance scaling for the other M>8 interface earthquakes in Japan: there is a much steeper attenuation of the short-period ground motions for distances more than 200 km. If an event has very different distance attenuation compared with the other events, then the between-event residual will depend on the average distance in the data and will not represent the differences in the source effects.

With the limitation of our regression approach that does not include event-specific distance attenuation, we did not want the large-distance data from the Tohoku earthquake to degrade the model at the short distances (less than 200 km) that often dominate the hazard in subduction zones. A model with event-specific distance slopes or non-ergodic path terms would solve this issue and allow the large distance Tohoku data to be included in the regression without degrading the fit at the shorter distances.

For eight earthquakes from northern Peru and Ecuador (latitudes between 2N to 7S), the average short-period between-event residual is about -0.7, indicating that the median ground motion from these earthquakes are about a factor of 2 lower than the ground motions in southern Peru and Chile. This large regional difference is calculated based on only eight earthquakes. We judged that there were not enough earthquakes from northern Peru and Ecuador to have a well-constrained regional constant; therefore, we included these eight earthquakes as part of the South America Region. If additional ground-motion data are collected for the latitude range 2N to 7S that also show a large reduction in short-period ground motions, then a scale factor should be applied to our South America GMM to account for this difference. This could also affect the estimate of the aleatory variability for the South America region.

7.2 MEDIAN GMM DECISIONS

We used region-independent magnitude break points in the large-magnitude scaling for subduction interface earthquakes. An alternative approach would use the region-dependent break points proposed by Campbell (2020). If finite-fault simulations confirm the relation between the magnitude break point and the down-dip width of the interface proposed by Campbell (2020), then these break points should be incorporated into our GMM. This adjustment may easily done by changing the C_1 values and adjusting the constant as described by Abrahamson et al. (2016).

One of the key points in the proposed GMM is the large adjustment applied to the median Cascadia and Alaska GMMs estimated in regression as discussed in Section 6.2. Currently, there is very little information to constrain this adjustment. With the available information, we consider the adjusted models to be better predictors of the expected ground motions from future large subduction earthquakes in these regions than the models estimated in regression. If a physical reason for a large reduction in the ground motions in these two regions with respect to other regions is found in the future, then these adjustments should be revised or removed. In future updates of the subduction GMMs, an improved approach would be to use a fully non-ergodic GMM with estimation of the epistemic uncertainty of the non-ergodic terms.

7.3 ALEATORY VARIABILITY DECISIONS

We considered the increase in between-event variability at short periods observed for Central America, Japan, and South America to be part of the within-event variability and transferred this increase to the ϕ model. This is not a standard approach used in ground-motion characterization; however, we think that it is more likely that the short-period increase in aleatory variability is caused by a regional site term than by a source term.

We modeled the within-event variability with a distance dependence: at large distances ($>$ 300 km), the ϕ values increase significantly. We consider these large standard deviations to be due to spatial differences in the path terms (linear R term) within a broad region with systematic and repeatable effects rather than aleatory variability. For sites located a large distances from subduction zones, the local ground-motion data should be evaluated to determine the path effects if the subduction zone is a significant contributor to the seismic hazard. If the path effects from local data are used to adjust the median model, then the increase in ϕ at large distances is not needed. An example of this type of adjustment to the large distance scaling is given in Geopentech (2015).

The Alaska region has the largest percentage of data that were identified as being outliers by visual inspection. It is likely that there are other incorrect data in this region that were not identified. Therefore, we did not consider the variability from the Alaska data to be reliable. We recommend using the Cascadia ϕ model for application to Alaska. If the quality of the dataset for the Alaska region is improved, this assumption should be checked.

7.4 MODEL APPLICATION

The GMM developed in this study is intended to replace the 2016 BCHydro model (Abrahamson et al., 2016). Based on the constraints applied to the magnitude scaling, the model is considered to be applicable to M6 to M9.5 for interface earthquakes and M5 to M8 for intraslab earthquakes. The applicable distance range is 500 km for sites in the fore-arc region with the exception that the Cascadia model is applicable to 800 km, including the back-arc. If the global GMM is used in a seismic hazard analysis, there should be additional epistemic uncertainty in the median to capture the range of the median ground motions as discussed in Section 6.7.

For the Cascadia and Alaska regions, we provided subjective adjustment factors that increase the ground motions from the regression to be more consistent with the scaling for other regions. To reflect the lower ground motions in the current dataset for these two regions, the region-specific models using the regression coefficients in Table 4.8 without adjustments can be used as alternative models to capture the epistemic uncertainty in this adjustment, which is similar to the Cascadia-specific alternative model given in Abrahamson et al. (2016).

REFERENCES

Abrahamson, N., Gregor, N., and Addo, K. (2016). "Bchydro ground-motion prediction equations for subduction earthquakes." *Earthquake Spectra*, 32(1), 23–44.

Abrahamson, N. and Silva, W. (1997). "Empirical response spectral attenuation relations for shallow crustal earthquakes." *Seism. Res. Let.*, 68(1), 94–127.

Abrahamson, N. and Silva, W. (2008). "Summary of the abrahamson and silva nga ground-motion relations." *Earthquake Spectra*, 24(1), 67–97.

Abrahamson, N. and Youngs, R. (1992). "A stable algorithm for regression analysis using the random effects model." *Bull. Seismol. Soc. Am.*, 82(1), 505–510.

Al-Atik, L. and Abrahamson, N. (2010). "Nonlinear site response effects on the standard deviations of predicted ground motions," bulletin of the seismological society of america." *Bull. Seismol. Soc. Am.*, 100(5), 1288–1292.

Anderson, J. G. and Uchiyama, Y. (2011). "A methodology to improve ground-motion prediction equations by including path corrections." *Bull. Seismol. Soc. Am.*, 101(4), 1822–1846.

Archuleta, R. and Ji, C. (2018). "A look at scaling of ground motion with magnitude." *Proceedings of the 11th National Conference on Earthquake Engineering, Los Angeles, CA*.

Atkinson, G. (2006). "Single-station sigma." *Bull. Seismol. Soc. Am.*, 96(2), 446–455.

Atkinson, G. and Macias, M. (2008). "Predicted ground motions for great interface earthquakes in the cascadia subduction zone." *Bull. Seismol. Soc. Am.*, 99(3), 1552–1578.

BCHydro (2012). "Dam safety probabilistic seismic hazard analysis (psha) model." *Report no.*, BCHydro Report No. E658, Vancouver, British Columbia.

Bozorgnia, Y., Abrahamson, N., Al-Atik, L., Ancheta, T., Atkinson, G., Baker, J., Baltay, A., Boore, D., Campbell, K., Chiou, B., Darragh, R., Day, S., Donahue, J., Graves, R., Gregor, N., Hanks, T., Idriss, I., Kamai, R., Kishida, T., Kottke, A., Mahin, S., Rezaeian, S., Rowshandel, B., Seyhan, E., Shahi, S., Shantz, T., Silva, W., Spudich, P., Stewart, J., Watson-Lamprey, J., Wooddell, K., and Youngs, R. (2014). "Nga-west2 research project." *Earthquake Spectra*, 30(3), 973–987.

Campbell, K. (2020). "Proposed methodology for estimating the magnitude at which subduction megathrust ground motions and source dimensions exhibit a break in magnitude scaling: Example for 79 global subduction zones." *Earthquake Spectra*, 36(3), 1271–1297.

Coppersmith, K., Bommer, J., Hanson, K., Coppersmith, R., Unruh, J., Wolf, L., Youngs, R., Al Atik, L., Rodriguez-Marek, A., and Toro, G. (2014). "Hanford sitewide probabilistic seismic hazard analysis." , Technical Report Prepared for the U.S. Department of Energy Under Contract DE-AC06076RL01830, and Energy Northwest, Pacific Northwest National Lab Report PNNL-23361, November.

Dawood, H. M. and Rodriguez-Marek, A. (2013). "A method for including path effects in ground-motion prediction equations: An example using the mw 9.0 tohoku earthquake aftershocks." *Bull. Seismol. Soc. Am.*, 103(2B), 1360–1372.

Frankel, A., Wirth, E., Marafi, N., Vidale, J., and Stephenson, W. (2018). "Broadband synthetic seismograms for magnitude 9 earthquakes on the cascadia megathrust based on 3d simulations and stochastic synthetics, part 1: Methodology and overall results." *Bull. Seismol. Soc. Am.*, 108(5a), 2347–12369.

Geopentech (2015). "Southwestern united states ground motion characterization sshac level 3, rev 2, march 2015." , Report to PG&E.

Gregor, N., Abrahamson, N., Atkinson, G., Boore, D., Bozorgnia, Y., Campbell, K., Chiou, B.-J., Idriss, I., Kamai, R., Seyhan, E., Silva, W., Stewart, J., and Youngs, R. (2014). "Comparison of nga-west2 gmpes." *Earthquake Spectra*, 30(3), 1179–1197.

Gregor, N., Silva, W., Wong, I., and Youngs, R. (2002). "Ground-motion attenuation relationships for cascadia subduction zone megathrust earthquakes based on a stochastic finite-fault modeling." *Bull. Seismol. Soc. Am.*, 92, 1923–1932.

Gregor, N., Silva, W., Wong, I., and Youngs, R. (2006). "Updated response spectral attenuation relationship for cascadia subduction zone megathrust earthquakes." *Seism. Res. Let.*, 77, 325–326.

Kotha, S. R., Bindi, D., and Cotton, F. (2016). "Partially non-ergodic region-specific gmpe for europe and middle-east." *Bull. Earthquake Eng.*, 14(4), 1245–1263.

Kuehn, N., Abrahamson, N., and Walling, M. (2019). "Incorporating non-ergodic path effects into the nga west 2 ground-motion prediction equations." *Bull. Seismol. Soc. Am.*, 109(2), 575–585.

Lanzano, G., Pacor, F., Luzi, L., D'Amico, M., Puglia, R., and C., F. (2017). "Systematic source, path and site effects on ground motion variability: the case study of northern italy." *Bull. Earthquake Eng*, 15(11), 4563–4583.

Lin, P.-S., Chiou, B., Abrahamson, N., Walling, M., Lee, C. T., and Cheng, C.-T. (2011). "Repeatable source, site, and path effects on the standard deviation for empirical ground-motion prediction models." *Bull. Seismol. Soc. Am.*, 101(5), 2281–2295.

Morikawa, N., Kanno, T., Narita, A., Fujiwara, H., Okumura, T., Fukushima, Y., and Guerpinar, A. (2008). "Strong motion uncertainty determined from observed records by dense network in japan." *Journal of Seismology*, 12(4), 529–546.

Phung, V., Loh, C., Chao, S., and Abrahamson, N. (2020). "Ground motion prediction equation for taiwan subduction zone earthquakes." *Earthquake Spectra*, 35(3), 1331–1358.

Renault, P., Heuberger, S., and Abrahamson, N. (2010). “Pegasos refinement project: An improved psha for swiss nuclear power plants.” *Proceedings of 14ECEE-European Conference of Earthquake Engineering*, paper ID 991.

Rodriguez-Marek, A., Rathje, E., Bommer, J., Scherbaum, F., and Stafford, P. (2014). “Application of single-station sigma and site-response characterization in a probabilistic seismic-hazard analysis for a new nuclear site.” *Bull. Seismol. Soc. Am.*, 104(4), 1601–1619.

Stewart, J. (2020). “Data resources for nga-subduction project.” , PEER Report 2020/02, Pacific Earthquake Engineering Research Center, University of California, Berkeley, CA.

Stewart, J., Afshari, K., and Goulet, G. A. (2017). “Non-ergodic site response in seismic hazard analysis.” *Earthquake Spectra*, 33(4), 1385–1414.

Villani, M. and Abrahamson, N. (2015). “Repeatable site and path effects on the ground-motion sigma based on empirical data from southern california and simulated waveforms from the cybershake platform.” *Bull. Seismol. Soc. Am.*, 105(5), 2681–2695.

Zhao, J., Jiang, F., Shi, P., Xing, H., Huang, H., Hou, R., Zhang, Y., Yu, P., Lan, X., Rhoades, D., and Somerville, P. (2016a). “Gground-motion prediction equations for subduction interface earthquakes in japan using site class and simple geometric attenuation functions.” *Bull. Seismol. Soc. Am.*, 106, 1535–1551.

Zhao, J., Liang, X., Jiang, F., Xing, H., a., Zhu, M., Hou, R., Zhang, Y., Lan, X., Rhoades, D., Irikura, K., and Fukushima, Y. (2016b). “Ground-motion prediction equations for subduction interface earthquakes in japan using site class and simple geometric attenuation functions.” *Bull. Seismol. Soc. Am.*, 106, 1518–1534.

Appendix A: Residual Plots

This appendix contains a complete set of plots of the between-event and within-event residuals for 24 periods.

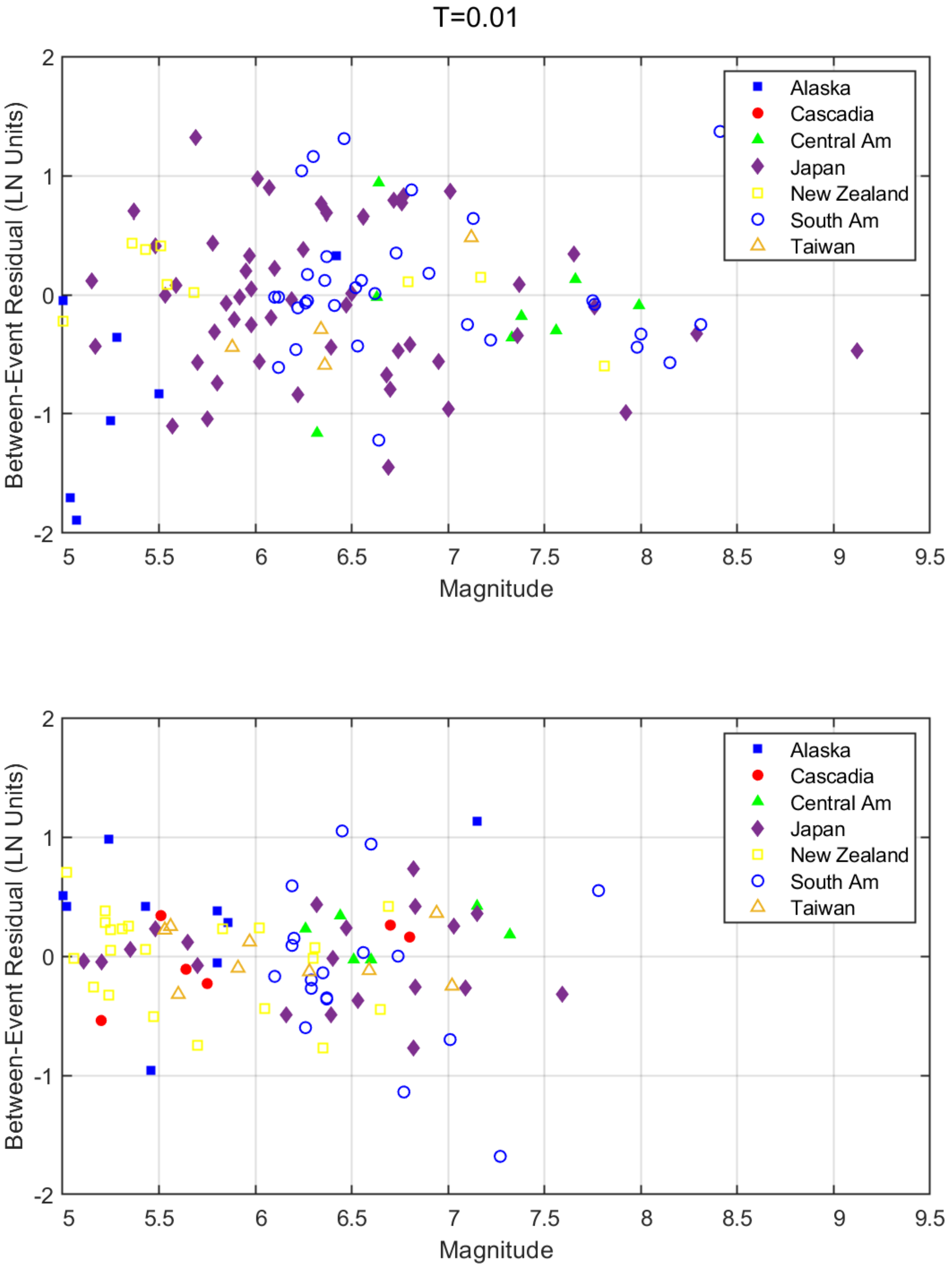

Figure A.1: Between-event residuals versus magnitude for T = 0.01 sec. Top frame: interface earthquakes. Bottom frame: intraslab earthquakes.

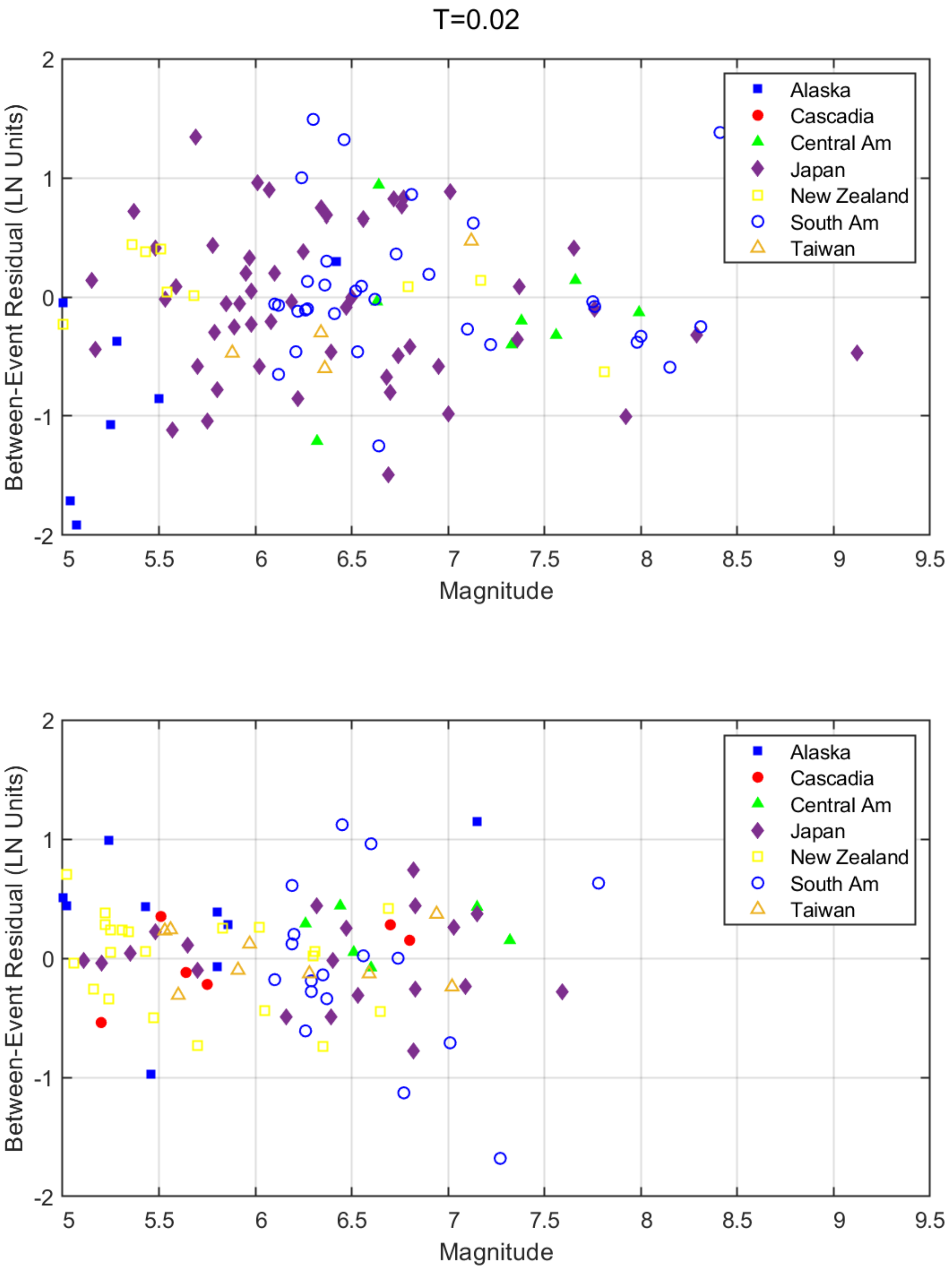

Figure A.2: Between-event residuals versus magnitude for T = 0.02 sec. Top frame: interface earthquakes. Bottom frame: intraslab earthquakes.

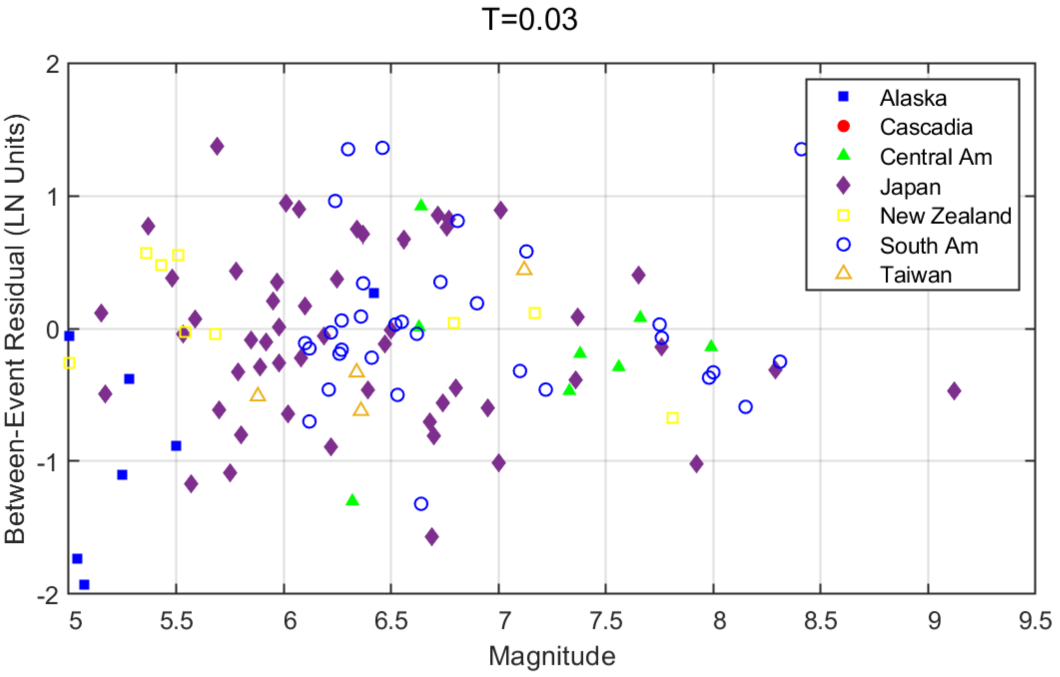

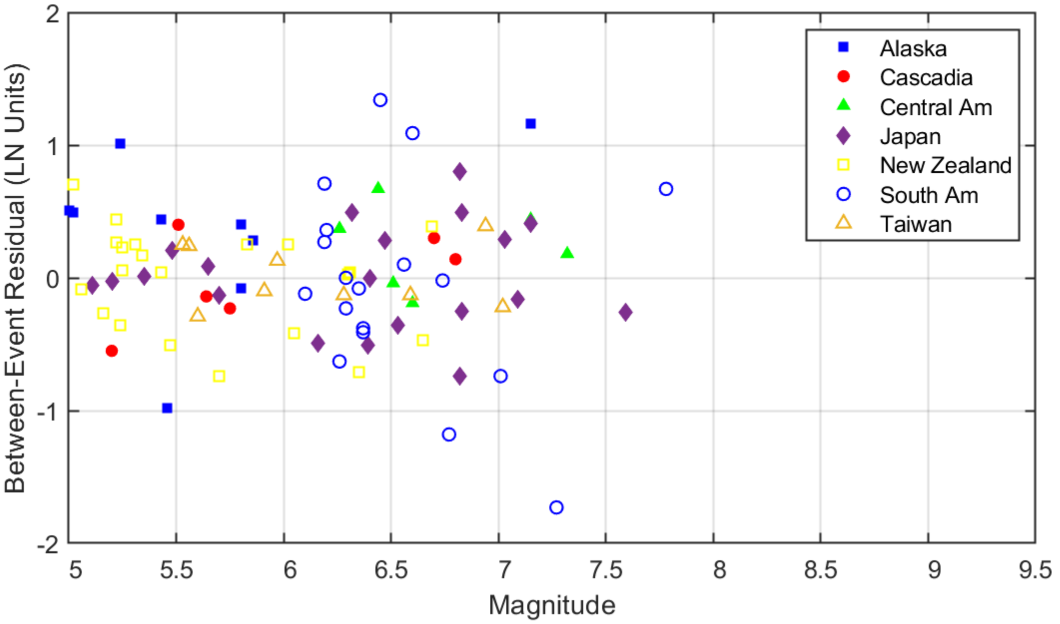

Figure A.3: Between-event residuals versus magnitude for T = 0.03 sec. Top frame: interface earthquakes. Bottom frame: intraslab earthquakes.

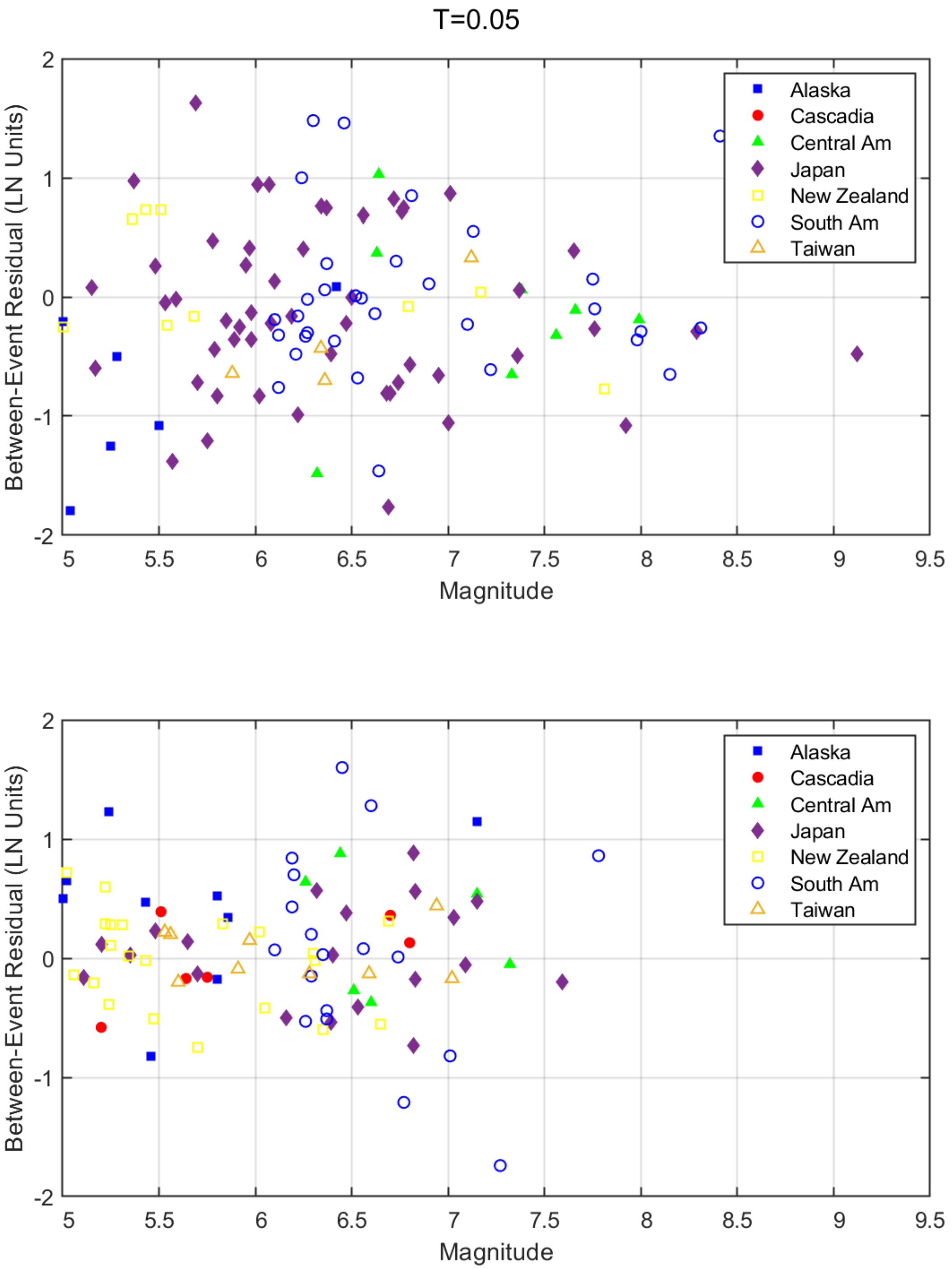

Figure A.4: Between-event residuals versus magnitude for T = 0.05 sec. Top frame: interface earthquakes. Bottom frame: intraslab earthquakes.

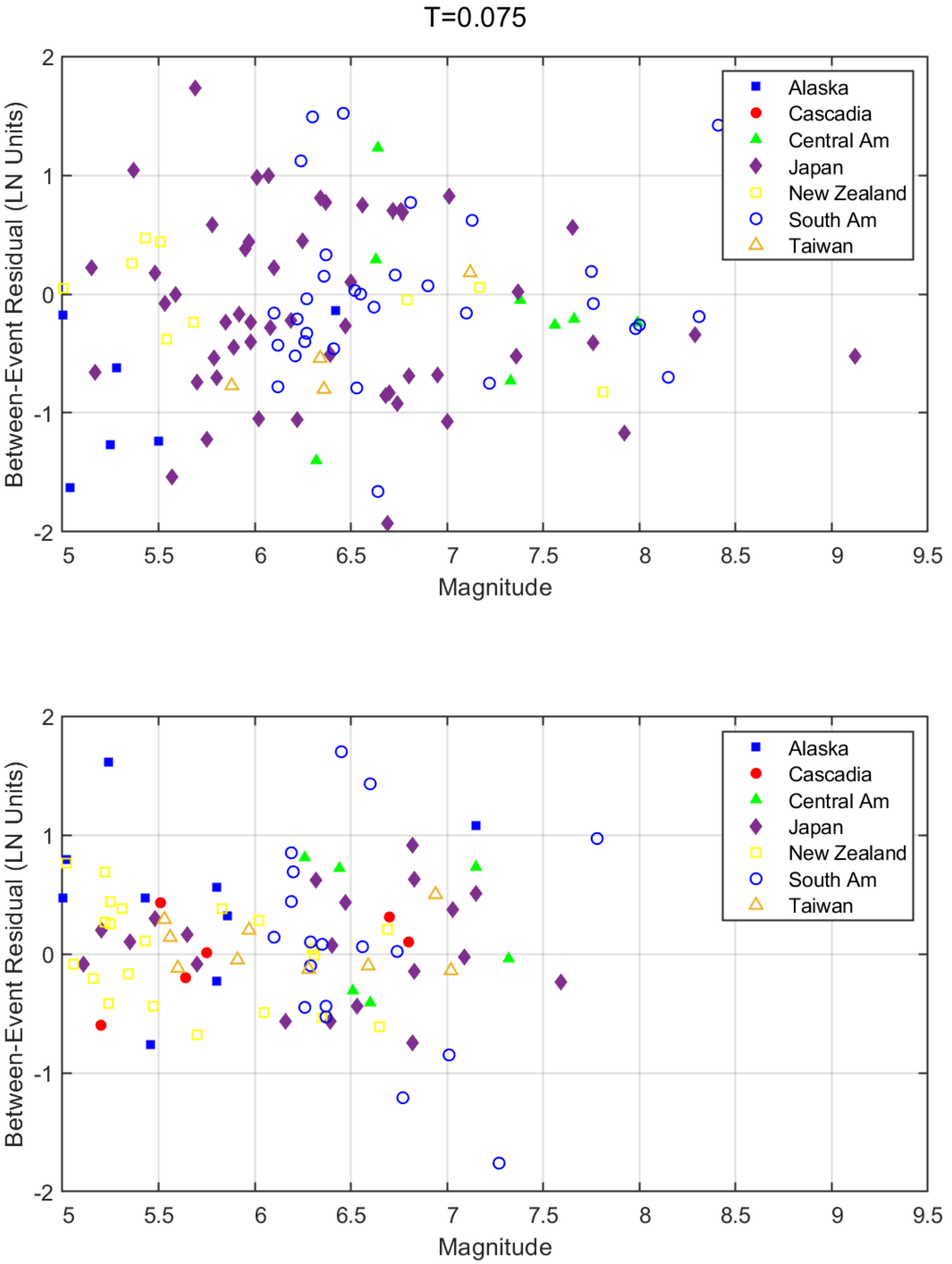

Figure A.5: Between-event residuals versus magnitude for T = 0.075 sec. Top frame: interface earthquakes. Bottom frame: intraslab earthquakes.

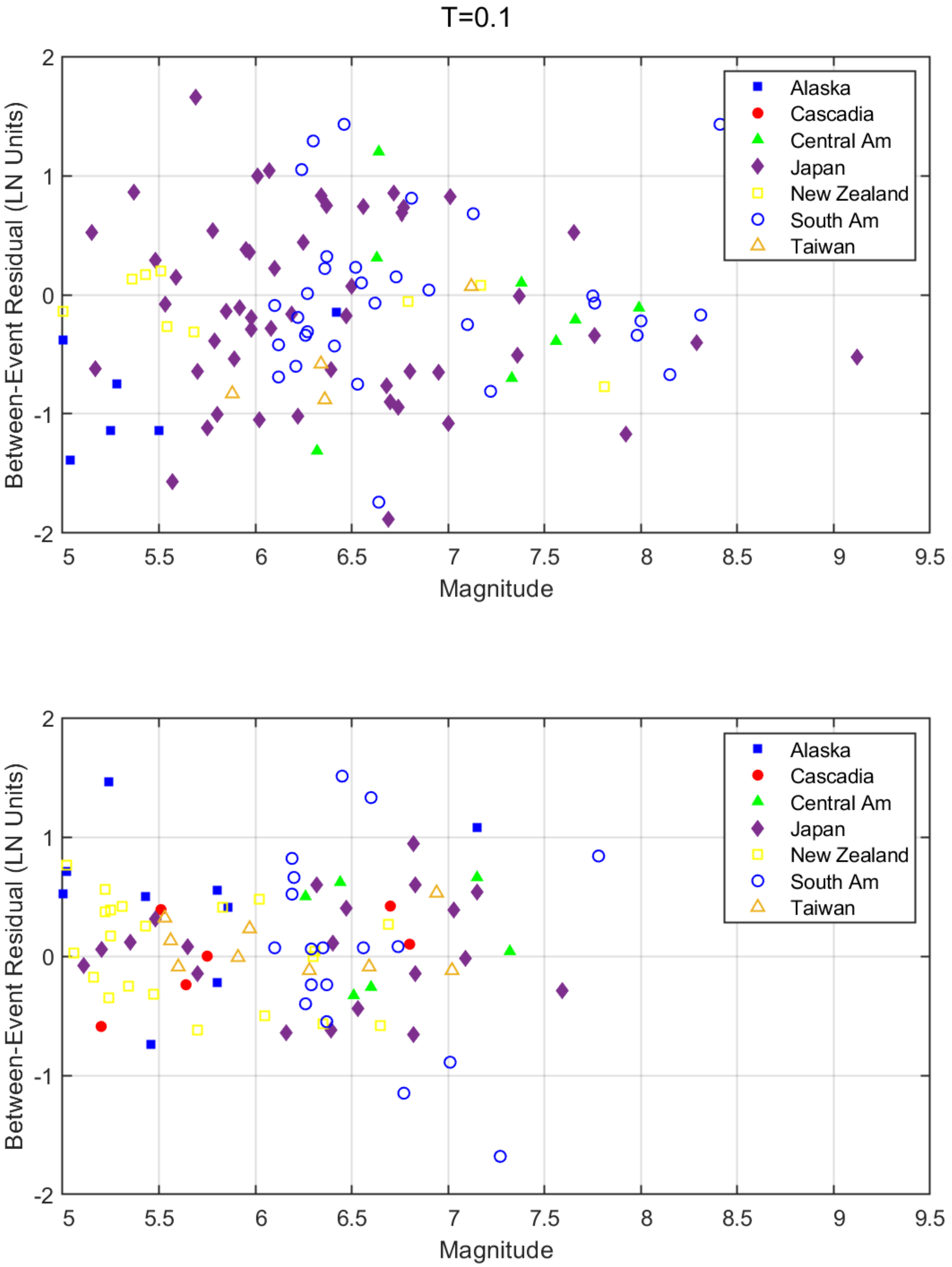

Figure A.6: Between-event residuals versus magnitude for T = 0.10 sec. Top frame: interface earthquakes. Bottom frame: intraslab earthquakes.

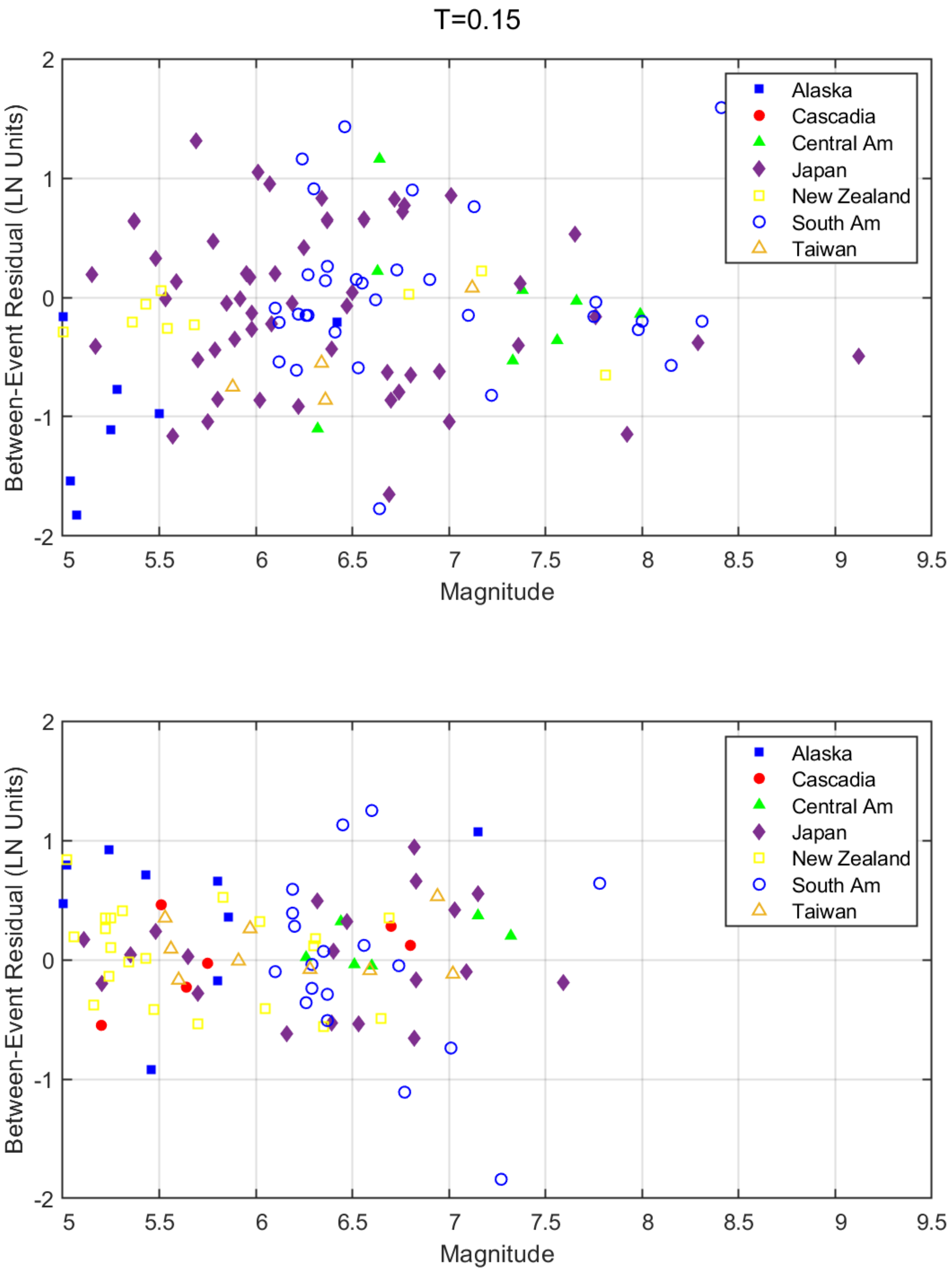

Figure A.7: **Between-event residuals versus magnitude for T = 0.15 sec. Top frame: interface earthquakes. Bottom frame: intraslab earthquakes.**

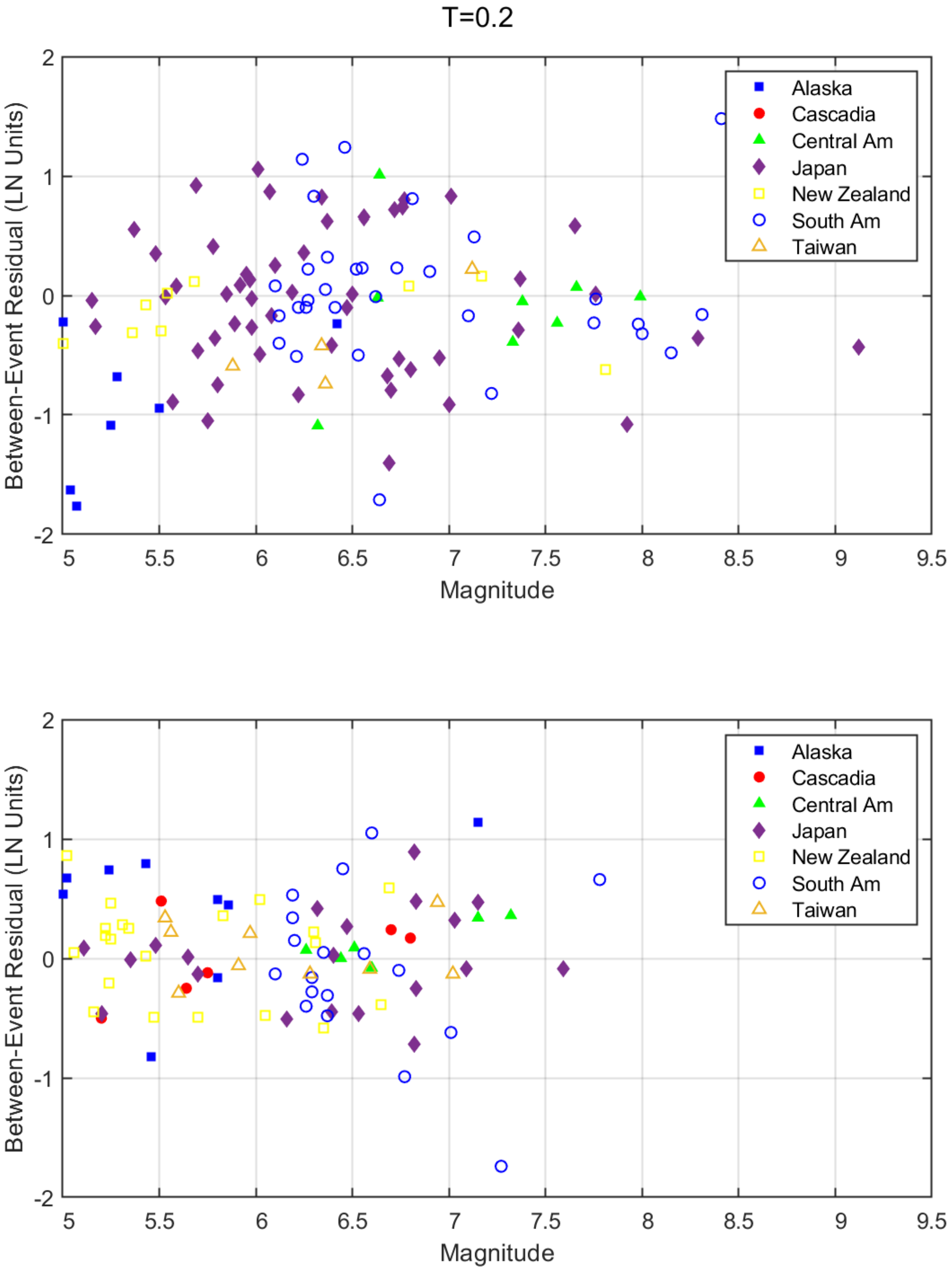

Figure A.8: Between-event residuals versus magnitude for T = 0.2 sec. Top frame: interface earthquakes. Bottom frame: intraslab earthquakes.

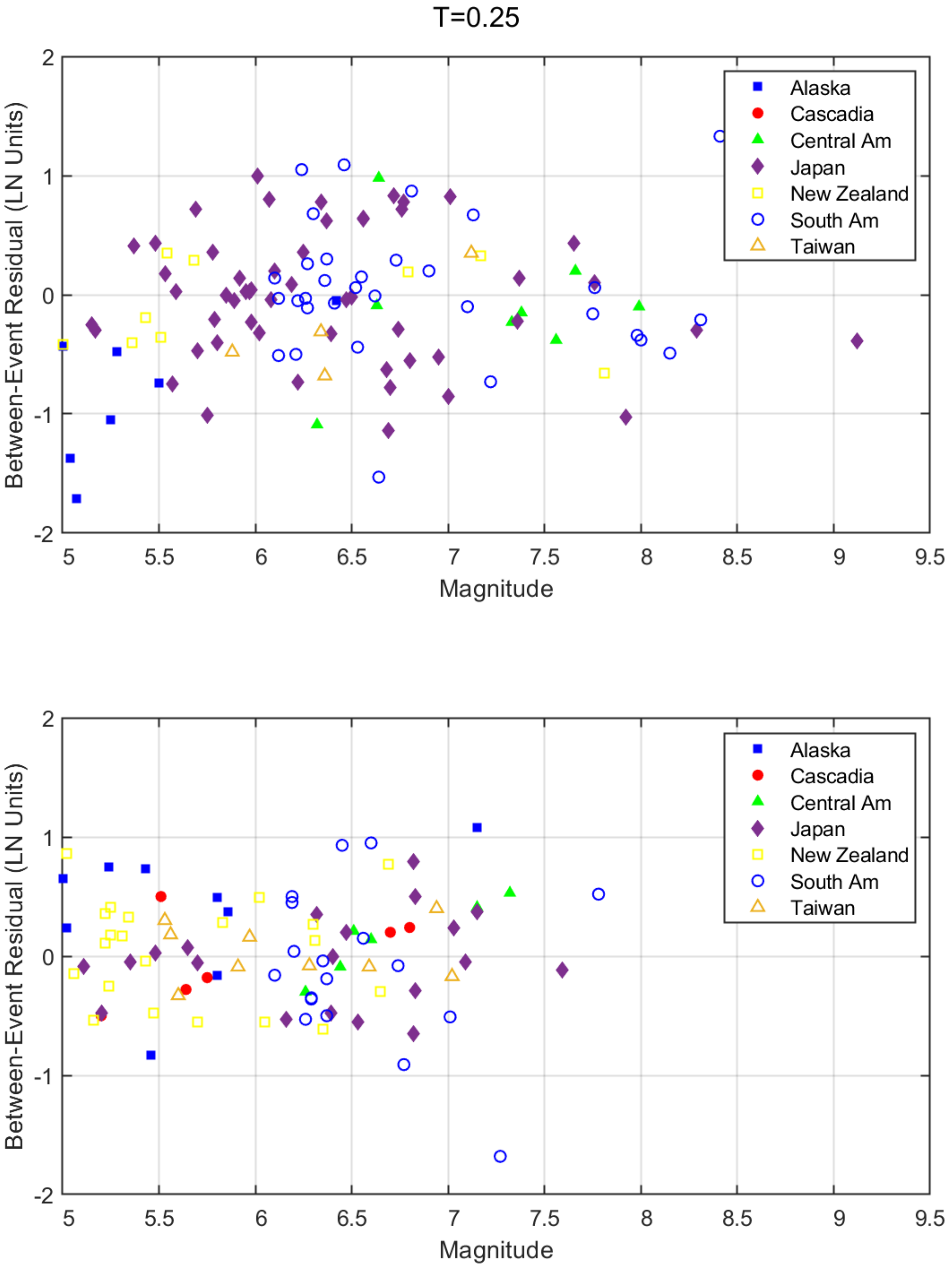

Figure A.9: Between-event residuals versus magnitude for T = 0.25 sec. Top frame: interface earthquakes. Bottom frame: intraslab earthquakes.

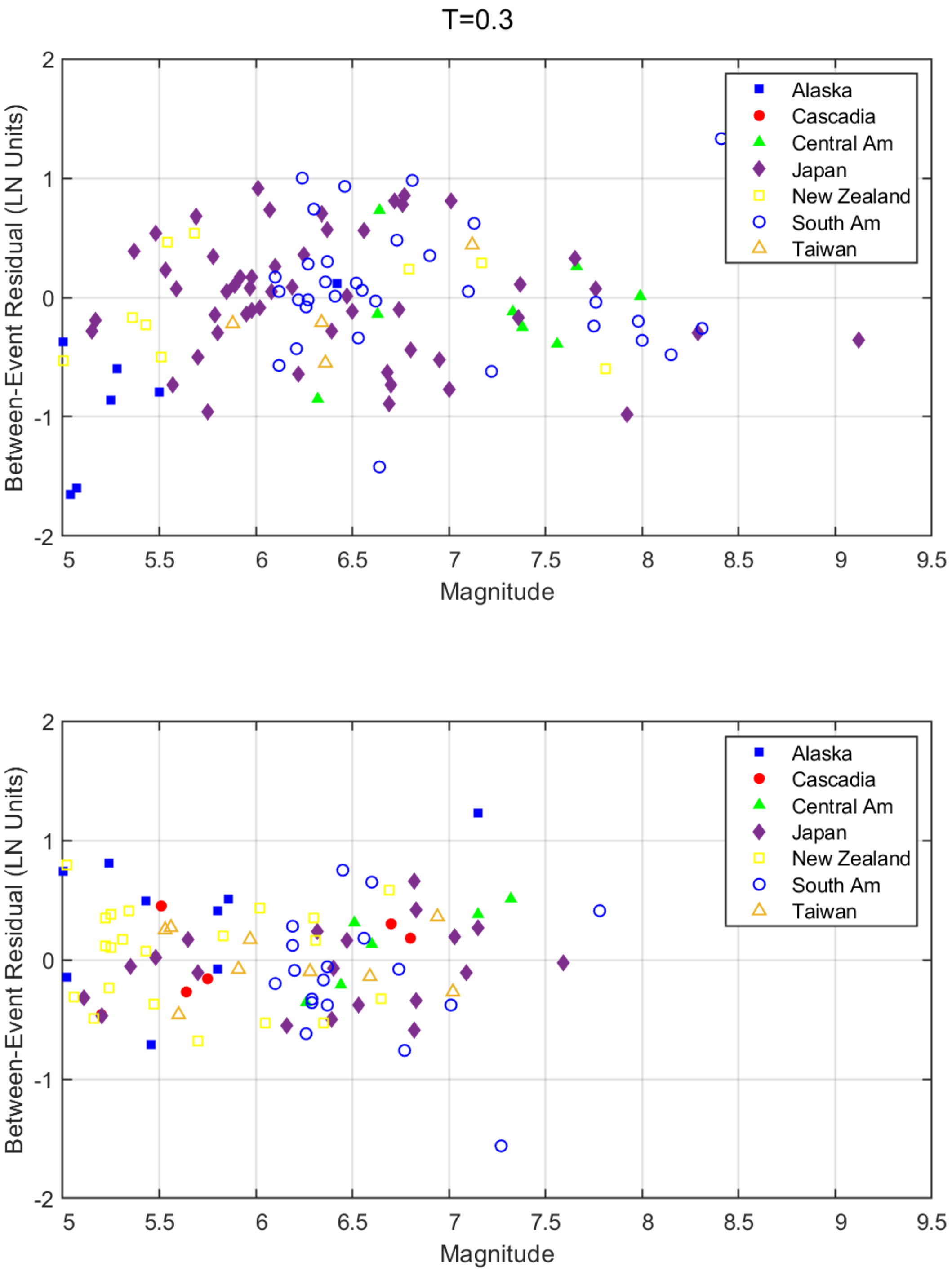

Figure A.10: Between-event residuals versus magnitude for T = 0.3 sec. Top frame: interface earthquakes. Bottom frame: intraslab earthquakes.

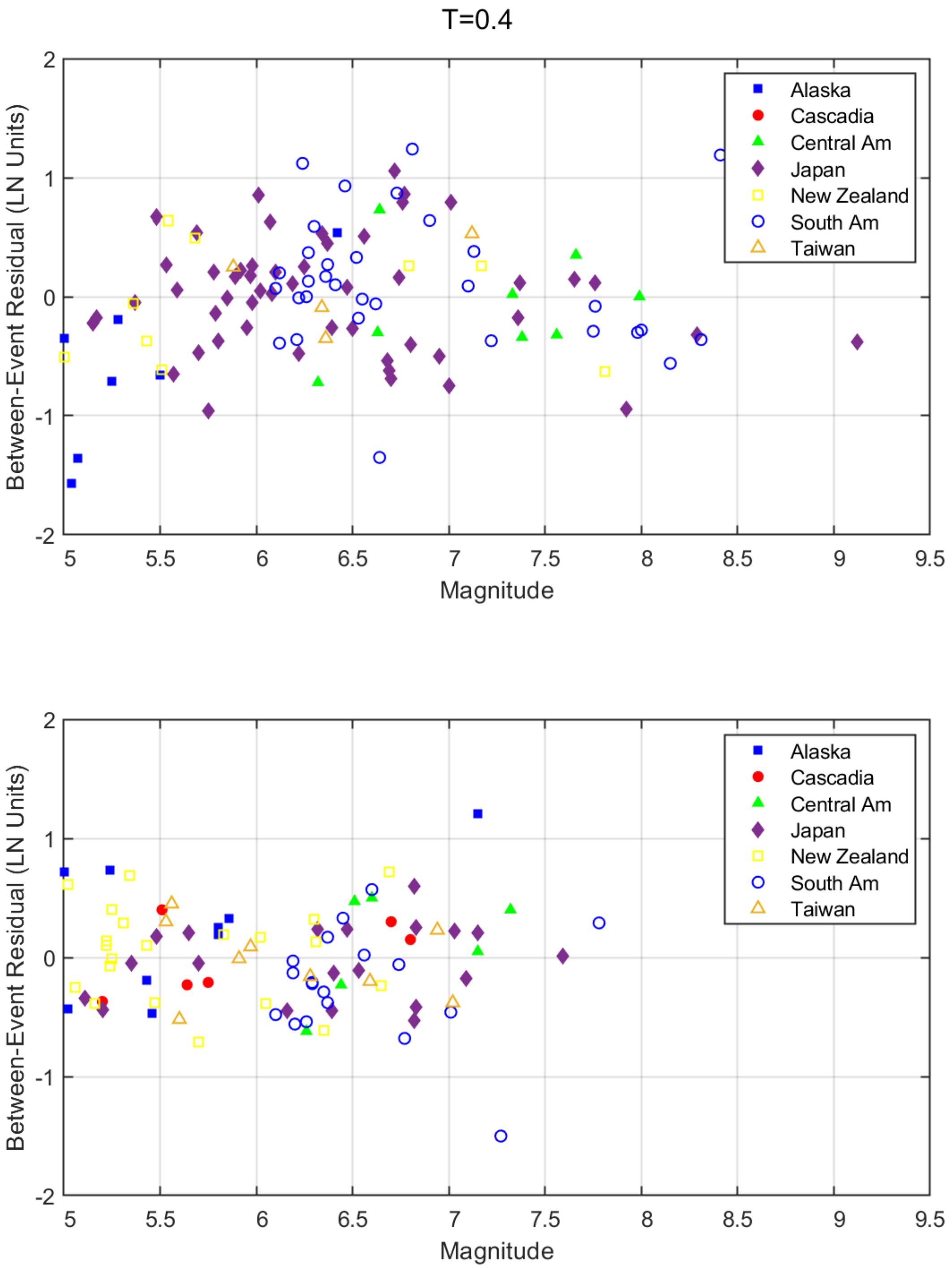

Figure A.11: Between-event residuals versus magnitude for T = 0.4 sec. Top frame: interface earthquakes. Bottom frame: intraslab earthquakes.

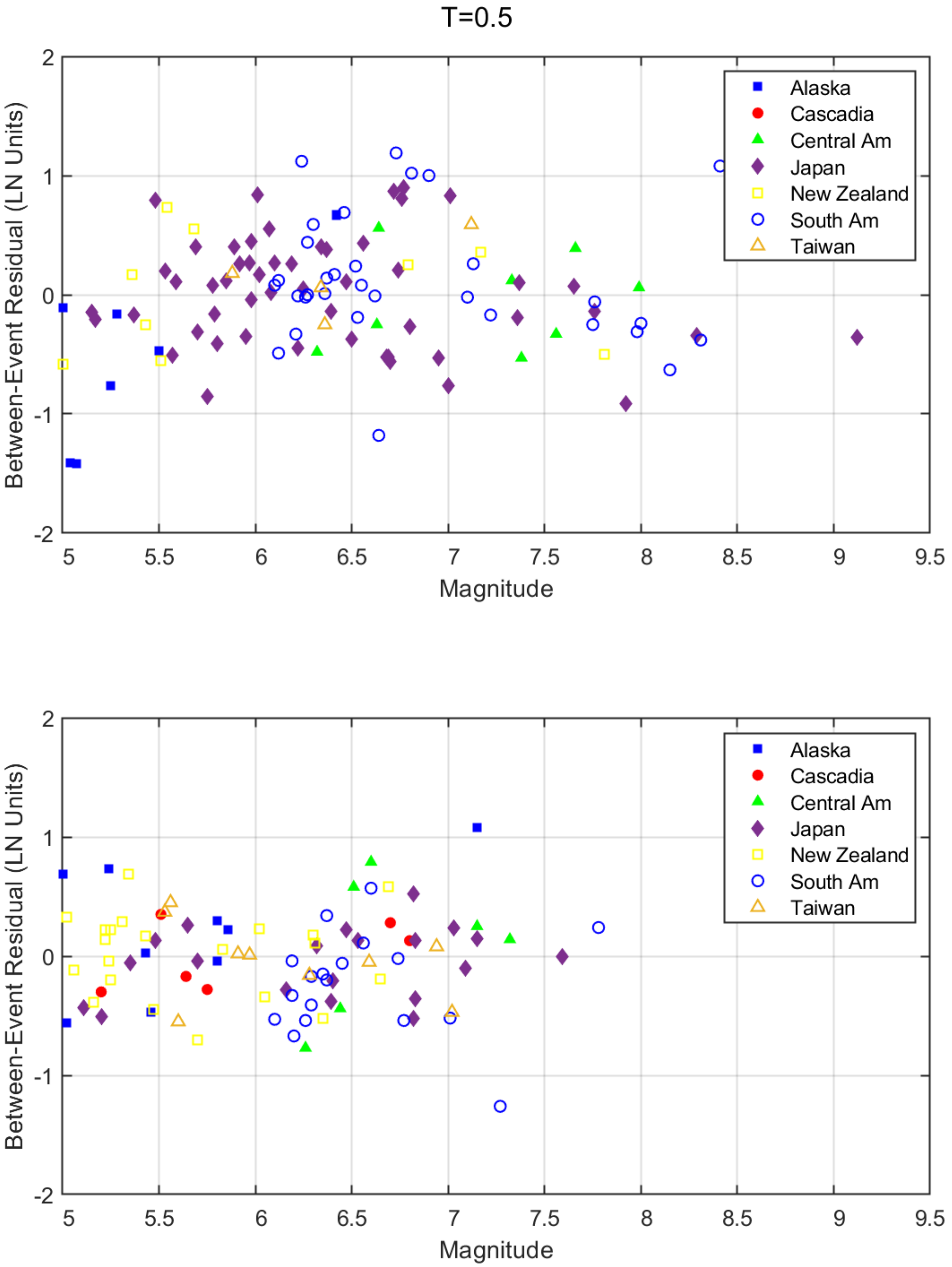

Figure A.12: Between-event residuals versus magnitude for T = 0.5 sec. Top frame: interface earthquakes. Bottom frame: intraslab earthquakes.

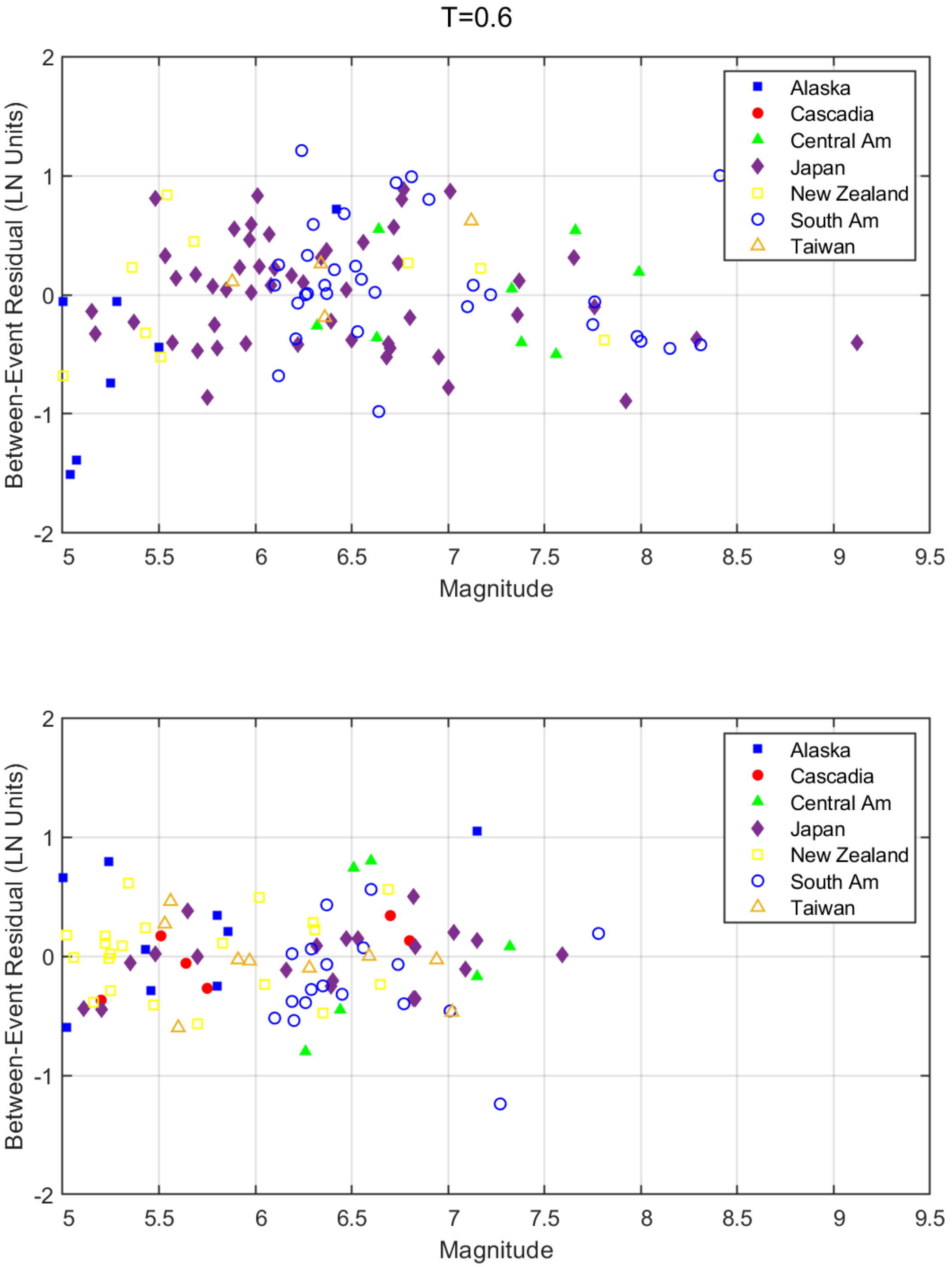

Figure A.13: Between-event residuals versus magnitude for T = 0.6 sec. Top frame: interface earthquakes. Bottom frame: intraslab earthquakes.

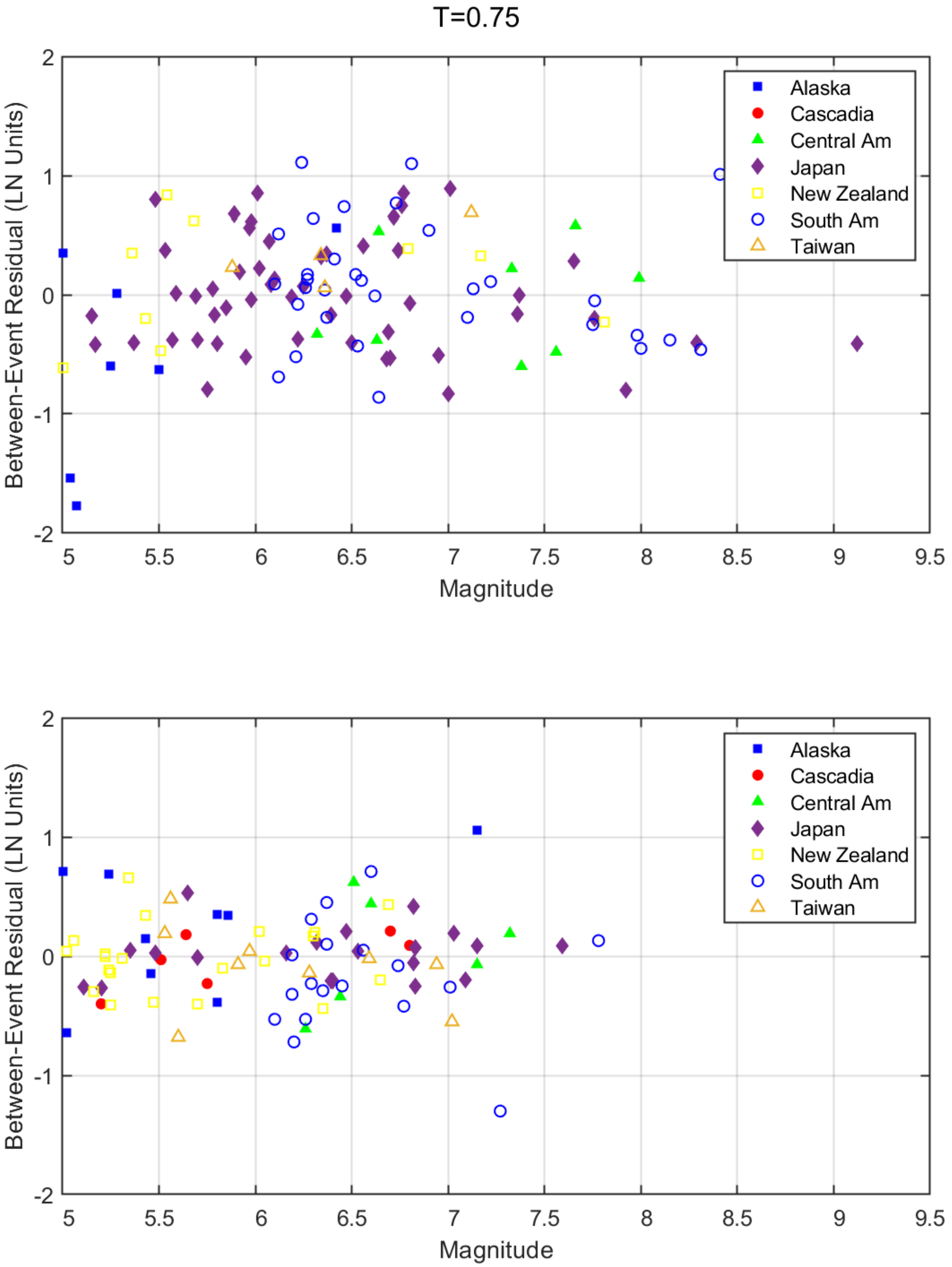

Figure A.14: Between-event residuals versus magnitude for T = 0.75 sec. Top frame: interface earthquakes. Bottom frame: intraslab earthquakes.

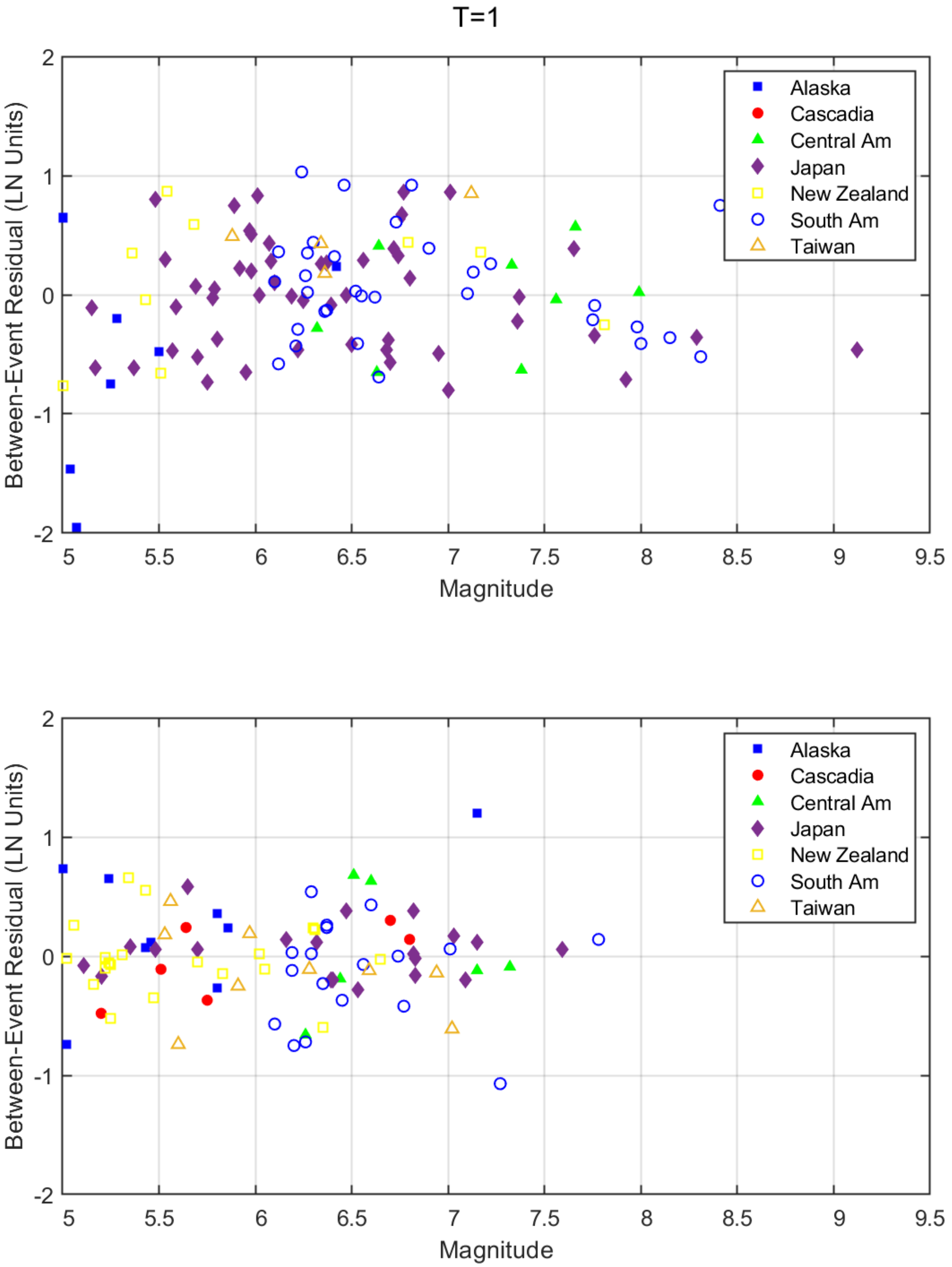

Figure A.15: Between-event residuals versus magnitude for T = 1.0 sec. Top frame: interface earthquakes. Bottom frame: intraslab earthquakes.

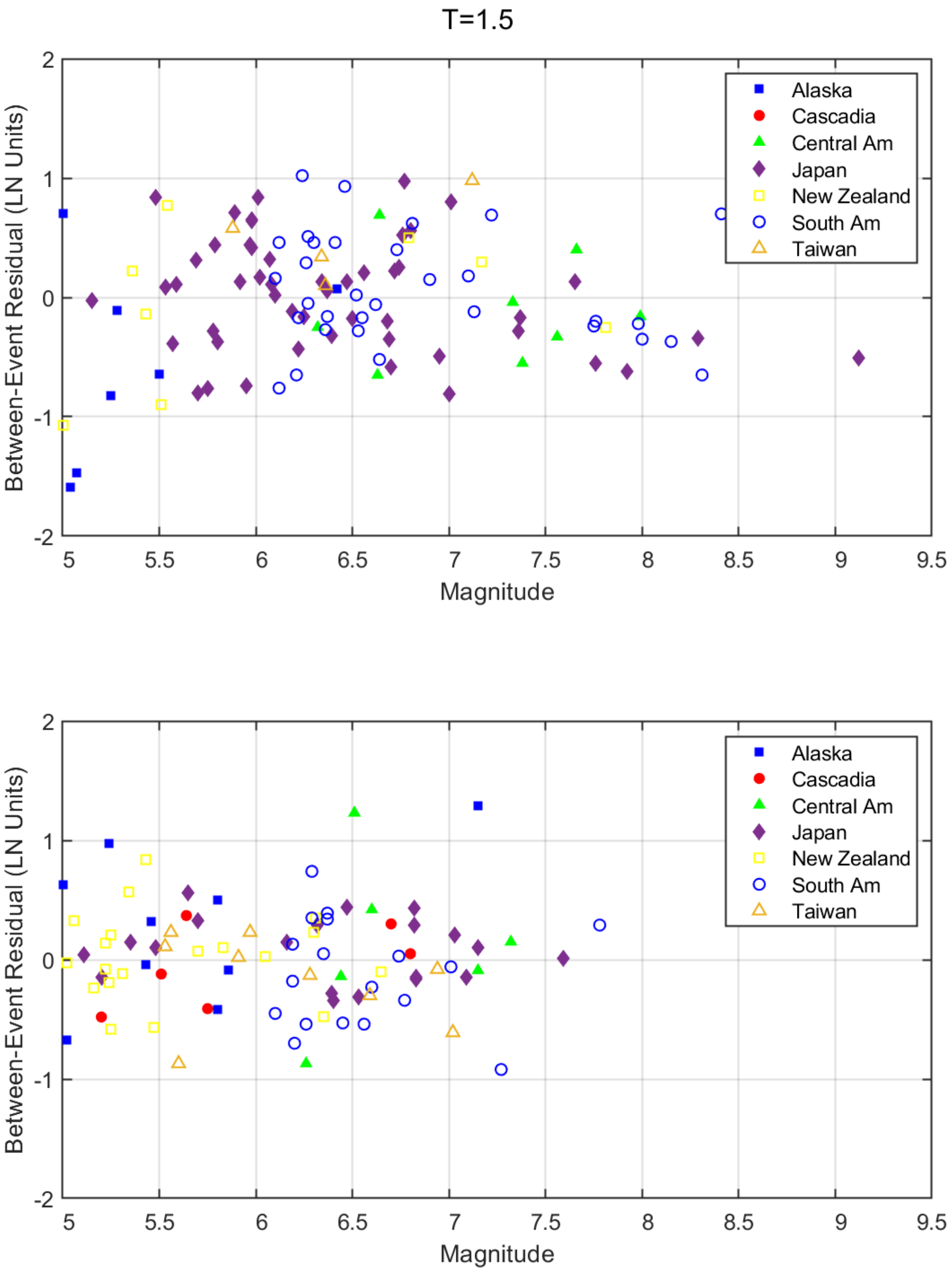

Figure A.16: Between-event residuals versus magnitude for T = 1.5 sec. Top frame: interface earthquakes. Bottom frame: intraslab earthquakes.

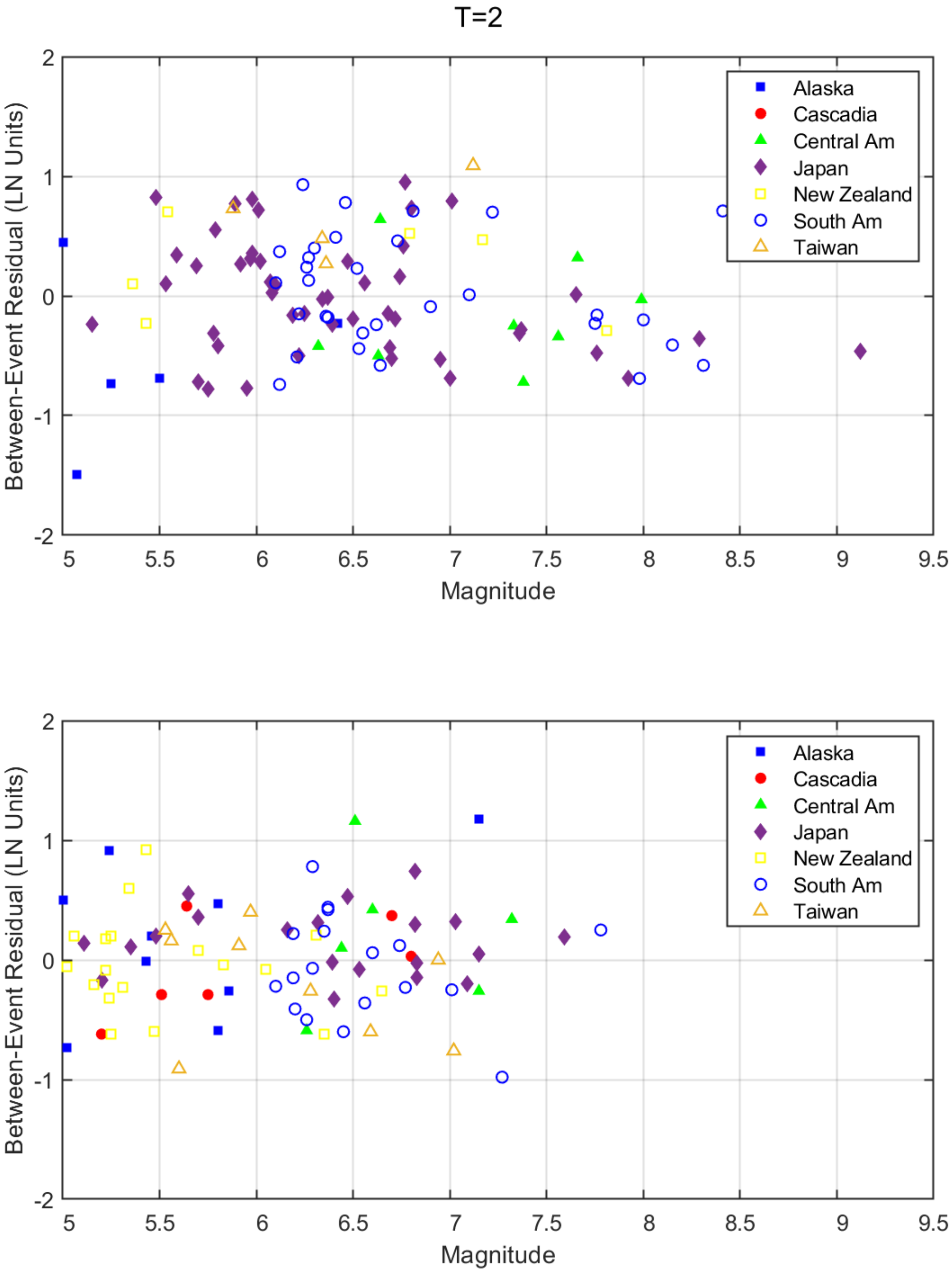

Figure A.17: Between-event residuals versus magnitude for T = 2.0 sec. Top frame: interface earthquakes. Bottom frame: intraslab earthquakes.

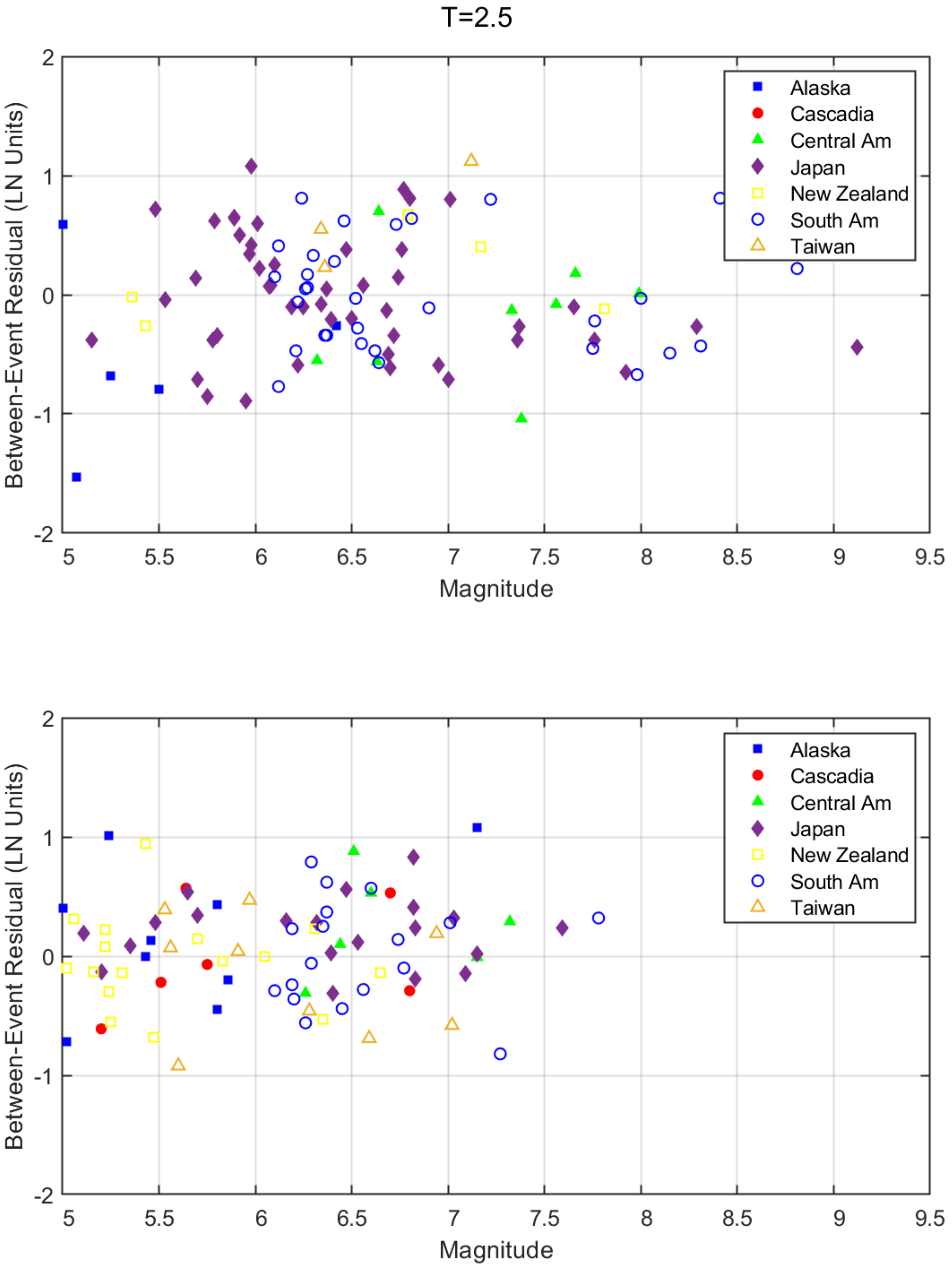

Figure A.18: Between-event residuals versus magnitude for T = 2.5 sec. Top frame: interface earthquakes. Bottom frame: intraslab earthquakes.

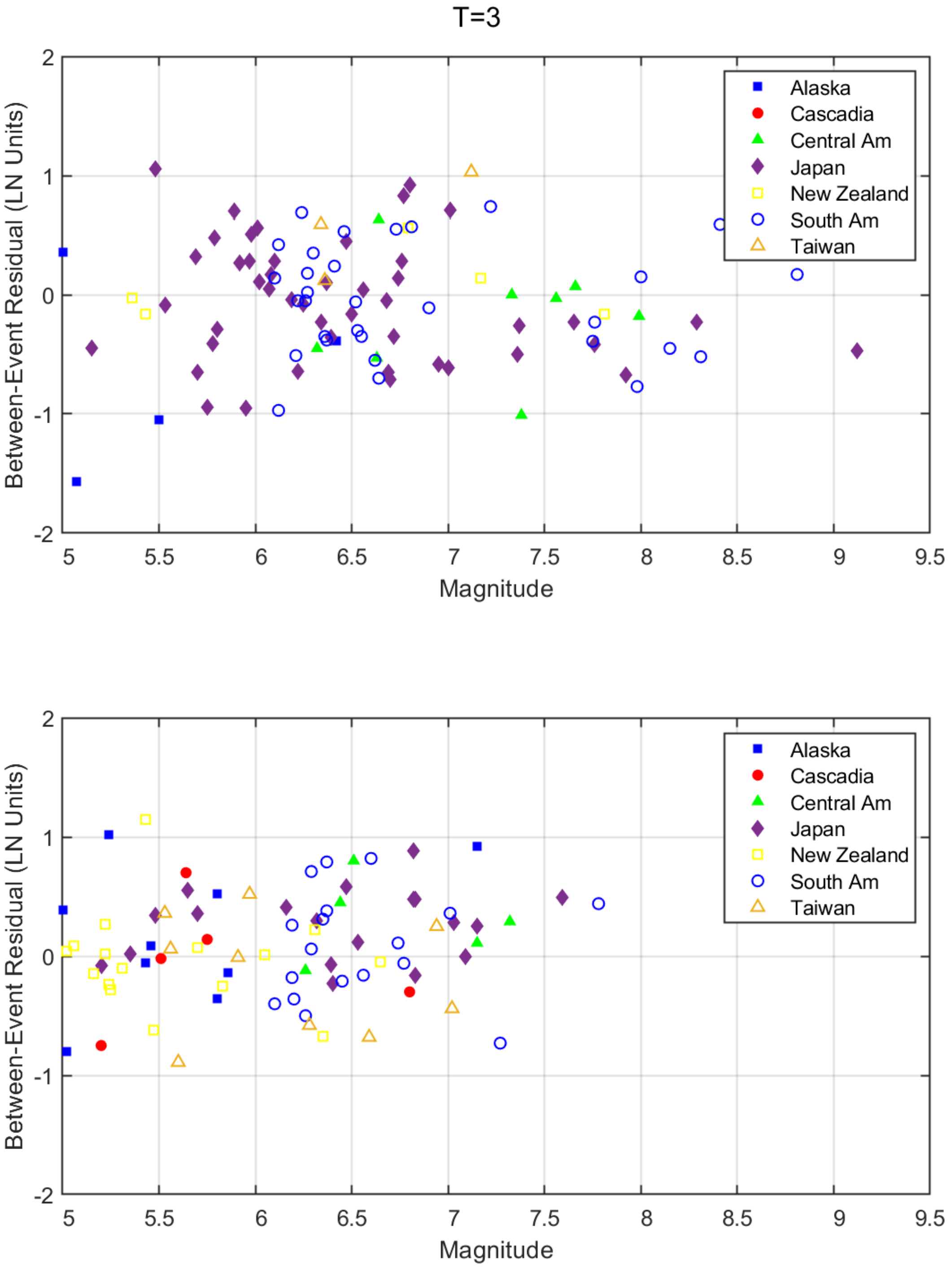

Figure A.19: Between-event residuals versus magnitude for T = 3.0 sec. Top frame: interface earthquakes. Bottom frame: intraslab earthquakes.

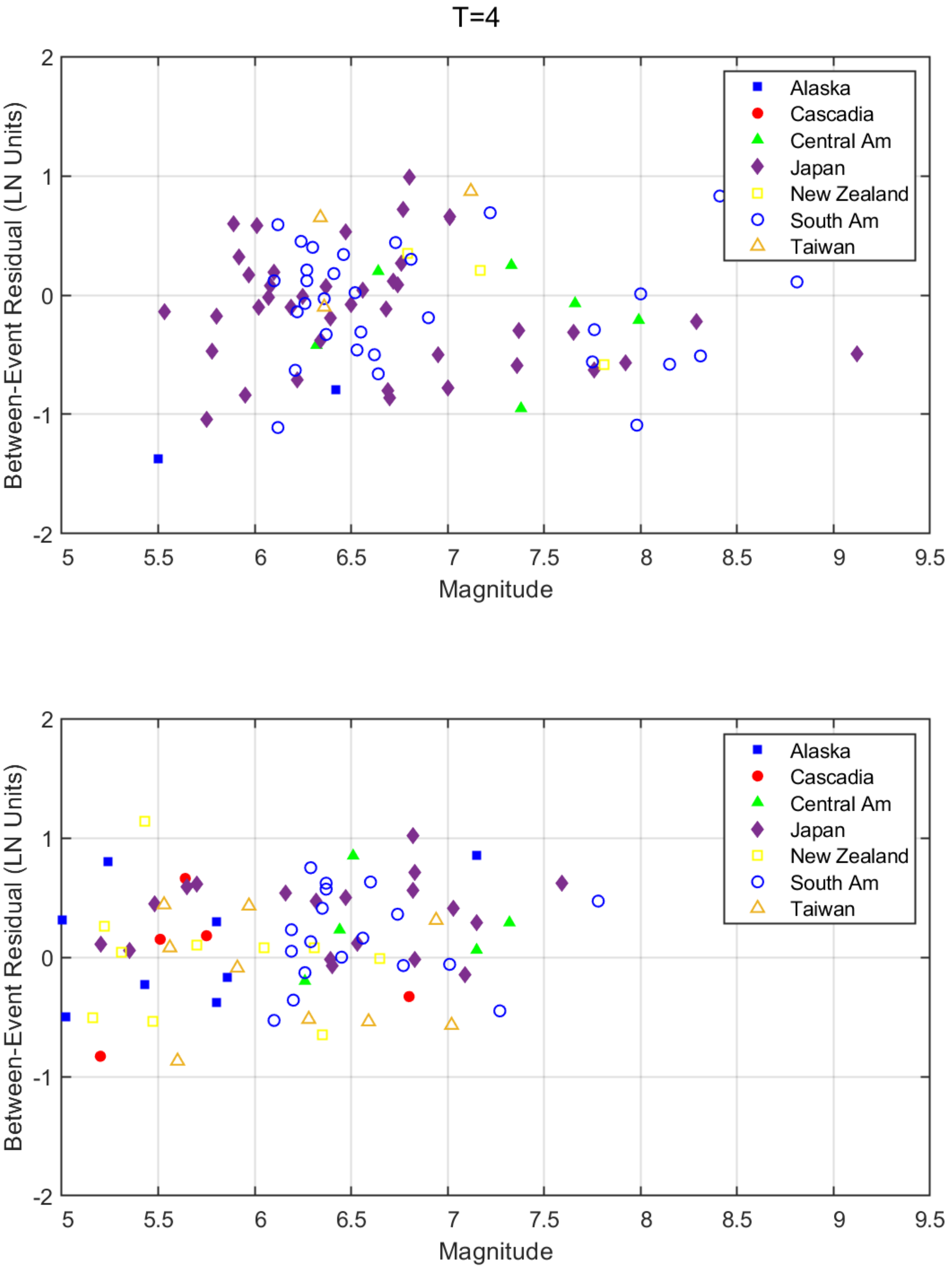

Figure A.20: Between-event residuals versus magnitude for T = 4.0 sec. Top frame: interface earthquakes. Bottom frame: intraslab earthquakes.

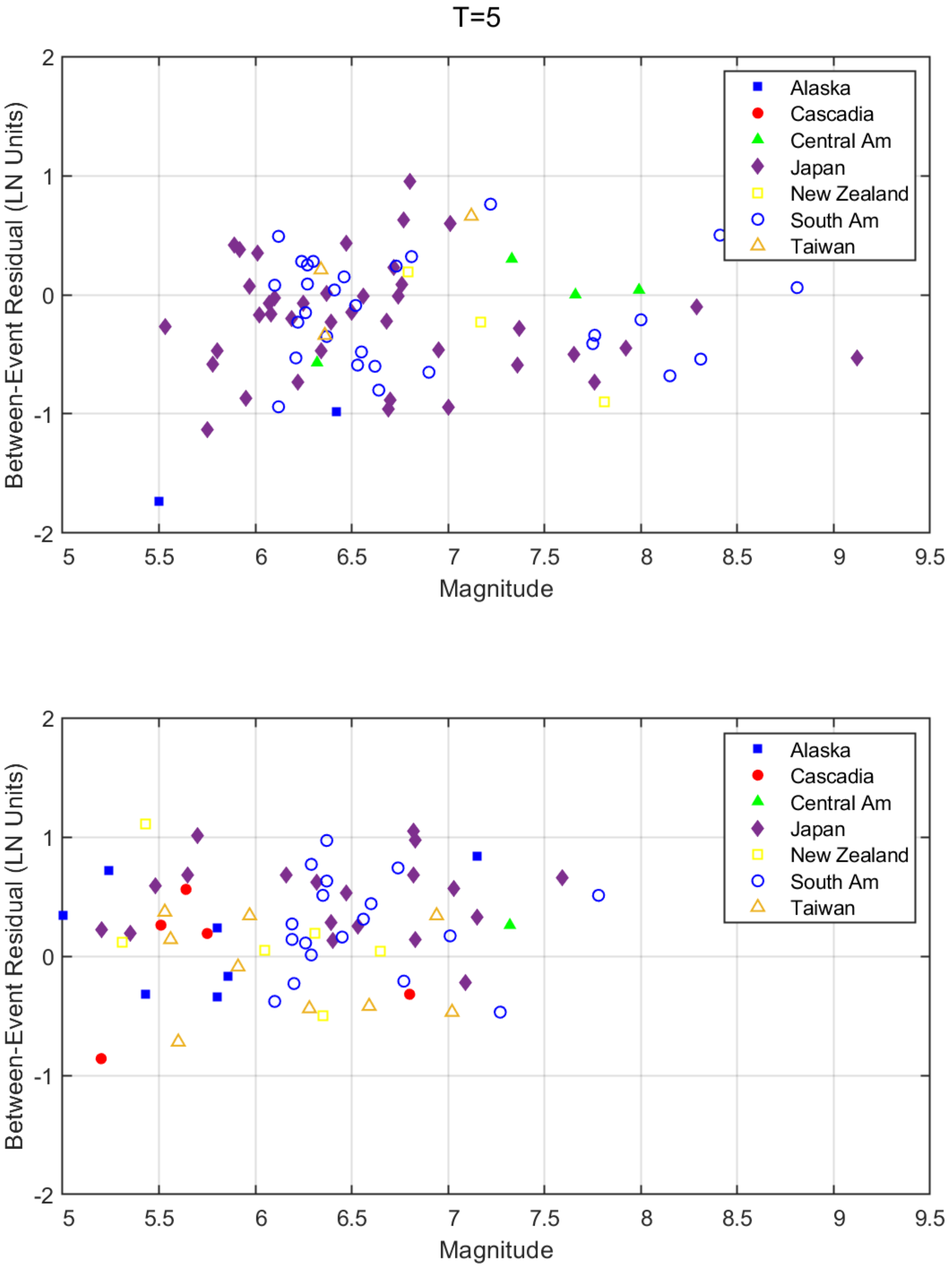

Figure A.21: Between-event residuals versus magnitude for T = 5.0 sec. Top frame: interface earthquakes. Bottom frame: intraslab earthquakes.

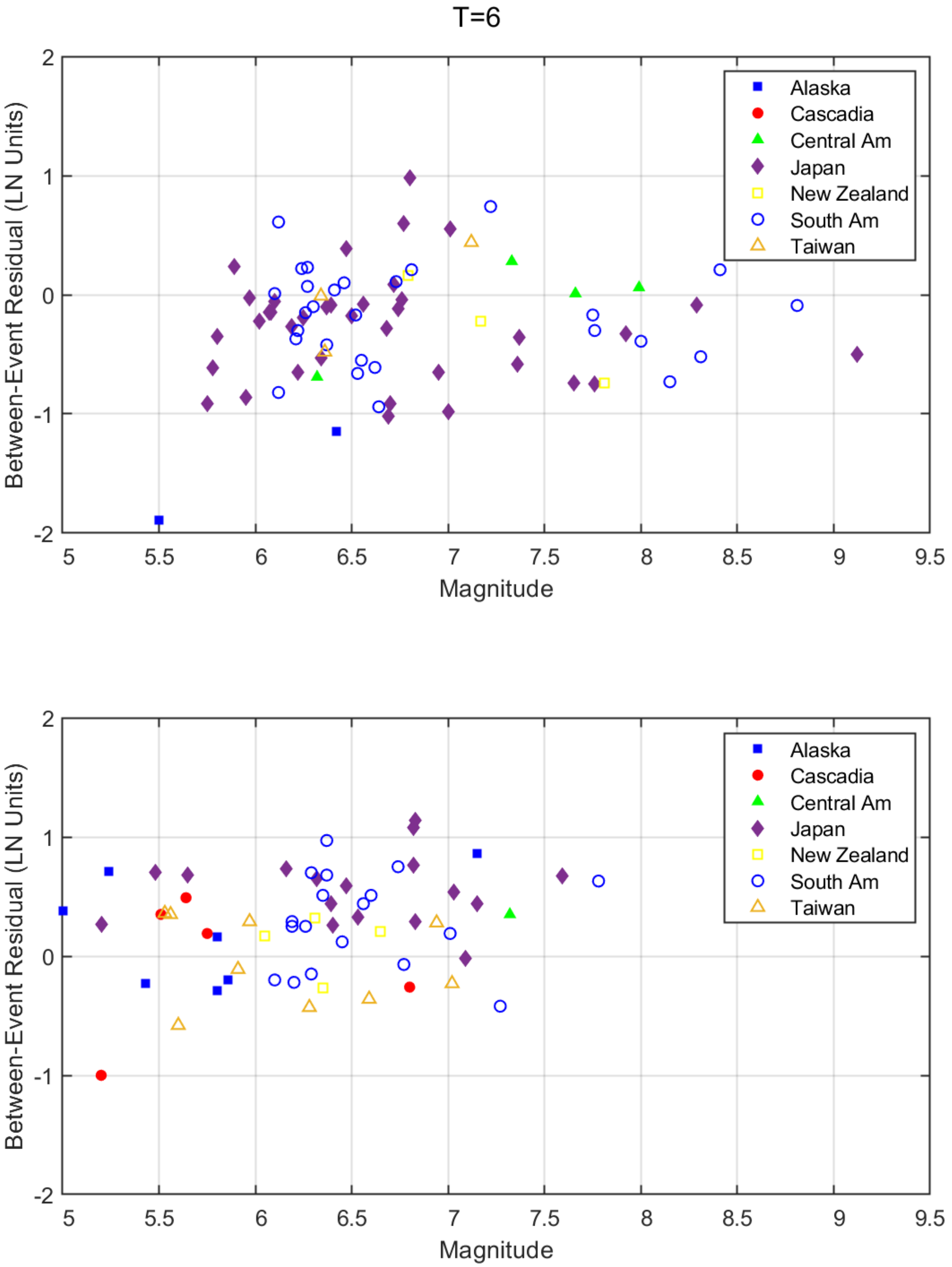

Figure A.22: Between-event residuals versus magnitude for T = 6.0 sec. Top frame: interface earthquakes. Bottom frame: intraslab earthquakes.

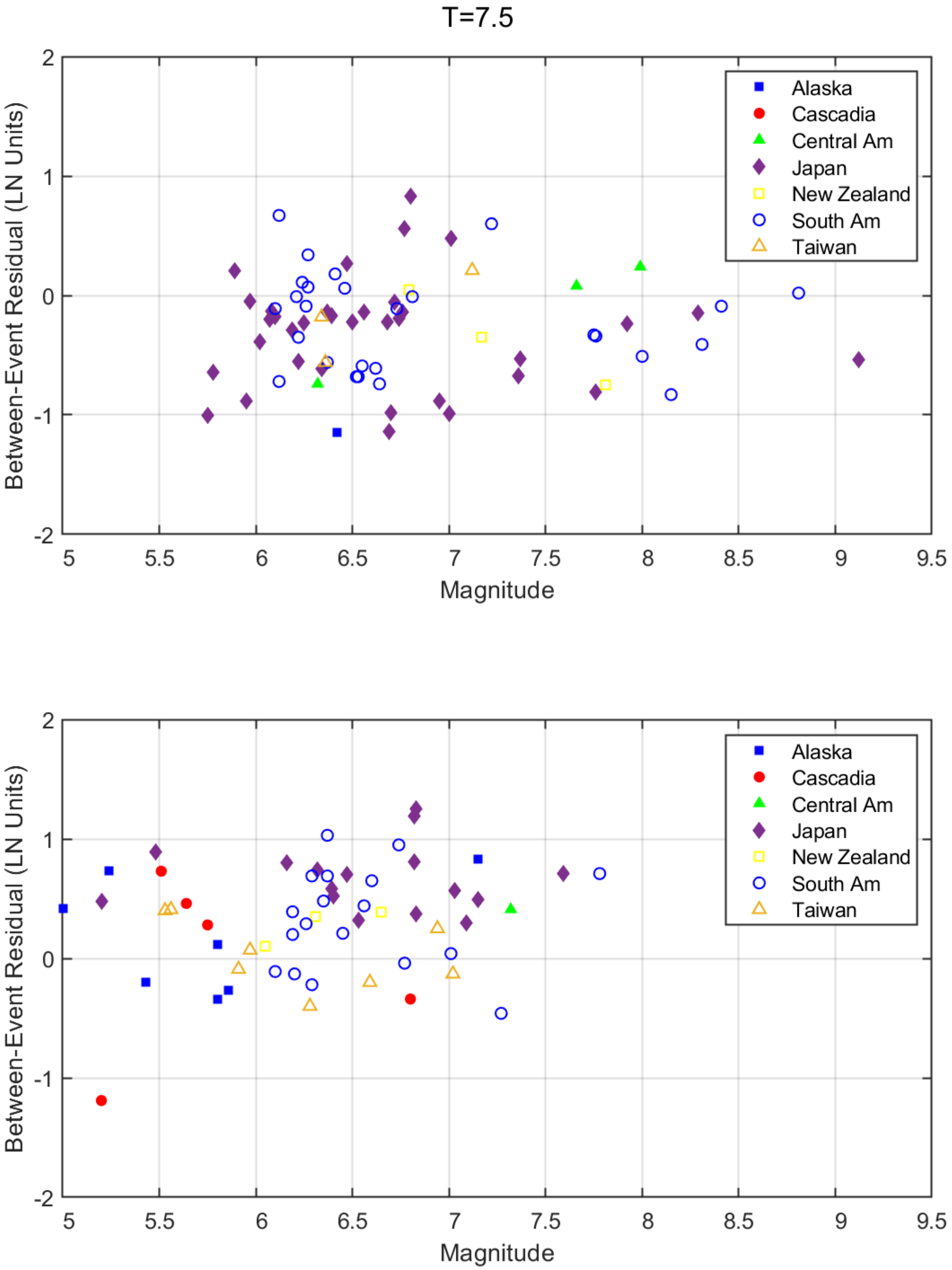

Figure A.23: Between-event residuals versus magnitude for T = 7.5 sec. Top frame: interface earthquakes. Bottom frame: intraslab earthquakes.

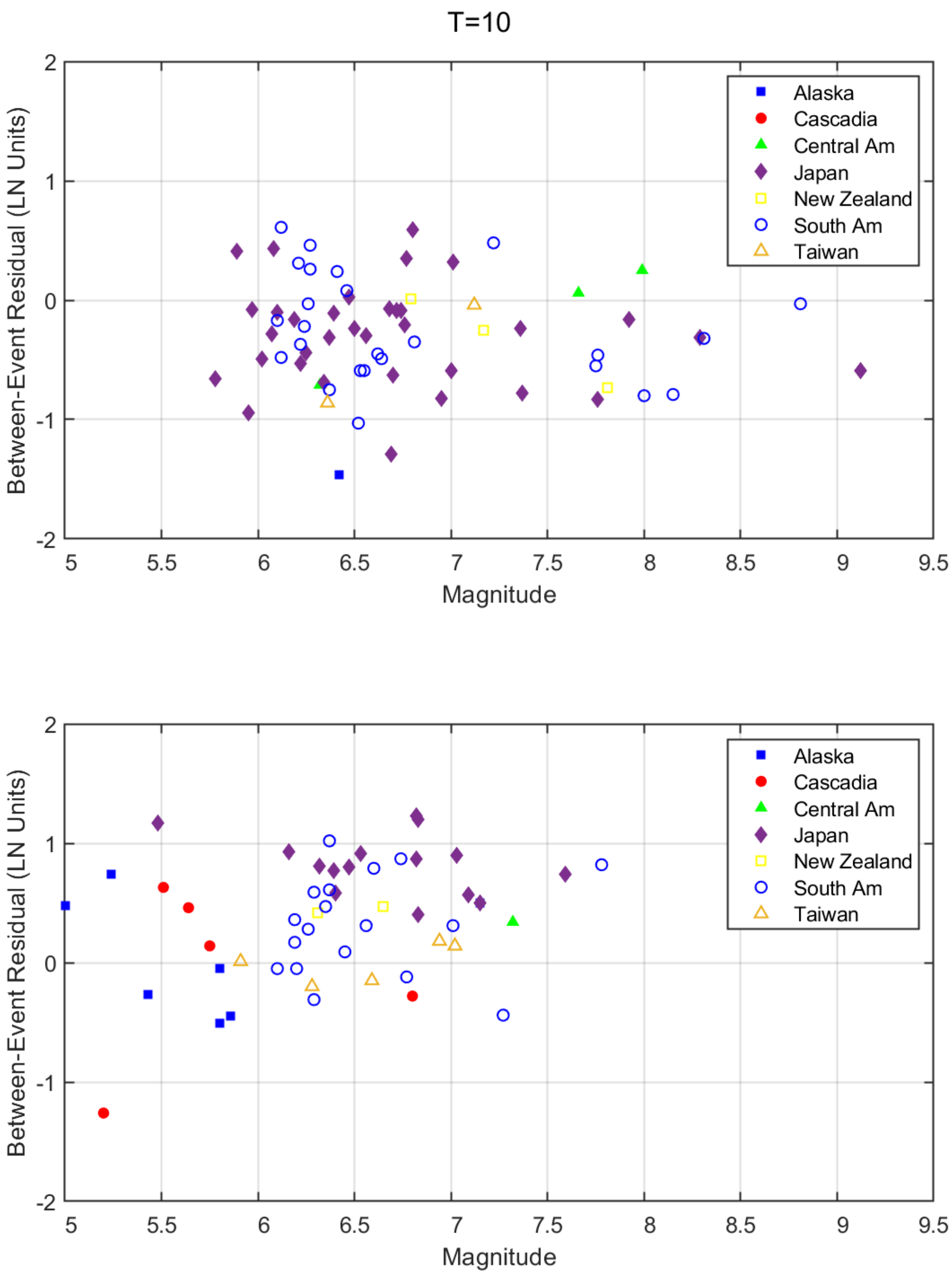

Figure A.24: Between-event residuals versus magnitude for T = 10.0 sec. Top frame: interface earthquakes. Bottom frame: intraslab earthquakes.

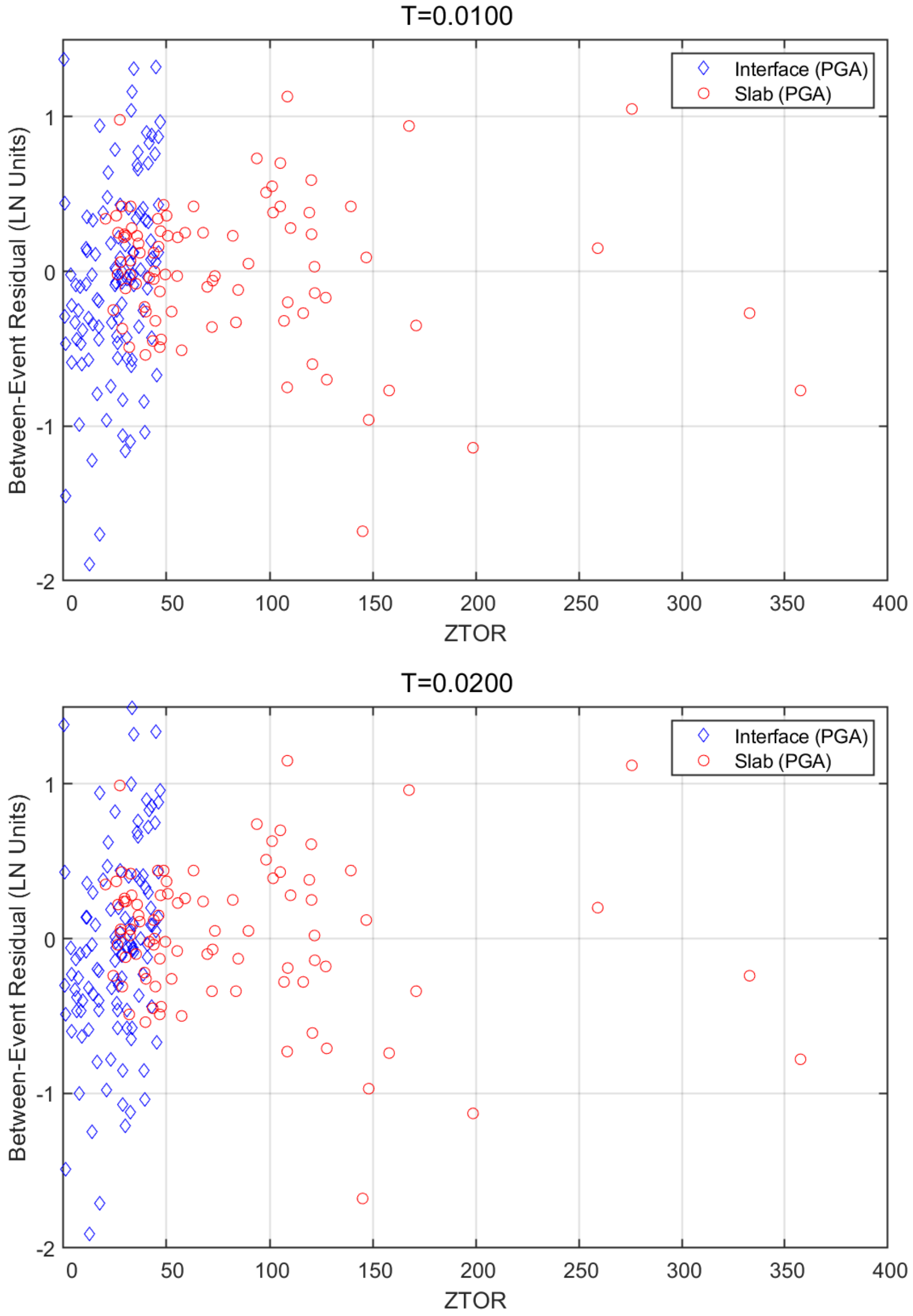

Figure A.25: Between-event residuals versus source depth. Top frame: T = 0.01 sec. Bottom frame: T = 0.02 sec.

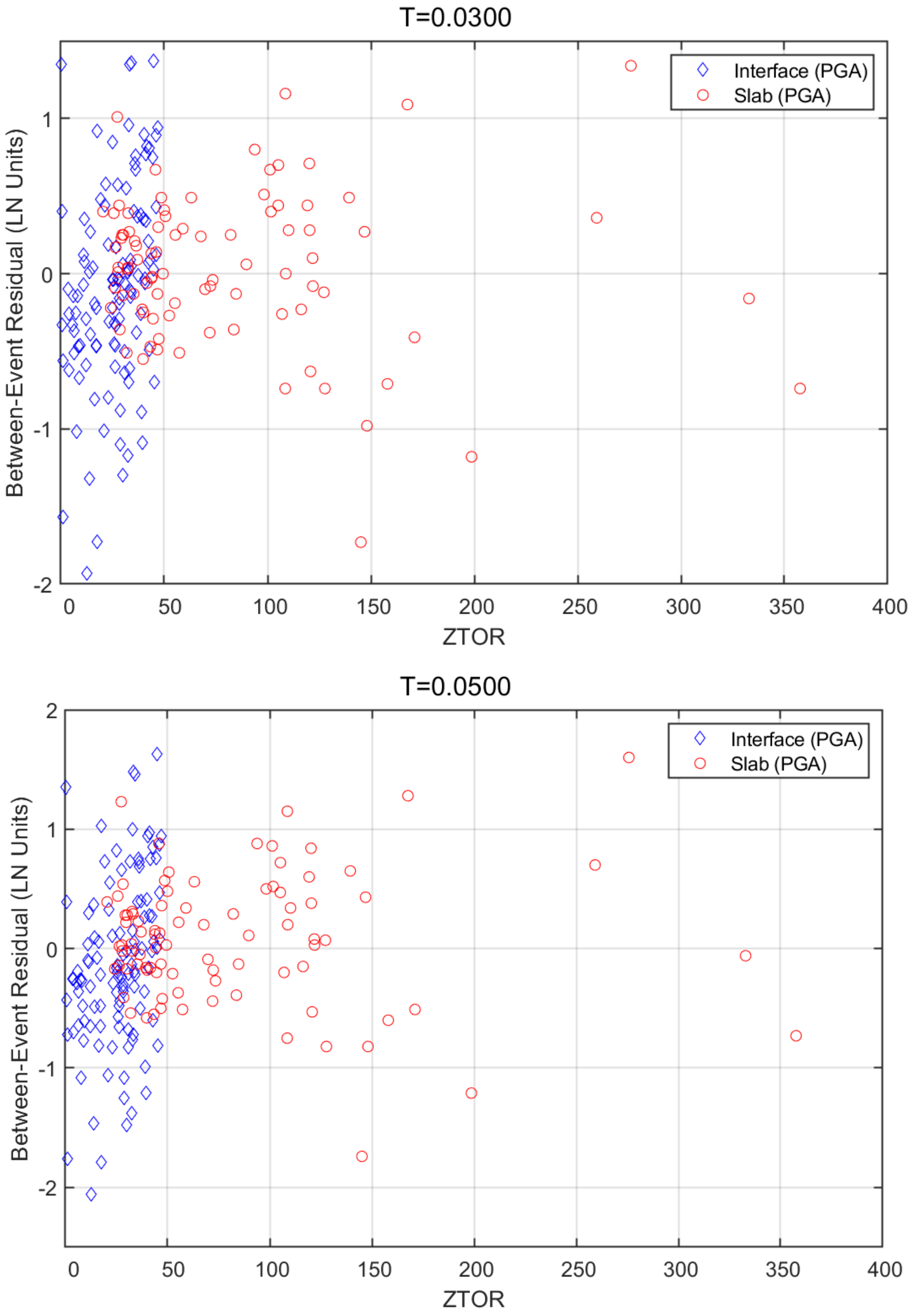

Figure A.26: Between-event residuals versus source depth. Top frame: T = 0.03 sec. Bottom frame: T = 0.05 sec.

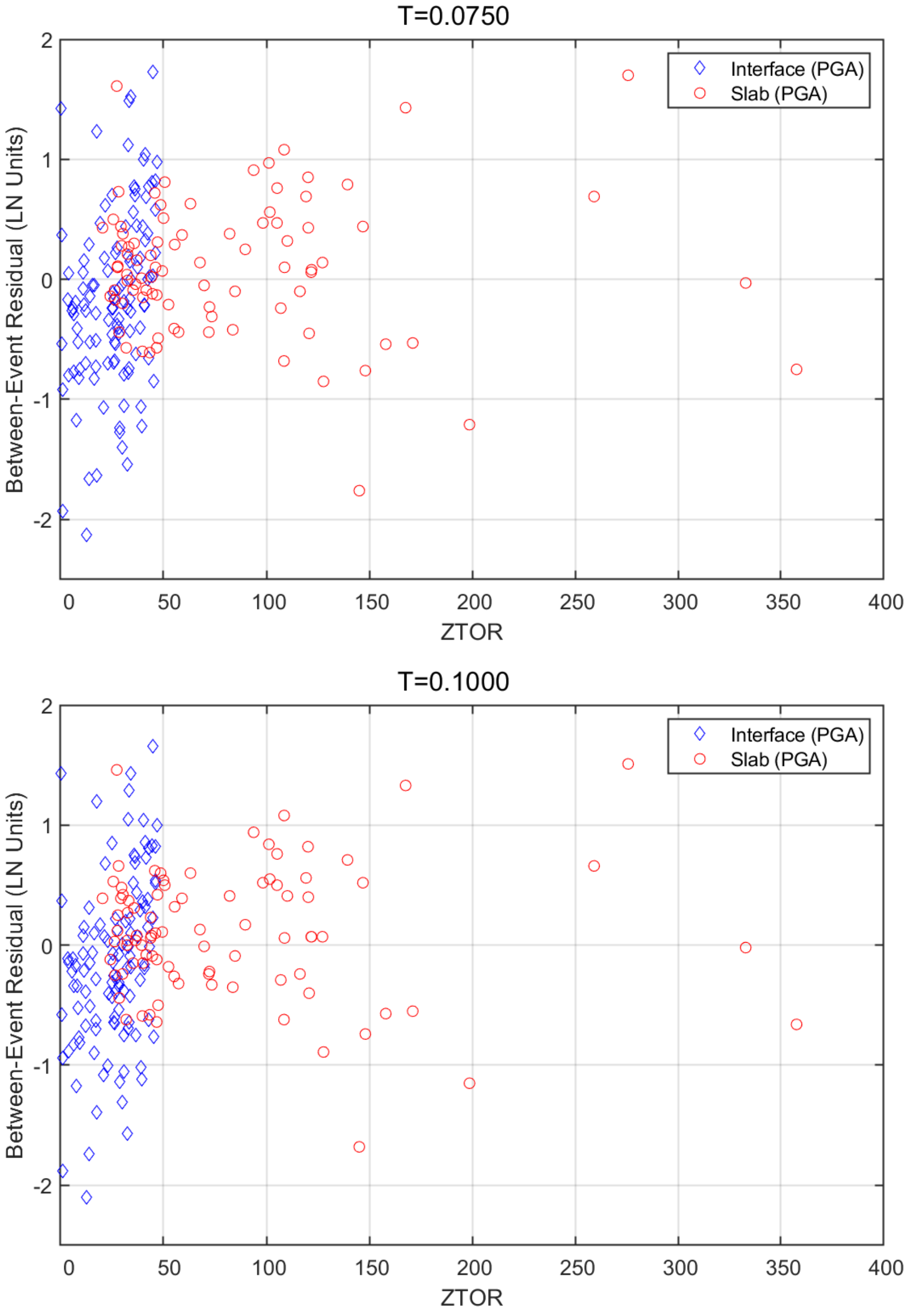

Figure A.27: Between-event residuals versus source depth. Top frame: T = 0.075 sec. Bottom frame: TT = 0.10 sec.

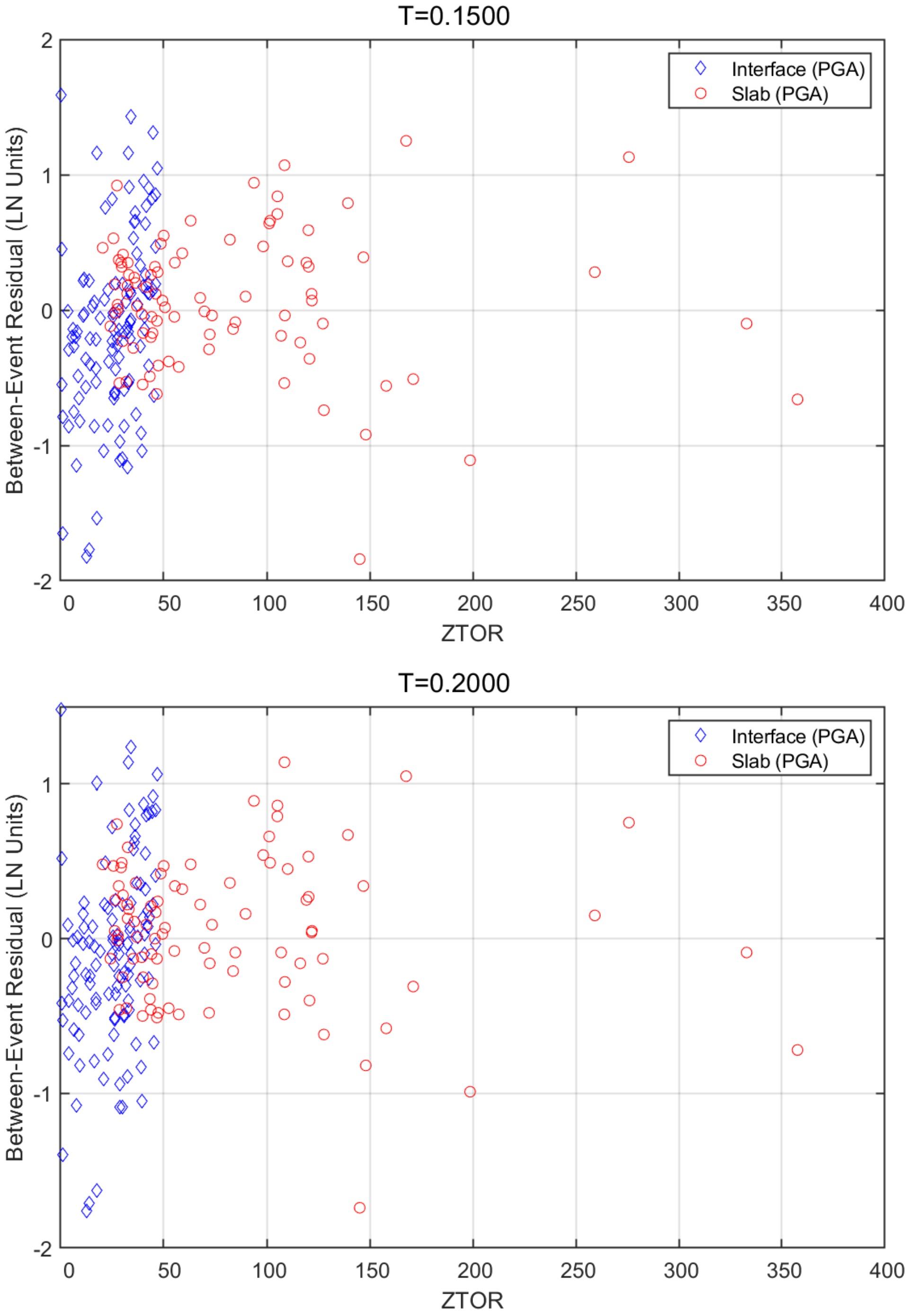

Figure A.28: Between-event residuals versus source depth. Top frame: T = 0.15 sec. Bottom frame: T = 0.20 sec.

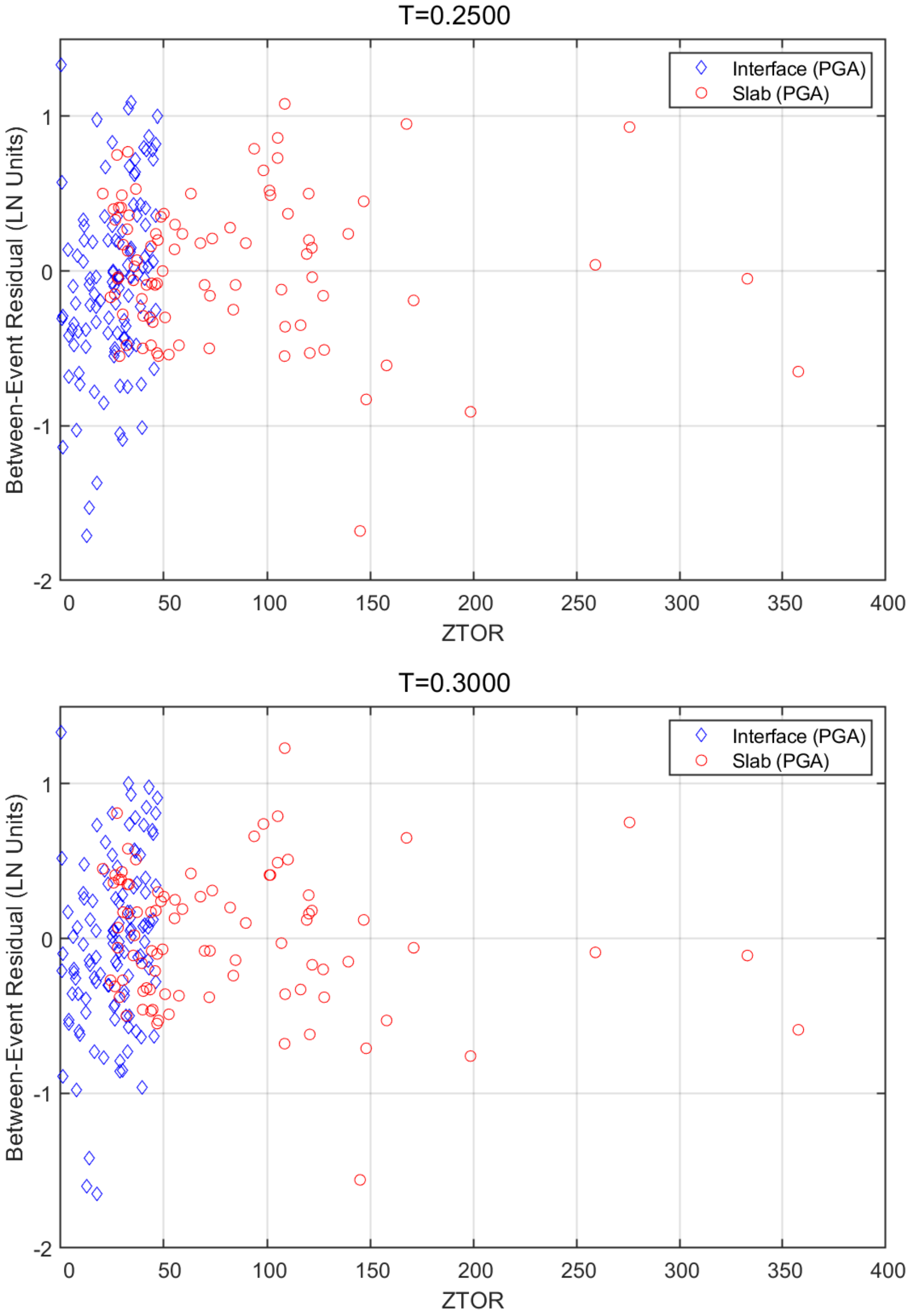

Figure A.29: Between-event residuals versus source depth. Top frame: T = 0.25 sec. Bottom frame: T = 0.30 sec.

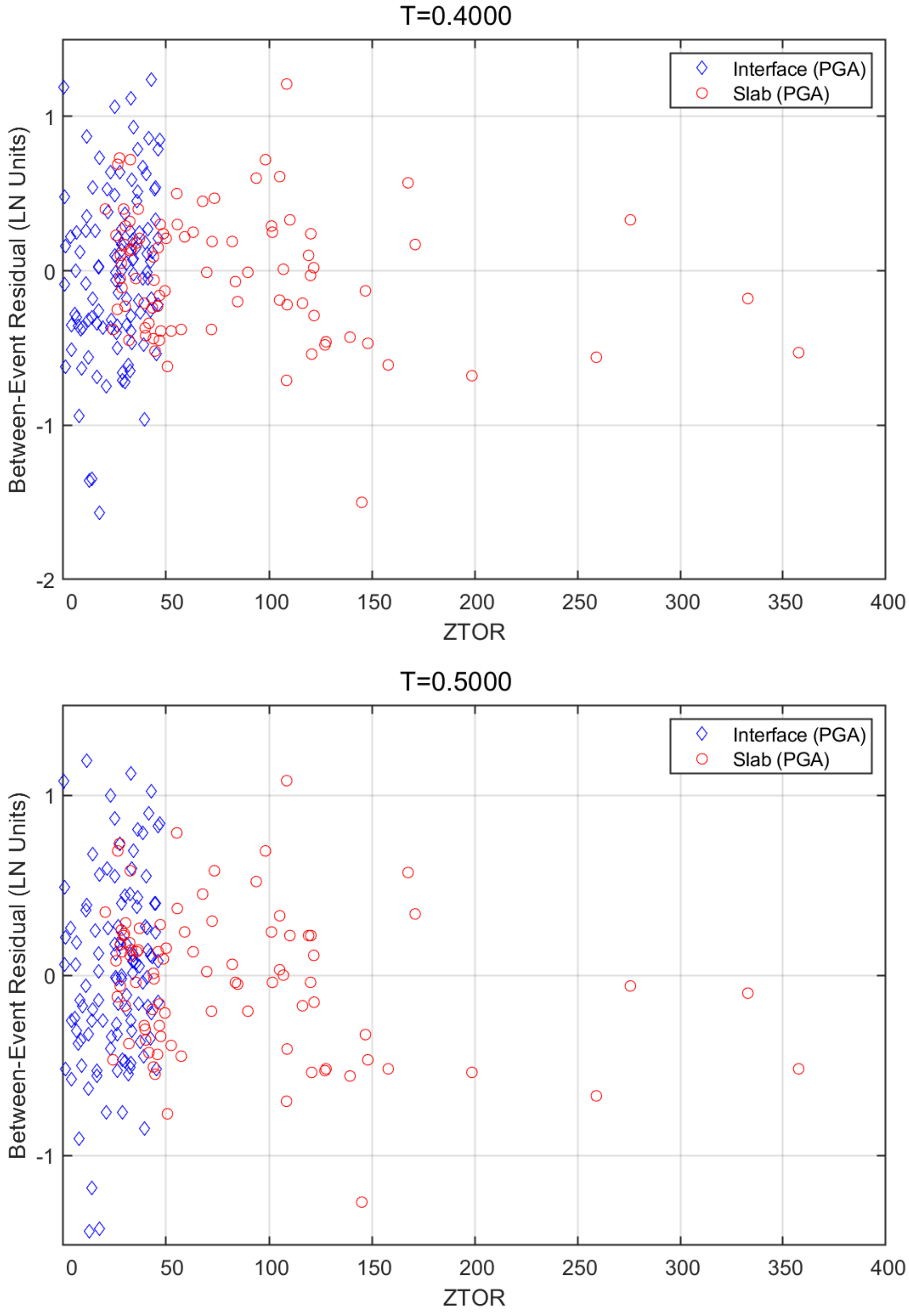

Figure A.30: Between-event residuals versus source depth. Top frame: T = 0.40 sec. Bottom frame: T = 0.50 sec.

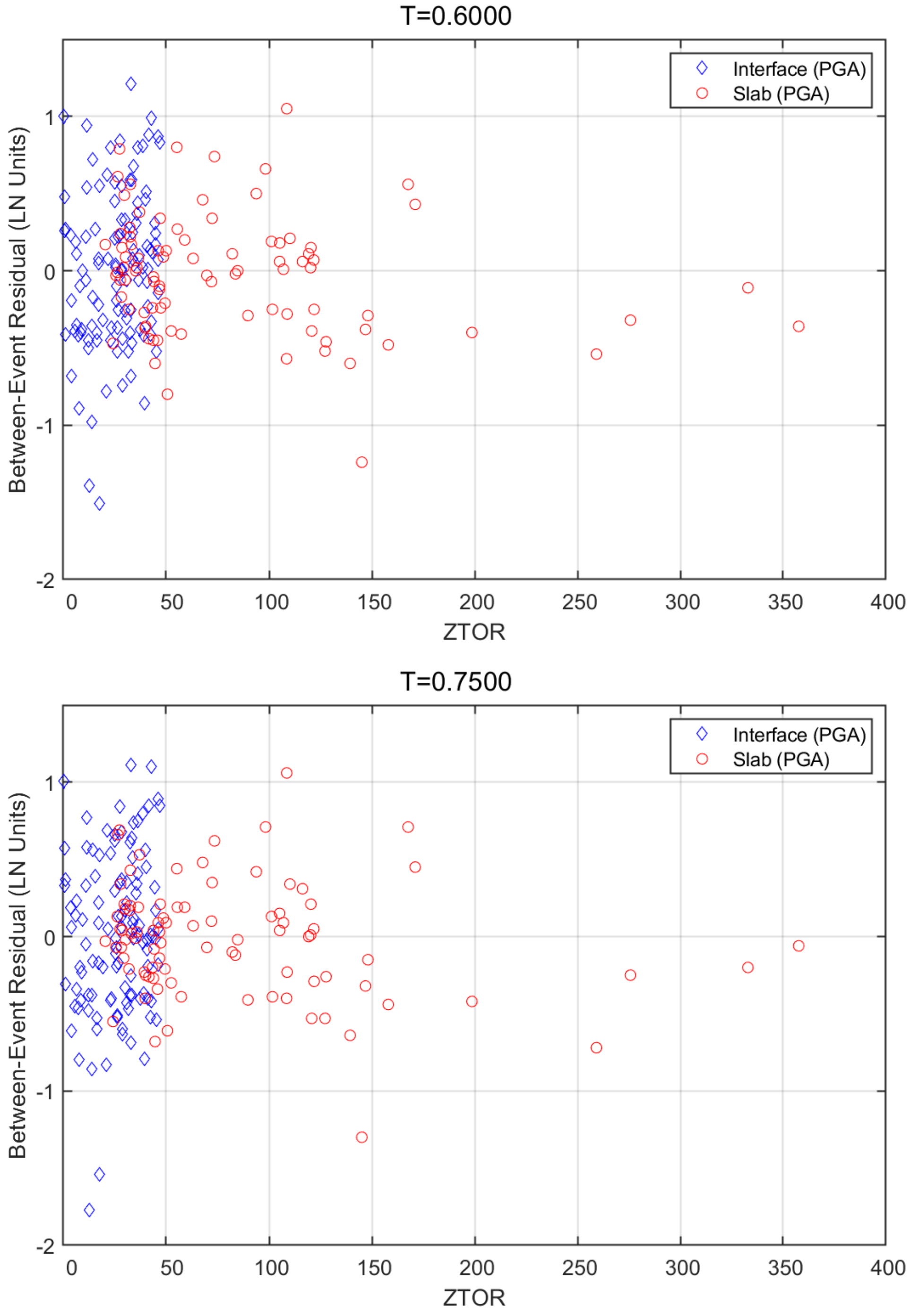

Figure A.31: Between-event residuals versus source depth. Top frame: T = 0.60 sec. Bottom frame: T = 0.75 sec.

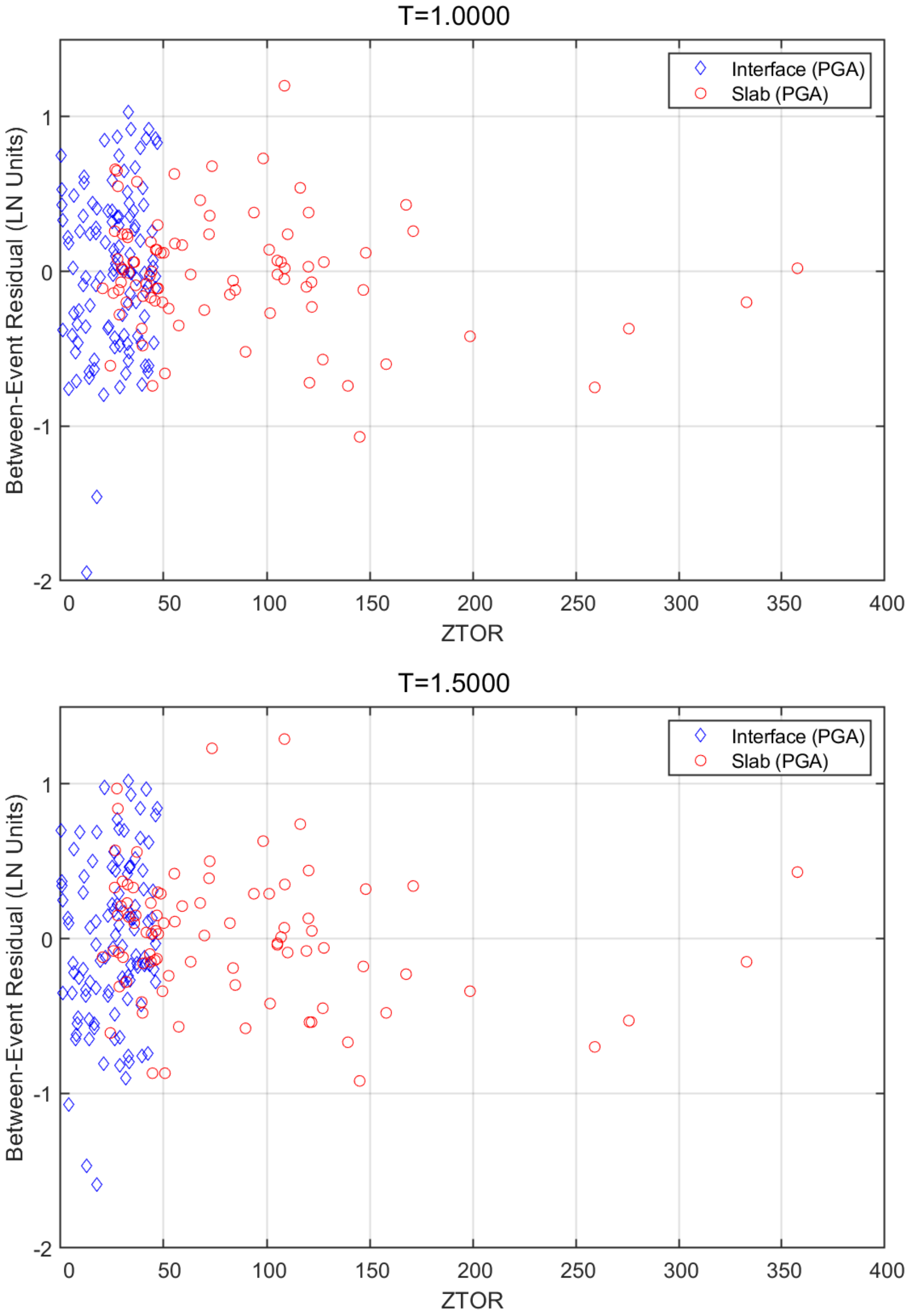

Figure A.32: Between-event residuals versus source depth. Top frame: T = 1.0 sec. Bottom frame: T = 1.5 sec.

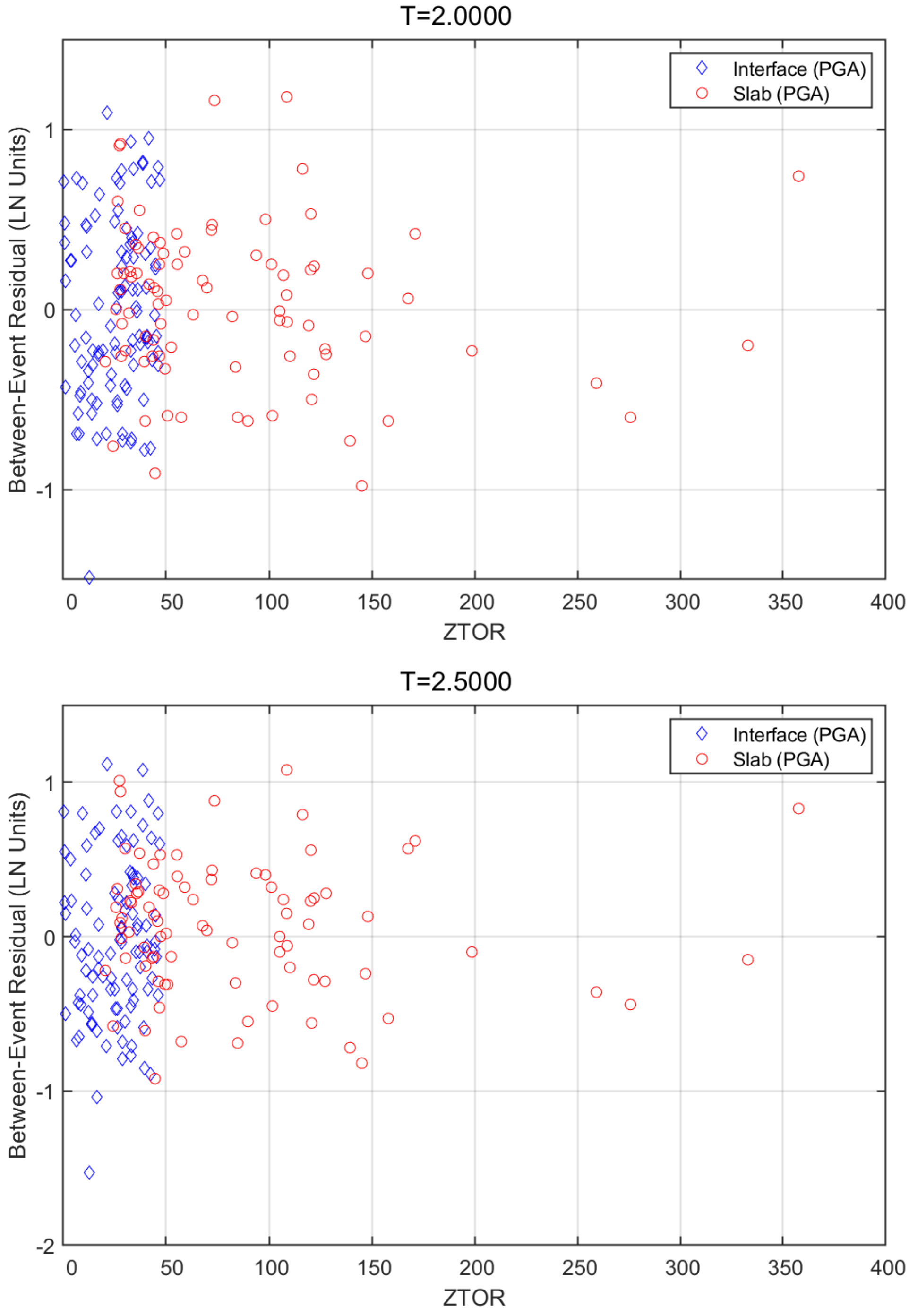

Figure A.33: Between-event residuals versus source depth. Top frame: T = 2.0 sec. Bottom frame: T = 2.5 sec.

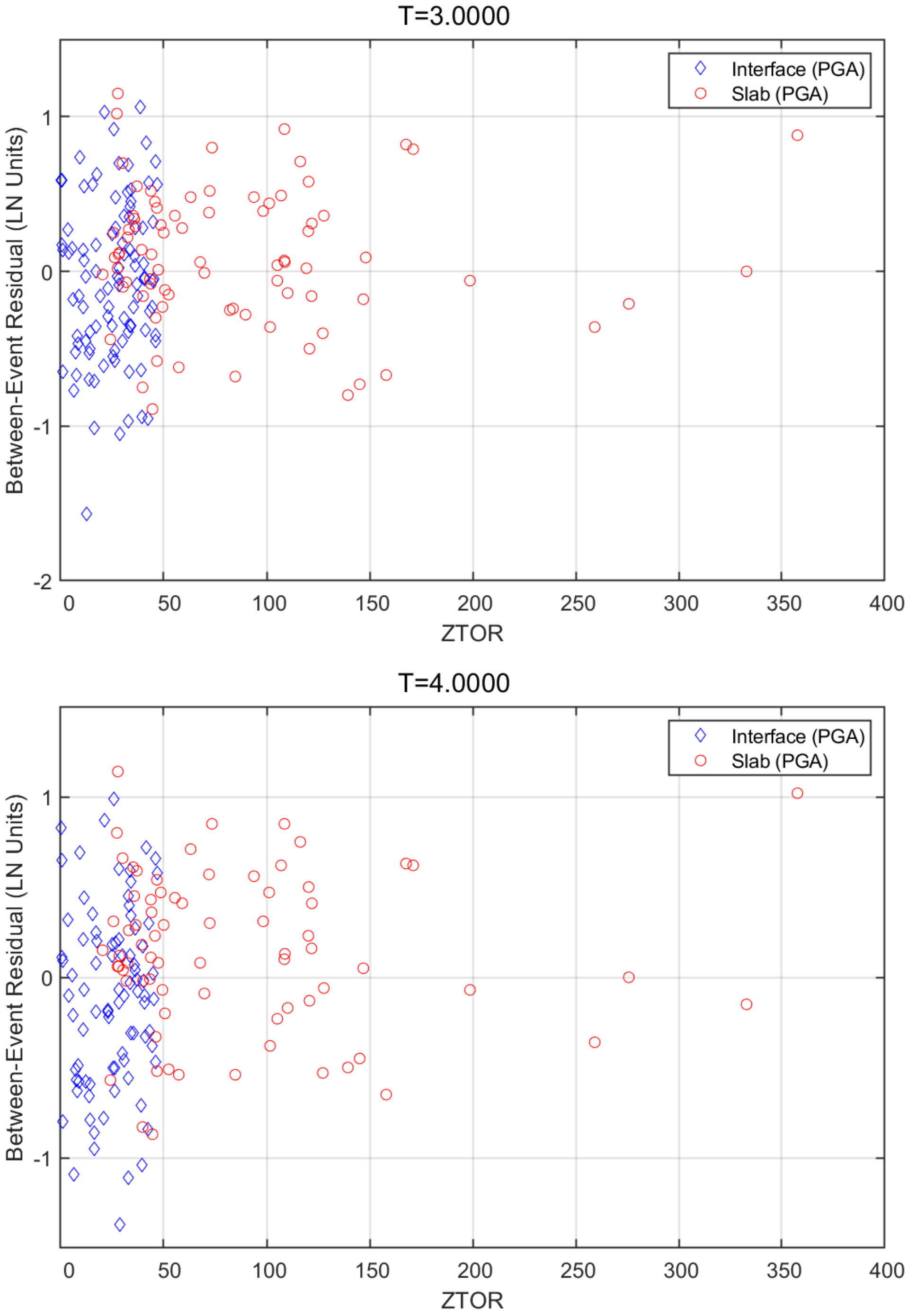

Figure A.34: Between-event residuals versus source depth. Top frame: T = 3.0 sec. Bottom frame: T = 4.0 sec.

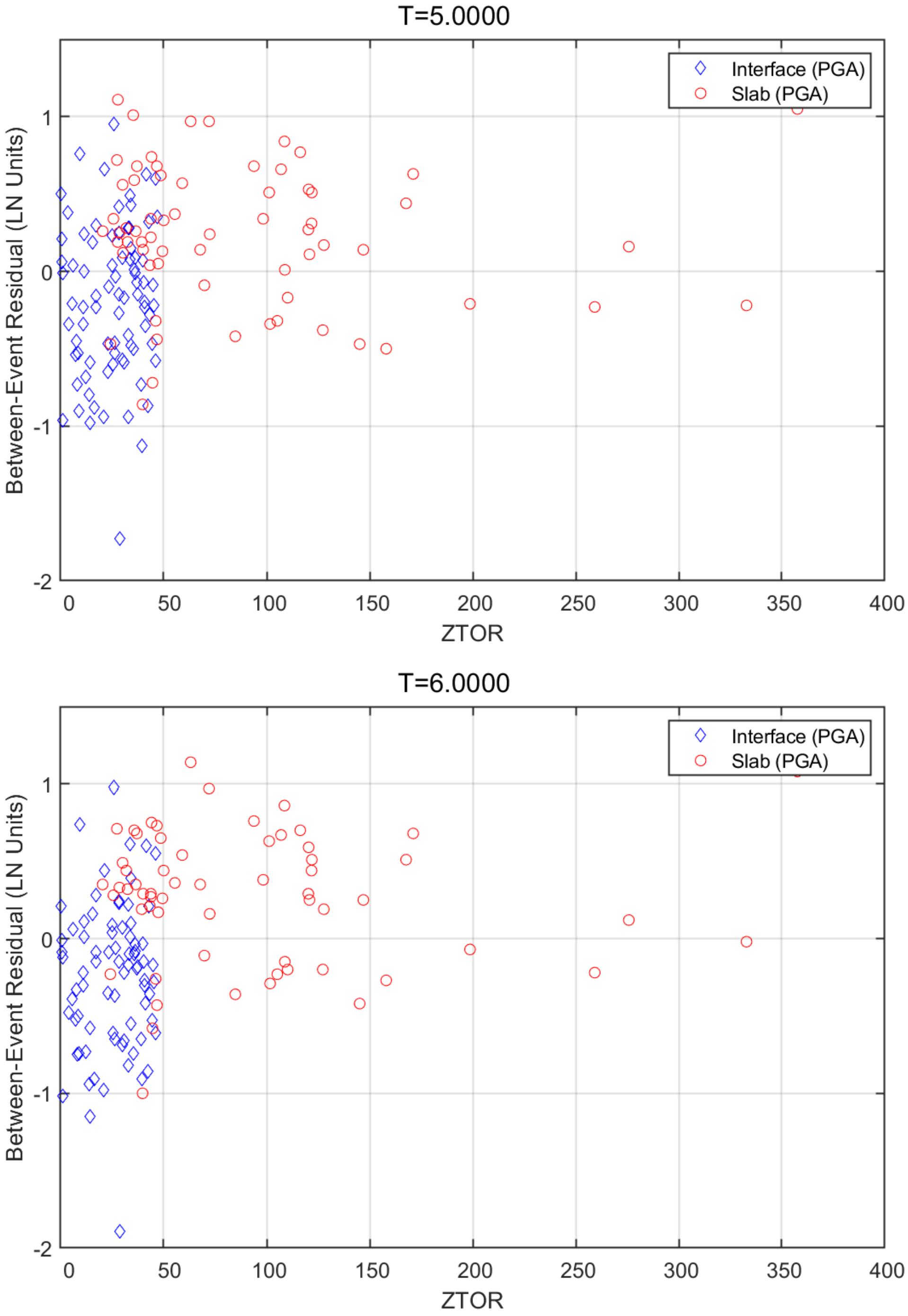

Figure A.35: Between-event residuals versus source depth. Top frame: T = 5.0 sec. Bottom frame: T = 6.0 sec.

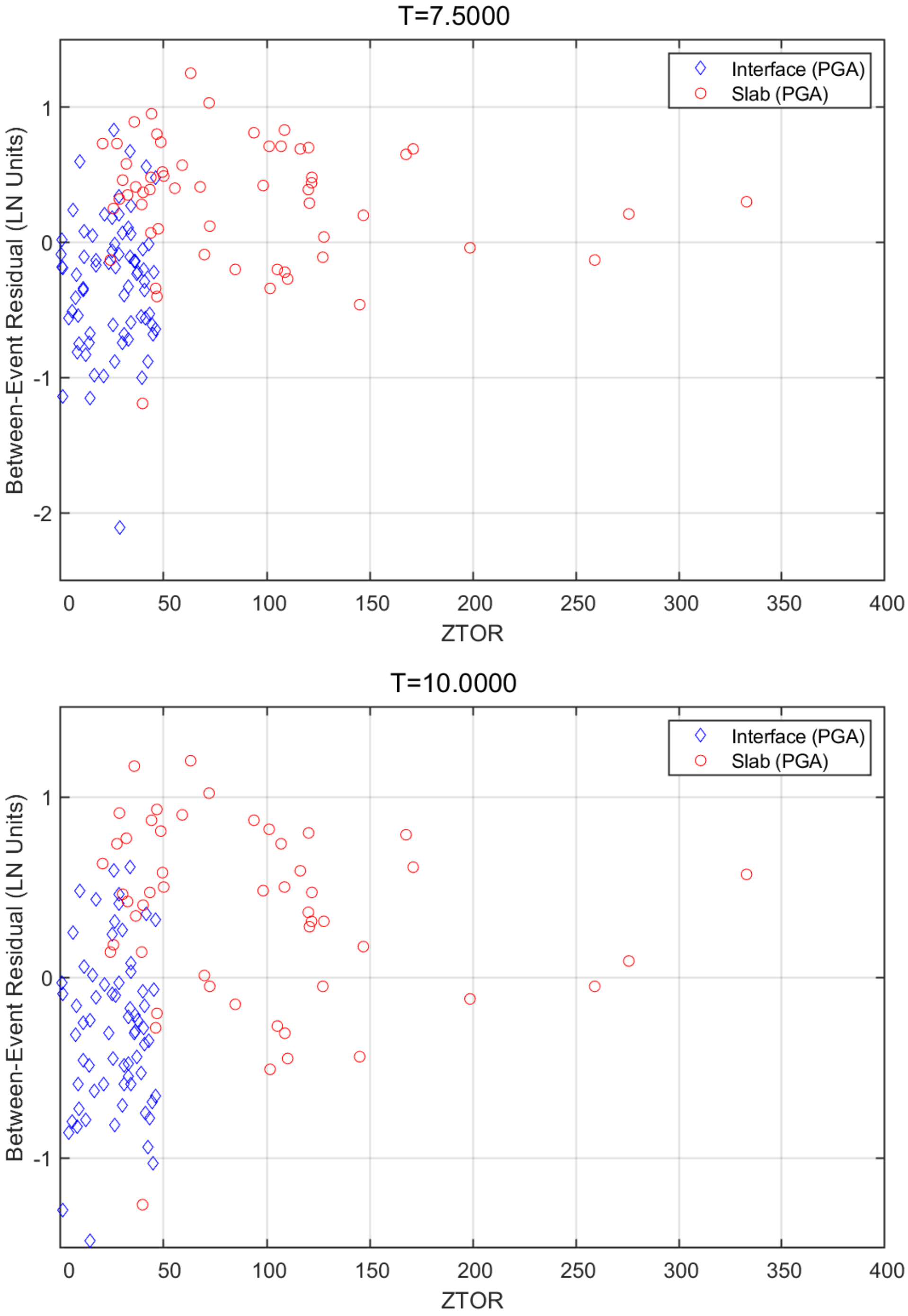

Figure A.36: Between-event residuals versus source depth. Top frame: T = 7.5 sec. Bottom frame: T = 10.0 sec.

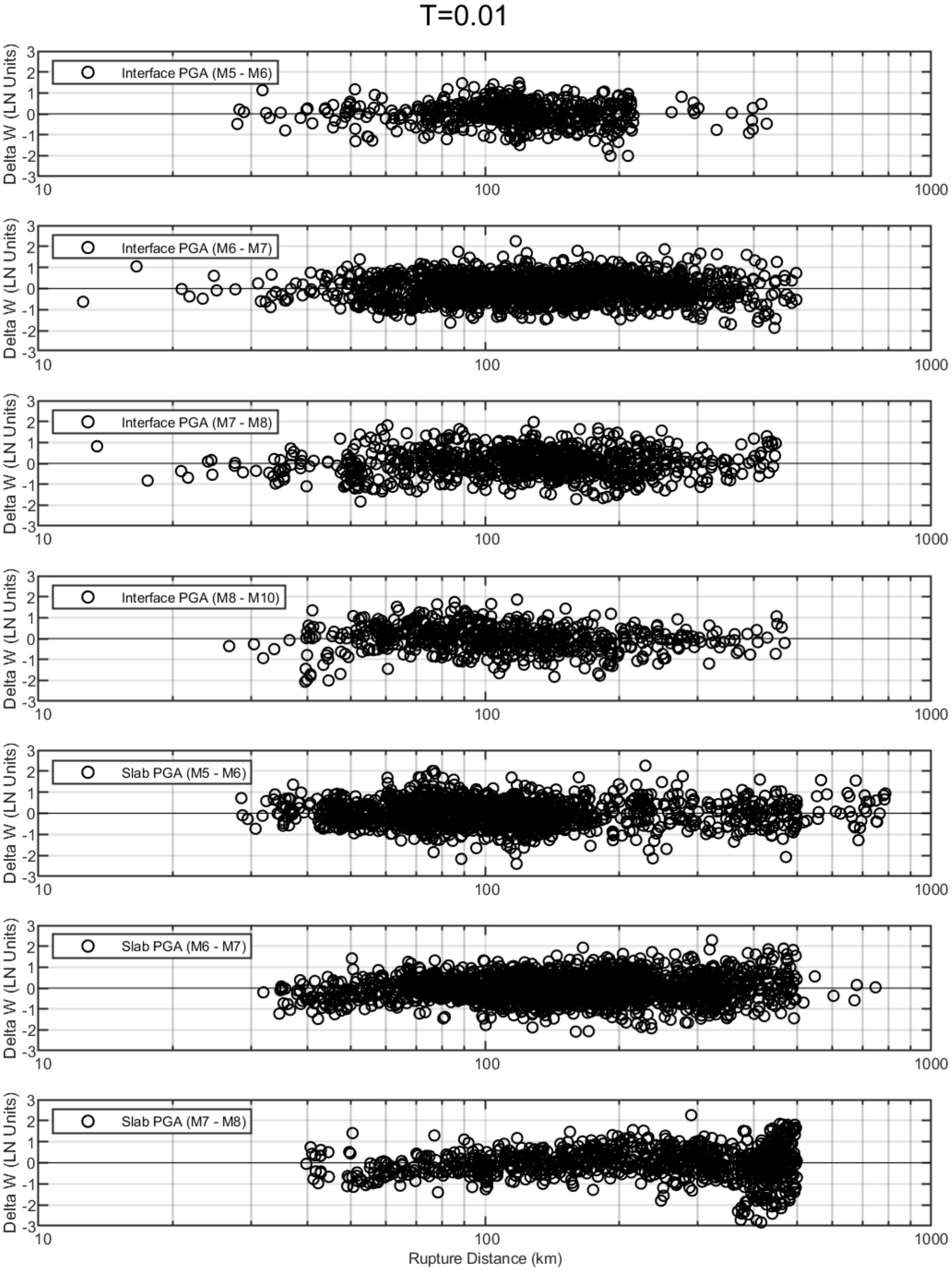

Figure A.37: Within-event residuals versus distance for T = 0.01 sec.

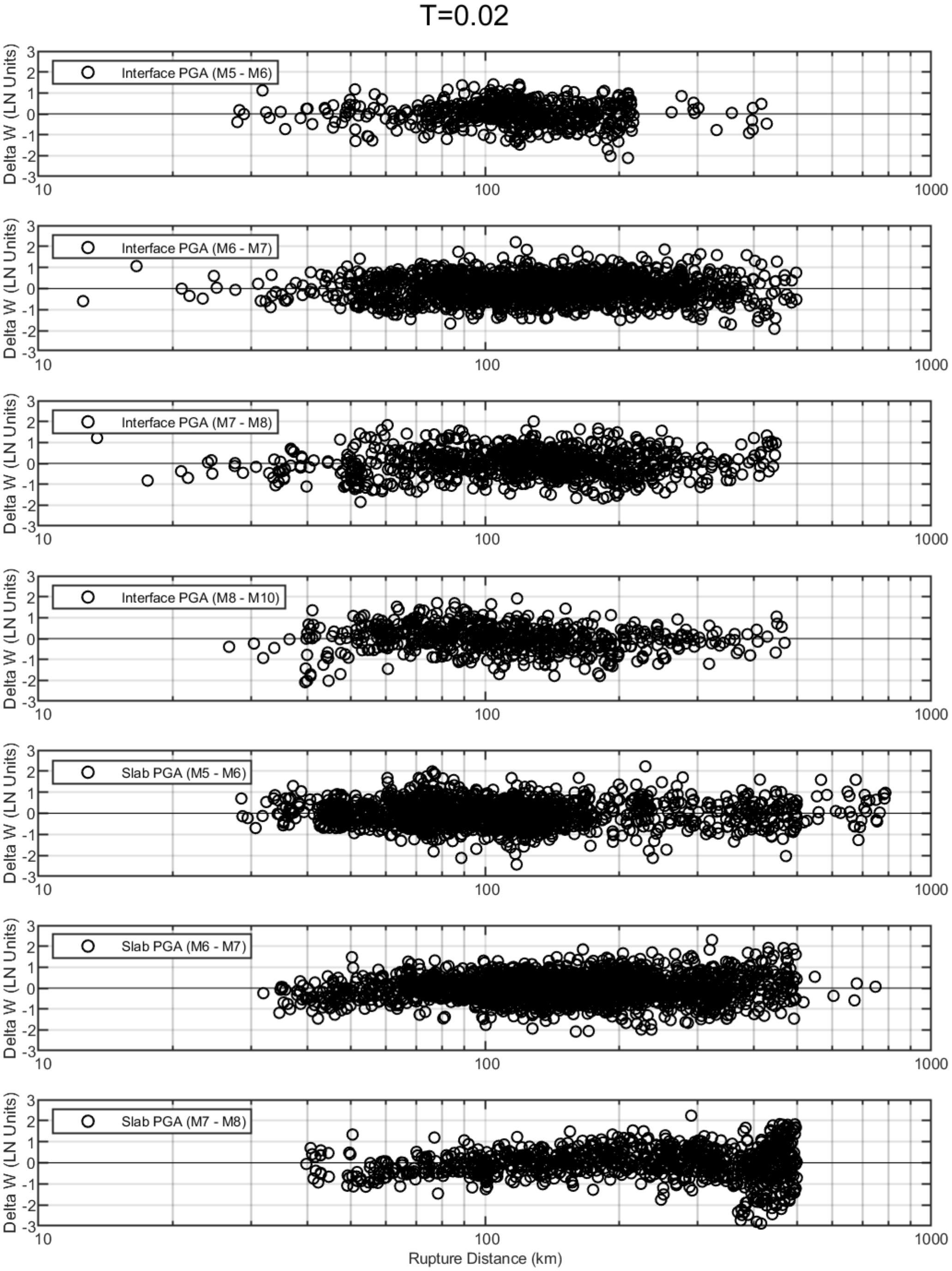

Figure A.38: Within-event residuals versus distance for T = 0.02 sec.

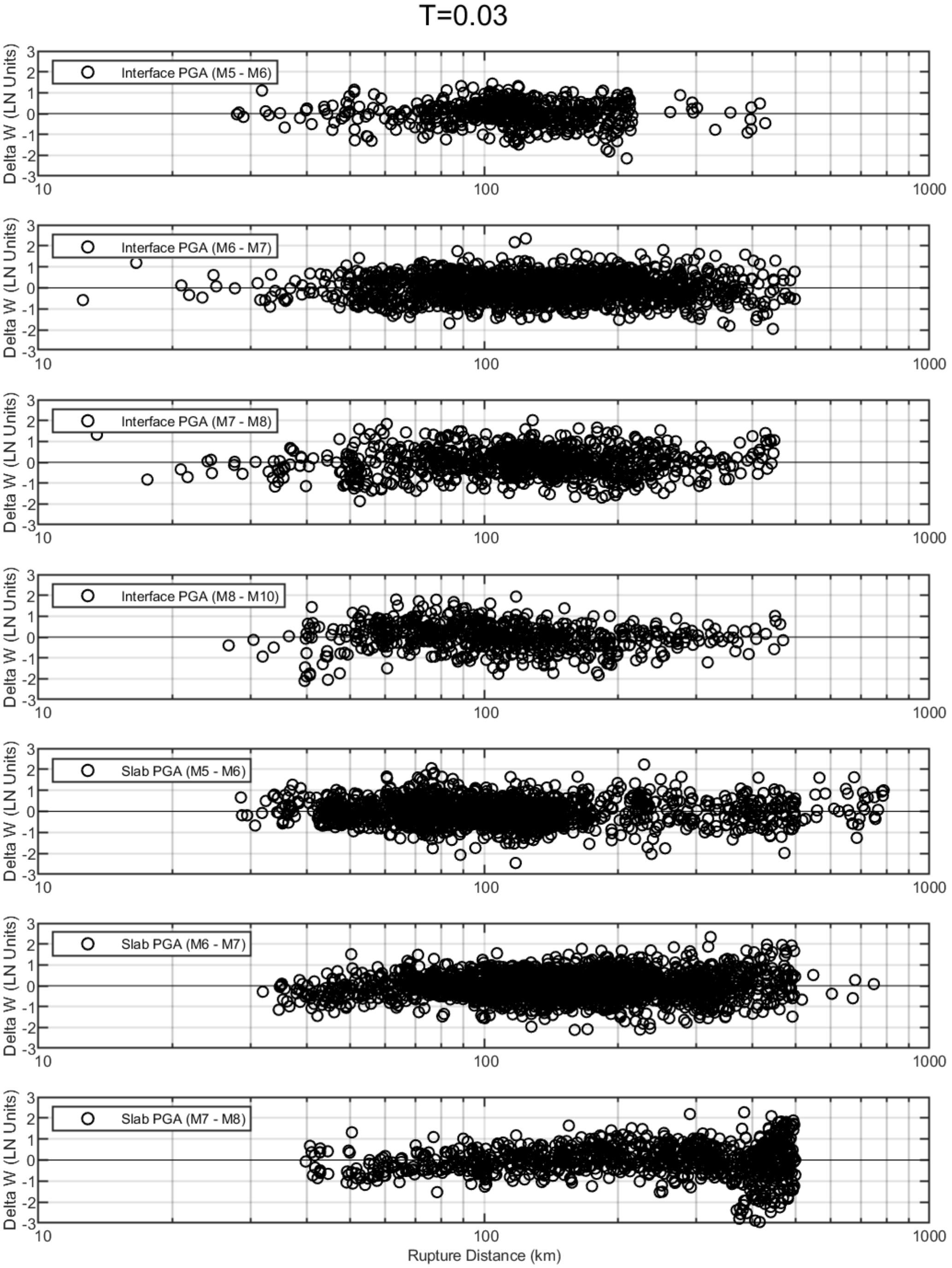

Figure A.39: Within-event residuals versus distance for T = 0.03 sec.

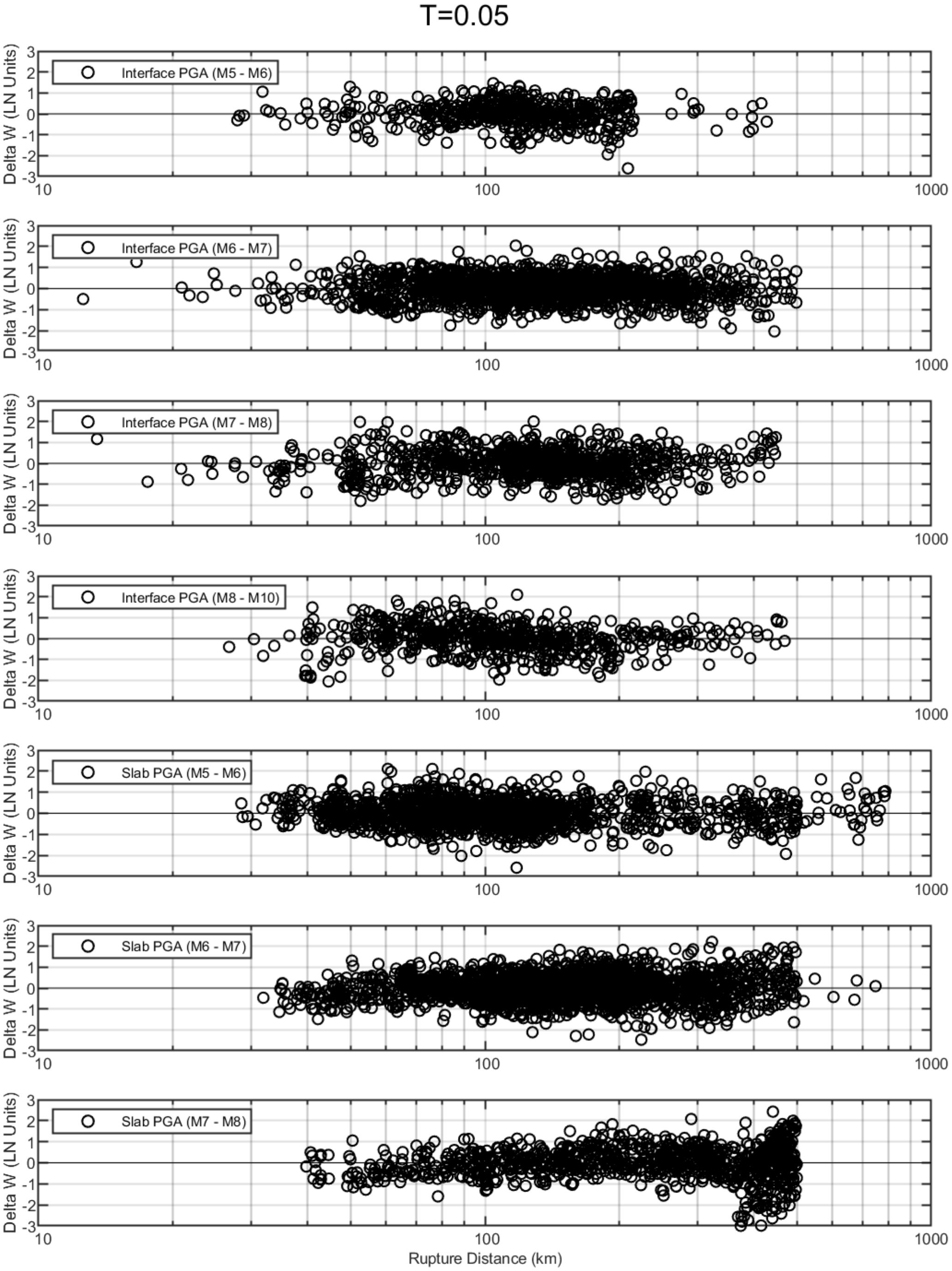

Figure A.40: Within-event residuals versus distance for T = 0.05 sec.

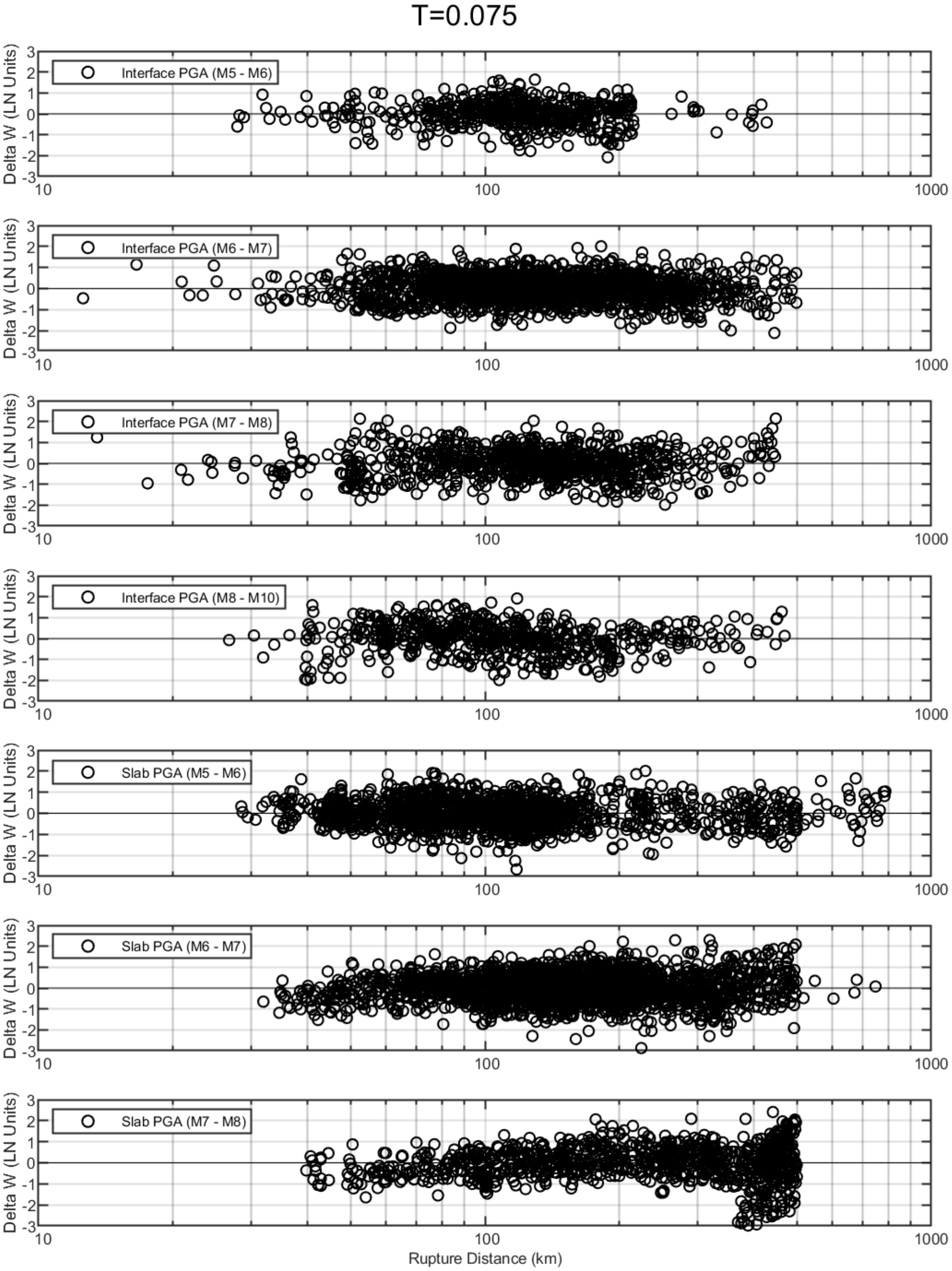

Figure A.41: Within-event residuals versus distance for T = 0.075 sec.

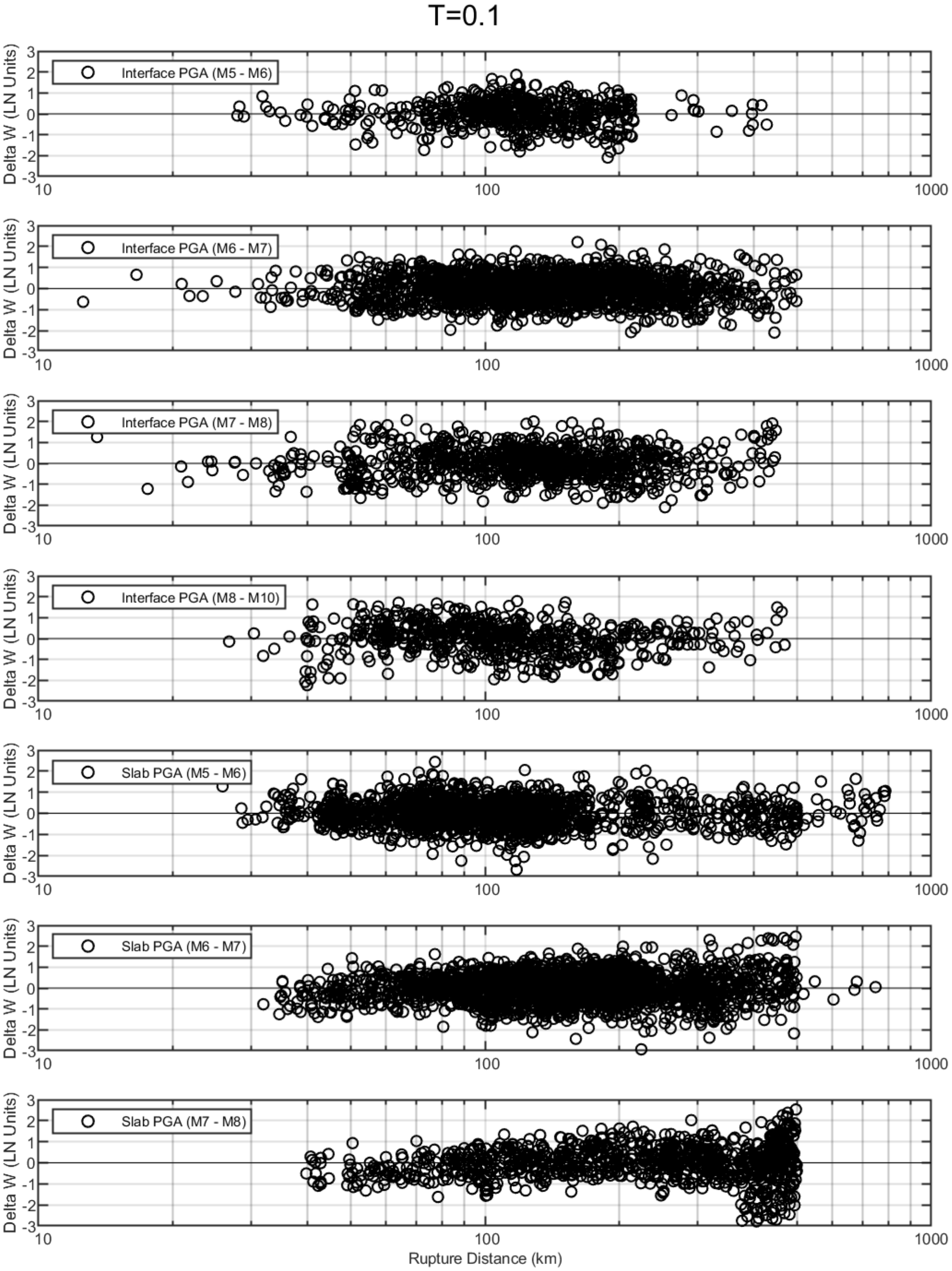

Figure A.42: Within-event residuals versus distance for T = 0.10 sec.

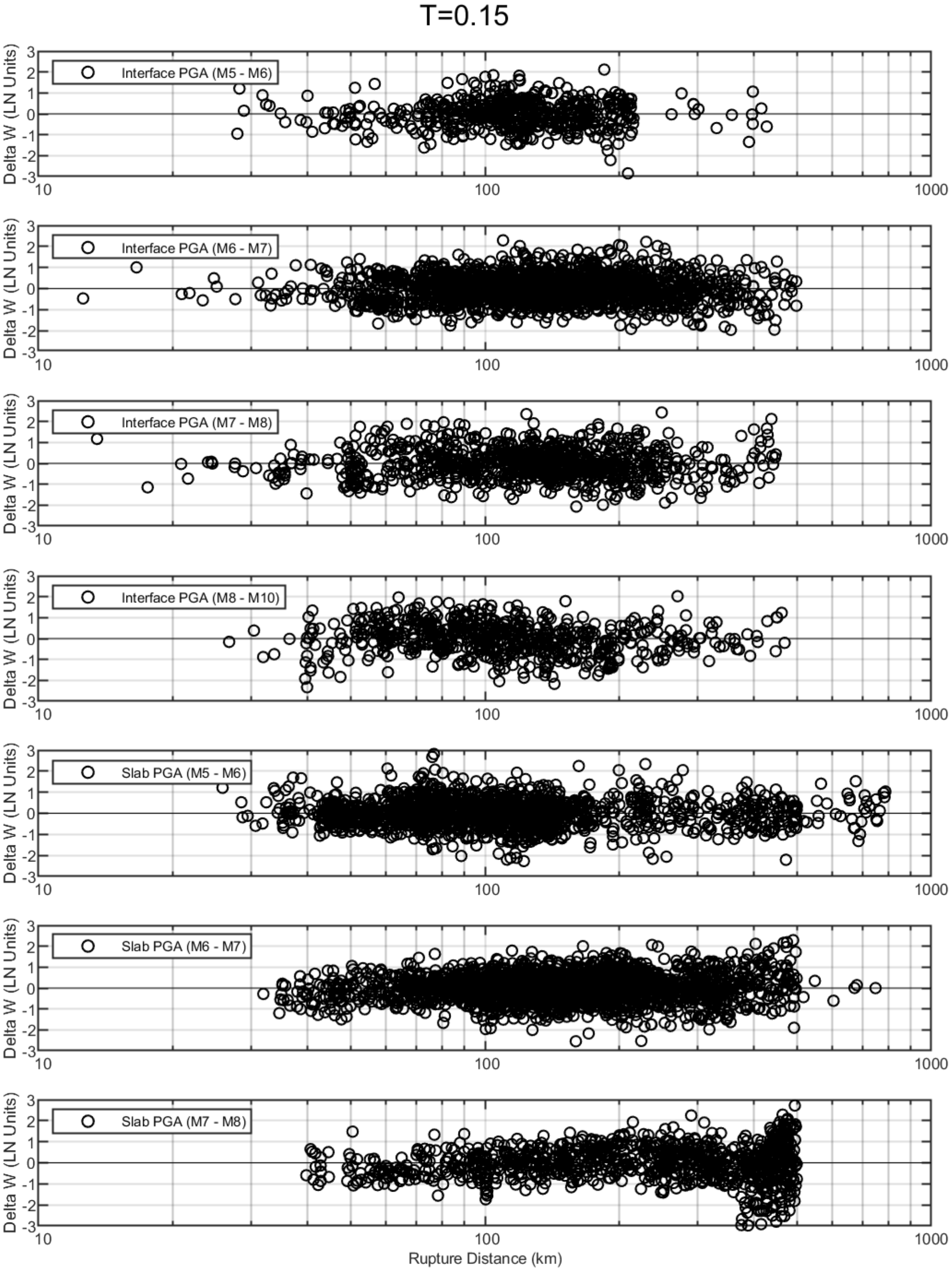

Figure A.43: Within-event residuals versus distance for T = 0.15 sec.

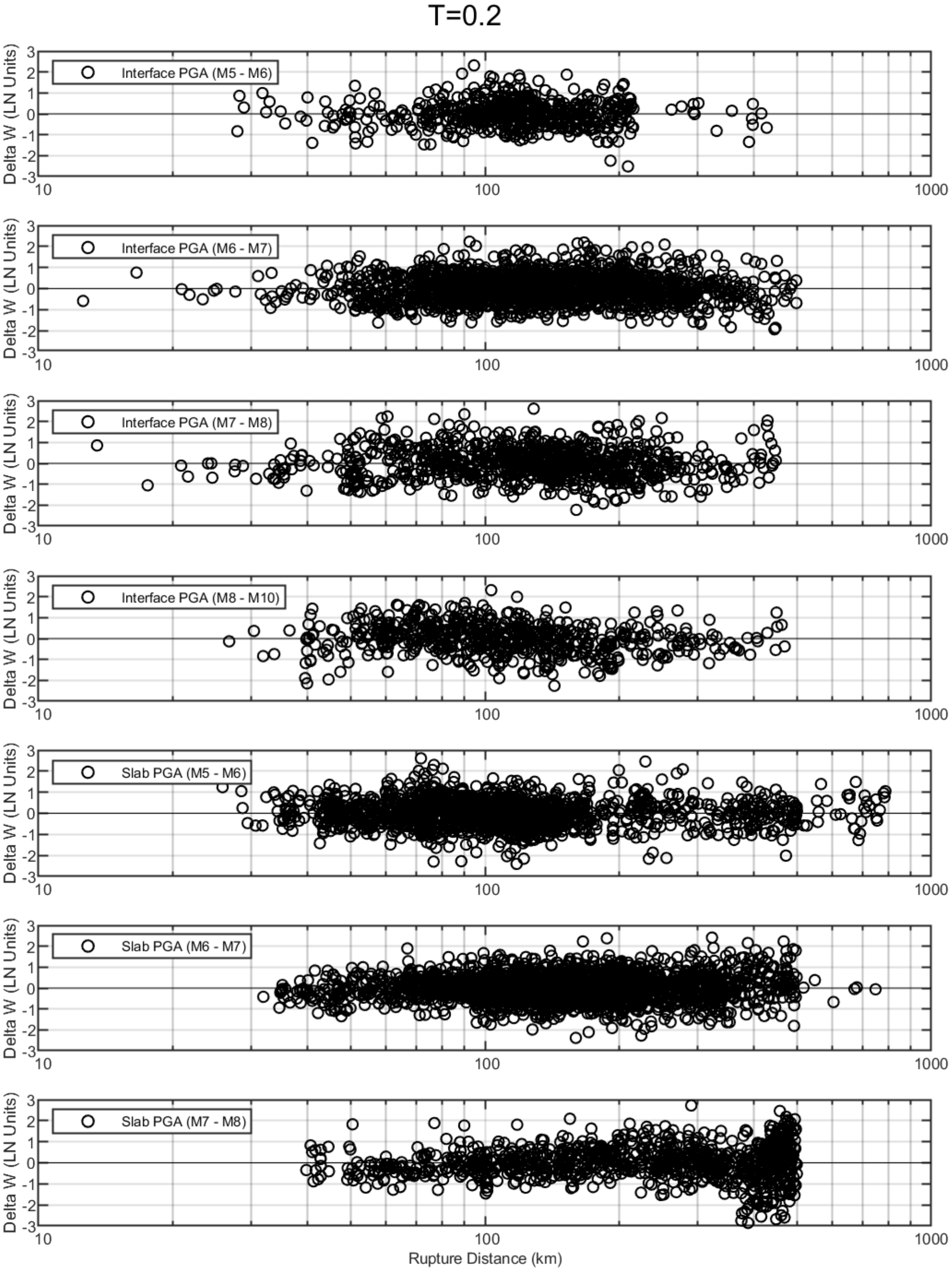

Figure A.44: Within-event residuals versus distance for T = 0.20 sec.

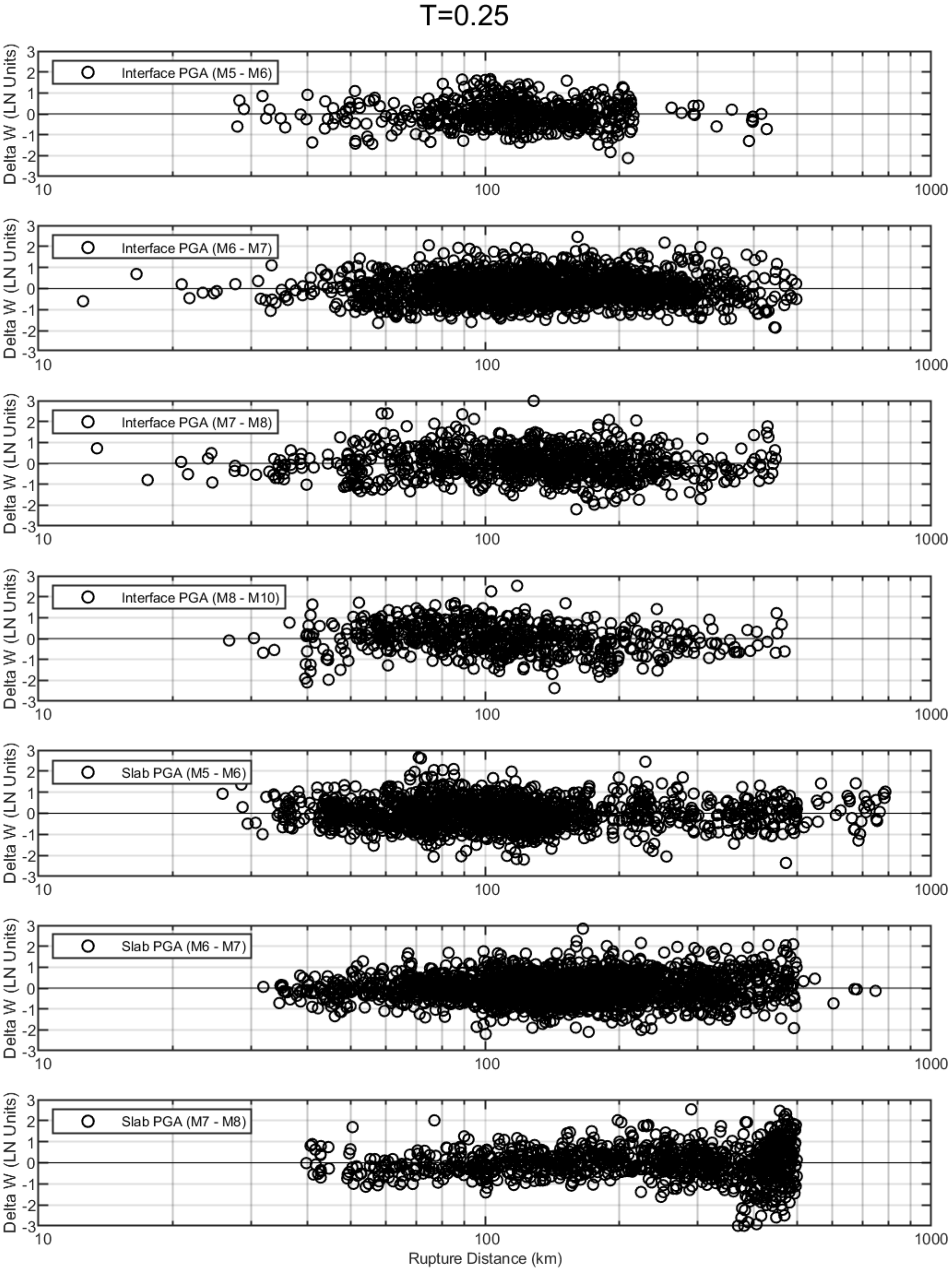

Figure A.45: Within-event residuals versus distance for T = 0.25 sec.

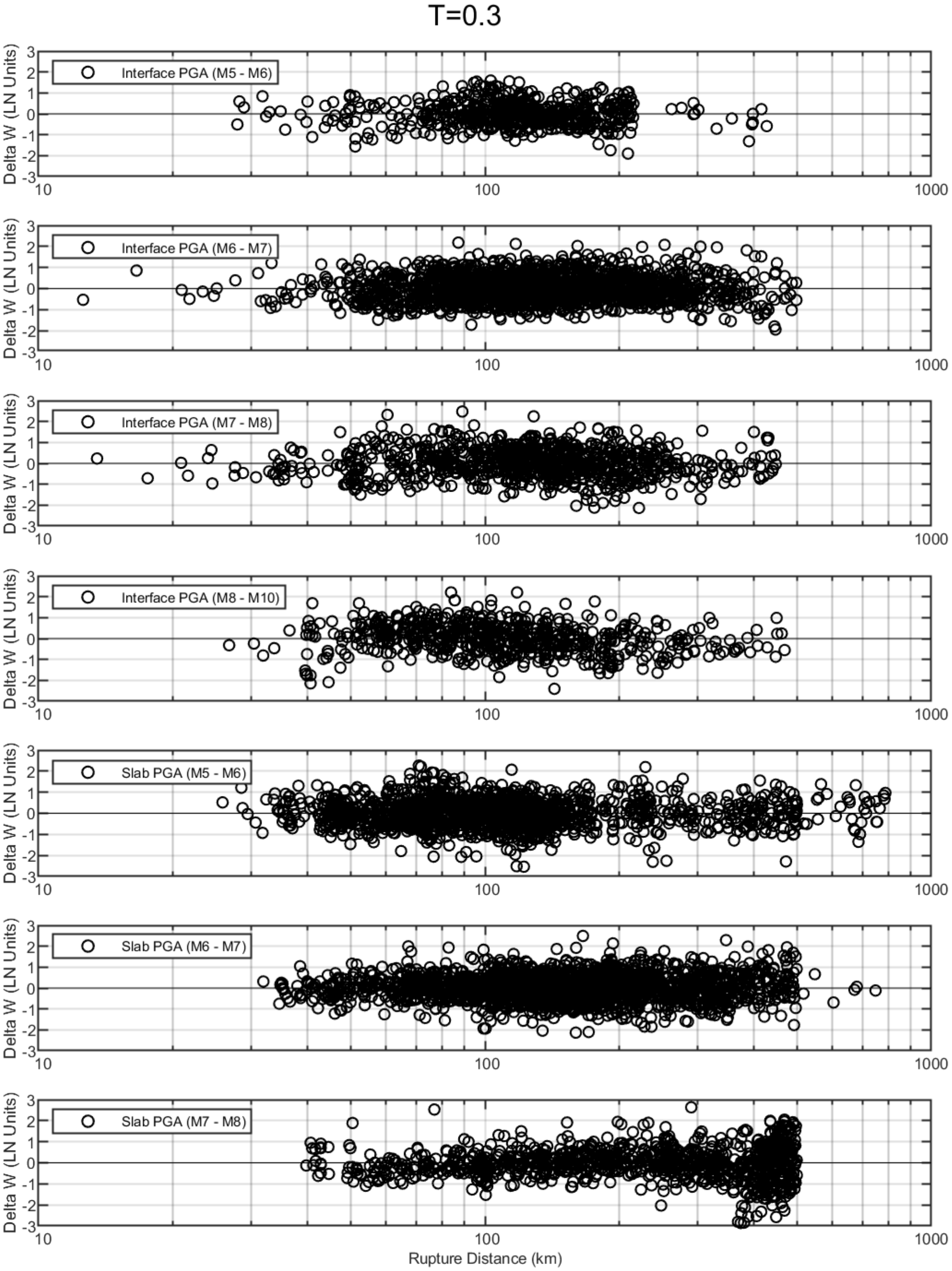

Figure A.46: Within-event residuals versus distance for T = 0.30 sec.

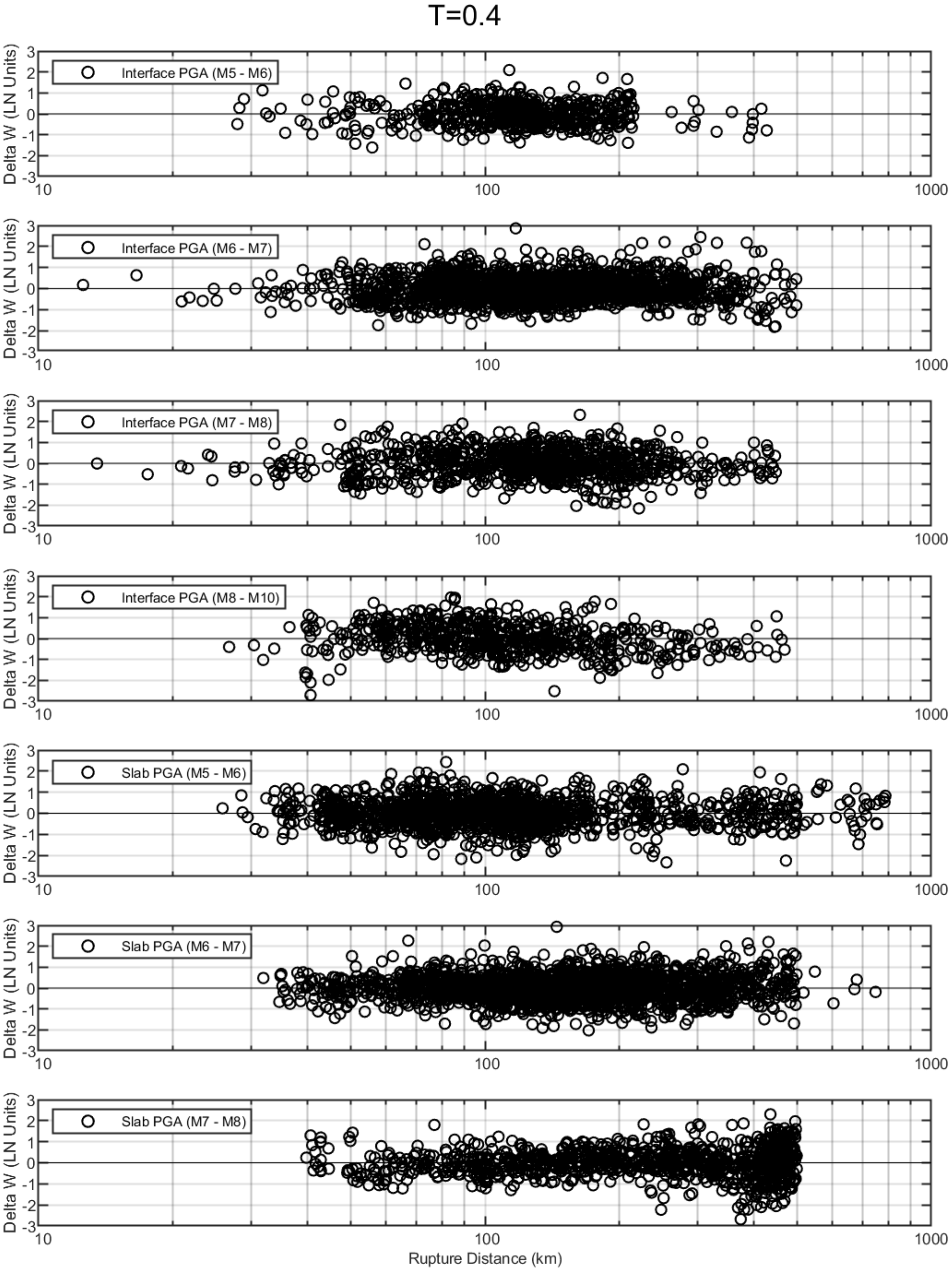

Figure A.47: Within-event residuals versus distance for T = 0.40 sec.

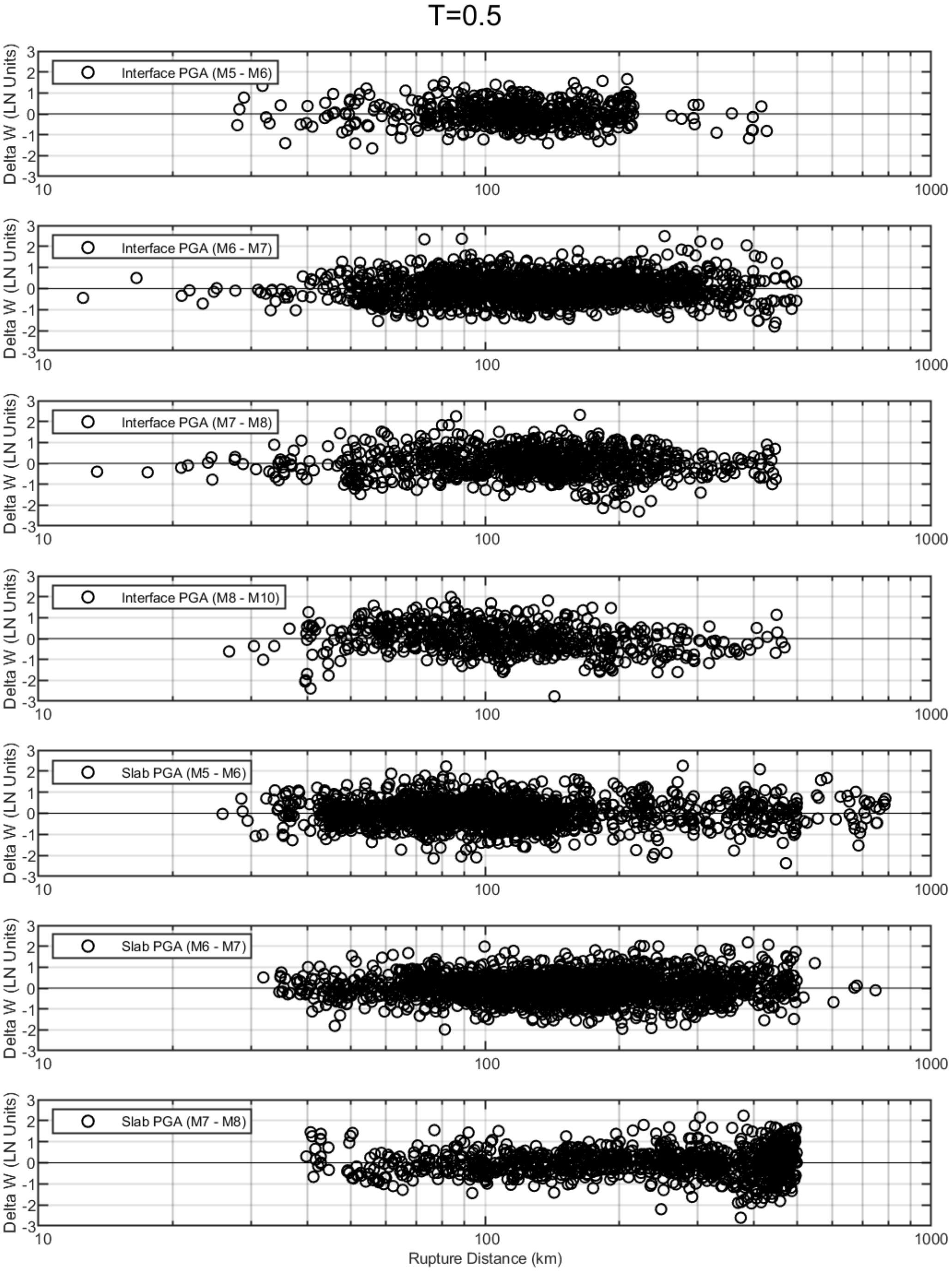

Figure A.48: Within-event residuals versus distance for T = 0.50 sec.

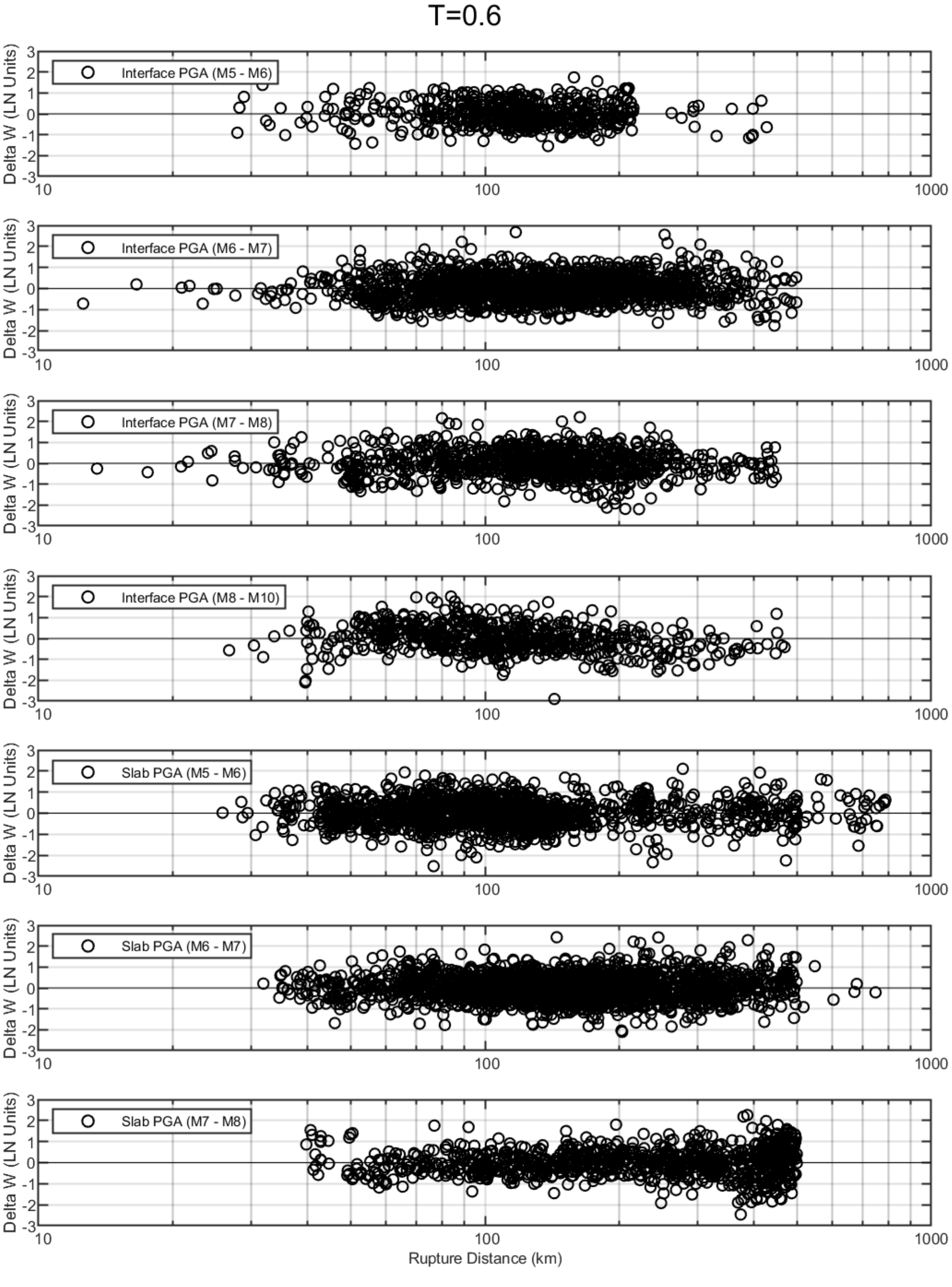

Figure A.49: Within-event residuals versus distance for T = 0.60 sec.

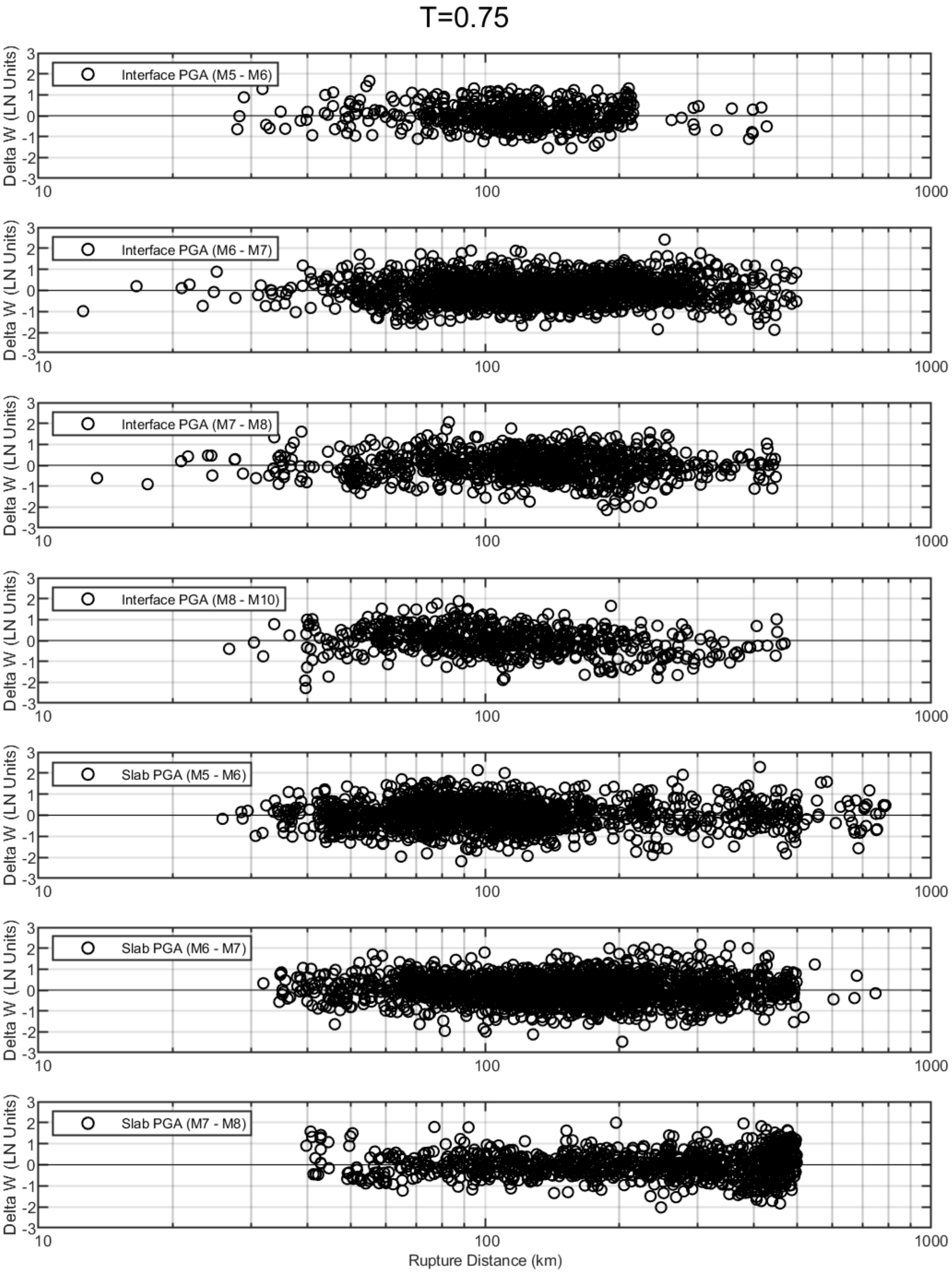

Figure A.50: Within-event residuals versus distance for T=0.75 sec.

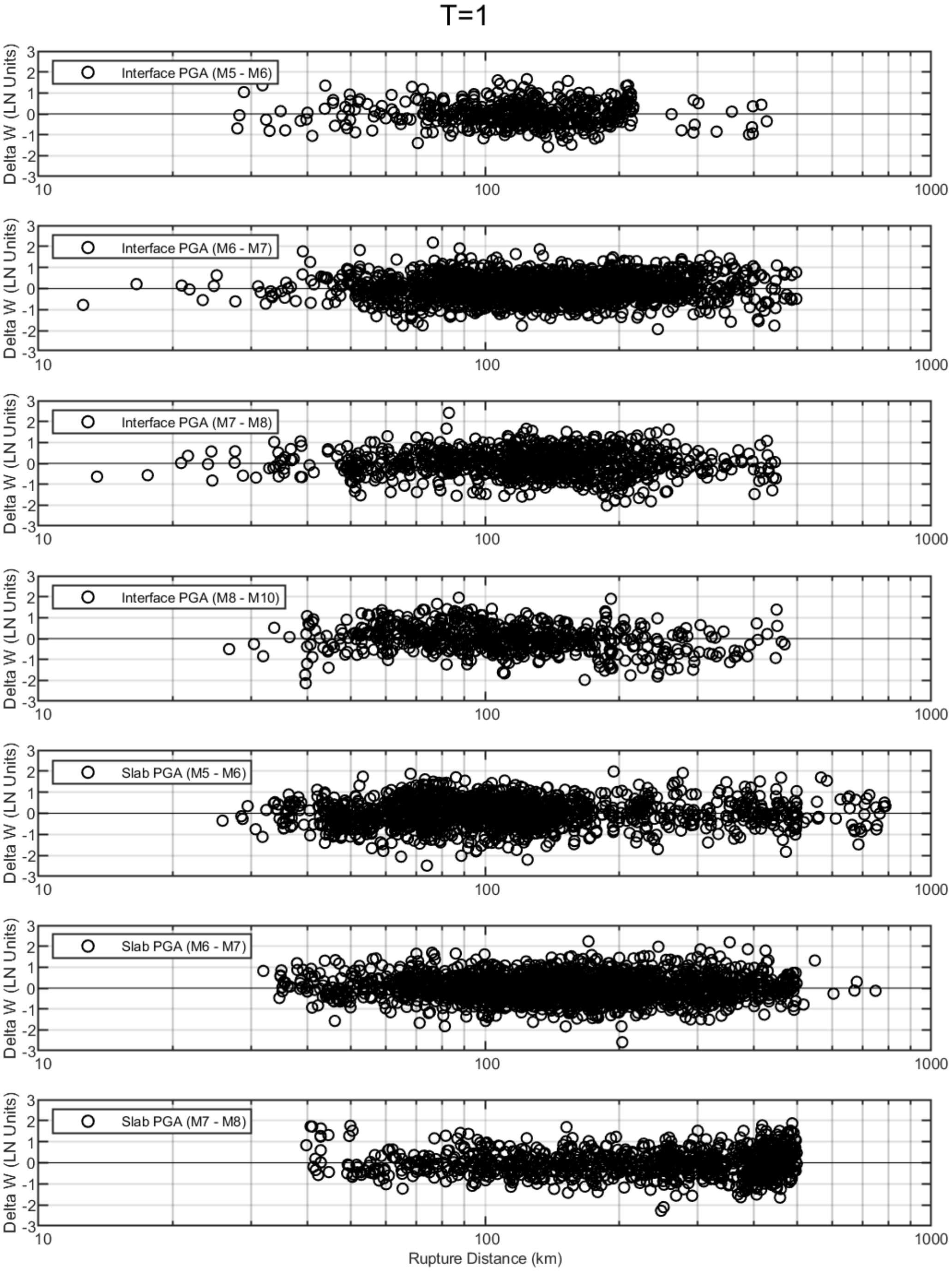

Figure A.51: Within-event residuals versus distance for T = 1.0 sec.

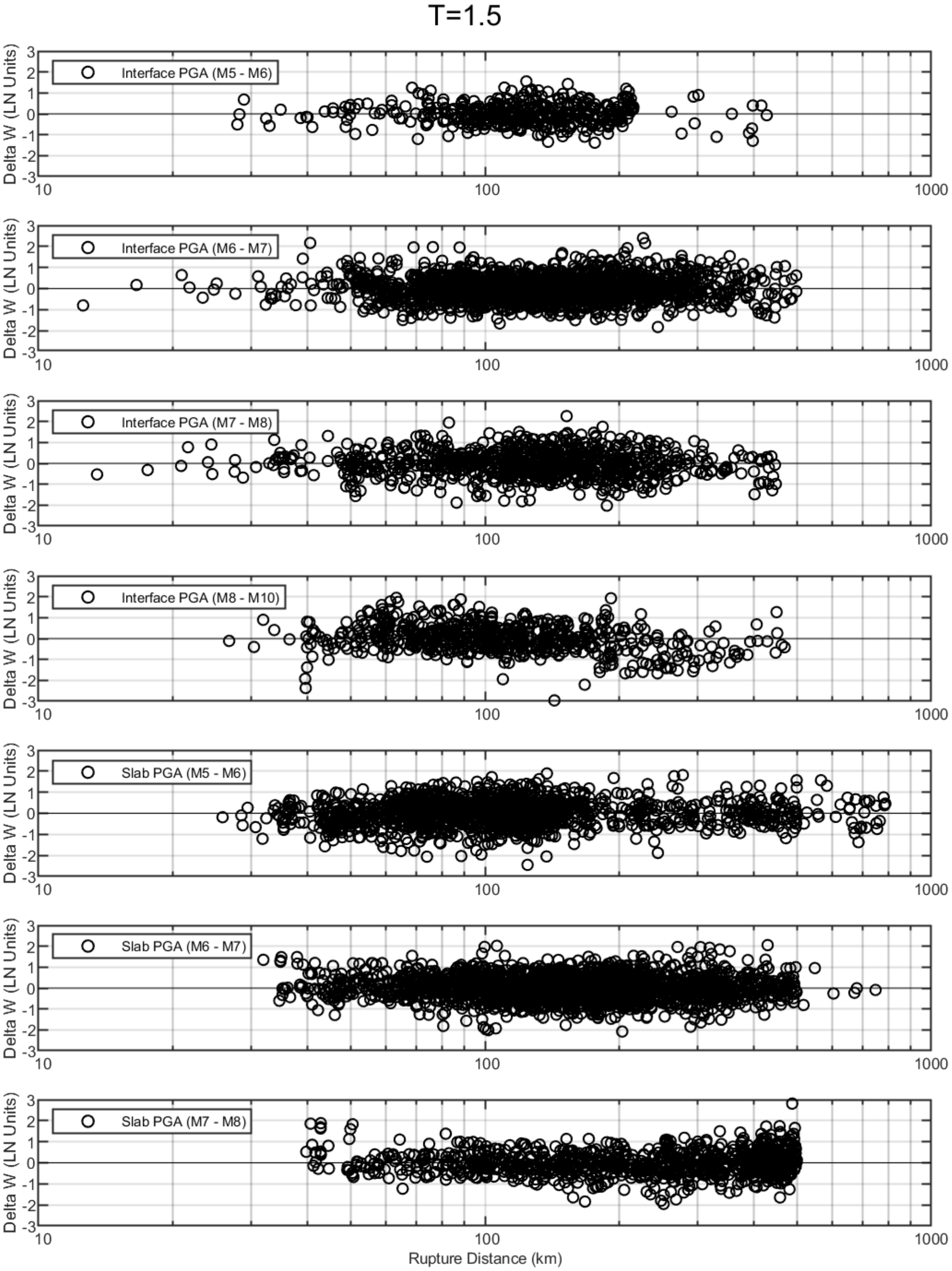

Figure A.52: Within-event residuals versus distance for T = 1.5 sec.

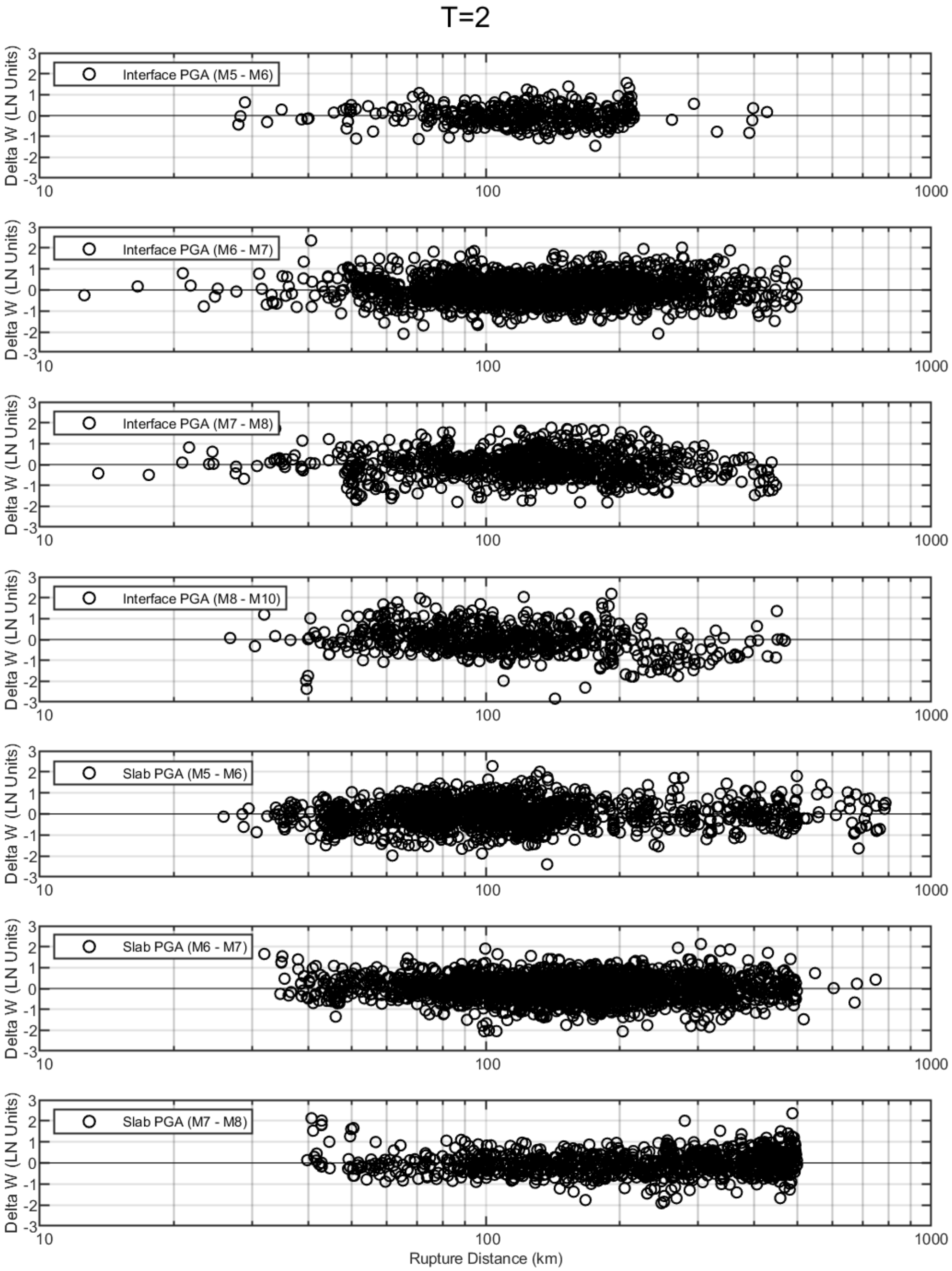

Figure A.53: Within-event residuals versus distance for T = 2.0 sec.

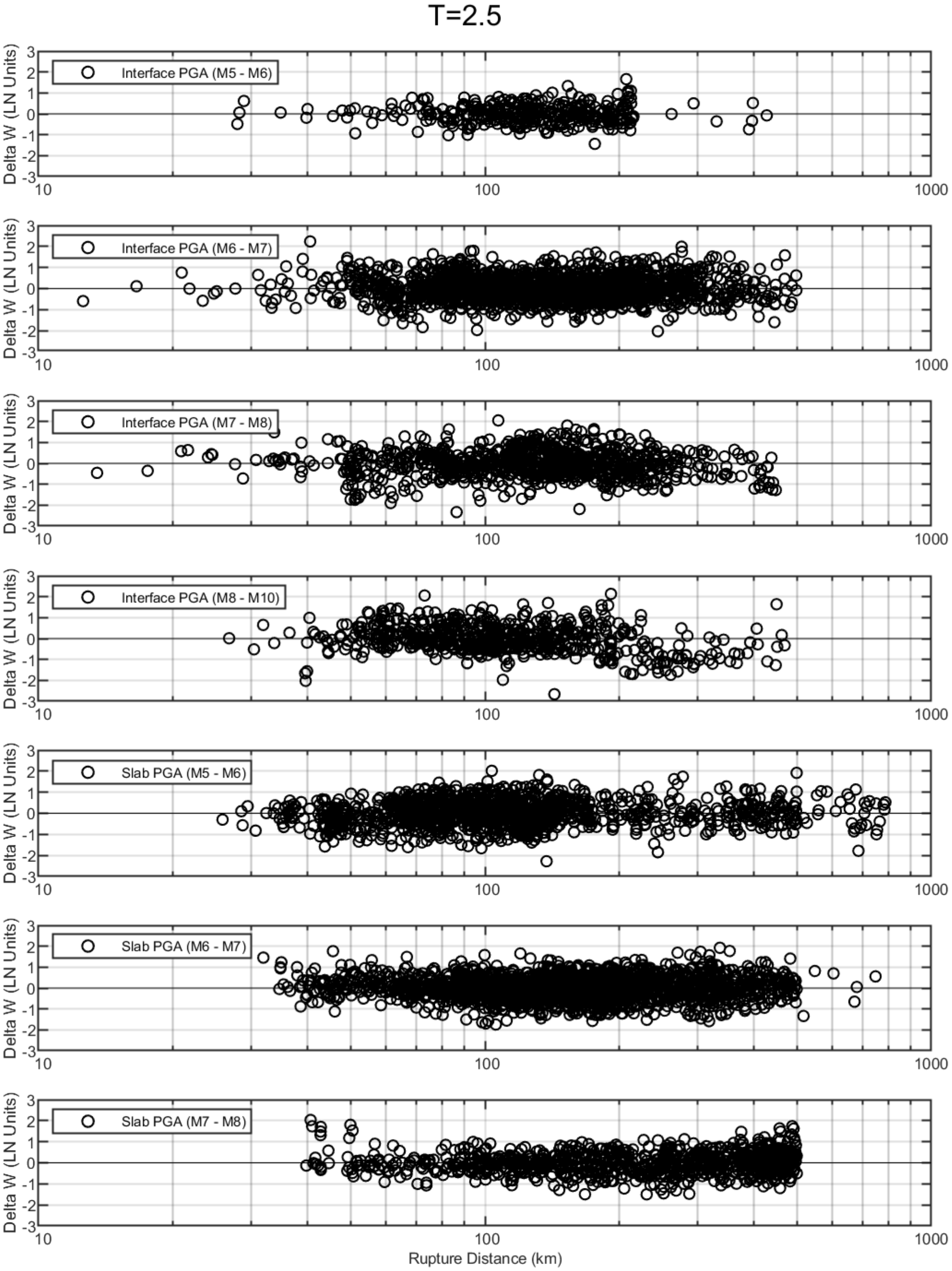

Figure A.54: Within-event residuals versus distance for T = 2.5 sec.

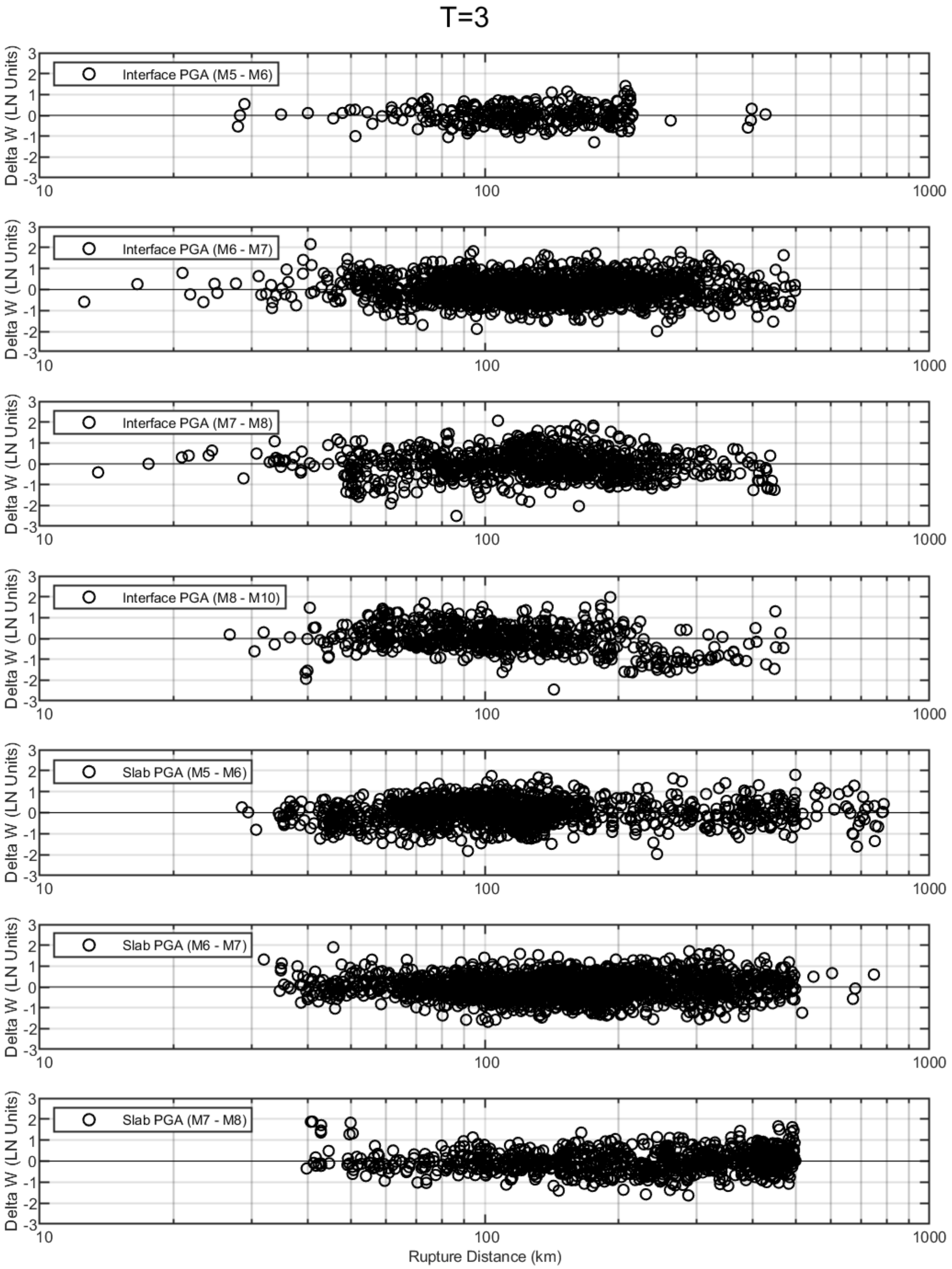

Figure A.55: Within-event residuals versus distance for T = 3.0 sec.

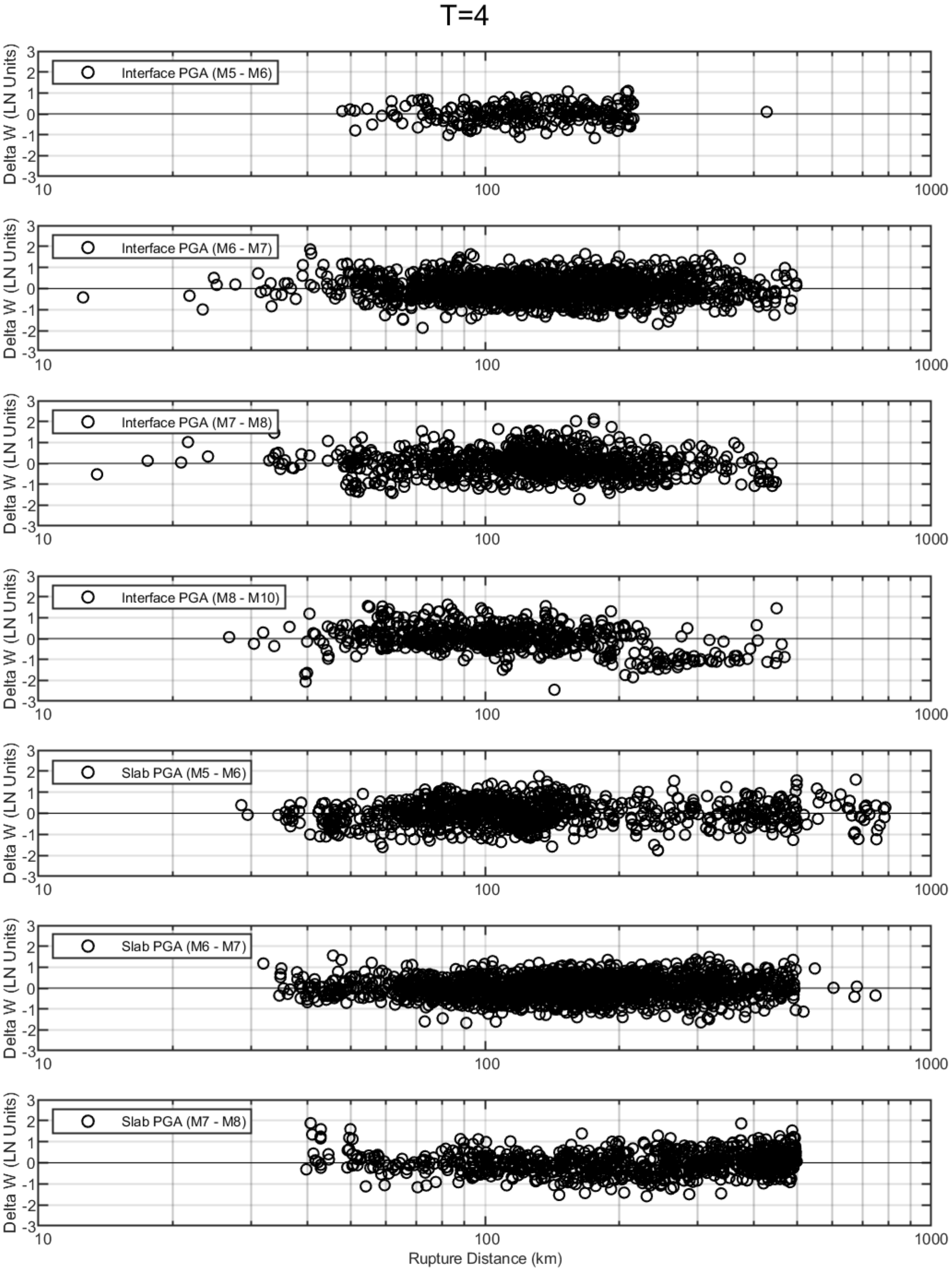

Figure A.56: Within-event residuals versus distance for T = 4.0 sec.

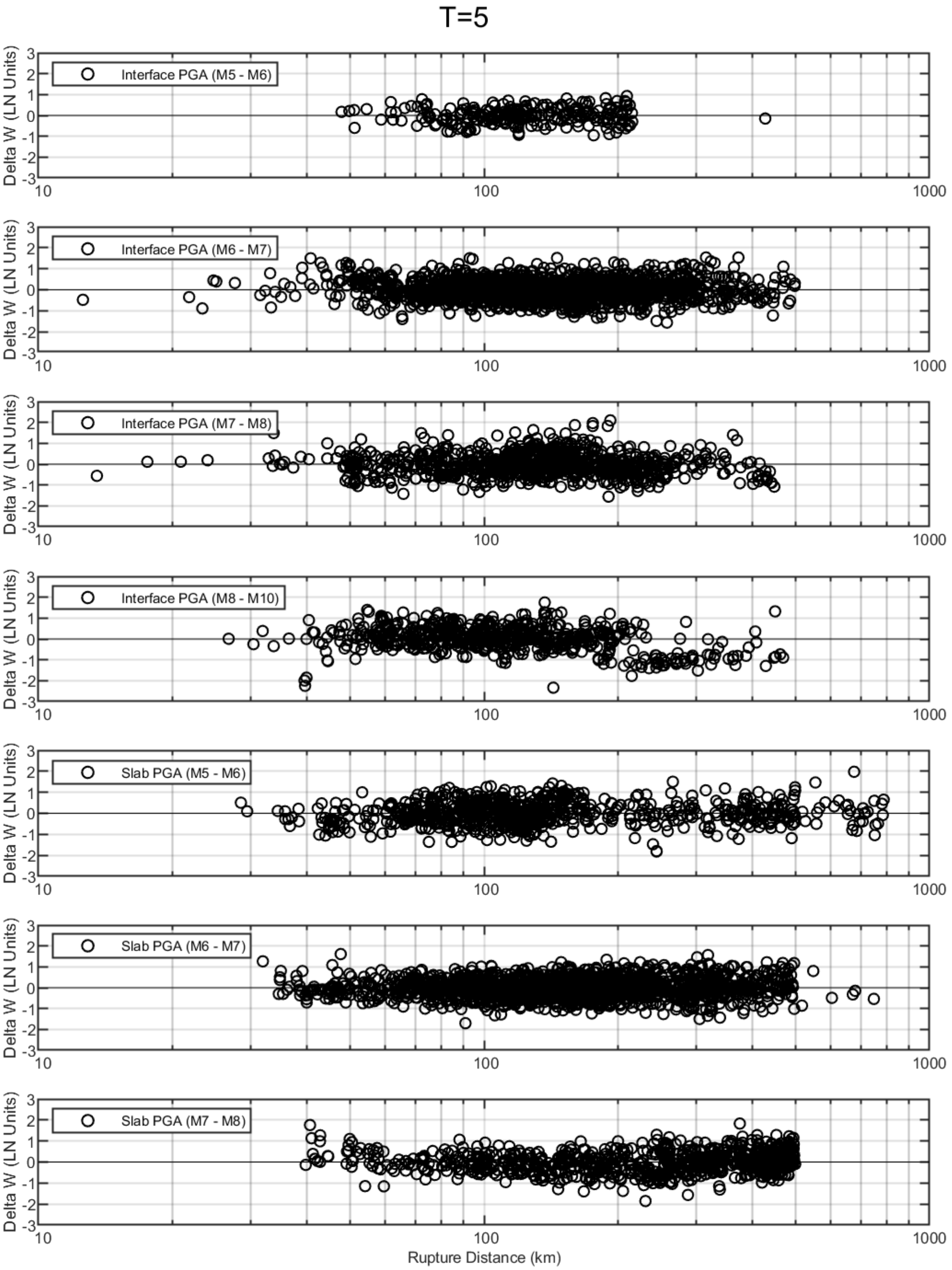

Figure A.57: Within-event residuals versus distance for T = 5.0 sec.

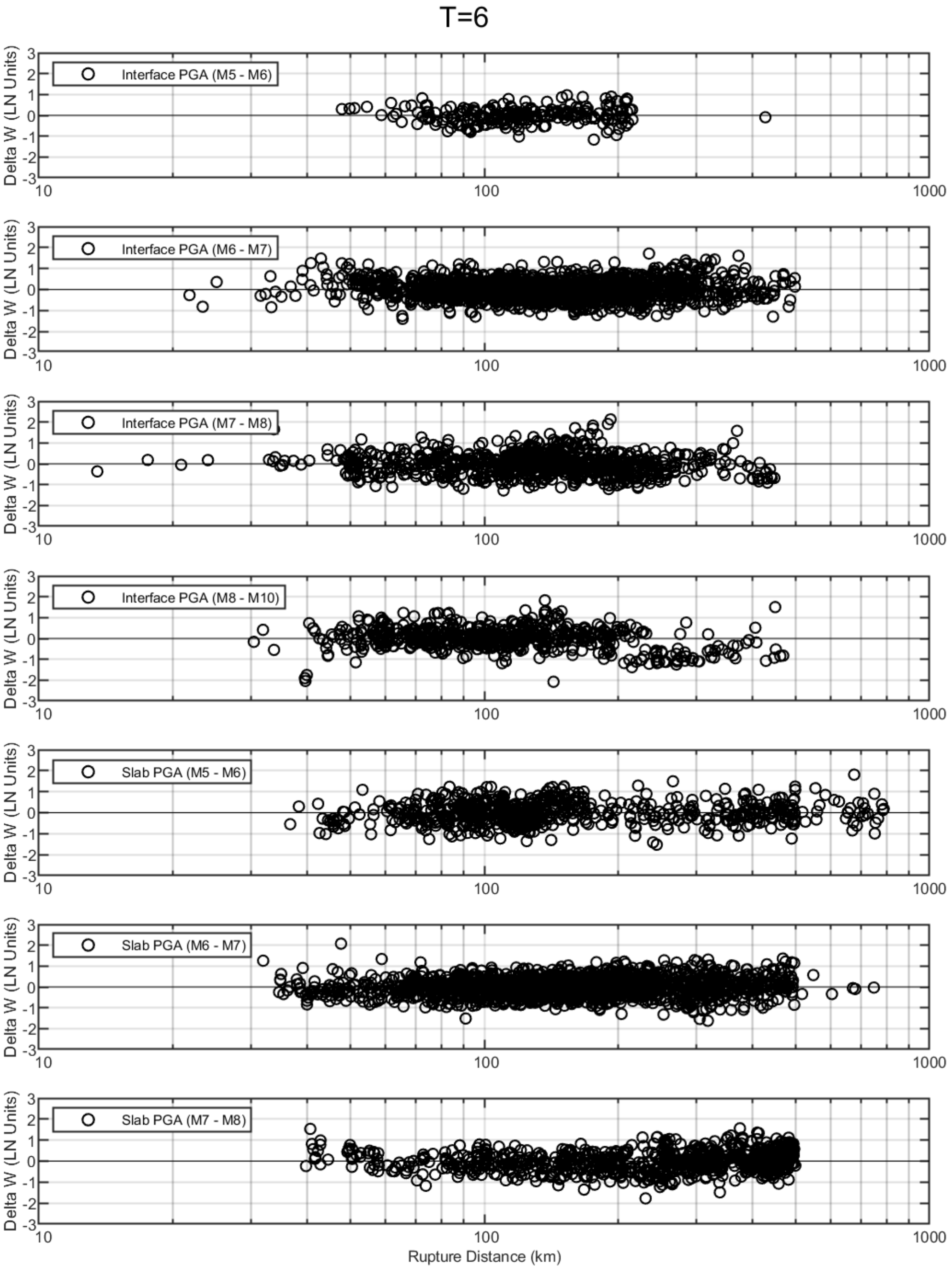

Figure A.58: Within-event residuals versus distance for T = 6.0 sec.

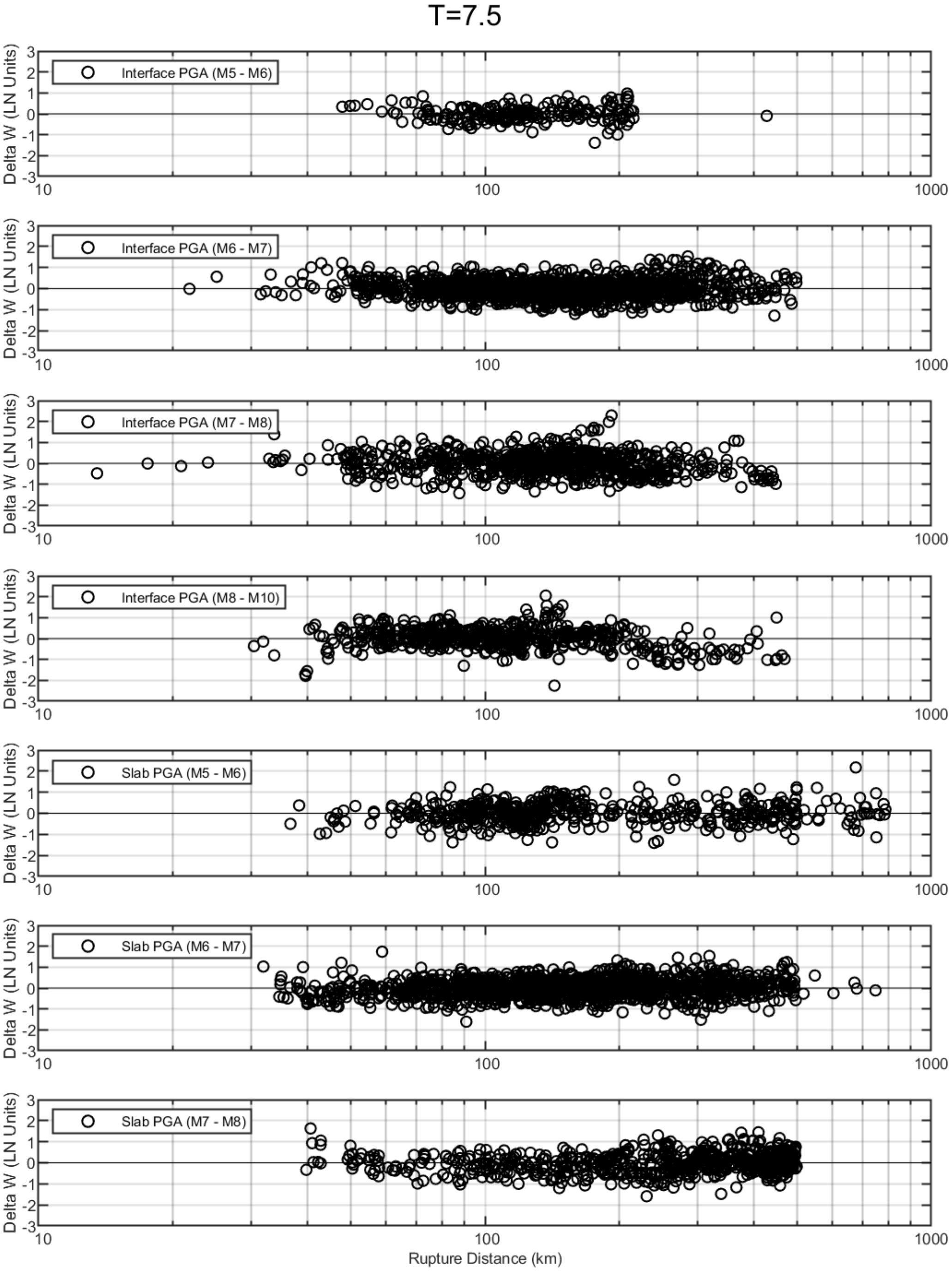

Figure A.59: Within-event residuals versus distance for T = 7.5 sec.

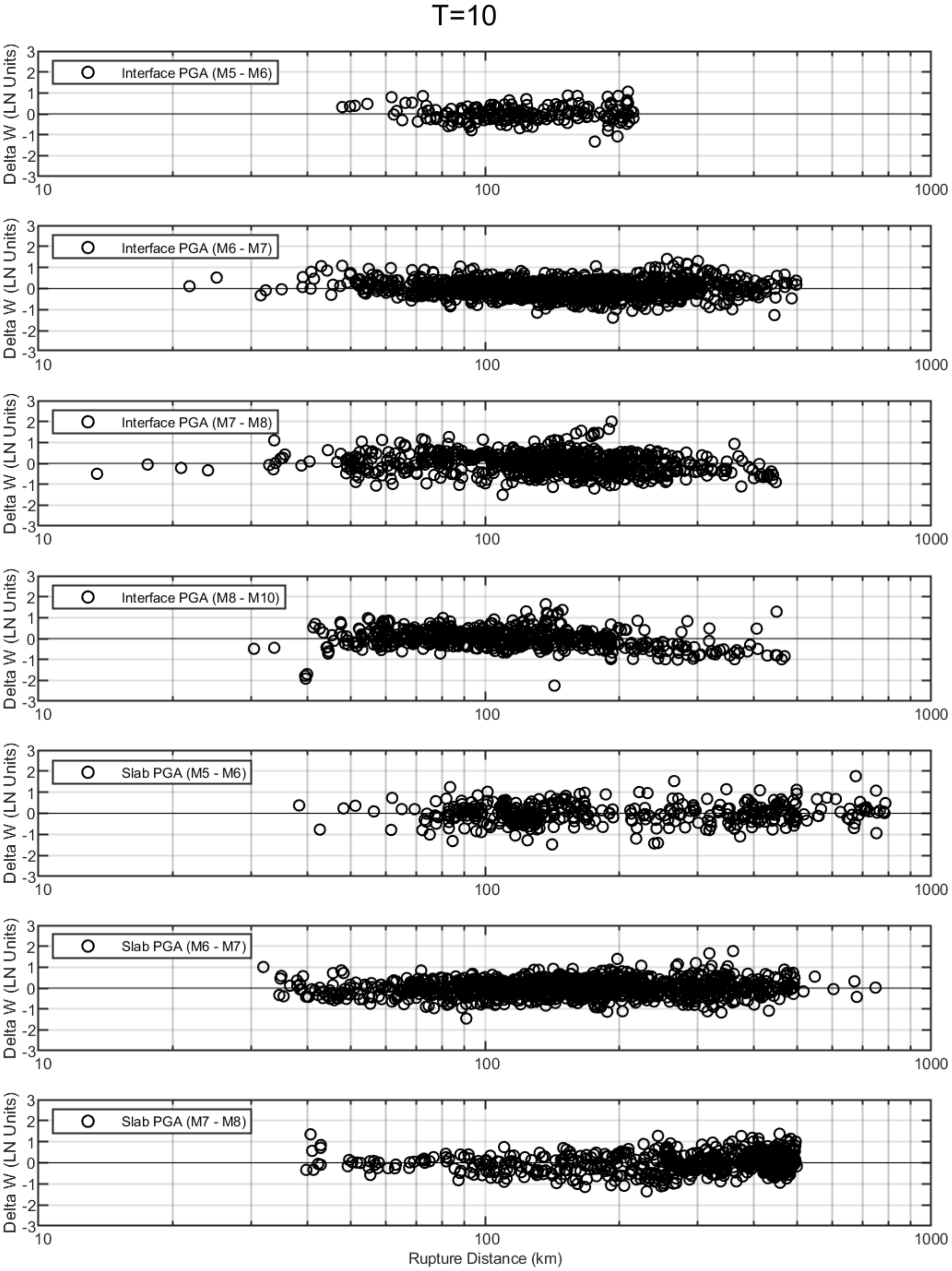

Figure A.60: Within-event residuals versus distance for T = 10.0 sec.

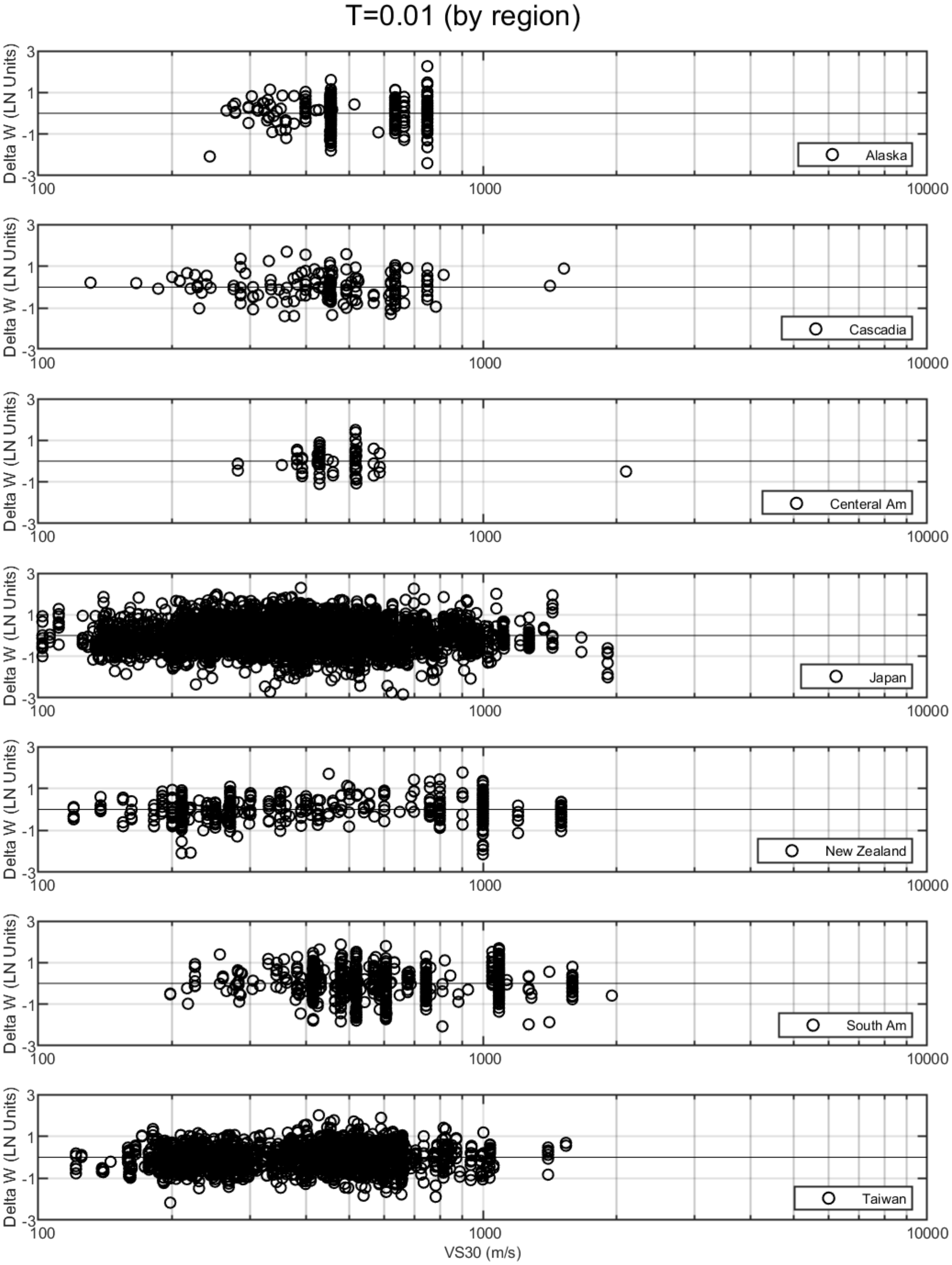

Figure A.61: Within-event residuals versus V_{S30} for T = 0.01 sec.

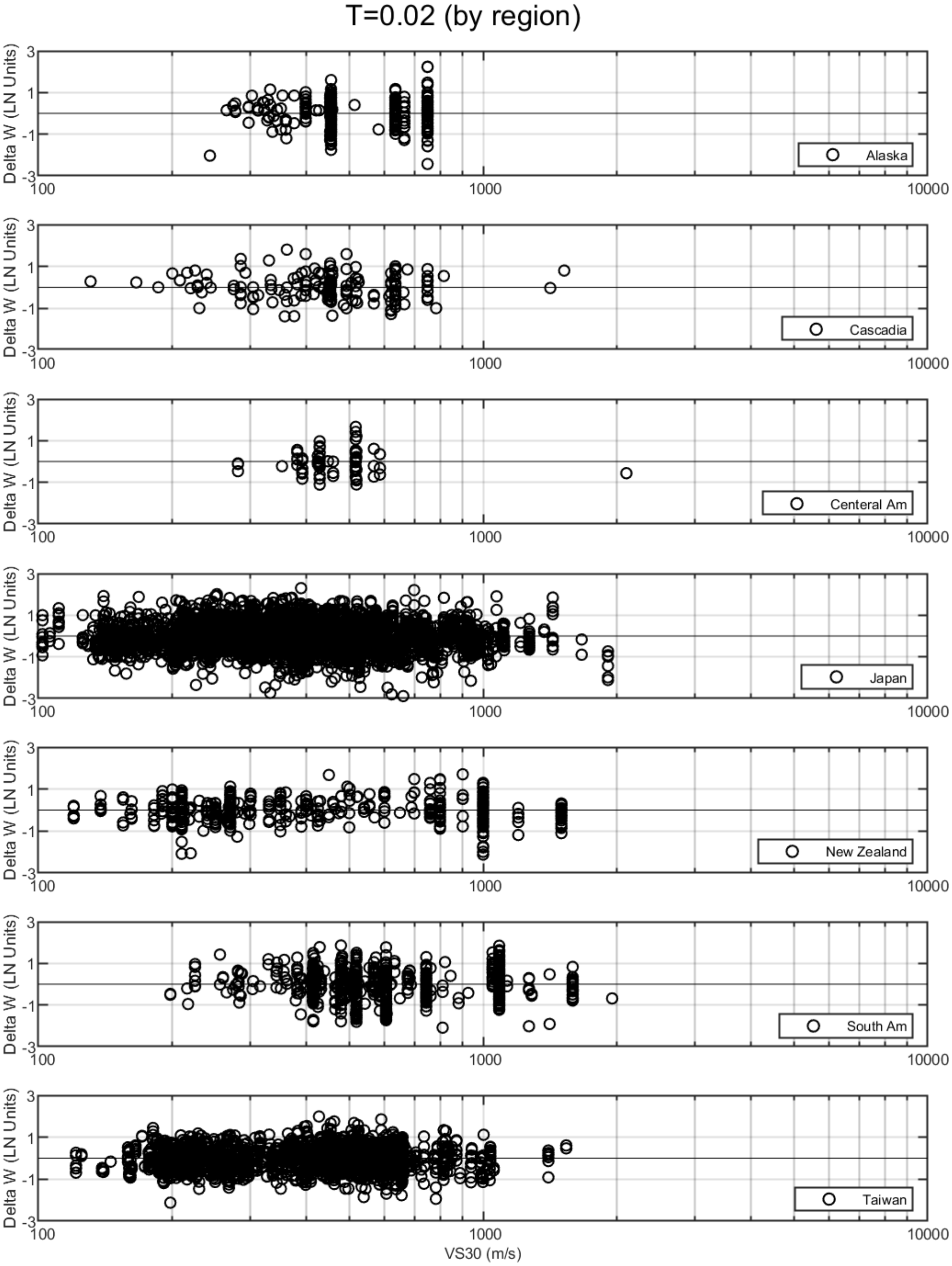

Figure A.62: Within-event residuals versus V_{S30} for T = 0.02 sec.

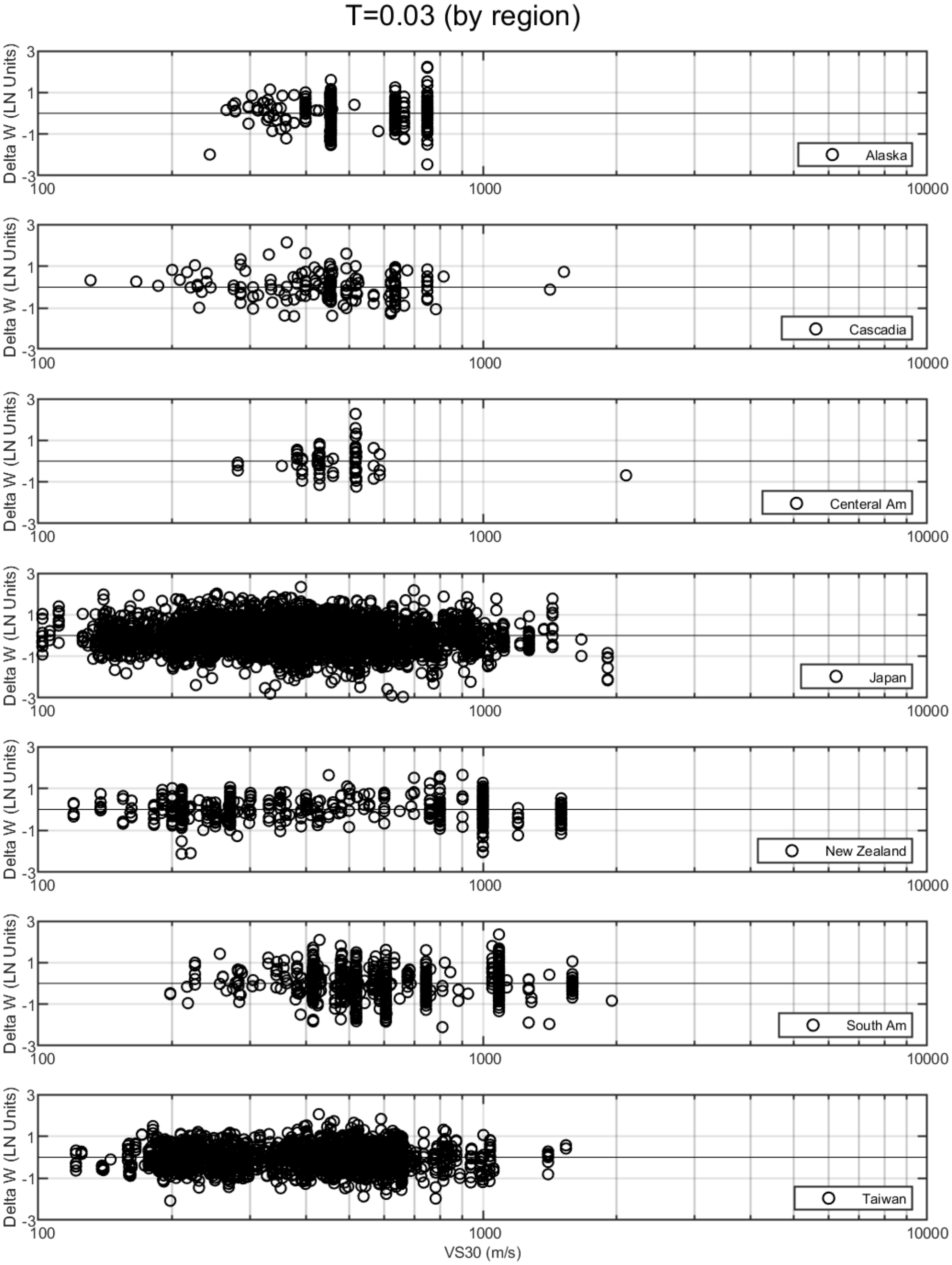

Figure A.63: Within-event residuals versus V_{S30} for T = 0.03 sec.

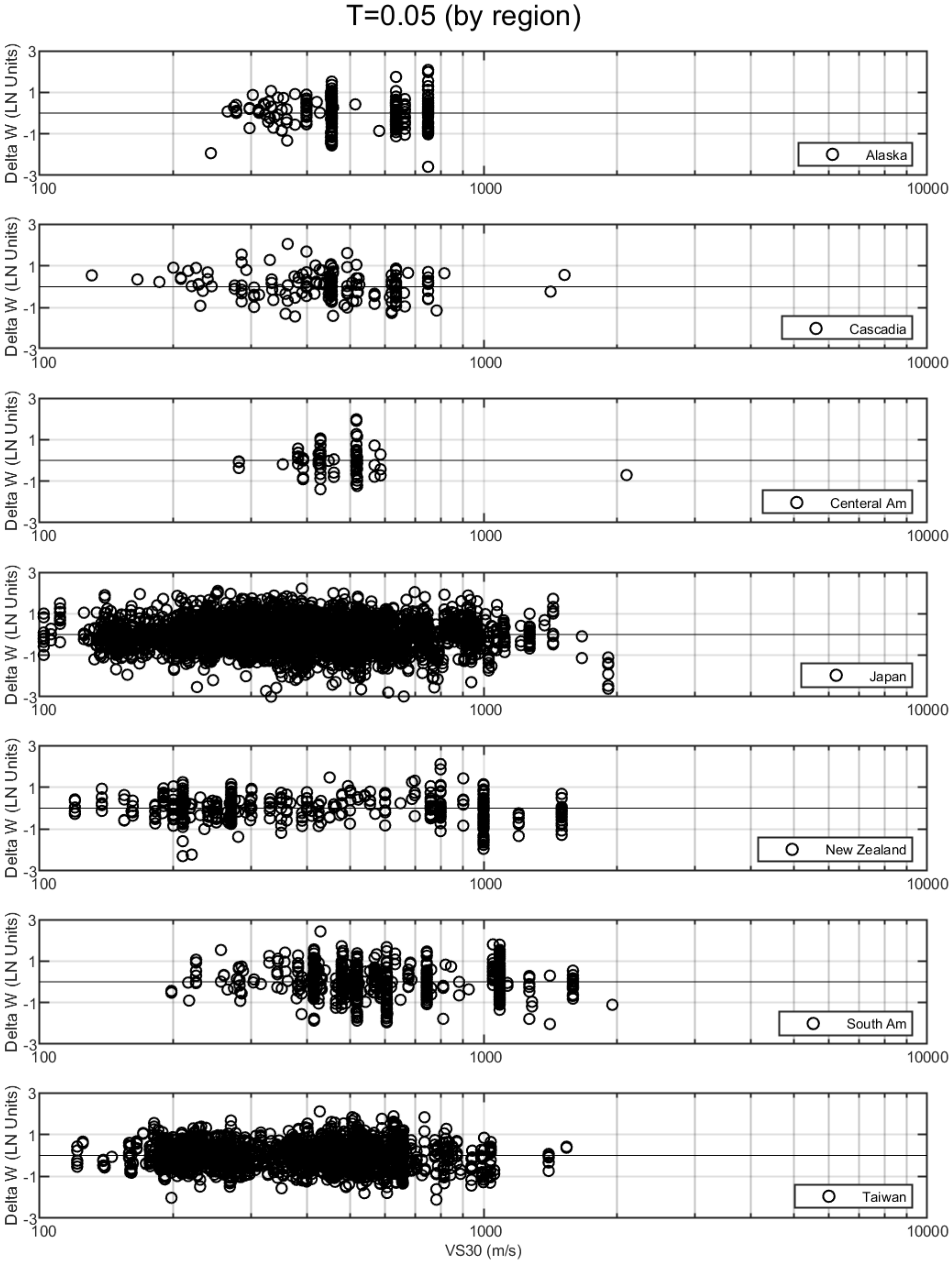

Figure A.64: Within-event residuals versus V_{S30} for T = 0.05 sec.

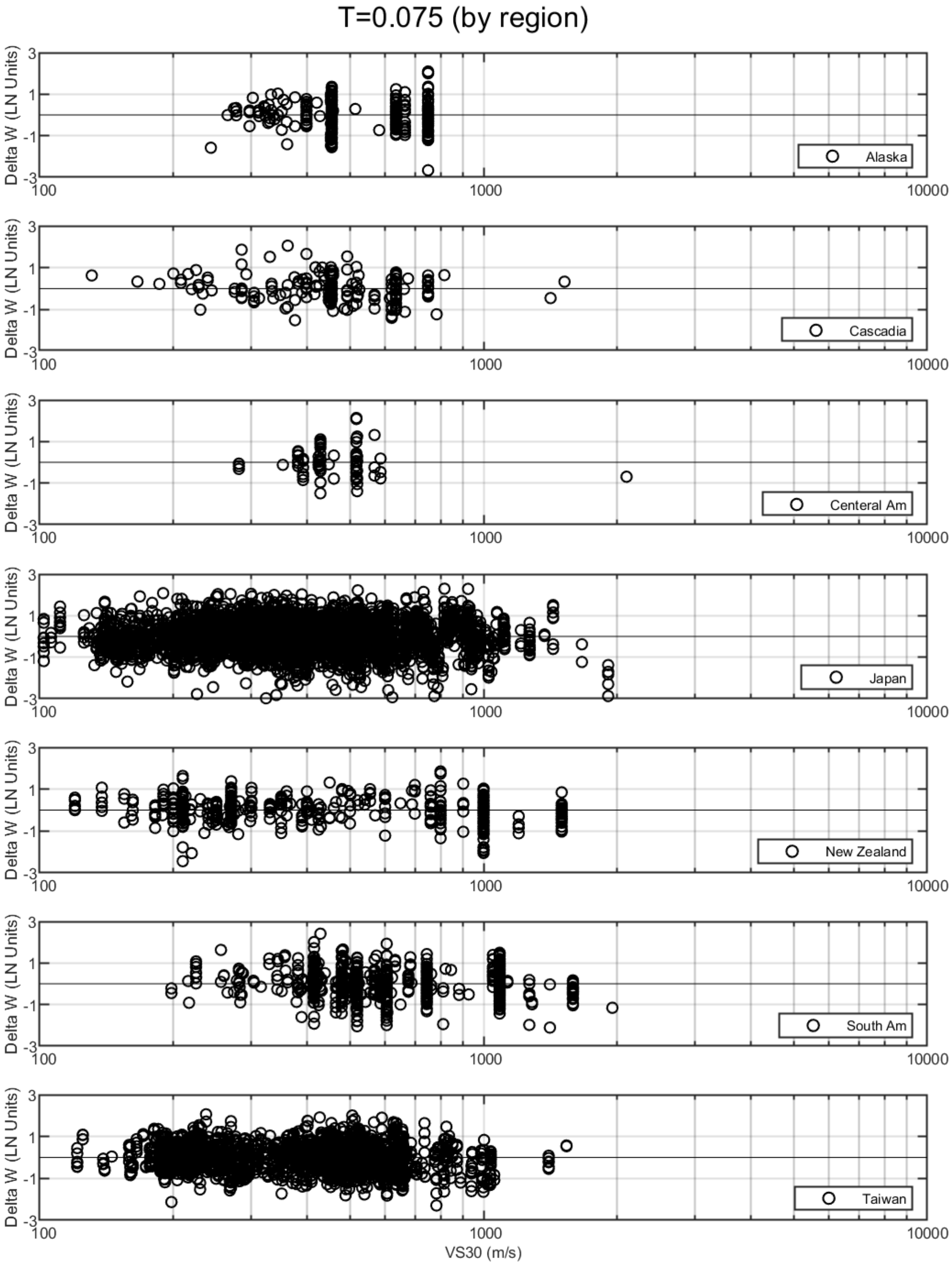

Figure A.65: Within-event residuals versus V_{S30} for T=0.075 sec.

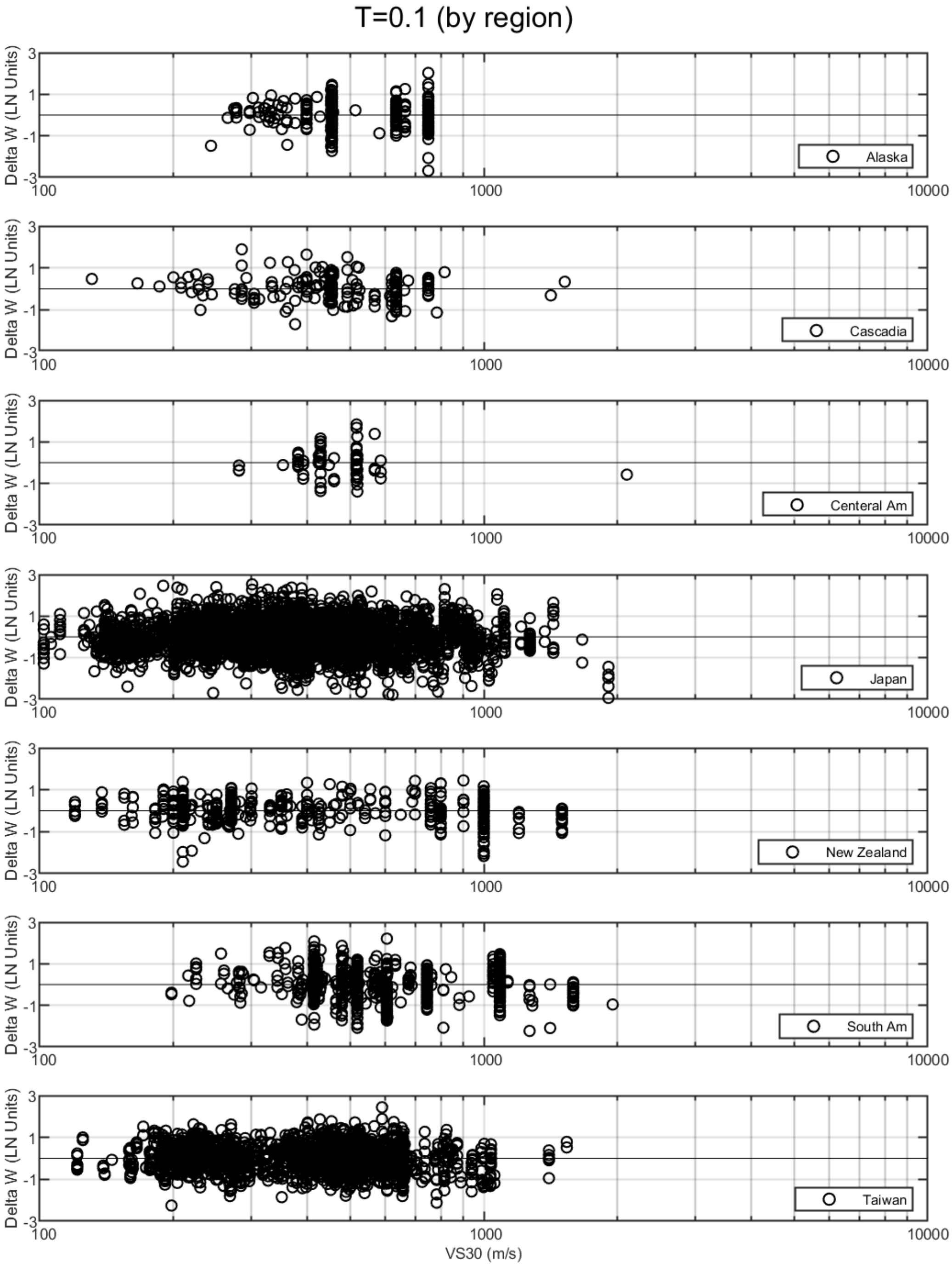

Figure A.66: Within-event residuals versus V_{S30} for T = 0.10 sec.

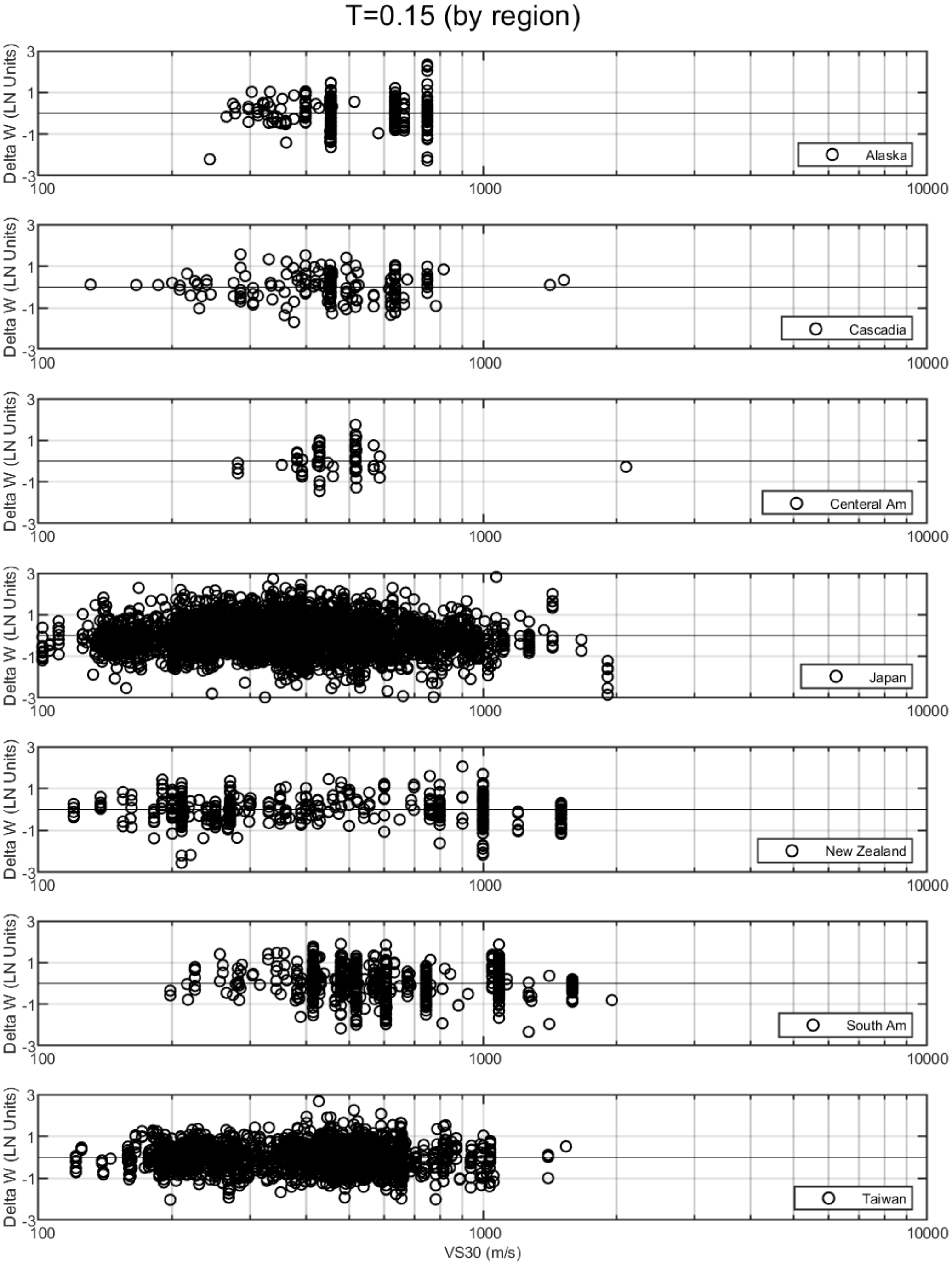

Figure A.67: Within-event residuals versus V_{S30} for T = 0.15 sec.

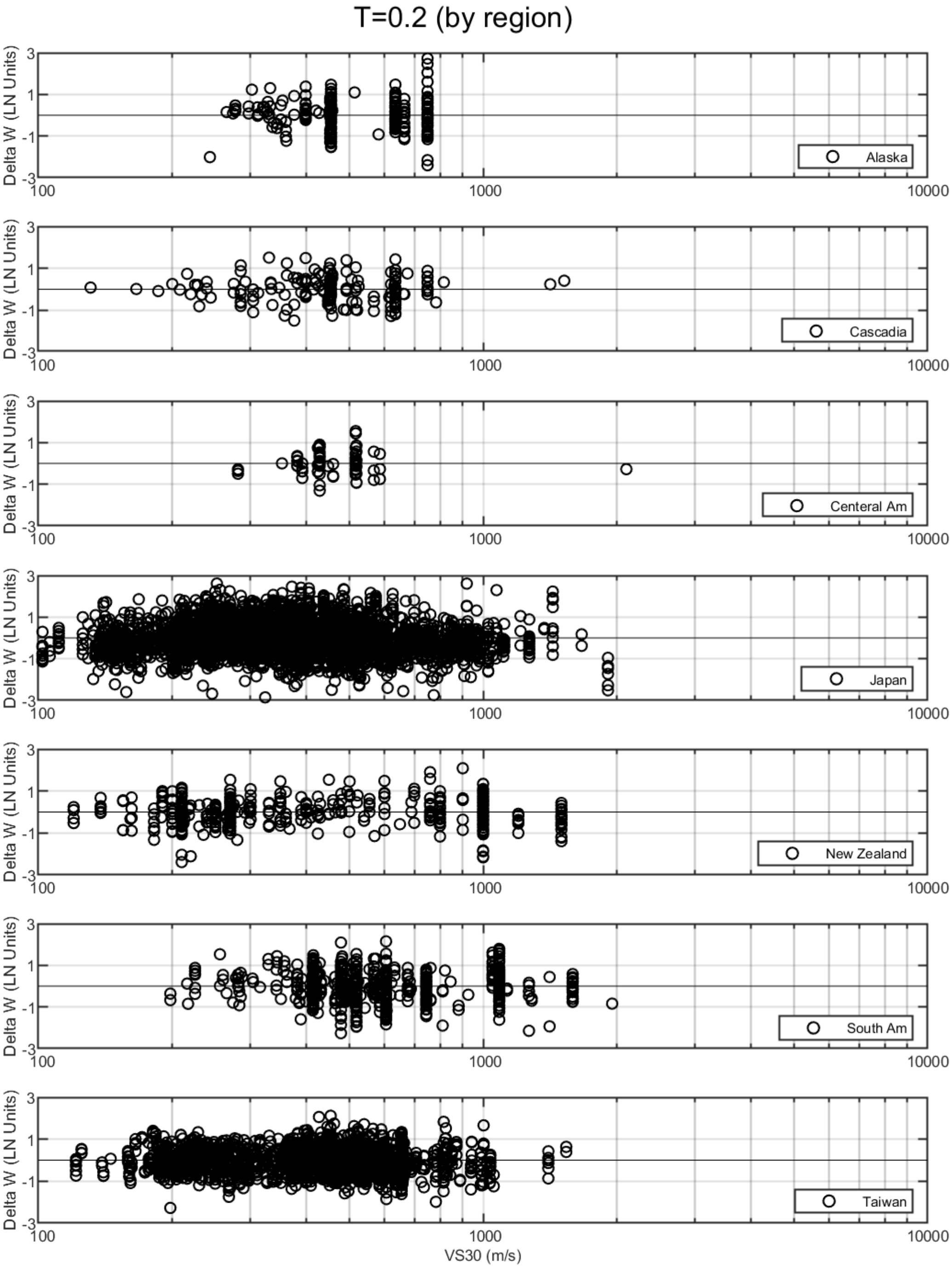

Figure A.68: Within-event residuals versus V_{S30} for T = 0.20 sec.

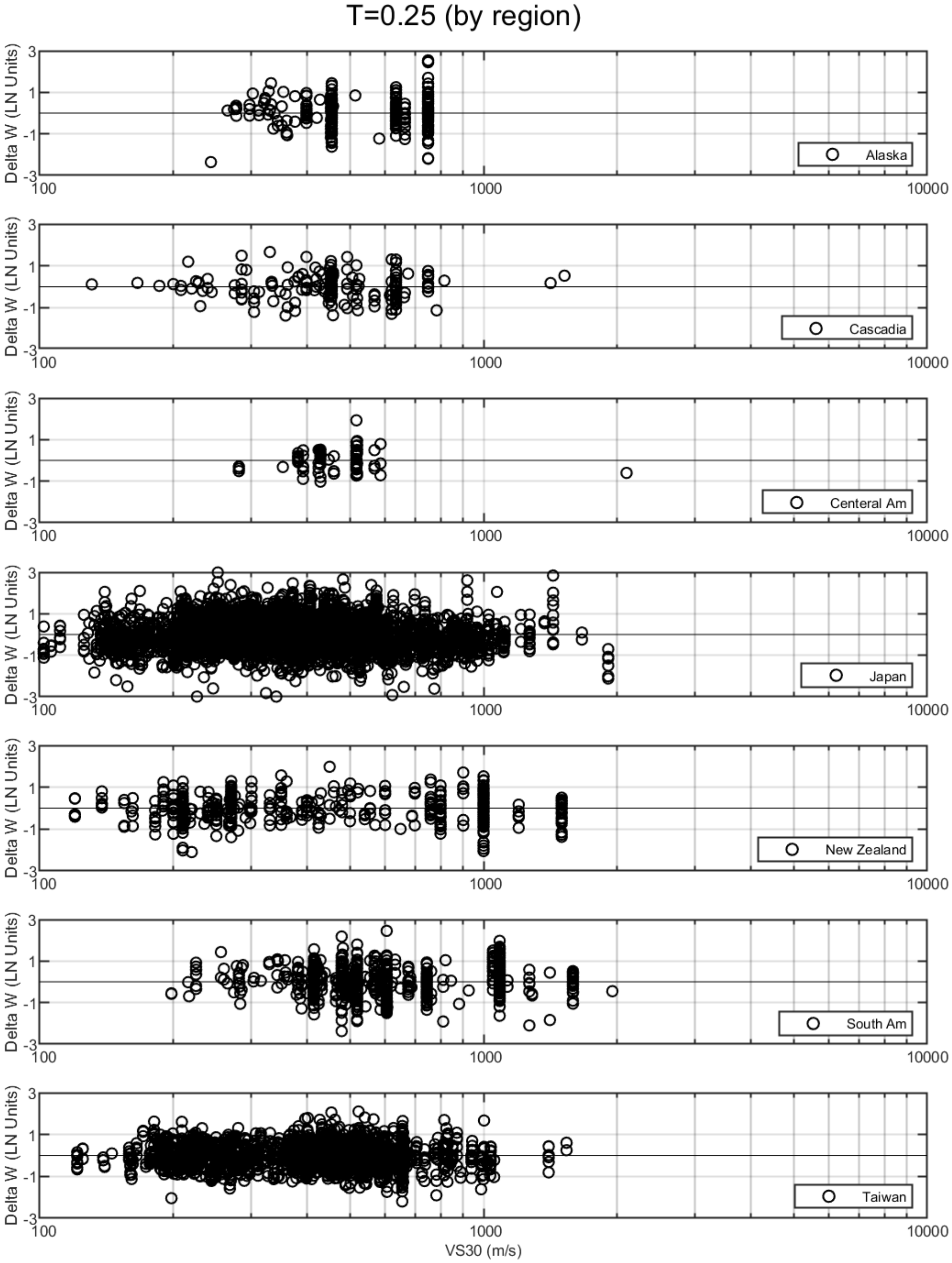

Figure A.69: Within-event residuals versus V_{S30} for T = 0.25 sec.

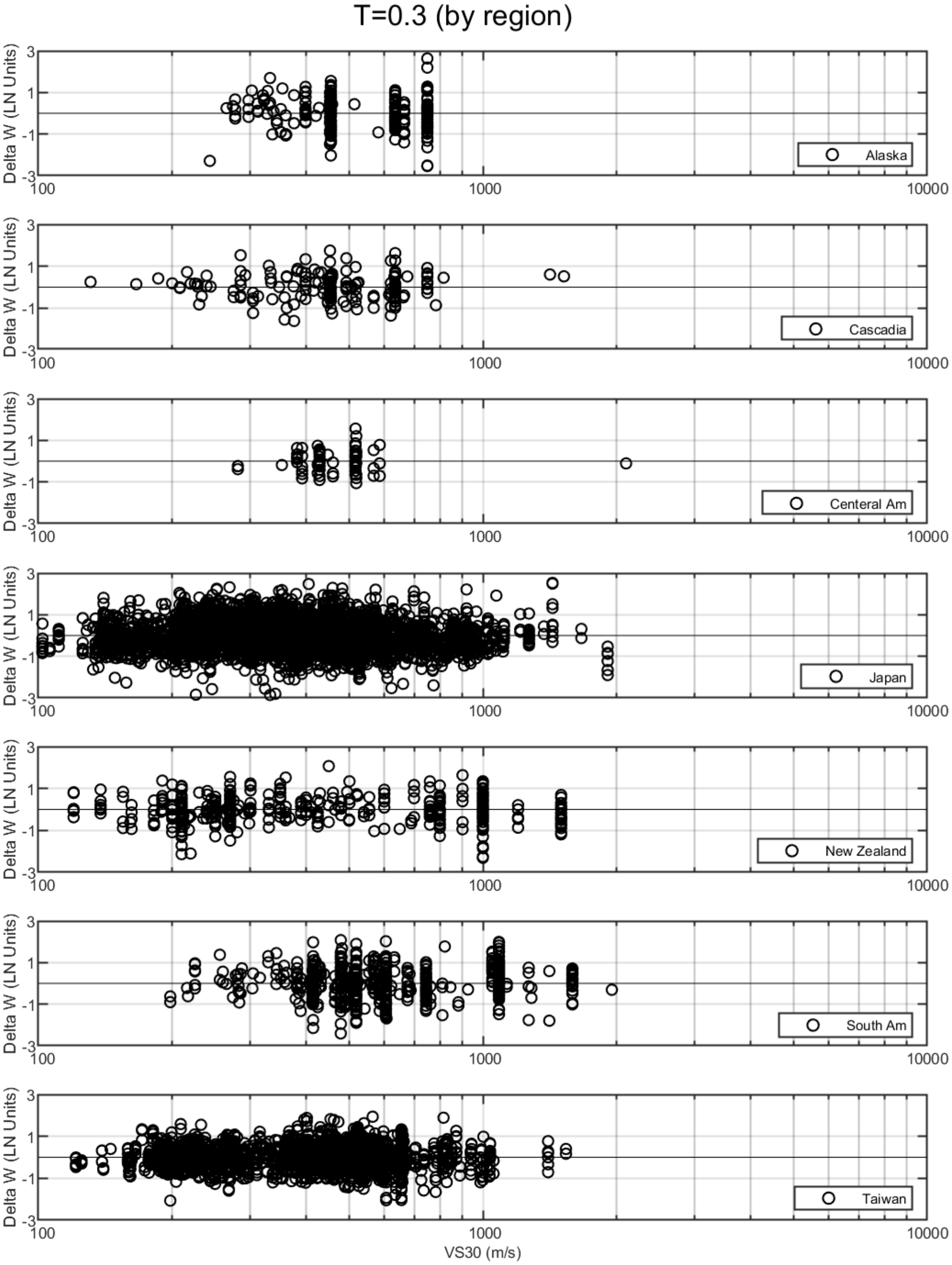

Figure A.70: Within-event residuals versus V_{S30} for T = 0.30 sec.

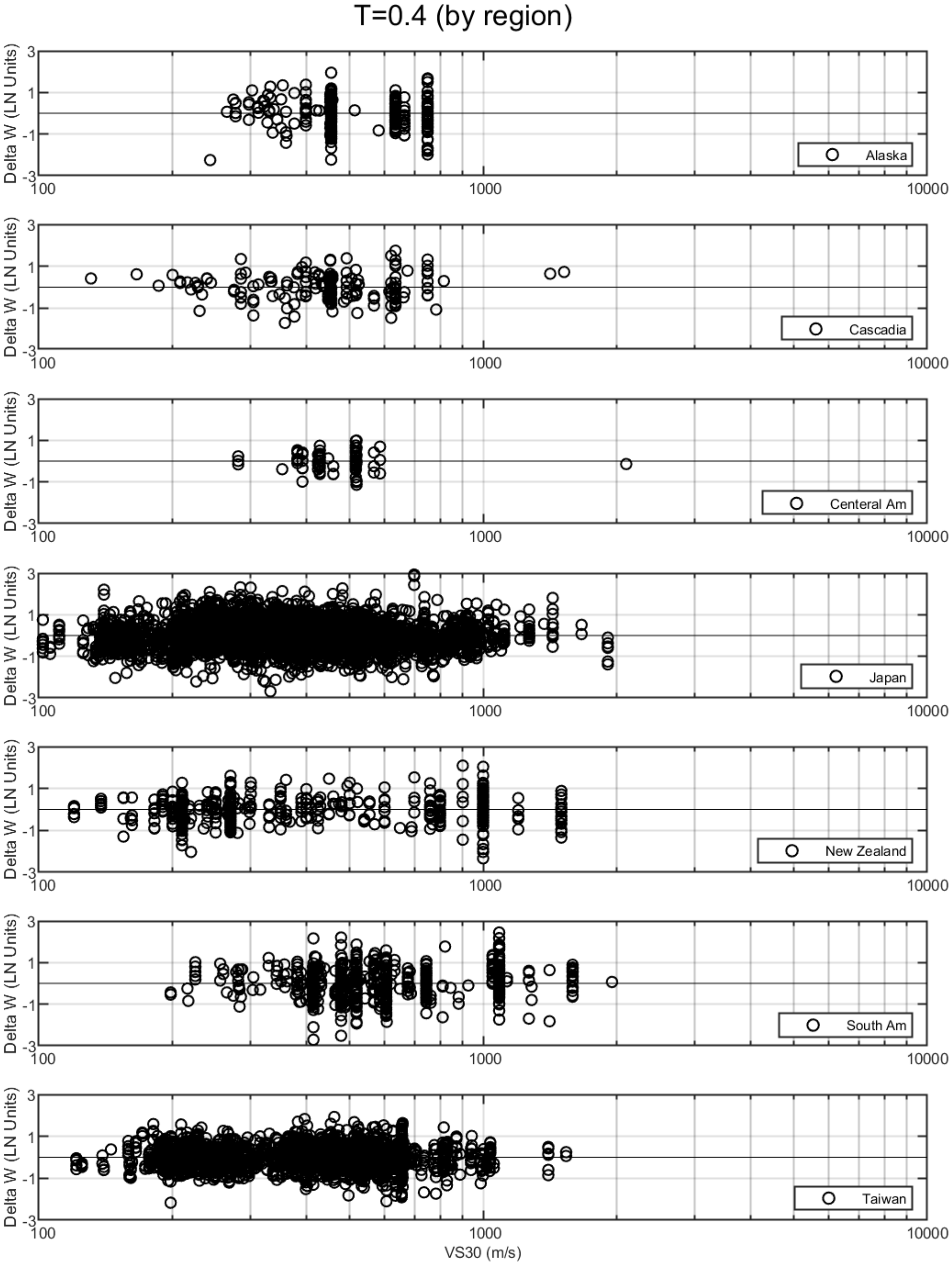

Figure A.71: Within-event residuals versus V_{S30} for T = 0.40 sec.

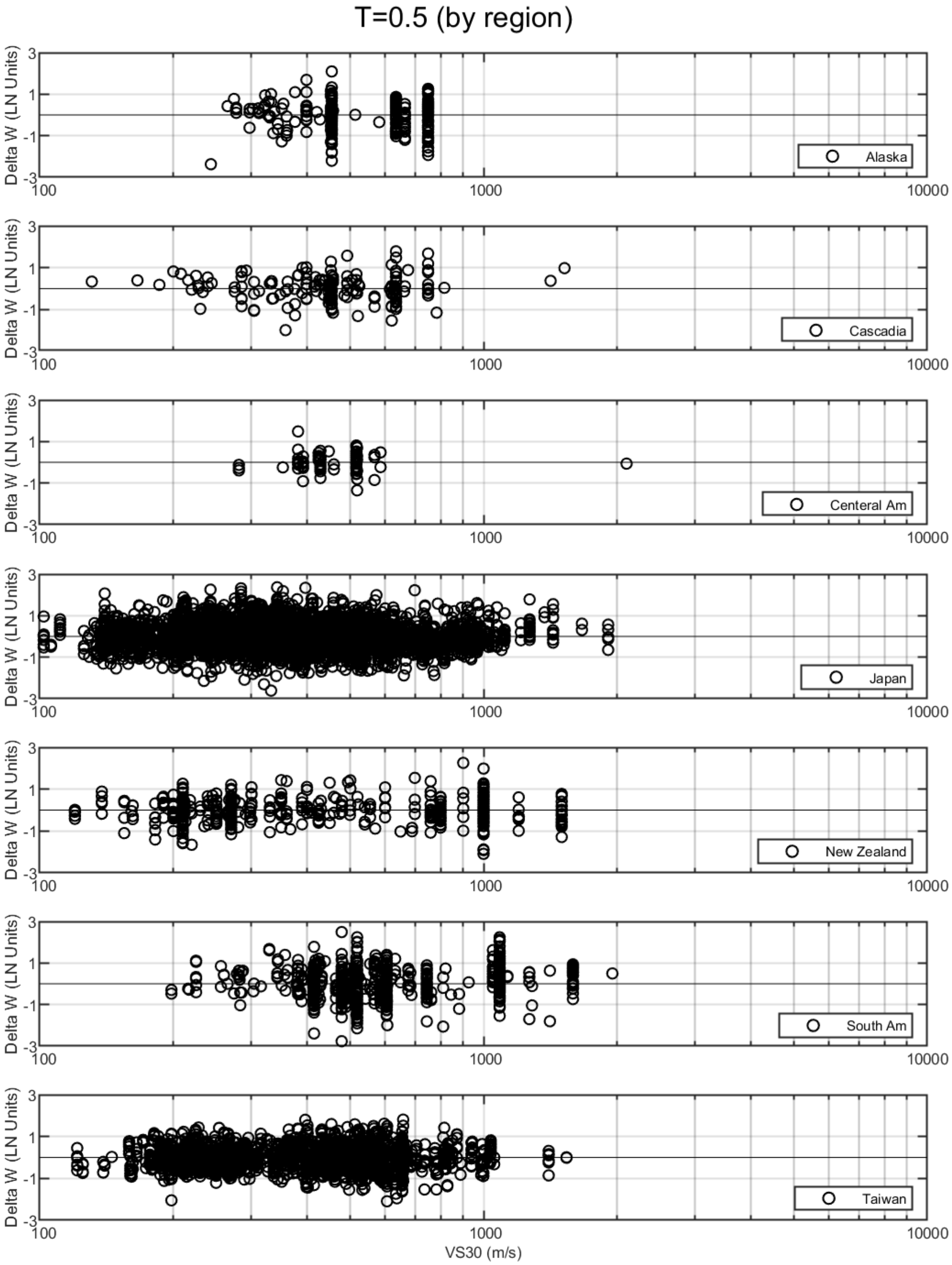

Figure A.72: Within-event residuals versus V_{S30} for T = 0.5 sec.

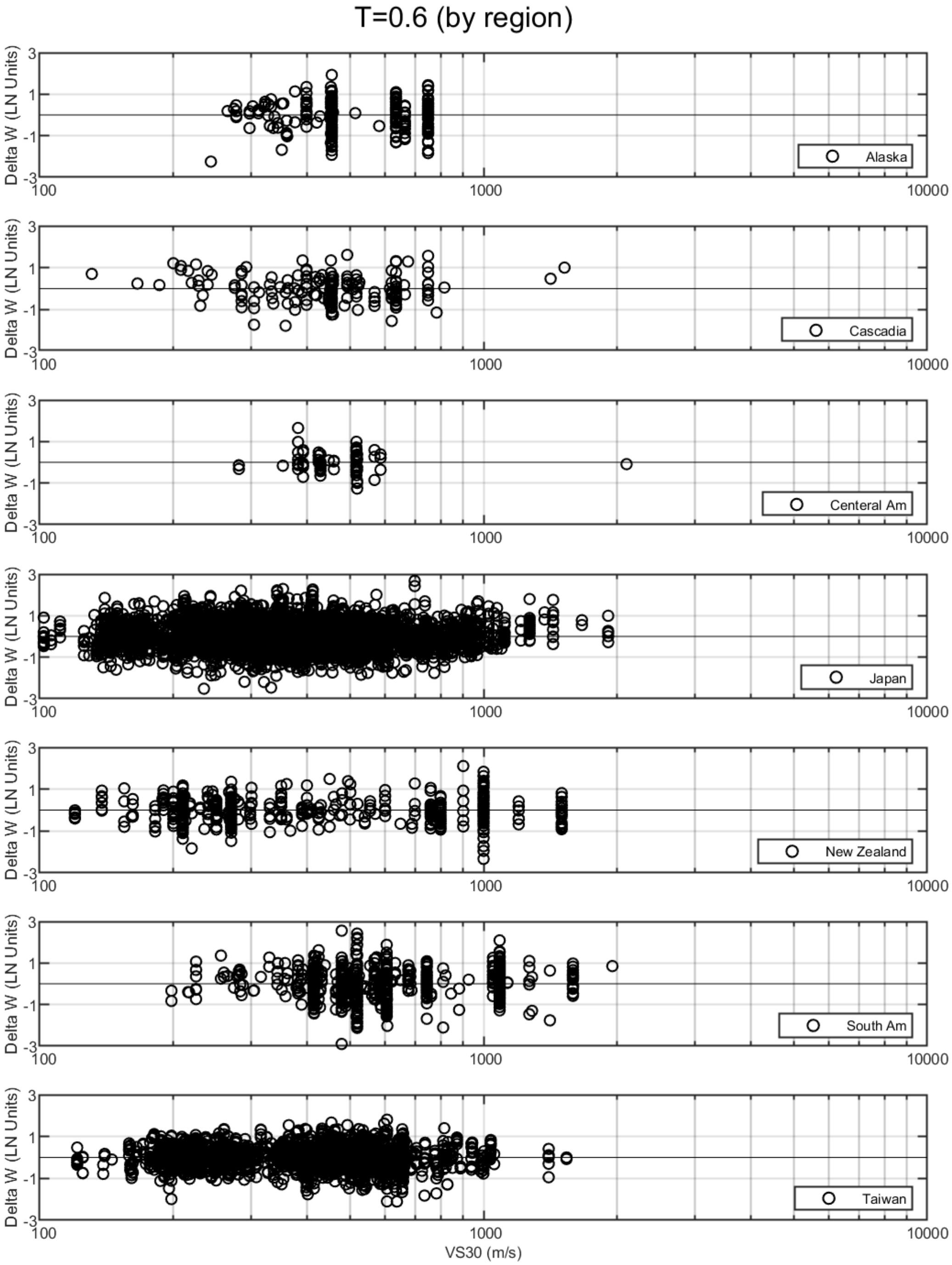

Figure A.73: Within-event residuals versus V_{S30} for T = 0.6 sec.

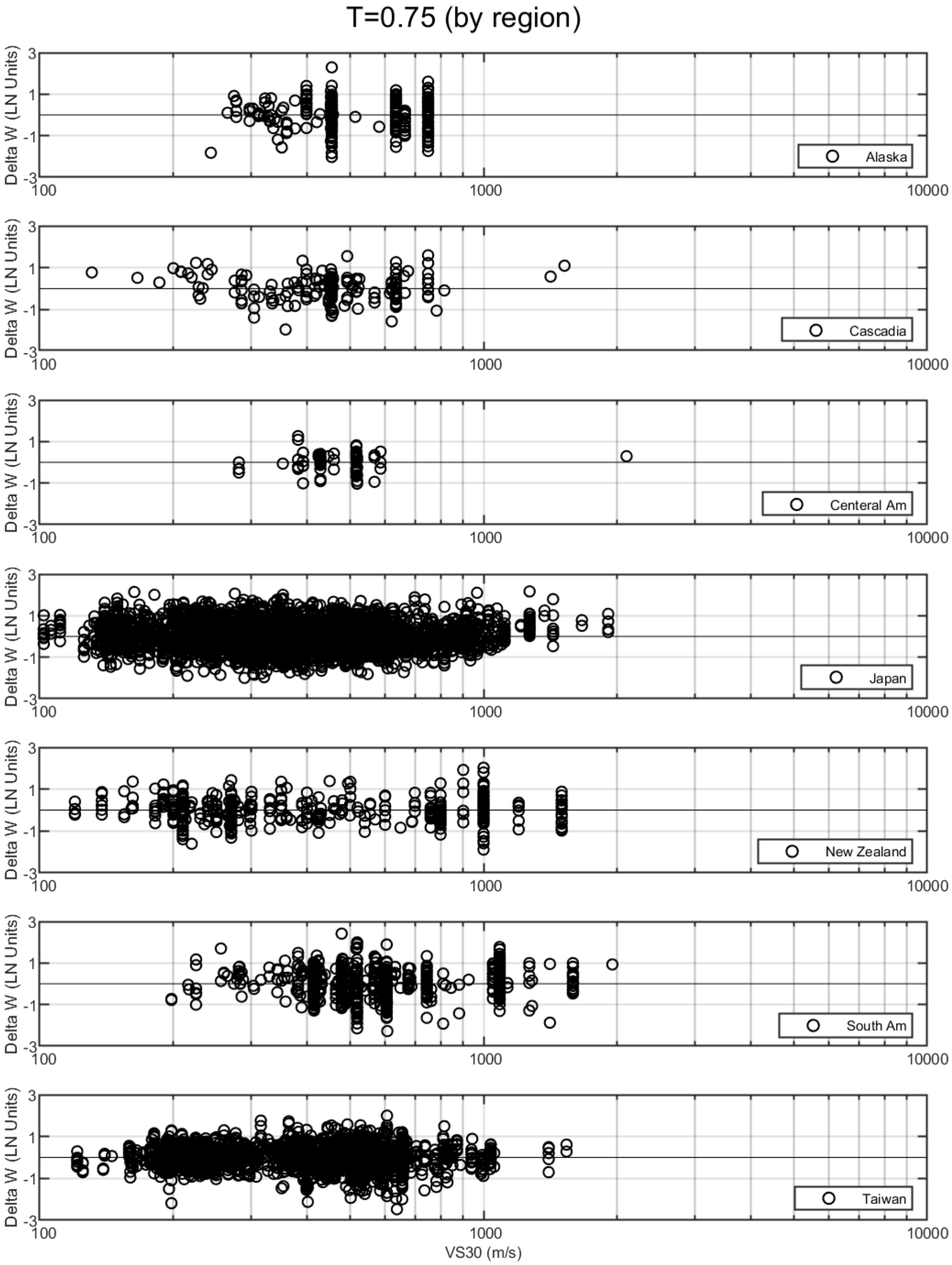

Figure A.74: Within-event residuals versus V_{S30} for TT = 0.75 sec.

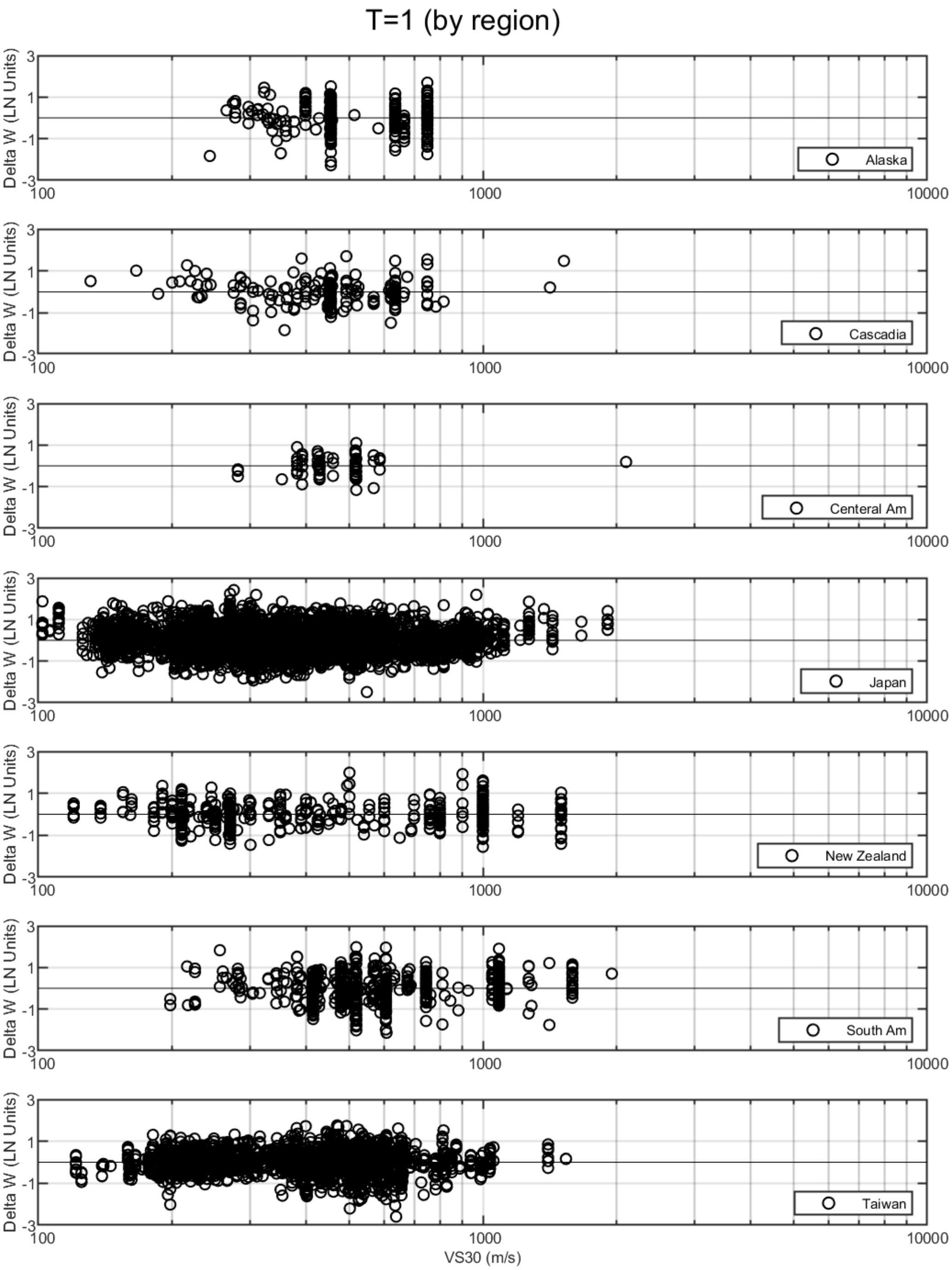

Figure A.75: Within-event residuals versus V_{S30} for T = 1.0 sec.

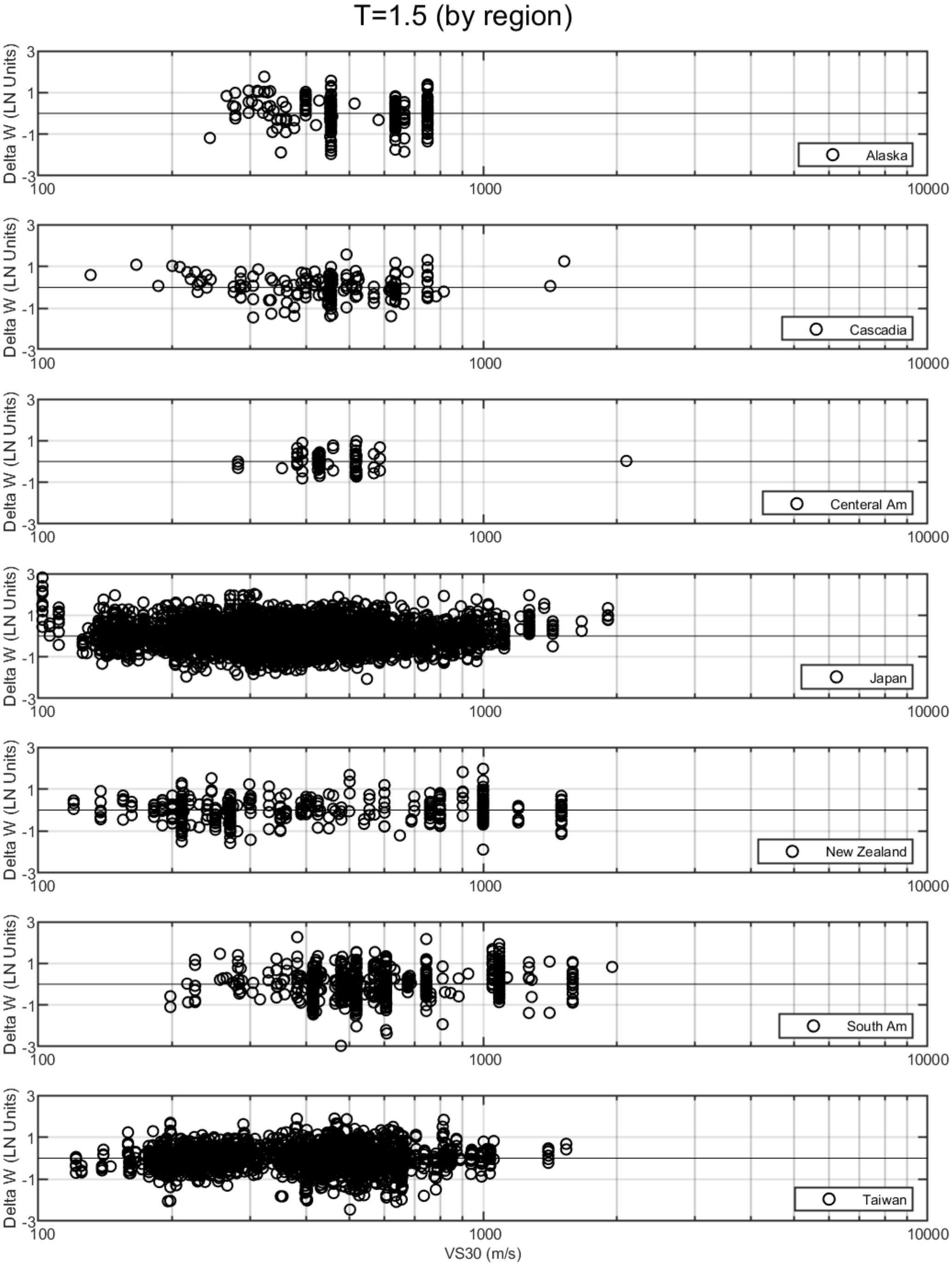

Figure A.76: Within-event residuals versus V_{S30} for T = 1.5 sec.

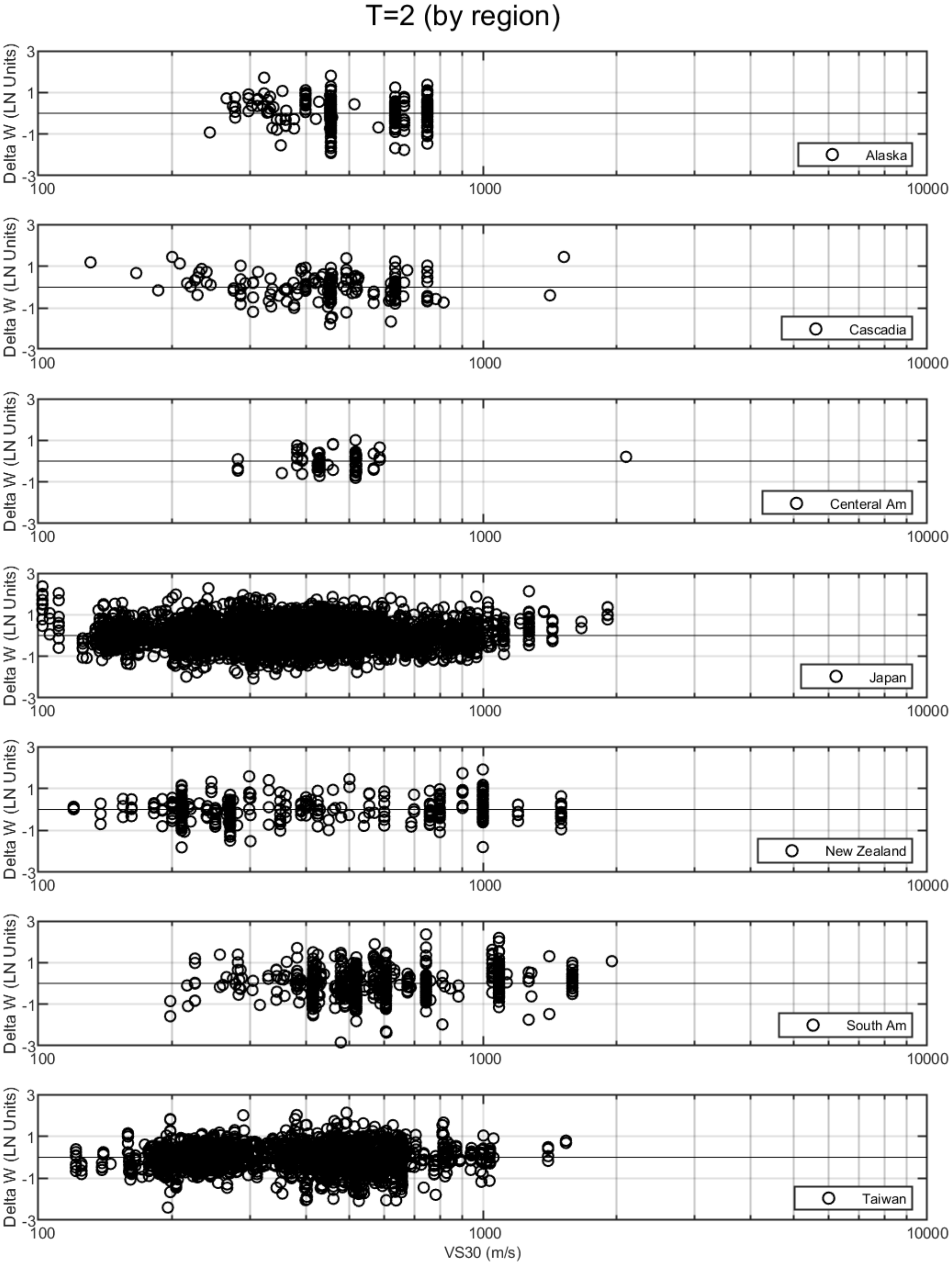

Figure A.77: Within-event residuals versus V_{S30} for T = 2.0 sec.

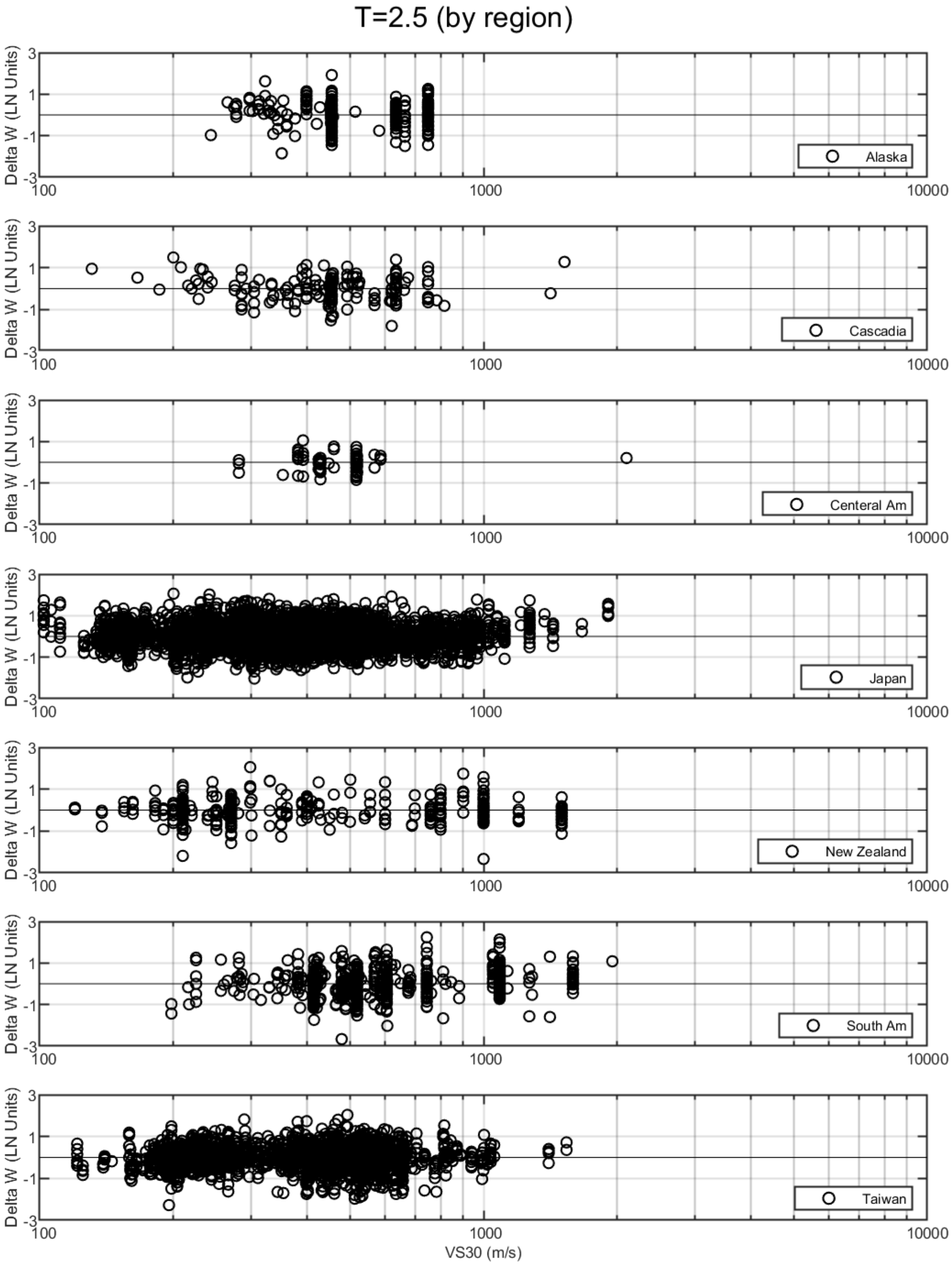

Figure A.78: Within-event residuals versus V_{S30} for T = 2.5 sec.

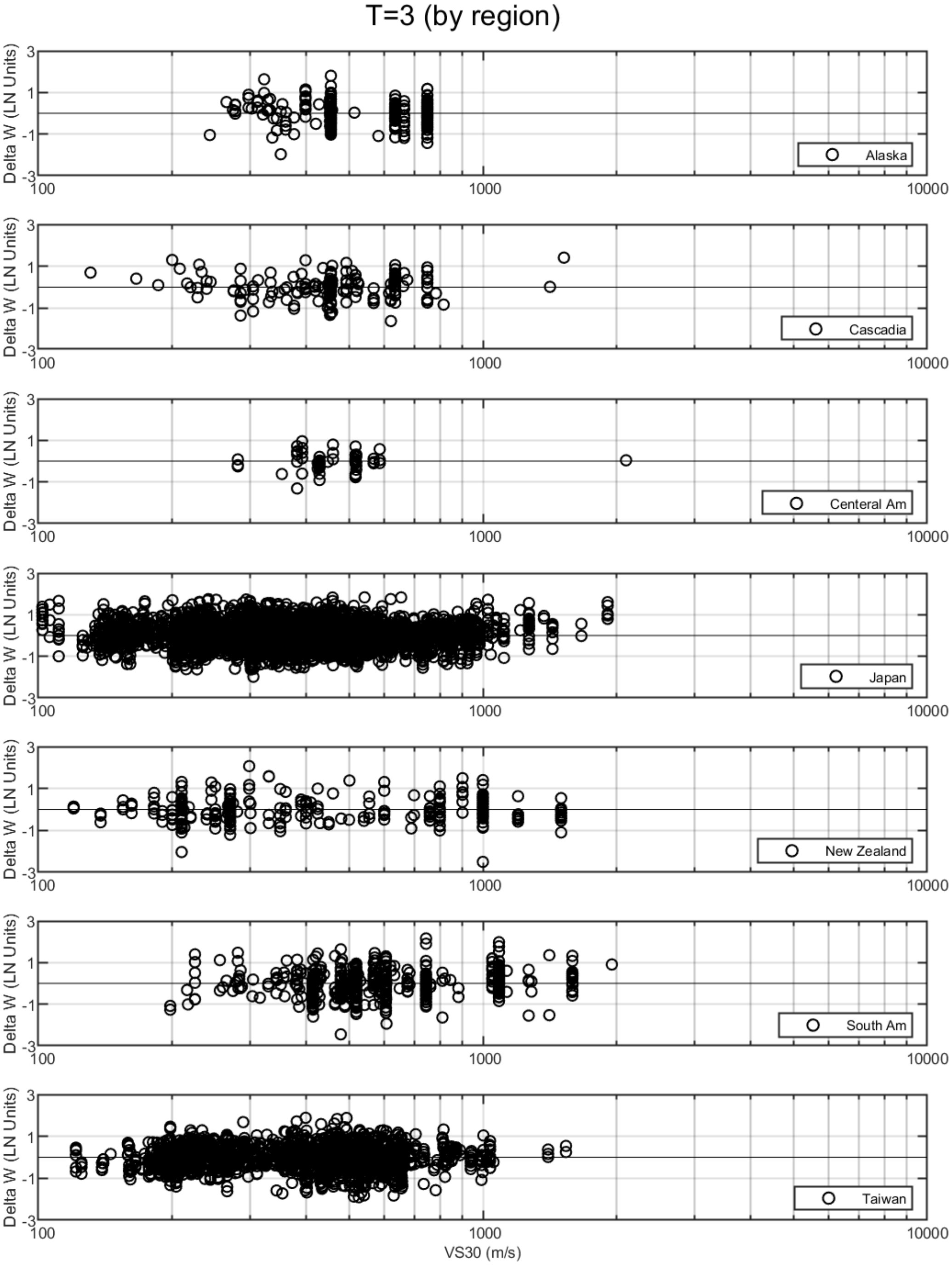

Figure A.79: Within-event residuals versus V_{S30} for T = 3.0 sec.

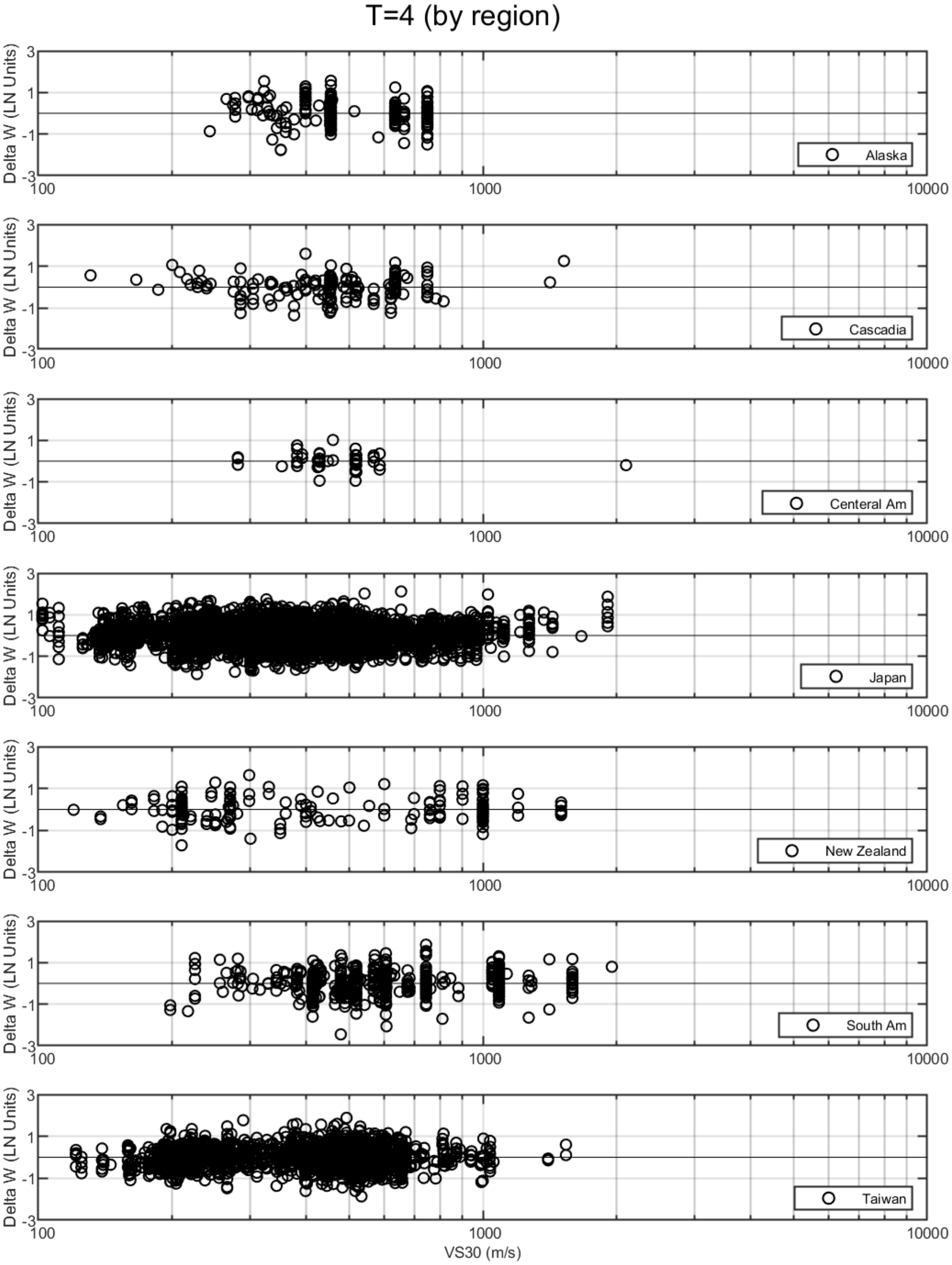

Figure A.80: Within-event residuals versus V_{S30} for T = 4.0 sec.

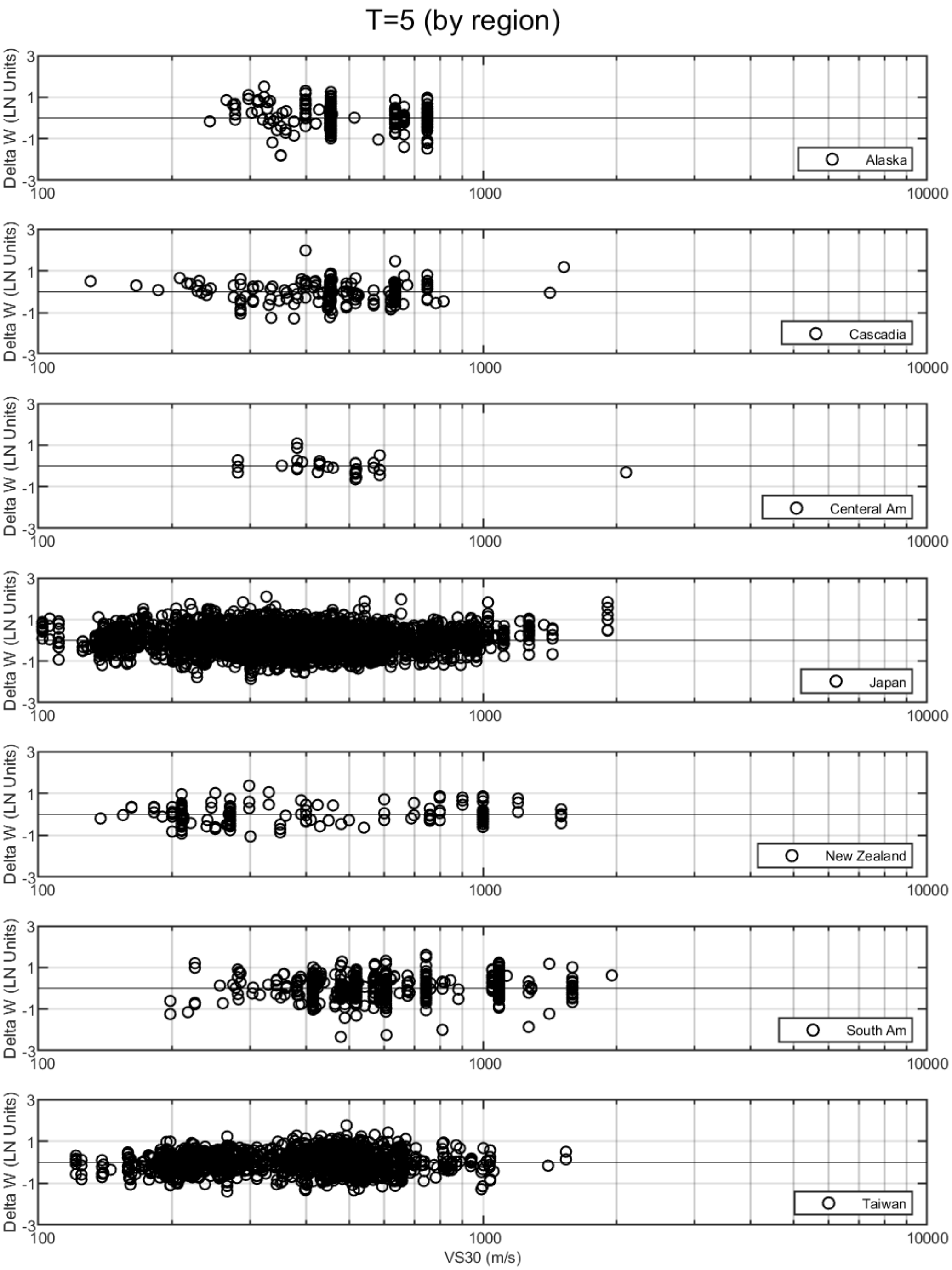

Figure A.81: Within-event residuals versus V_{S30} for T = 5.0 sec.

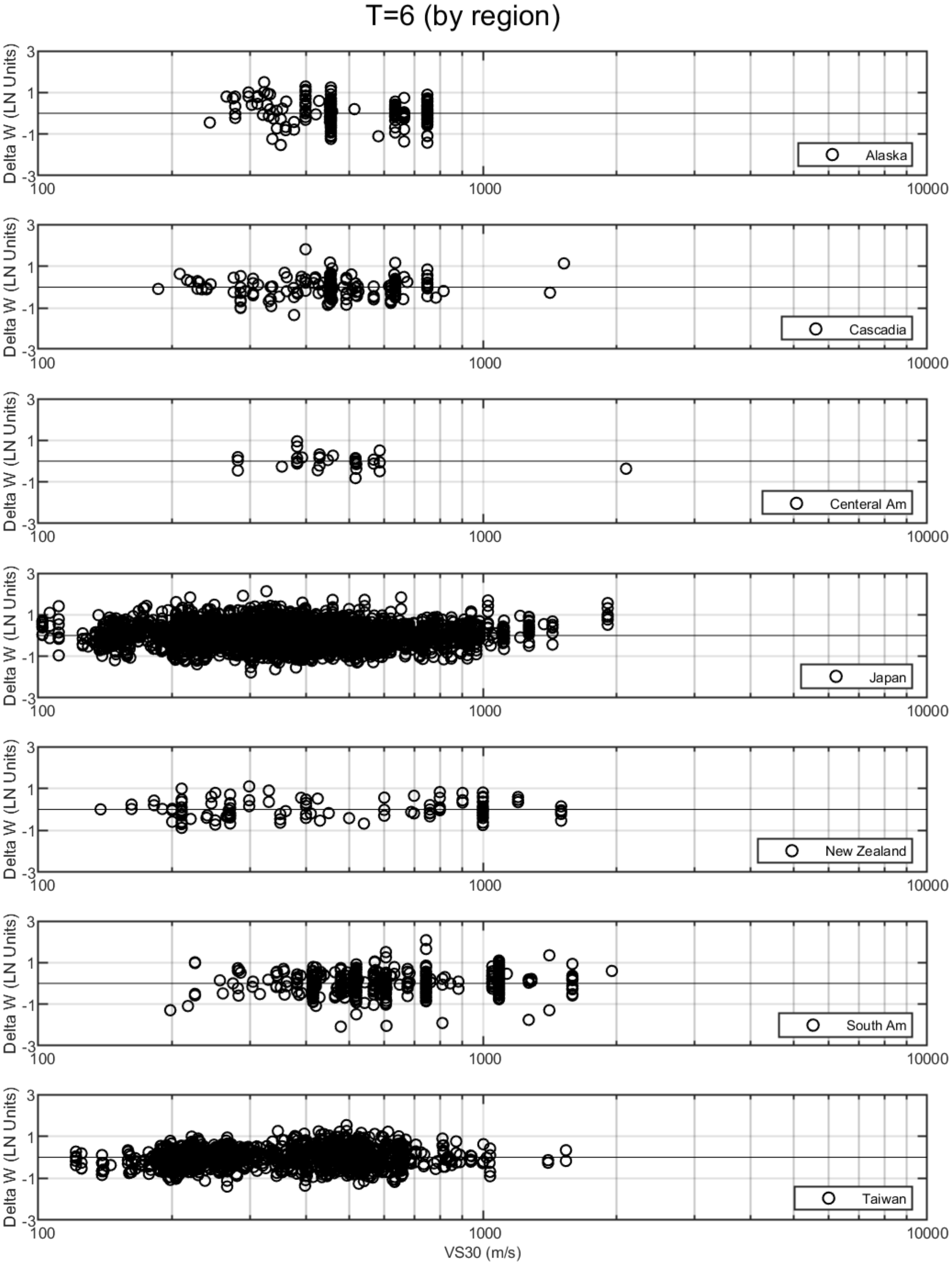

Figure A.82: Within-event residuals versus V_{S30} for T = 6.0 sec.

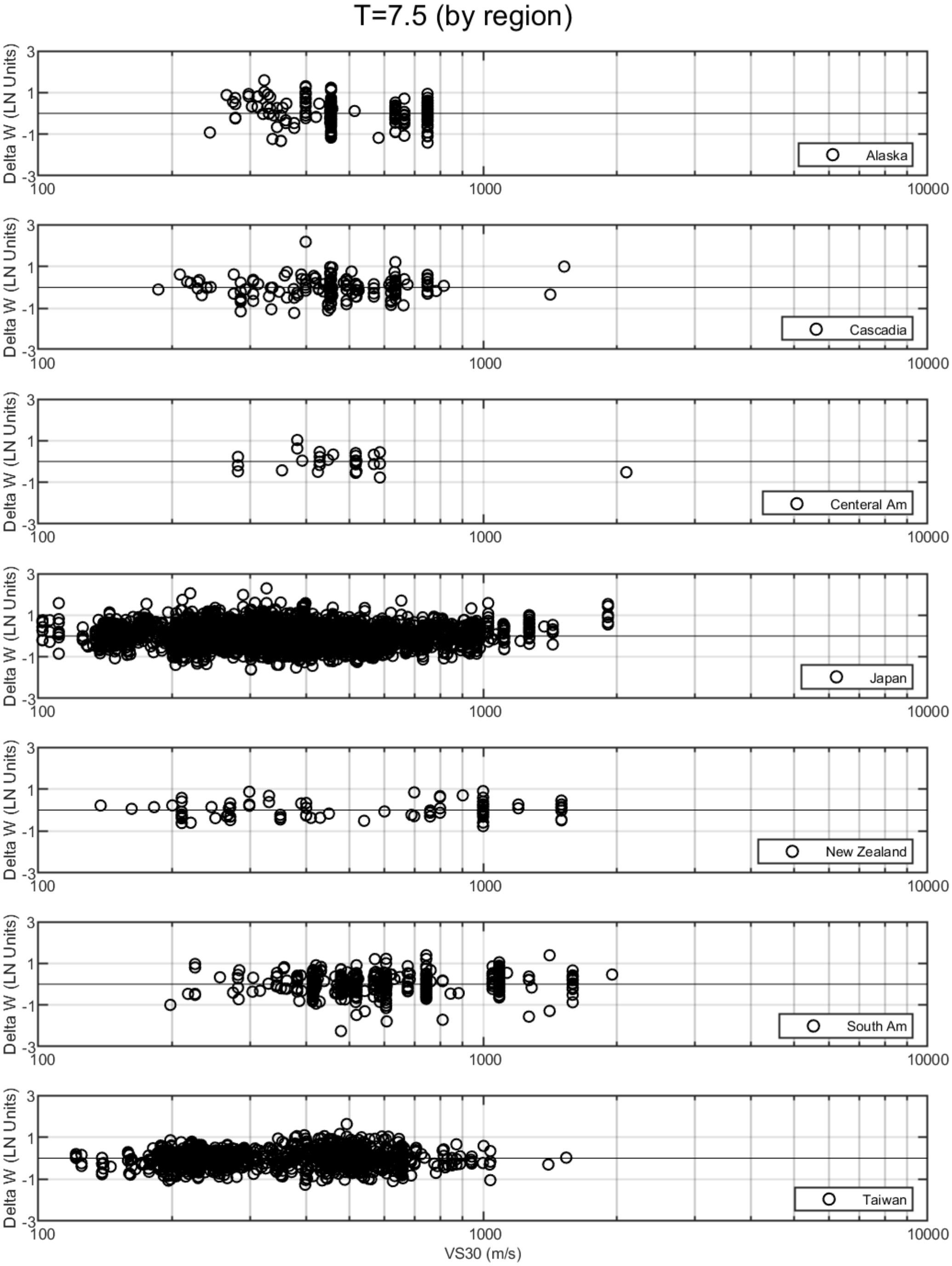

Figure A.83: Within-event residuals versus V_{S30} for T = 7.5 sec.

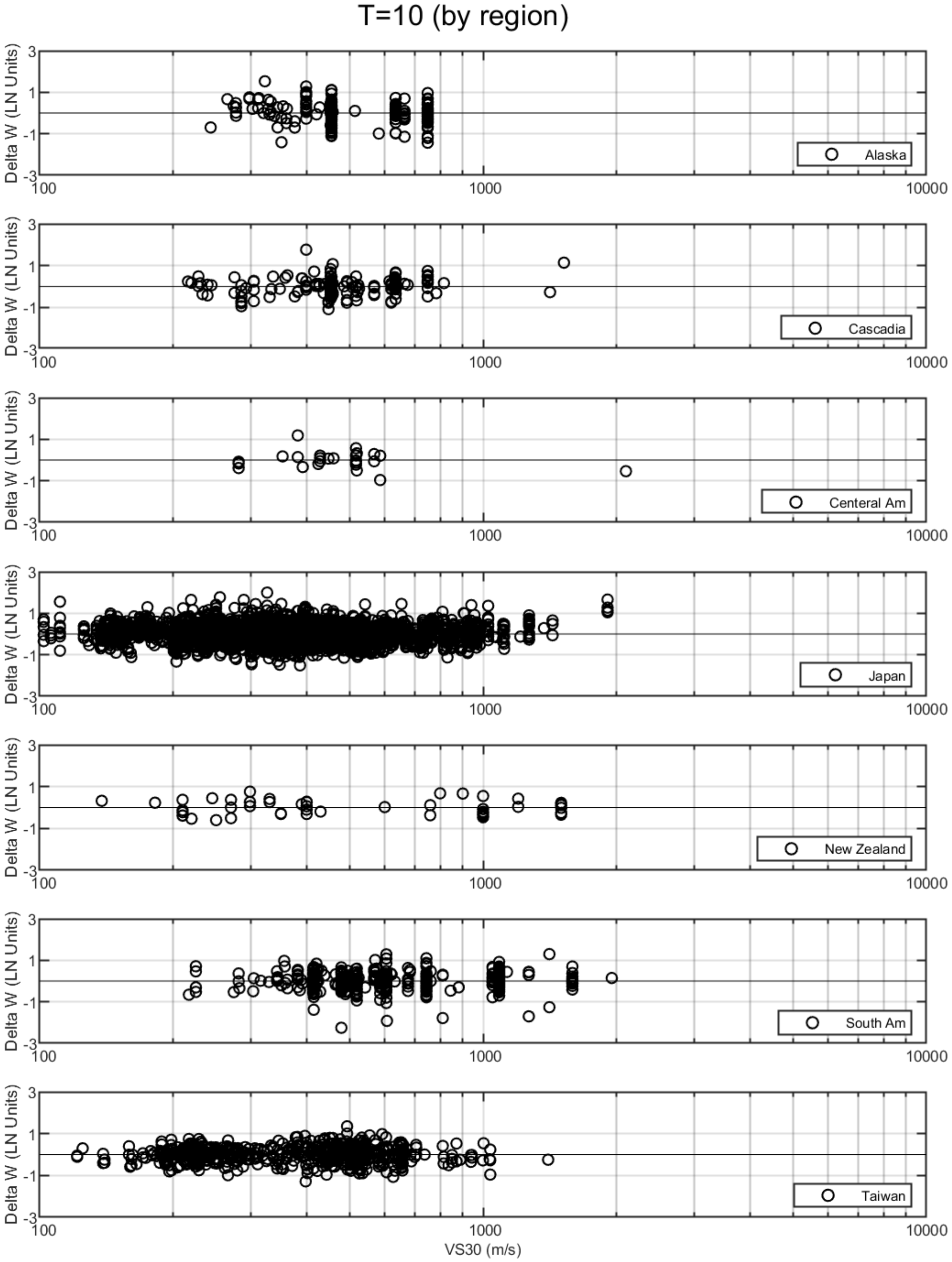

Figure A.84: Within-event residuals versus V_{S30} for T = 10.0 sec.

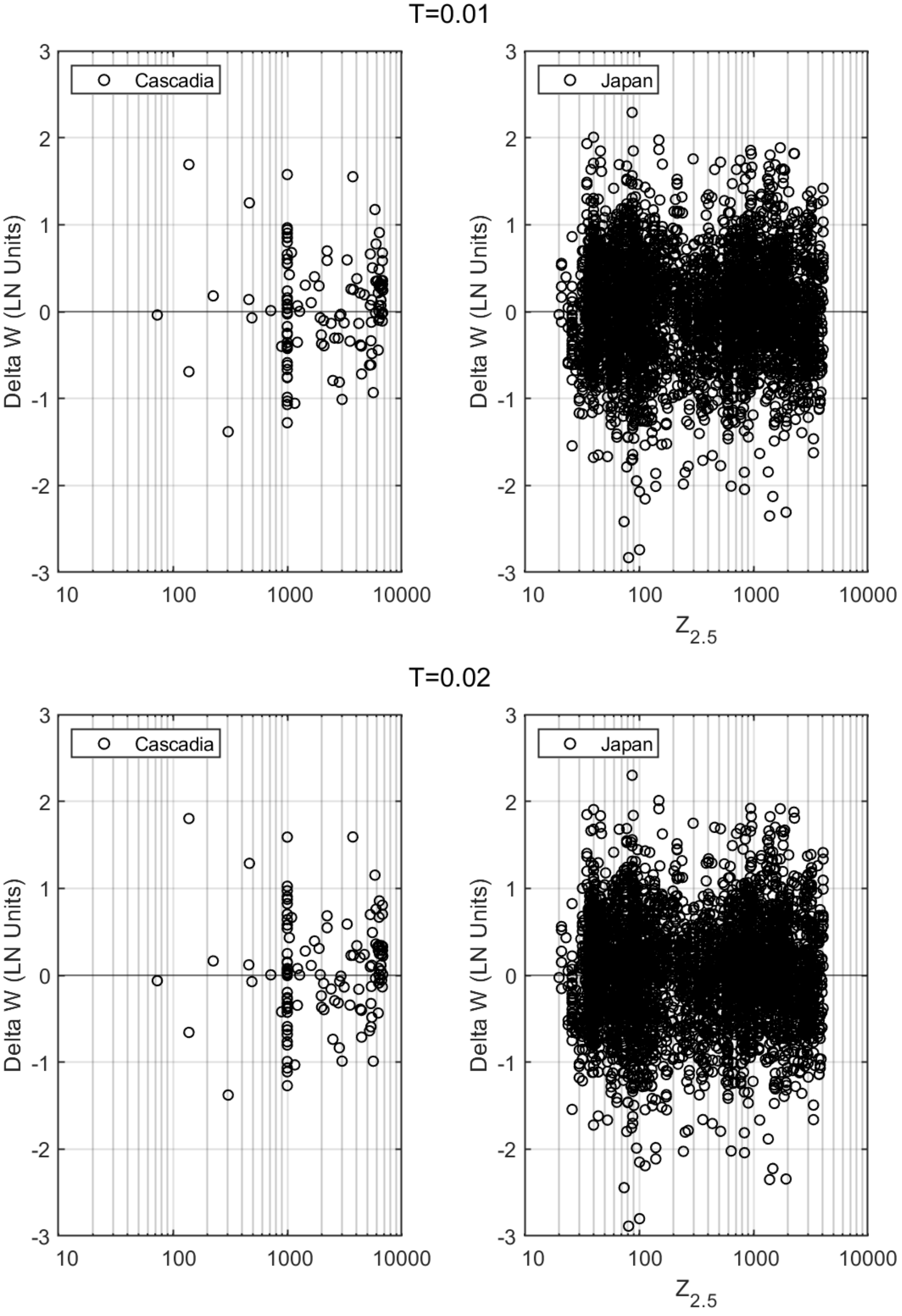

Figure A.85: Within-event residuals versus basin depth. Top frame: T = 0.01 sec. Bottom frame: T=0.02 sec.

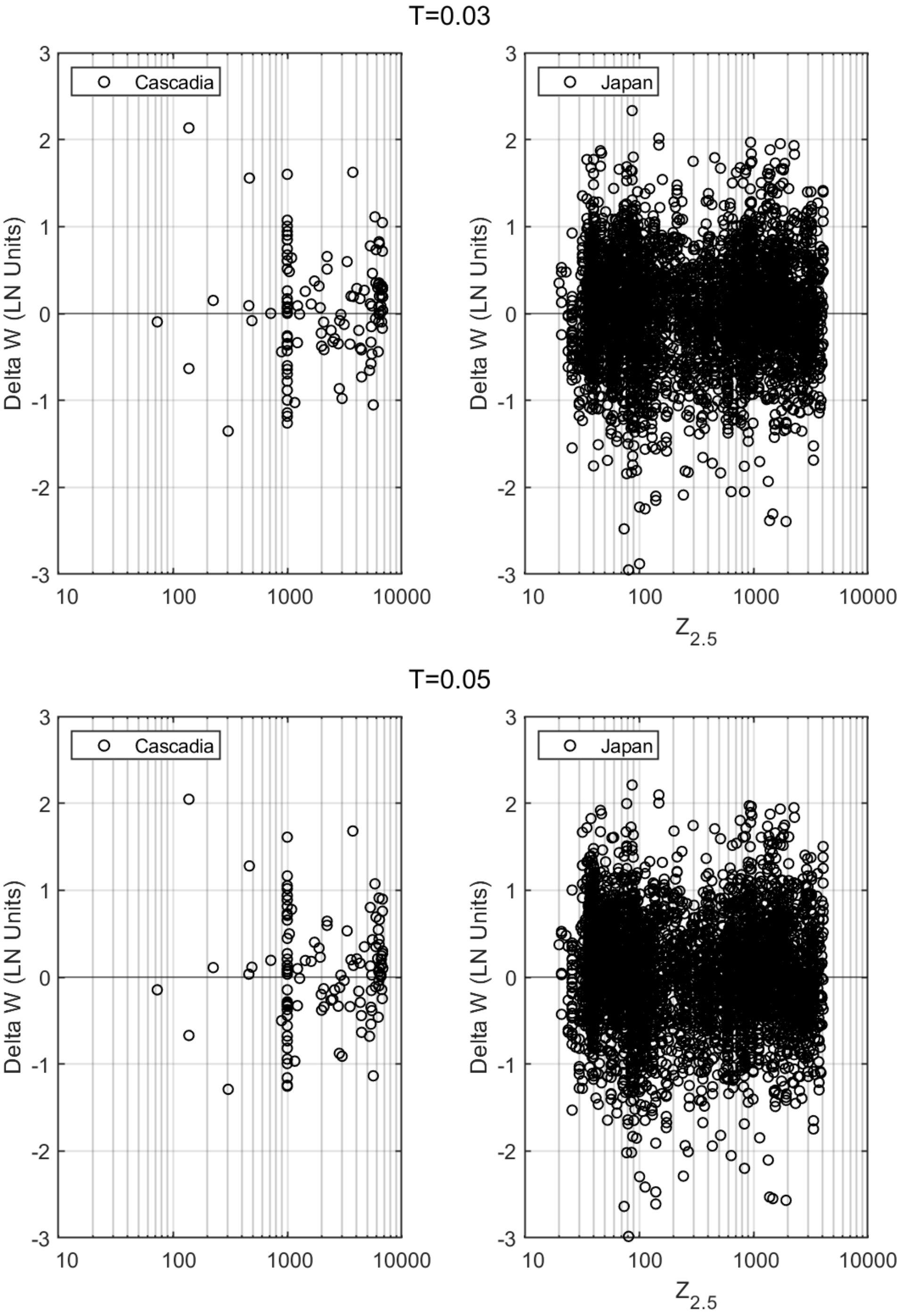

Figure A.86: Within-event residuals versus basin depth. Top frame: T = 0.03 sec. Bottom frame: T = 0.05 sec.

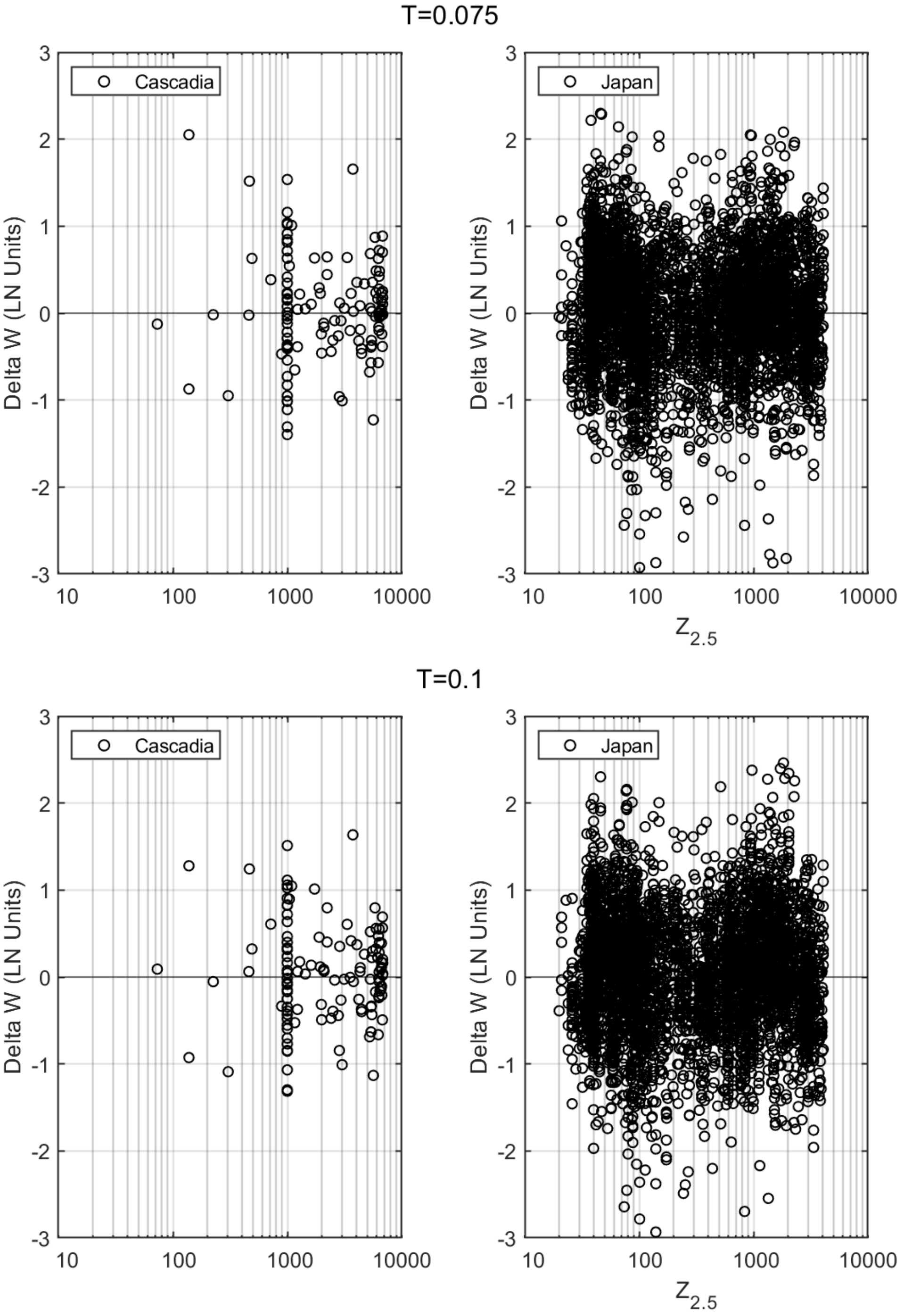

Figure A.87: Within-event residuals versus basin depth. Top frame: T = 0.075 sec. Bottom frame: T = 0.10 sec.

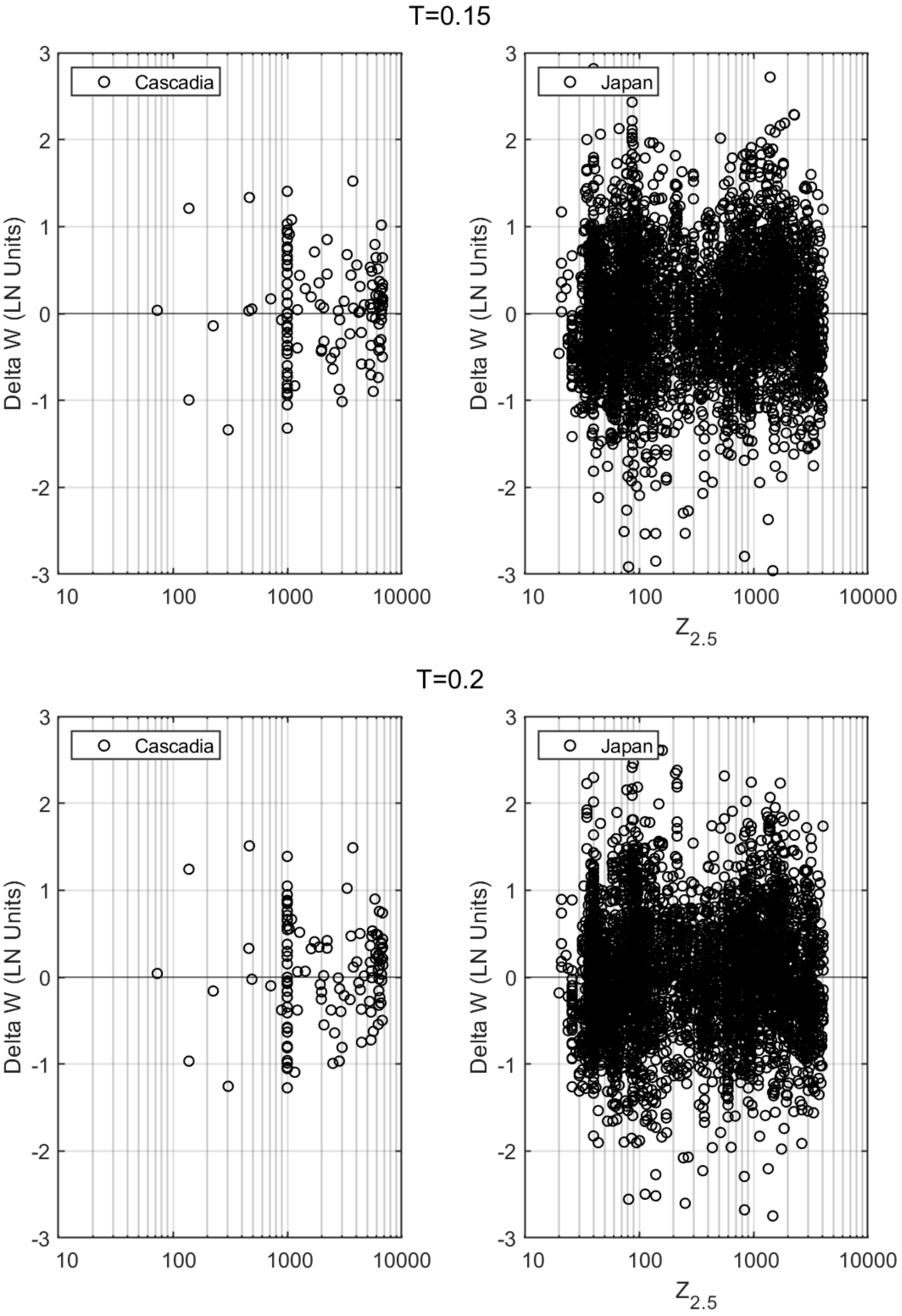

Figure A.88: Within-event residuals versus basin depth. Top frame: T = 0.15 sec. Bottom frame: T = 0.20 sec.

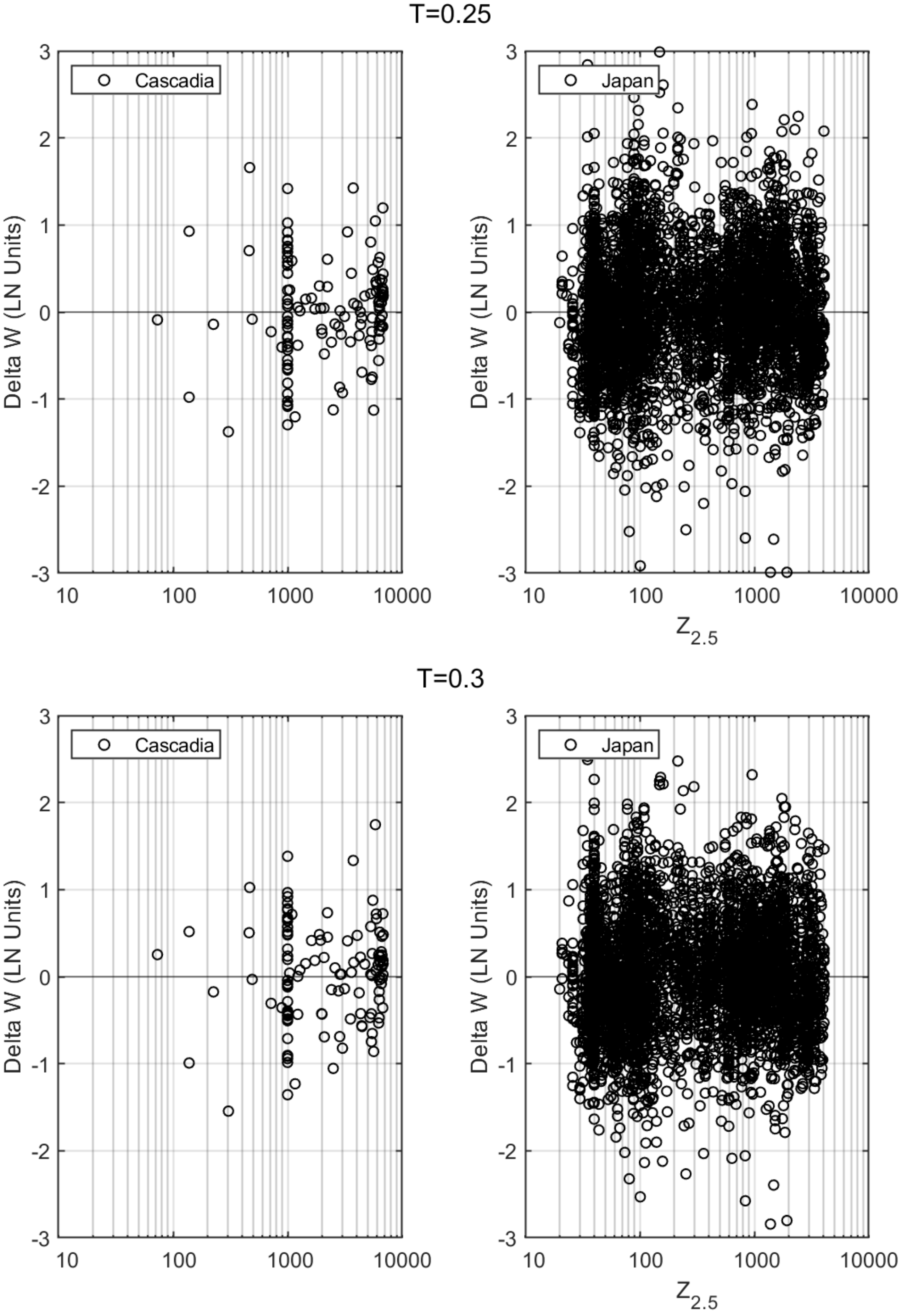

Figure A.89: Within-event residuals versus basin depth. Top frame: T = 0.25 sec. Bottom frame: T = 0.30 sec.

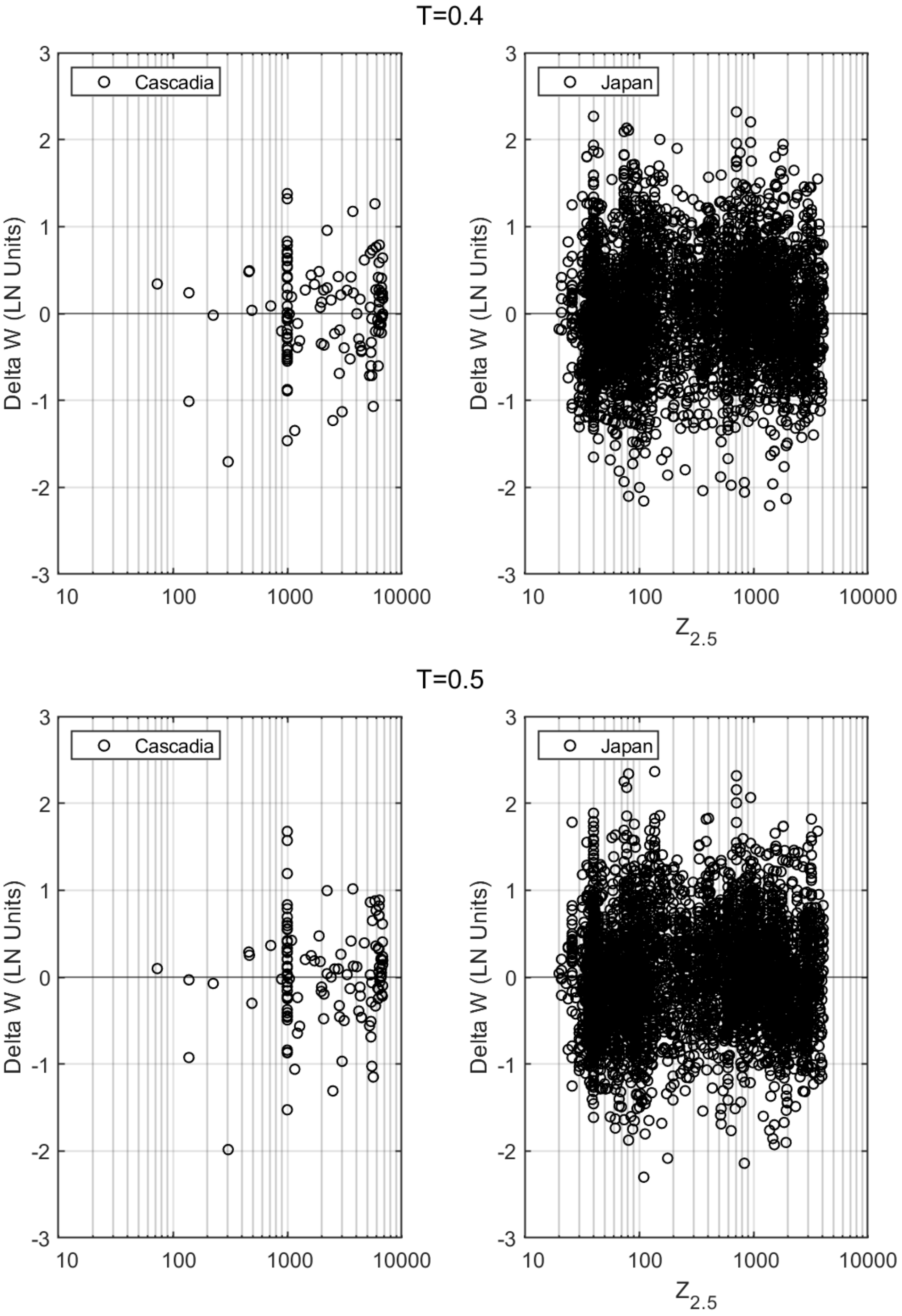

Figure A.90: Within-event residuals versus basin depth. Top frame: T = 0.40 sec. Bottom frame: T = 0.50 sec.

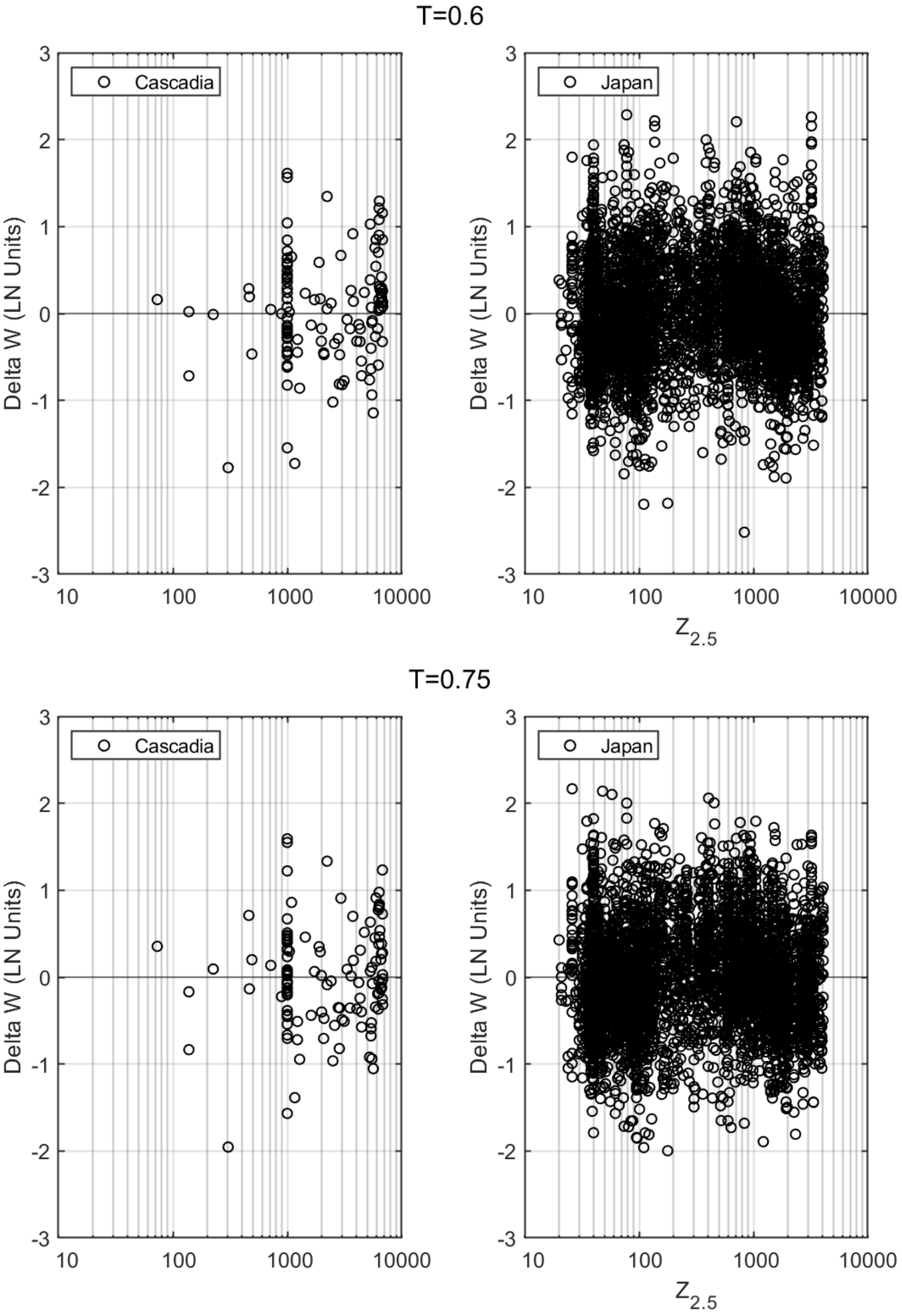

Figure A.91: Within-event residuals versus basin depth. Top frame: T = 0.60 sec. Bottom frame: T = 0.75 sec.

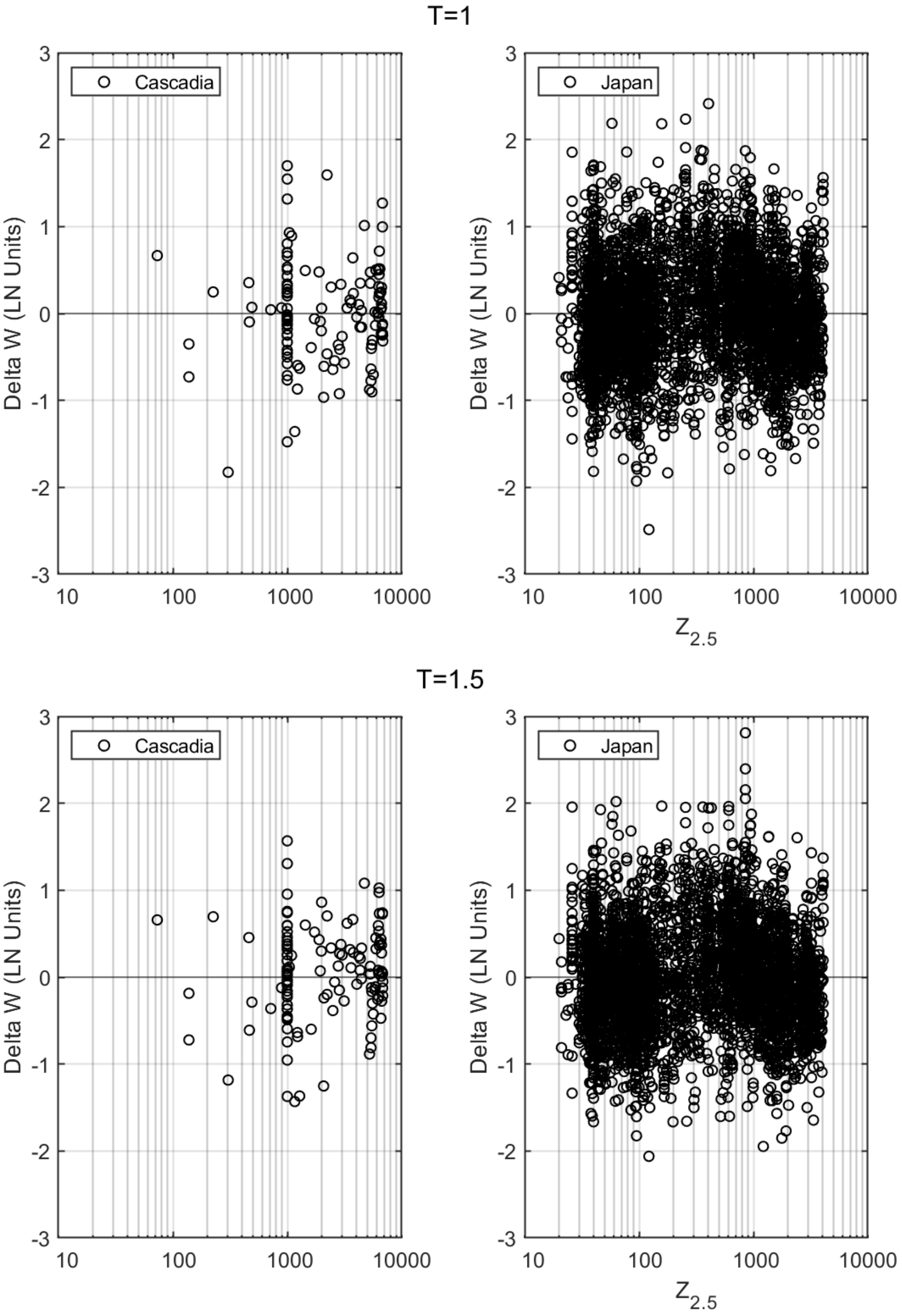

Figure A.92: Within-event residuals versus basin depth. Top frame: T = 1.0 sec. Bottom frame: T = 1.5 sec.

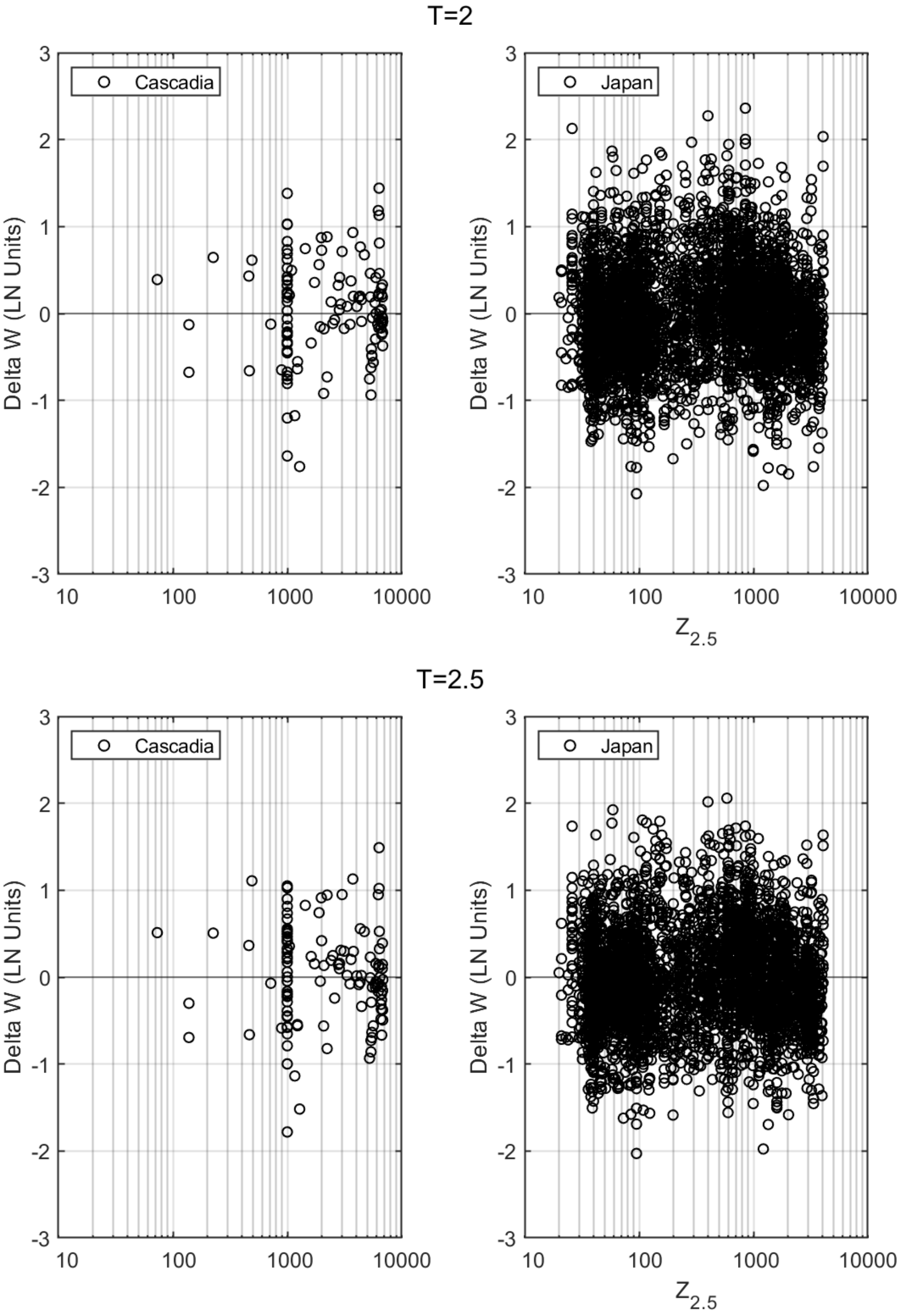

Figure A.93: Within-event residuals versus basin depth. Top frame: T = 2.0 sec. Bottom frame: T = 2.5 sec.

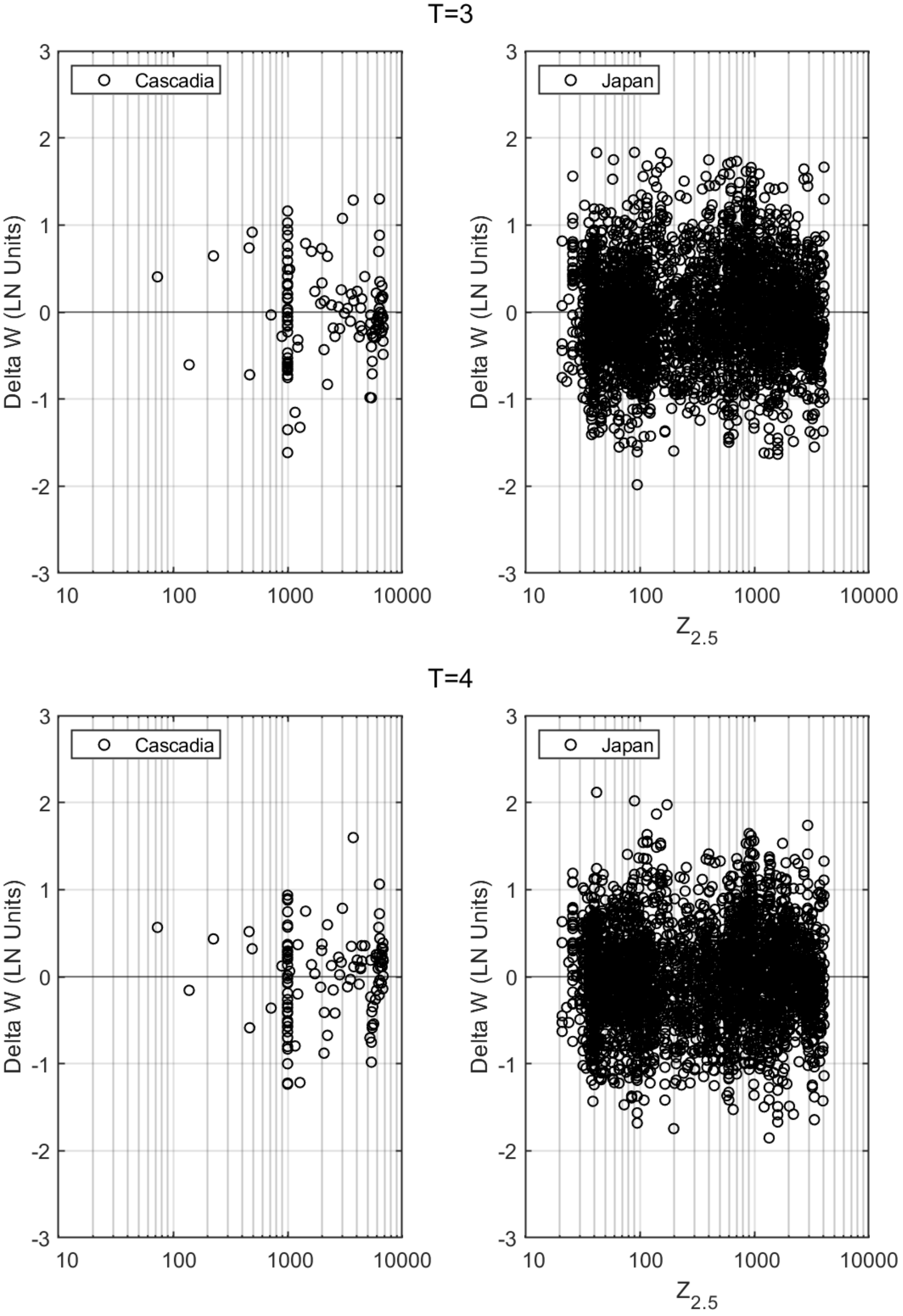

Figure A.94: Within-event residuals versus basin depth. Top frame: T = 3.0 sec. Bottom frame: T = 4.0 sec.

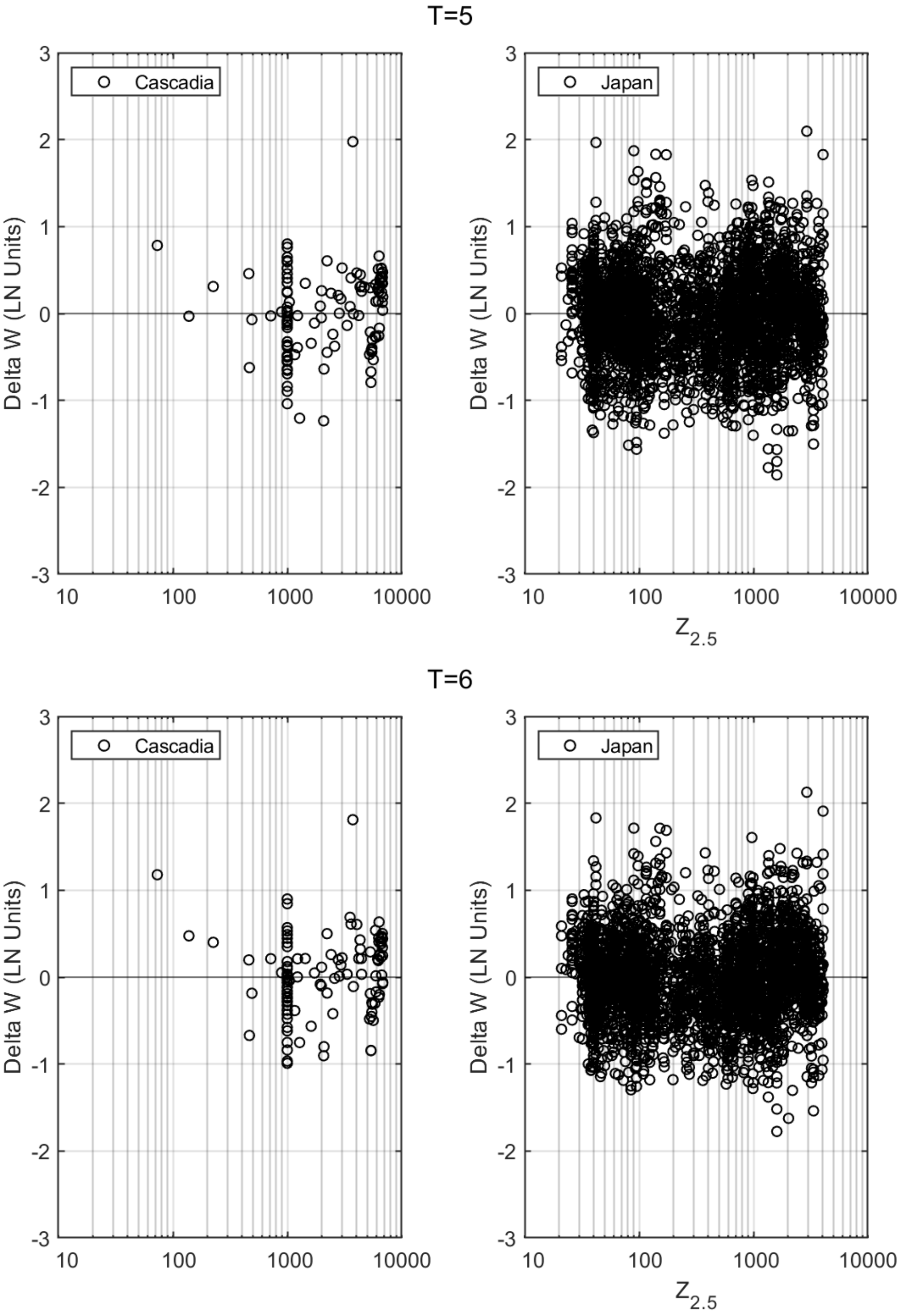

Figure A.95: Within-event residuals versus basin depth. Top frame: T = 5.0 sec. Bottom frame: T = 6.0 sec.

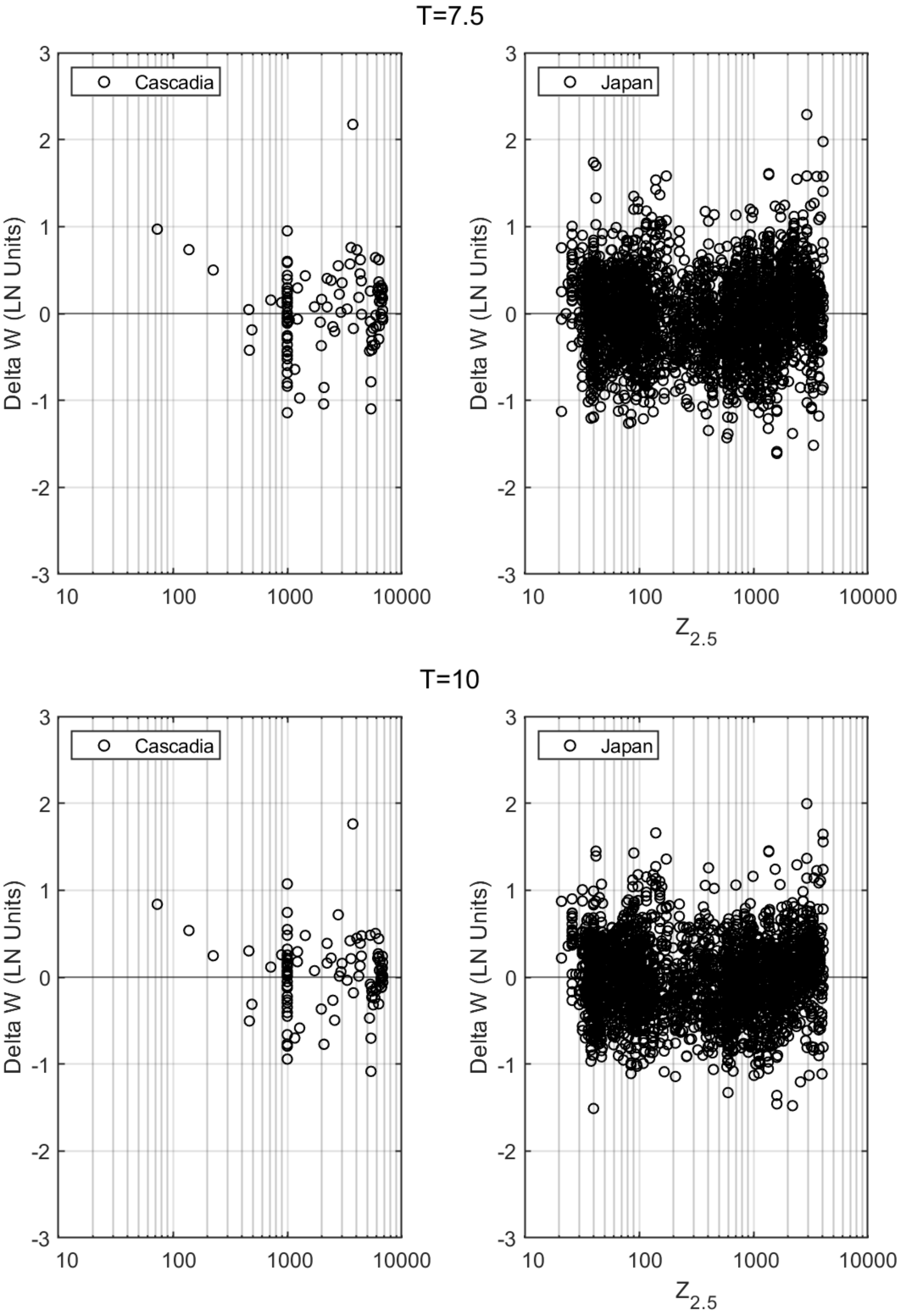

Figure A.96: Within-event residuals versus basin depth. Top frame: T=7.5 sec. Bottom frame: T = 10.0 sec.

PEER REPORTS

PEER reports are available as a free PDF download from https://peer.berkeley.edu/peer-reports. In addition, printed hard copies of PEER reports can be ordered directly from our printer by following the instructions at https://peer.berkeley.edu/peer-reports. For other related questions about the PEER Report Series, contact the Pacific Earthquake Engineering Research Center, 325 Davis Hall, Mail Code 1792, Berkeley, CA 94720. Tel.: (510) 642-3437; and Email: peer_center@berkeley.edu.

PEER 2020/24 *Seismic Performance of Single-Family Wood-Frame Houses: Comparing Analytical and Industry Catastrophe Models* (PEER-CEA Project). Evan Reis. December 2020.

PEER 2020/23 *Earthquake Damage Workshop* (PEER-CEA Project). Kylin Vail, Bret Lizundia, David P. Welch, and Evan Reis. December 2020.

PEER 2020/22 *Technical Background Report for Structural Analysis and Performance Assessment* (PEER-CEA Project). David P. Welch and Gregory G. Deierlein. December 2020.

PEER 2020/21 *Comparison of the Response of Small- and Large-Component Cripple Wall Specimens Tested under Simulated Seismic Loading* (PEER-CEA Project). Brandon Schiller, Tara Hutchinson, and Kelly Cobeen. December 2020.

PEER 2020/20 *Large-Component Seismic Testing for Existing and Retrofitted Single-Family Wood-Frame Dwellings* (PEER-CEA Project). Kelly Cobeen, Vahid Mahdavifar, Tara Hutchinson, Brandon Schiller, David P. Welch, Grace S. Kang, and Yousef Bozorgnia. December 2020.

PEER 2020/19 *Cripple Wall Small-Component Test Program: Comparisons* (PEER-CEA Project). Brandon Schiller, Tara Hutchinson, and Kelly Cobeen. December 2020.

PEER 2020/18 *Cripple Wall Small-Component Test Program: Wet Specimens II* (PEER-CEA Project). Brandon Schiller, Tara Hutchinson, and Kelly Cobeen. December 2020.

PEER 2020/17 *Cripple Wall Small-Component Test Program: Dry Specimens* (PEER-CEA Project). Brandon Schiller, Tara Hutchinson, and Kelly Cobeen. December 2020.

PEER 2020/16 *Cripple Wall Small-Component Test Program: Wet Specimens I* (PEER-CEA Project). Brandon Schiller, Tara Hutchinson, and Kelly Cobeen. December 2020.

PEER 2020/15 *Development of Testing Protocol for Cripple Wall Components* (PEER-CEA Project). Farzin Zareian and Joel Lanning. December 2020.

PEER 2020/14 *Probabilistic Seismic Hazard Analysis and Selecting and Scaling of Ground-Motion Records* (PEER-CEA Project). Silvia Mazzoni, Nicholas Gregor, Linda Al Atik, Yousef Bozorgnia, David P. Welch, Gregory G. Deierlein. December 2020.

PEER 2020/13 *Development of Index Buildings* (PEER-CEA Project). Evan Reis. December 2020.

PEER 2020/12 *Project Technical Summary* (PEER-CEA Project). Evan Reis,in collaboration with Yousef Bozorgnia, Henry Burton, Kelly Cobeen, Gregory G. Deierlein, Tara Hutchinson, Grace S. Kang, Bret Lizundia, Silvia Mazzoni, Sharyl Rabinovici, Brandon Schiller, David P. Welch, and Farzin Zareian. December 2020.

PEER 2020/11 *Hybrid Simulations for the Seismic Evaluation of Resilient Highway Bridge Systems*. Yingjie Wu, Selim Gunay, and Khalid M. Mosalam. November 2020**.**

PEER 2020/10 *Low Seismic Damage Columns for Accelerated Bridge Construction*. Arpit Nema and Jose I. Restrepo. November 2020**.**

PEER 2020/09 *Blind Prediction of Shaking Table Tests of a New Bridge Ben Design.* Selim Gunay, Fan Hu, Khalid Mosalam, Arpit Nema, Jose Restrepo, Adam Zsarnoczay, and Jack Baker, November 2020.

PEER 2020/08 *PEER Activities Report 2018_2020.* Khalid M. Mosalam and Amarnath Kasalanati, November 2020.

PEER 2020/07 *Comparison of NGA-Sub Ground-Motion Models.* Nicholas Gregor, Kofi Addo, Linda Al Atik, David M. Boore, Yousef Bozorgnia, Kenneth W. Campbell, Brian S.-J. Choiu, Zeynep Gülerce, Behzad Hassani, Tadahiro Kishida, Nico Kuehn, Saburoh Midorikawa, Silvia Mazzoni, Grace A. Parker, Hongjun Si, Jonathan P. Stewart, and Robert R. Youngs. November 2020.

PEER 2020/06 *Development of NGA-Sub Ground-Motion Model of 5%-Damped Pseudo-Spectral Acceleration based on Database for Subduction Earthquakes in Japan.* Hongjun Si, Saburoh Midorikawa, and Tadahiro Kishida. November 2020.

PEER 2020/05 *Conditional Ground-Motion Model for Peak Ground Velocity for Active Crustal Regions.* Norman A. Abrahamson and Sarabjot Bhasin. October 2020.

PEER 2020/05 *Conditional Ground-Motion Model for Peak Ground Velocity for Active Crustal Regions.* Norman A. Abrahamson and Sarabjot Bhasin. October 2020.

PEER 2020/04 *Partially Non-Ergodic Ground-Motion Model for Subduction Regions using the NGA-Subduction Database.* Nicolas Kuehn, Yousef Bozognia, Kenneth W. Campbell, and Nicholas Gregor. September 2020.

PEER 2020/03 *NGA-Subduction Global Ground-Motion Models with Regional Adjustment Factors.* Grace A. Parker, Jonathan P. Stewart, David M. Boore, Gail M. Atkinson, and Behzad Hassani. September 2020.

PEER 2020/02 *Data Resources for NGA-Subduction Project.* Yousef Bozorgnia (PI) and Jonathan P. Stewart (Editor). March 2020.

PEER 2020/01 *Modeling Viscous Damping in Nonlinear Response History Analysis for Steel Moment-Frame Buildings.* Xin Qian, Anil K. Chopra, and Frank McKenna. June 2020.

PEER 2019/09 Seismic Behavior of Special Concentric Braced Frames under Short- and Long-Duration Ground Motions. Ali Hammad and Mohamed A. Moustafa. December 2019.

PEER 2019/08 Influence of Vertical Ground Motion on Bridges Isolated with Spherical Sliding Bearings. Rushil Mojidra and Keri L. Ryan. December 2019.

PEER 2019/07 *PEER Hub ImageNet* (ϕ-Net): *A Large-Scale Multi-Attribute Benchmark Dataset of Structural Images*. Yuqing Gao, and Khalid. M. Mosalam. November 2019.

PEER 2019/06 *Fluid-Structure Interaction and Python-Scripting Capabilities in OpenSees*. Minjie Zhu and Michael H. Scott. August 2019.

PEER 2019/05 *Expected Earthquake Performance of Buildings Designed to the California Building Code (California Alfred E. Alquist Seismic Safety Publication 19-01).* Grace S. Kang, Sifat Muin, Jorge Archbold, Bitanoosh Woods, and Khalid Mosalam. July 2019.

PEER 2019/04 *Aftershock Seismic Vulnerability and Time-Dependent Risk Assessment of Bridges*. Sujith Mangalathu, Mehrdad Shokrabadi, and Henry V. Burton. May 2019.

PEER 2019/03 *Ground-Motion Directivity Modeling for Seismic Hazard Applications.* Jennifer L. Donahue, Jonathan P. Stewart, Nicolas Gregor, and Yousef Bozorgnia. Review Panel: Jonathan D. Bray, Stephen A. Mahin, I. M. Idriss, Robert W. Graves, and Tom Shantz. May 2019.

PEER 2019/02 *Direct-Finite-Element Method for Nonlinear Earthquake Analysis of Concrete Dams Including Dam–Water–Foundation Rock Interaction.* Arnkjell Løkke and Anil K. Chopra. March 2019.

PEER 2019/01 *Flow-Failure Case History of the Las Palmas, Chile, Tailings Dam.* R. E. S. Moss, T. R. Gebhart, D. J. Frost, and C. Ledezma. January 2019.

PEER 2018/08 *Central and Eastern North America Ground-Motion Characterization: NGA-East Final Report*. Christine Goulet, Yousef Bozorgnia, Norman Abrahamson, Nicolas Kuehn, Linda Al Atik, Robert Youngs, Robert Graves, and Gail Atkinson. December 2018.

PEER 2018/07 *An Empirical Model for Fourier Amplitude Spectra using the NGA-West2 Database*. Jeff Bayless, and Norman A. Abrahamson. December 2018.

PEER 2018/06 *Estimation of Shear Demands on Rock-Socketed Drilled Shafts subjected to Lateral Loading*. Pedro Arduino, Long Chen, and Christopher R. McGann. December 2018.

PEER 2018/05 *Selection of Random Vibration Procedures for the NGA-East Project*. Albert Kottke, Norman A. Abrahamson, David M. Boore, Yousef Bozorgnia, Christine Goulet, Justin Hollenback, Tadahiro Kishida, Armen Der Kiureghian, Olga-Joan Ktenidou, Nicolas Kuehn, Ellen M. Rathje, Walter J. Silva, Eric Thompson, and Xiaoyue Wang. December 2018.

PEER 2018/04 *Capturing Directivity Effects in the Mean and Aleatory Variability of the NGA-West 2 Ground Motion Prediction Equations.* Jennie A. Watson-Lamprey. November 2018.

PEER 2018/03 *Probabilistic Seismic Hazard Analysis Code Verification*. Christie Hale, Norman Abrahamson, and Yousef Bozorgnia. July 2018.

PEER 2018/02 *Update of the BCHydro Subduction Ground-Motion Model using the NGA-Subduction Dataset.* Norman Abrahamson, Nicolas Kuehn, Zeynep Gulerce, Nicholas Gregor, Yousef Bozorgnia, Grace Parker, Jonathan Stewart, Brian Chiou, I. M. Idriss, Kenneth Campbell, and Robert Youngs. June 2018.

PEER 2018/01 *PEER Annual Report 2017–2018*. Khalid Mosalam, Amarnath Kasalanati, and Selim Günay. June 2018.

PEER 2017/12 *Experimental Investigation of the Behavior of Vintage and Retrofit Concentrically Braced Steel Frames under Cyclic Loading*. Barbara G. Simpson, Stephen A. Mahin, and Jiun-Wei Lai, December 2017.

PEER 2017/11 *Preliminary Studies on the Dynamic Response of a Seismically Isolated Prototype Gen-IV Sodium-Cooled Fast Reactor* (*PGSFR*). Benshun Shao, Andreas H. Schellenberg, Matthew J. Schoettler, and Stephen A. Mahin. December 2017.

PEER 2017/10 *Development of Time Histories for IEEE693 Testing and Analysis (including Seismically Isolated Equipment).* Shakhzod M. Takhirov, Eric Fujisaki, Leon Kempner, Michael Riley, and Brian Low. December 2017.

PEER 2017/09 *“”R” Package for Computation of Earthquake Ground-Motion Response Spectra.* Pengfei Wang, Jonathan P. Stewart, Yousef Bozorgnia, David M. Boore, and Tadahiro Kishida. December 2017.

PEER 2017/08 *Influence of Kinematic SSI on Foundation Input Motions for Bridges on Deep Foundations*. Benjamin J. Turner, Scott J. Brandenberg, and Jonathan P. Stewart. November 2017.

PEER 2017/07 *A Nonlinear Kinetic Model for Multi-Stage Friction Pendulum Systems*. Paul L. Drazin and Sanjay Govindjee. September 2017.

PEER 2017/06 *Guidelines for Performance-Based Seismic Design of Tall Buildings, Version 2.02*. TBI Working Group led by co-chairs Ron Hamburger and Jack Moehle: Jack Baker, Jonathan Bray, C.B. Crouse, Greg Deierlein, John Hooper, Marshall Lew, Joe Maffei, Stephen Mahin, James Malley, Farzad Naeim, Jonathan Stewart, and John Wallace. May 2017.

PEER 2017/05 *Recommendations for Ergodic Nonlinear Site Amplification in Central and Eastern North America*. Youssef M.A. Hashash, Joseph A. Harmon, Okan Ilhan, Grace A. Parker, and Jonathan P. Stewart. March 2017.

PEER 2017/04 *Expert Panel Recommendations for Ergodic Site Amplification in Central and Eastern North America*. Jonathan P. Stewart, Grace A. Parker, Joseph P. Harmon, Gail M. Atkinson, David M. Boore, Robert B. Darragh, Walter J. Silva, and Youssef M.A. Hashash. March 2017.

PEER 2017/03 *NGA-East Ground-Motion Models for the U.S. Geological Survey National Seismic Hazard Maps*. Christine A. Goulet, Yousef Bozorgnia, Nicolas Kuehn, Linda Al Atik, Robert R. Youngs, Robert W. Graves, and Gail M. Atkinson. March 2017.

PEER 2017/02 *U.S.–New Zealand–Japan Workshop: Liquefaction-Induced Ground Movements Effects, University of California, Berkeley, California, 2–4 November 2016.* Jonathan D. Bray, Ross W. Boulanger, Misko Cubrinovski, Kohji Tokimatsu, Steven L. Kramer, Thomas O’Rourke, Ellen Rathje, Russell A. Green, Peter K. Robinson, and Christine Z. Beyzaei. March 2017.

PEER 2017/01 *2016 PEER Annual Report*. Khalid M. Mosalam, Amarnath Kasalanati, and Grace Kang. March 2017.

PEER 2016/10 *Performance-Based Robust Nonlinear Seismic Analysis with Application to Reinforced Concrete Bridge Systems*. Xiao Ling and Khalid M. Mosalam. December 2016.

PEER 2017/09 *Detailing Requirements for Column Plastic Hinges subjected to Combined Flexural, Axial, and Torsional Seismic Loading.* Gabriel Hurtado and Jack P. Moehle. December 2016.

PEER 2016/08 *Resilience of Critical Structures, Infrastructure, and Communities*. Gian Paolo Cimellaro, Ali Zamani-Noori, Omar Kamouh, Vesna Terzic, and Stephen A. Mahin. December 2016.

PEER 2016/07 *Hybrid Simulation Theory for a Classical Nonlinear Dynamical System*. Paul L. Drazin and Sanjay Govindjee. September 2016.

PEER 2016/06 *California Earthquake Early Warning System Benefit Study*. Laurie A. Johnson, Sharyl Rabinovici, Grace S. Kang, and Stephen A. Mahin. July 2006.

PEER 2016/05 *Ground-Motion Prediction Equations for Arias Intensity Consistent with the NGA-West2 Ground-Motion Models.* Charlotte Abrahamson, Hao-Jun Michael Shi, and Brian Yang. July 2016.

PEER 2016/04 *The M_W 6.0 South Napa Earthquake of August 24, 2014: A Wake-Up Call for Renewed Investment in Seismic Resilience Across California.* Prepared for the California Seismic Safety Commission, Laurie A. Johnson and Stephen A. Mahin. May 2016.

PEER 2016/03 *Simulation Confidence in Tsunami-Driven Overland Flow.* Patrick Lynett. May 2016.

PEER 2016/02 *Semi-Automated Procedure for Windowing time Series and Computing Fourier Amplitude Spectra for the NGA-West2 Database.* Tadahiro Kishida, Olga-Joan Ktenidou, Robert B. Darragh, and Walter J. Silva. May 2016.

PEER 2016/01 *A Methodology for the Estimation of Kappa (κ) from Large Datasets: Example Application to Rock Sites in the NGA-East Database and Implications on Design Motions.* Olga-Joan Ktenidou, Norman A. Abrahamson, Robert B. Darragh, and Walter J. Silva. April 2016.

PEER 2015/13 *Self-Centering Precast Concrete Dual-Steel-Shell Columns for Accelerated Bridge Construction: Seismic Performance, Analysis, and Design*. Gabriele Guerrini, José I. Restrepo, Athanassios Vervelidis, and Milena Massari. December 2015.

PEER 2015/12 *Shear-Flexure Interaction Modeling for Reinforced Concrete Structural Walls and Columns under Reversed Cyclic Loading*. Kristijan Kolozvari, Kutay Orakcal, and John Wallace. December 2015.

PEER 2015/11 *Selection and Scaling of Ground Motions for Nonlinear Response History Analysis of Buildings in Performance-Based Earthquake Engineering*. N. Simon Kwong and Anil K. Chopra. December 2015.

PEER 2015/10 *Structural Behavior of Column-Bent Cap Beam-Box Girder Systems in Reinforced Concrete Bridges Subjected to Gravity and Seismic Loads. Part II: Hybrid Simulation and Post-Test Analysis*. Mohamed A. Moustafa and Khalid M. Mosalam. November 2015.

PEER 2015/09 *Structural Behavior of Column-Bent Cap Beam-Box Girder Systems in Reinforced Concrete Bridges Subjected to Gravity and Seismic Loads. Part I: Pre-Test Analysis and Quasi-Static Experiments*. Mohamed A. Moustafa and Khalid M. Mosalam. September 2015.

PEER 2015/08 *NGA-East: Adjustments to Median Ground-Motion Models for Center and Eastern North America*. August 2015.

PEER 2015/07 *NGA-East: Ground-Motion Standard-Deviation Models for Central and Eastern North America*. Linda Al Atik. June 2015.

PEER 2015/06 *Adjusting Ground-Motion Intensity Measures to a Reference Site for which V_{S30} = 3000 m/sec*. David M. Boore. May 2015.

PEER 2015/05 *Hybrid Simulation of Seismic Isolation Systems Applied to an APR-1400 Nuclear Power Plant.* Andreas H. Schellenberg, Alireza Sarebanha, Matthew J. Schoettler, Gilberto Mosqueda, Gianmario Benzoni, and Stephen A. Mahin. April 2015.

PEER 2015/04 *NGA-East: Median Ground-Motion Models for the Central and Eastern North America Region*. April 2015.

PEER 2015/03 *Single Series Solution for the Rectangular Fiber-Reinforced Elastomeric Isolator Compression Modulus*. James M. Kelly and Niel C. Van Engelen. March 2015.

PEER 2015/02 *A Full-Scale, Single-Column Bridge Bent Tested by Shake-Table Excitation.* Matthew J. Schoettler, José I. Restrepo, Gabriele Guerrini, David E. Duck, and Francesco Carrea. March 2015.

PEER 2015/01 *Concrete Column Blind Prediction Contest 2010: Outcomes and Observations.* Vesna Terzic, Matthew J. Schoettler, José I. Restrepo, and Stephen A Mahin. March 2015.

PEER 2014/20 *Stochastic Modeling and Simulation of Near-Fault Ground Motions for Performance-Based Earthquake Engineering*. Mayssa Dabaghi and Armen Der Kiureghian. December 2014.

PEER 2014/19 *Seismic Response of a Hybrid Fiber-Reinforced Concrete Bridge Column Detailed for Accelerated Bridge Construction*. Wilson Nguyen, William Trono, Marios Panagiotou, and Claudia P. Ostertag. December 2014.

PEER 2014/18 *Three-Dimensional Beam-Truss Model for Reinforced Concrete Walls and Slabs Subjected to Cyclic Static or Dynamic Loading*. Yuan Lu, Marios Panagiotou, and Ioannis Koutromanos. December 2014.

PEER 2014/17 *PEER NGA-East Database.* Christine A. Goulet, Tadahiro Kishida, Timothy D. Ancheta, Chris H. Cramer, Robert B. Darragh, Walter J. Silva, Youssef M.A. Hashash, Joseph Harmon, Jonathan P. Stewart, Katie E. Wooddell, and Robert R. Youngs. October 2014.

PEER 2014/16 *Guidelines for Performing Hazard-Consistent One-Dimensional Ground Response Analysis for Ground Motion Prediction*. Jonathan P. Stewart, Kioumars Afshari, and Youssef M.A. Hashash. October 2014.

PEER 2014/15 *NGA-East Regionalization Report: Comparison of Four Crustal Regions within Central and Eastern North America using Waveform Modeling and 5%-Damped Pseudo-Spectral Acceleration Response*. Jennifer Dreiling, Marius P. Isken, Walter D. Mooney, Martin C. Chapman, and Richard W. Godbee. October 2014.

PEER 2014/14 *Scaling Relations between Seismic Moment and Rupture Area of Earthquakes in Stable Continental Regions*. Paul Somerville. August 2014.

PEER 2014/13 *PEER Preliminary Notes and Observations on the August 24, 2014, South Napa Earthquake*. Grace S. Kang and Stephen A. Mahin, Editors. September 2014.

PEER 2014/12 *Reference-Rock Site Conditions for Central and Eastern North America: Part II – Attenuation (Kappa) Definition*. Kenneth W. Campbell, Youssef M.A. Hashash, Byungmin Kim, Albert R. Kottke, Ellen M. Rathje, Walter J. Silva, and Jonathan P. Stewart. August 2014.

PEER 2014/11 *Reference-Rock Site Conditions for Central and Eastern North America: Part I - Velocity Definition*. Youssef M.A. Hashash, Albert R. Kottke, Jonathan P. Stewart, Kenneth W. Campbell, Byungmin Kim, Ellen M. Rathje, Walter J. Silva, Sissy Nikolaou, and Cheryl Moss. August 2014.

PEER 2014/10 *Evaluation of Collapse and Non-Collapse of Parallel Bridges Affected by Liquefaction and Lateral Spreading*. Benjamin Turner, Scott J. Brandenberg, and Jonathan P. Stewart. August 2014.

PEER 2014/09 *PEER Arizona Strong-Motion Database and GMPEs Evaluation*. Tadahiro Kishida, Robert E. Kayen, Olga-Joan Ktenidou, Walter J. Silva, Robert B. Darragh, and Jennie Watson-Lamprey. June 2014.

PEER 2014/08 *Unbonded Pretensioned Bridge Columns with Rocking Detail*. Jeffrey A. Schaefer, Bryan Kennedy, Marc O. Eberhard, and John F. Stanton. June 2014.

PEER 2014/07 *Northridge 20 Symposium Summary Report: Impacts, Outcomes, and Next Steps*. May 2014.

PEER 2014/06 *Report of the Tenth Planning Meeting of NEES/E-Defense Collaborative Research on Earthquake Engineering*. December 2013.

PEER 2014/05 *Seismic Velocity Site Characterization of Thirty-One Chilean Seismometer Stations by Spectral Analysis of Surface Wave Dispersion*. Robert Kayen, Brad D. Carkin, Skye Corbet, Camilo Pinilla, Allan Ng, Edward Gorbis, and Christine Truong. April 2014.

PEER 2014/04 Effect of Vertical Acceleration on Shear Strength of Reinforced Concrete Columns. Hyerin Lee and Khalid M. Mosalam. April 2014.

PEER 2014/03 *Retest of Thirty-Year-Old Neoprene Isolation Bearings.* James M. Kelly and Niel C. Van Engelen. March 2014.

PEER 2014/02 *Theoretical Development of Hybrid Simulation Applied to Plate Structures.* Ahmed A. Bakhaty, Khalid M. Mosalam, and Sanjay Govindjee. January 2014.

PEER 2014/01 *Performance-Based Seismic Assessment of Skewed Bridges.* Peyman Kaviani, Farzin Zareian, and Ertugrul Taciroglu. January 2014.

PEER 2013/26 *Urban Earthquake Engineerin*g. Proceedings of the U.S.-Iran Seismic Workshop. December 2013.

PEER 2013/25 *Earthquake Engineering for Resilient Communities: 2013 PEER Internship Program Research Report Collection.* Heidi Tremayne (Editor), Stephen A. Mahin (Editor), Jorge Archbold Monterossa, Matt Brosman, Shelly Dean, Katherine deLaveaga, Curtis Fong, Donovan Holder, Rakeeb Khan, Elizabeth Jachens, David Lam, Daniela Martinez Lopez, Mara Minner, Geffen Oren, Julia Pavicic, Melissa Quinonez, Lorena Rodriguez, Sean Salazar, Kelli Slaven, Vivian Steyert, Jenny Taing, and Salvador Tena. December 2013.

PEER 2013/24 *NGA-West2 Ground Motion Prediction Equations for Vertical Ground Motions*. September 2013.

PEER 2013/23 *Coordinated Planning and Preparedness for Fire Following Major Earthquakes*. Charles Scawthorn. November 2013.

PEER 2013/22 *GEM-PEER Task 3 Project: Selection of a Global Set of Ground Motion Prediction Equations.* Jonathan P. Stewart, John Douglas, Mohammad B. Javanbarg, Carola Di Alessandro, Yousef Bozorgnia, Norman A. Abrahamson, David M. Boore, Kenneth W. Campbell, Elise Delavaud, Mustafa Erdik, and Peter J. Stafford. December 2013.

PEER 2013/21 *Seismic Design and Performance of Bridges with Columns on Rocking Foundations*. Grigorios Antonellis and Marios Panagiotou. September 2013.

PEER 2013/20 *Experimental and Analytical Studies on the Seismic Behavior of Conventional and Hybrid Braced Frames*. Jiun-Wei Lai and Stephen A. Mahin. September 2013.

PEER 2013/19 *Toward Resilient Communities: A Performance-Based Engineering Framework for Design and Evaluation of the Built Environment.* Michael William Mieler, Bozidar Stojadinovic, Robert J. Budnitz, Stephen A. Mahin, and Mary C. Comerio. September 2013.

PEER 2013/18 *Identification of Site Parameters that Improve Predictions of Site Amplification*. Ellen M. Rathje and Sara Navidi. July 2013.

PEER 2013/17 *Response Spectrum Analysis of Concrete Gravity Dams Including Dam-Water-Foundation Interaction*. Arnkjell Løkke and Anil K. Chopra. July 2013.

PEER 2013/16 *Effect of Hoop Reinforcement Spacing on the Cyclic Response of Large Reinforced Concrete Special Moment Frame Beams.* Marios Panagiotou, Tea Visnjic, Grigorios Antonellis, Panagiotis Galanis, and Jack P. Moehle. June 2013.

PEER 2013/15 *A Probabilistic Framework to Include the Effects of Near-Fault Directivity in Seismic Hazard Assessment*. Shrey Kumar Shahi, Jack W. Baker. October 2013.

PEER 2013/14 *Hanging-Wall Scaling using Finite-Fault Simulations.* Jennifer L. Donahue and Norman A. Abrahamson. September 2013.

PEER 2013/13 *Semi-Empirical Nonlinear Site Amplification and its Application in NEHRP Site Factors*. Jonathan P. Stewart and Emel Seyhan. November 2013.

PEER 2013/12 *Nonlinear Horizontal Site Response for the NGA-West2 Project.* Ronnie Kamai, Norman A. Abramson, Walter J. Silva. May 2013.

PEER 2013/11 *Epistemic Uncertainty for NGA-West2 Models.* Linda Al Atik and Robert R. Youngs. May 2013.

PEER 2013/10 *NGA-West 2 Models for Ground-Motion Directionality.* Shrey K. Shahi and Jack W. Baker. May 2013.

PEER 2013/09 *Final Report of the NGA-West2 Directivity Working Group.* Paul Spudich, Jeffrey R. Bayless, Jack W. Baker, Brian S.J. Chiou, Badie Rowshandel, Shrey Shahi, and Paul Somerville. May 2013.

PEER 2013/08 *NGA-West2 Model for Estimating Average Horizontal Values of Pseudo-Absolute Spectral Accelerations Generated by Crustal Earthquakes*. I. M. Idriss. May 2013.

PEER 2013/07 *Update of the Chiou and Youngs NGA Ground Motion Model for Average Horizontal Component of Peak Ground Motion and Response Spectra*. Brian Chiou and Robert Youngs. May 2013.

PEER 2013/06 *NGA-West2 Campbell-Bozorgnia Ground Motion Model for the Horizontal Components of PGA, PGV, and 5%-Damped Elastic Pseudo-Acceleration Response Spectra for Periods Ranging from 0.01 to 10 sec.* Kenneth W. Campbell and Yousef Bozorgnia. May 2013.

PEER 2013/05 *NGA-West 2 Equations for Predicting Response Spectral Accelerations for Shallow Crustal Earthquakes*. David M. Boore, Jonathan P. Stewart, Emel Seyhan, and Gail M. Atkinson. May 2013.

PEER 2013/04 *Update of the AS08 Ground-Motion Prediction Equations Based on the NGA-West2 Data Set*. Norman Abrahamson, Walter Silva, and Ronnie Kamai. May 2013.

PEER 2013/03 *PEER NGA-West2 Database.* Timothy D. Ancheta, Robert B. Darragh, Jonathan P. Stewart, Emel Seyhan, Walter J. Silva, Brian S.J. Chiou, Katie E. Wooddell, Robert W. Graves, Albert R. Kottke, David M. Boore, Tadahiro Kishida, and Jennifer L. Donahue. May 2013.

PEER 2013/02 *Hybrid Simulation of the Seismic Response of Squat Reinforced Concrete Shear Walls*. Catherine A. Whyte and Bozidar Stojadinovic. May 2013.

PEER 2013/01 *Housing Recovery in Chile: A Qualitative Mid-program Review*. Mary C. Comerio. February 2013.

PEER 2012/08 *Guidelines for Estimation of Shear Wave Velocity.* Bernard R. Wair, Jason T. DeJong, and Thomas Shantz. December 2012.

PEER 2012/07 *Earthquake Engineering for Resilient Communities: 2012 PEER Internship Program Research Report Collection.* Heidi Tremayne (Editor), Stephen A. Mahin (Editor), Collin Anderson, Dustin Cook, Michael Erceg, Carlos Esparza, Jose Jimenez, Dorian Krausz, Andrew Lo, Stephanie Lopez, Nicole McCurdy, Paul Shipman, Alexander Strum, Eduardo Vega. December 2012.

PEER 2012/06 *Fragilities for Precarious Rocks at Yucca Mountain.* Matthew D. Purvance, Rasool Anooshehpoor, and James N. Brune. December 2012.

PEER 2012/05 *Development of Simplified Analysis Procedure for Piles in Laterally Spreading Layered Soils.* Christopher R. McGann, Pedro Arduino, and Peter Mackenzie–Helnwein. December 2012.

PEER 2012/04 *Unbonded Pre-Tensioned Columns for Bridges in Seismic Regions.* Phillip M. Davis, Todd M. Janes, Marc O. Eberhard, and John F. Stanton. December 2012.

PEER 2012/03 *Experimental and Analytical Studies on Reinforced Concrete Buildings with Seismically Vulnerable Beam-Column Joints*. Sangjoon Park and Khalid M. Mosalam. October 2012.

PEER 2012/02 *Seismic Performance of Reinforced Concrete Bridges Allowed to Uplift during Multi-Directional Excitation*. Andres Oscar Espinoza and Stephen A. Mahin. July 2012.

PEER 2012/01 *Spectral Damping Scaling Factors for Shallow Crustal Earthquakes in Active Tectonic Regions.* Sanaz Rezaeian, Yousef Bozorgnia, I. M. Idriss, Kenneth Campbell, Norman Abrahamson, and Walter Silva. July 2012.

PEER 2011/10 *Earthquake Engineering for Resilient Communities: 2011 PEER Internship Program Research Report Collection*. Heidi Faison and Stephen A. Mahin, Editors. December 2011.

PEER 2011/09 *Calibration of Semi-Stochastic Procedure for Simulating High-Frequency Ground Motions*. Jonathan P. Stewart, Emel Seyhan, and Robert W. Graves. December 2011.

PEER 2011/08 *Water Supply in regard to Fire Following Earthquake*. Charles Scawthorn. November 2011.

PEER 2011/07 *Seismic Risk Management in Urban Areas*. Proceedings of a U.S.-Iran-Turkey Seismic Workshop. September 2011.

PEER 2011/06 *The Use of Base Isolation Systems to Achieve Complex Seismic Performance Objectives*. Troy A. Morgan and Stephen A. Mahin. July 2011.

PEER 2011/05 *Case Studies of the Seismic Performance of Tall Buildings Designed by Alternative Means.* Task 12 Report for the Tall Buildings Initiative. Jack Moehle, Yousef Bozorgnia, Nirmal Jayaram, Pierson Jones, Mohsen Rahnama, Nilesh Shome, Zeynep Tuna, John Wallace, Tony Yang, and Farzin Zareian. July 2011.

PEER 2011/04 *Recommended Design Practice for Pile Foundations in Laterally Spreading Ground.* Scott A. Ashford, Ross W. Boulanger, and Scott J. Brandenberg. June 2011.

PEER 2011/03 *New Ground Motion Selection Procedures and Selected Motions for the PEER Transportation Research Program*. Jack W. Baker, Ting Lin, Shrey K. Shahi, and Nirmal Jayaram. March 2011.

PEER 2011/02 *A Bayesian Network Methodology for Infrastructure Seismic Risk Assessment and Decision Support*. Michelle T. Bensi, Armen Der Kiureghian, and Daniel Straub. March 2011.

PEER 2011/01 *Demand Fragility Surfaces for Bridges in Liquefied and Laterally Spreading Ground.* Scott J. Brandenberg, Jian Zhang, Pirooz Kashighandi, Yili Huo, and Minxing Zhao. March 2011.

PEER 2010/05 *Guidelines for Performance-Based Seismic Design of Tall Buildings.* Developed by the Tall Buildings Initiative. November 2010.

PEER 2010/04 *Application Guide for the Design of Flexible and Rigid Bus Connections between Substation Equipment Subjected to Earthquakes.* Jean-Bernard Dastous and Armen Der Kiureghian. September 2010.

PEER 2010/03 *Shear Wave Velocity as a Statistical Function of Standard Penetration Test Resistance and Vertical Effective Stress at Caltrans Bridge Sites.* Scott J. Brandenberg, Naresh Bellana, and Thomas Shantz. June 2010.

PEER 2010/02 *Stochastic Modeling and Simulation of Ground Motions for Performance-Based Earthquake Engineering.* Sanaz Rezaeian and Armen Der Kiureghian. June 2010.

PEER 2010/01 *Structural Response and Cost Characterization of Bridge Construction Using Seismic Performance Enhancement Strategies.* Ady Aviram, Božidar Stojadinović, Gustavo J. Parra-Montesinos, and Kevin R. Mackie. March 2010.

PEER 2009/03 *The Integration of Experimental and Simulation Data in the Study of Reinforced Concrete Bridge Systems Including Soil-Foundation-Structure Interaction.* Matthew Dryden and Gregory L. Fenves. November 2009.

PEER 2009/02 *Improving Earthquake Mitigation through Innovations and Applications in Seismic Science, Engineering, Communication, and Response*. Proceedings of a U.S.-Iran Seismic Workshop. October 2009.

PEER 2009/01 *Evaluation of Ground Motion Selection and Modification Methods: Predicting Median Interstory Drift Response of Buildings*. Curt B. Haselton, Editor. June 2009.

PEER 2008/10 *Technical Manual for Strata.* Albert R. Kottke and Ellen M. Rathje. February 2009.

PEER 2008/09 *NGA Model for Average Horizontal Component of Peak Ground Motion and Response Spectra.* Brian S.-J. Chiou and Robert R. Youngs. November 2008.

PEER 2008/08 *Toward Earthquake-Resistant Design of Concentrically Braced Steel Structures*. Patxi Uriz and Stephen A. Mahin. November 2008.

PEER 2008/07 *Using OpenSees for Performance-Based Evaluation of Bridges on Liquefiable Soils*. Stephen L. Kramer, Pedro Arduino, and HyungSuk Shin. November 2008.

PEER 2008/06 *Shaking Table Tests and Numerical Investigation of Self-Centering Reinforced Concrete Bridge Columns*. Hyung IL Jeong, Junichi Sakai, and Stephen A. Mahin. September 2008.

PEER 2008/05 *Performance-Based Earthquake Engineering Design Evaluation Procedure for Bridge Foundations Undergoing Liquefaction-Induced Lateral Ground Displacement*. Christian A. Ledezma and Jonathan D. Bray. August 2008.

PEER 2008/04 *Benchmarking of Nonlinear Geotechnical Ground Response Analysis Procedures.* Jonathan P. Stewart, Annie On-Lei Kwok, Youssef M. A. Hashash, Neven Matasovic, Robert Pyke, Zhiliang Wang, and Zhaohui Yang. August 2008.

PEER 2008/03 *Guidelines for Nonlinear Analysis of Bridge Structures in California.* Ady Aviram, Kevin R. Mackie, and Božidar Stojadinović. August 2008.

PEER 2008/02 *Treatment of Uncertainties in Seismic-Risk Analysis of Transportation Systems*. Evangelos Stergiou and Anne S. Kiremidjian. July 2008.

PEER 2008/01 *Seismic Performance Objectives for Tall Buildings.* William T. Holmes, Charles Kircher, William Petak, and Nabih Youssef. August 2008.

PEER 2007/12 *An Assessment to Benchmark the Seismic Performance of a Code-Conforming Reinforced Concrete Moment-Frame Building.* Curt Haselton, Christine A. Goulet, Judith Mitrani-Reiser, James L. Beck, Gregory G. Deierlein, Keith A. Porter, Jonathan P. Stewart, and Ertugrul Taciroglu. August 2008.

PEER 2007/11 *Bar Buckling in Reinforced Concrete Bridge Columns.* Wayne A. Brown, Dawn E. Lehman, and John F. Stanton. February 2008.

PEER 2007/10 *Computational Modeling of Progressive Collapse in Reinforced Concrete Frame Structures*. Mohamed M. Talaat and Khalid M. Mosalam. May 2008.

PEER 2007/09 *Integrated Probabilistic Performance-Based Evaluation of Benchmark Reinforced Concrete Bridges*. Kevin R. Mackie, John-Michael Wong, and Božidar Stojadinović. January 2008.

PEER 2007/08 *Assessing Seismic Collapse Safety of Modern Reinforced Concrete Moment-Frame Buildings*. Curt B. Haselton and Gregory G. Deierlein. February 2008.

PEER 2007/07 *Performance Modeling Strategies for Modern Reinforced Concrete Bridge Columns*. Michael P. Berry and Marc O. Eberhard. April 2008.

PEER 2007/06 *Development of Improved Procedures for Seismic Design of Buried and Partially Buried Structures*. Linda Al Atik and Nicholas Sitar. June 2007.

PEER 2007/05 *Uncertainty and Correlation in Seismic Risk Assessment of Transportation Systems*. Renee G. Lee and Anne S. Kiremidjian. July 2007.

PEER 2007/04 *Numerical Models for Analysis and Performance-Based Design of Shallow Foundations Subjected to Seismic Loading*. Sivapalan Gajan, Tara C. Hutchinson, Bruce L. Kutter, Prishati Raychowdhury, José A. Ugalde, and Jonathan P. Stewart. May 2008.

PEER 2007/03 *Beam-Column Element Model Calibrated for Predicting Flexural Response Leading to Global Collapse of RC Frame Buildings*. Curt B. Haselton, Abbie B. Liel, Sarah Taylor Lange, and Gregory G. Deierlein. May 2008.

PEER 2007/02 *Campbell-Bozorgnia NGA Ground Motion Relations for the Geometric Mean Horizontal Component of Peak and Spectral Ground Motion Parameters*. Kenneth W. Campbell and Yousef Bozorgnia. May 2007.

PEER 2007/01 *Boore-Atkinson NGA Ground Motion Relations for the Geometric Mean Horizontal Component of Peak and Spectral Ground Motion Parameters*. David M. Boore and Gail M. Atkinson. May 2007.

PEER 2006/12 Societal Implications of Performance-Based Earthquake Engineering. Peter J. May. May 2007.

PEER 2006/11 *Probabilistic Seismic Demand Analysis Using Advanced Ground Motion Intensity Measures, Attenuation Relationships, and Near-Fault Effects*. Polsak Tothong and C. Allin Cornell. March 2007.

PEER 2006/10 *Application of the PEER PBEE Methodology to the I-880 Viaduct*. Sashi Kunnath. February 2007.

PEER 2006/09 *Quantifying Economic Losses from Travel Forgone Following a Large Metropolitan Earthquake*. James Moore, Sungbin Cho, Yue Yue Fan, and Stuart Werner. November 2006.

PEER 2006/08 *Vector-Valued Ground Motion Intensity Measures for Probabilistic Seismic Demand Analysis*. Jack W. Baker and C. Allin Cornell. October 2006.

PEER 2006/07 *Analytical Modeling of Reinforced Concrete Walls for Predicting Flexural and Coupled–Shear-Flexural Responses*. Kutay Orakcal, Leonardo M. Massone, and John W. Wallace. October 2006.

PEER 2006/06 *Nonlinear Analysis of a Soil-Drilled Pier System under Static and Dynamic Axial Loading*. Gang Wang and Nicholas Sitar. November 2006.

PEER 2006/05 *Advanced Seismic Assessment Guidelines.* Paolo Bazzurro, C. Allin Cornell, Charles Menun, Maziar Motahari, and Nicolas Luco. September 2006.

PEER 2006/04 *Probabilistic Seismic Evaluation of Reinforced Concrete Structural Components and Systems*. Tae Hyung Lee and Khalid M. Mosalam. August 2006.

PEER 2006/03 *Performance of Lifelines Subjected to Lateral Spreading.* Scott A. Ashford and Teerawut Juirnarongrit. July 2006.

PEER 2006/02 *Pacific Earthquake Engineering Research Center Highway Demonstration Project.* Anne Kiremidjian, James Moore, Yue Yue Fan, Nesrin Basoz, Ozgur Yazali, and Meredith Williams. April 2006.

PEER 2006/01 *Bracing Berkeley. A Guide to Seismic Safety on the UC Berkeley Campus.* Mary C. Comerio, Stephen Tobriner, and Ariane Fehrenkamp. January 2006.

PEER 2005/17 *Earthquake Simulation Tests on Reducing Residual Displacements of Reinforced Concrete Bridges.* Junichi Sakai, Stephen A Mahin, and Andres Espinoza. December 2005.

PEER 2005/16 *Seismic Response and Reliability of Electrical Substation Equipment and Systems.* Junho Song, Armen Der Kiureghian, and Jerome L. Sackman. April 2006.

PEER 2005/15 *CPT-Based Probabilistic Assessment of Seismic Soil Liquefaction Initiation.* R. E. S. Moss, R. B. Seed, R. E. Kayen, J. P. Stewart, and A. Der Kiureghian. April 2006.

PEER 2005/14 *Workshop on Modeling of Nonlinear Cyclic Load-Deformation Behavior of Shallow Foundations.* Bruce L. Kutter, Geoffrey Martin, Tara Hutchinson, Chad Harden, Sivapalan Gajan, and Justin Phalen. March 2006.

PEER 2005/13 *Stochastic Characterization and Decision Bases under Time-Dependent Aftershock Risk in Performance-Based Earthquake Engineering*. Gee Liek Yeo and C. Allin Cornell. July 2005.

PEER 2005/12 *PEER Testbed Study on a Laboratory Building: Exercising Seismic Performance Assessment.* Mary C. Comerio, Editor. November 2005.

PEER 2005/11 *Van Nuys Hotel Building Testbed Report: Exercising Seismic Performance Assessment.* Helmut Krawinkler, Editor. October 2005.

PEER 2005/10 *First NEES/E-Defense Workshop on Collapse Simulation of Reinforced Concrete Building Structures.* September 2005.

PEER 2005/09 *Test Applications of Advanced Seismic Assessment Guidelines.* Joe Maffei, Karl Telleen, Danya Mohr, William Holmes, and Yuki Nakayama. August 2006.

PEER 2005/08 *Damage Accumulation in Lightly Confined Reinforced Concrete Bridge Columns.* R. Tyler Ranf, Jared M. Nelson, Zach Price, Marc O. Eberhard, and John F. Stanton. April 2006.

PEER 2005/07 *Experimental and Analytical Studies on the Seismic Response of Freestanding and Anchored Laboratory Equipment.* Dimitrios Konstantinidis and Nicos Makris. January 2005.

PEER 2005/06 *Global Collapse of Frame Structures under Seismic Excitations*. Luis F. Ibarra and Helmut Krawinkler. September 2005.

PEER 2005//05 *Performance Characterization of Bench- and Shelf-Mounted Equipment.* Samit Ray Chaudhuri and Tara C. Hutchinson. May 2006.

PEER 2005/04 *Numerical Modeling of the Nonlinear Cyclic Response of Shallow Foundations.* Chad Harden, Tara Hutchinson, Geoffrey R. Martin, and Bruce L. Kutter. August 2005.

PEER 2005/03 *A Taxonomy of Building Components for Performance-Based Earthquake Engineering.* Keith A. Porter. September 2005.

PEER 2005/02 *Fragility Basis for California Highway Overpass Bridge Seismic Decision Making*. Kevin R. Mackie and Božidar Stojadinović. June 2005.

PEER 2005/01 *Empirical Characterization of Site Conditions on Strong Ground Motion.* Jonathan P. Stewart, Yoojoong Choi, and Robert W. Graves. June 2005.

PEER 2004/09 *Electrical Substation Equipment Interaction: Experimental Rigid Conductor Studies.* Christopher Stearns and André Filiatrault. February 2005.

PEER 2004/08 *Seismic Qualification and Fragility Testing of Line Break 550-kV Disconnect Switches.* Shakhzod M. Takhirov, Gregory L. Fenves, and Eric Fujisaki. January 2005.

PEER 2004/07 *Ground Motions for Earthquake Simulator Qualification of Electrical Substation Equipment.* Shakhzod M. Takhirov, Gregory L. Fenves, Eric Fujisaki, and Don Clyde. January 2005.

PEER 2004/06 *Performance-Based Regulation and Regulatory Regimes.* Peter J. May and Chris Koski. September 2004.

PEER 2004/05 *Performance-Based Seismic Design Concepts and Implementation: Proceedings of an International Workshop.* Peter Fajfar and Helmut Krawinkler, Editors. September 2004.

PEER 2004/04 *Seismic Performance of an Instrumented Tilt-up Wall Building.* James C. Anderson and Vitelmo V. Bertero. July 2004.

PEER 2004/03 *Evaluation and Application of Concrete Tilt-up Assessment Methodologies.* Timothy Graf and James O. Malley. October 2004.

PEER 2004/02 *Analytical Investigations of New Methods for Reducing Residual Displacements of Reinforced Concrete Bridge Columns.* Junichi Sakai and Stephen A. Mahin. August 2004.

PEER 2004/01 *Seismic Performance of Masonry Buildings and Design Implications.* Kerri Anne Taeko Tokoro, James C. Anderson, and Vitelmo V. Bertero. February 2004.

PEER 2003/18 *Performance Models for Flexural Damage in Reinforced Concrete Columns.* Michael Berry and Marc Eberhard. August 2003.

PEER 2003/17 *Predicting Earthquake Damage in Older Reinforced Concrete Beam-Column Joints.* Catherine Pagni and Laura Lowes. October 2004.

PEER 2003/16 *Seismic Demands for Performance-Based Design of Bridges.* Kevin Mackie and Božidar Stojadinović. August 2003.

PEER 2003/15 *Seismic Demands for Nondeteriorating Frame Structures and Their Dependence on Ground Motions.* Ricardo Antonio Medina and Helmut Krawinkler. May 2004.

PEER 2003/14 *Finite Element Reliability and Sensitivity Methods for Performance-Based Earthquake Engineering*. Terje Haukaas and Armen Der Kiureghian. April 2004.

PEER 2003/13 *Effects of Connection Hysteretic Degradation on the Seismic Behavior of Steel Moment-Resisting Frames.* Janise E. Rodgers and Stephen A. Mahin. March 2004.

PEER 2003/12 *Implementation Manual for the Seismic Protection of Laboratory Contents: Format and Case Studies*. William T. Holmes and Mary C. Comerio. October 2003.

PEER 2003/11 *Fifth U.S.-Japan Workshop on Performance-Based Earthquake Engineering Methodology for Reinforced Concrete Building Structures*. February 2004.

PEER 2003/10 *A Beam-Column Joint Model for Simulating the Earthquake Response of Reinforced Concrete Frames.* Laura N. Lowes, Nilanjan Mitra, and Arash Altoontash. February 2004.

PEER 2003/09 *Sequencing Repairs after an Earthquake: An Economic Approach.* Marco Casari and Simon J. Wilkie. April 2004.

PEER 2003/08 *A Technical Framework for Probability-Based Demand and Capacity Factor Design (DCFD) Seismic Formats*. Fatemeh Jalayer and C. Allin Cornell. November 2003.

PEER 2003/07 *Uncertainty Specification and Propagation for Loss Estimation Using FOSM Methods.* Jack W. Baker and C. Allin Cornell. September 2003.

PEER 2003/06 *Performance of Circular Reinforced Concrete Bridge Columns under Bidirectional Earthquake Loading*. Mahmoud M. Hachem, Stephen A. Mahin, and Jack P. Moehle. February 2003.

PEER 2003/05 *Response Assessment for Building-Specific Loss Estimation.* Eduardo Miranda and Shahram Taghavi. September 2003.

PEER 2003/04 *Experimental Assessment of Columns with Short Lap Splices Subjected to Cyclic Loads*. Murat Melek, John W. Wallace, and Joel Conte. April 2003.

PEER 2003/03 *Probabilistic Response Assessment for Building-Specific Loss Estimation*. Eduardo Miranda and Hesameddin Aslani. September 2003.

PEER 2003/02 *Software Framework for Collaborative Development of Nonlinear Dynamic Analysis Program*. Jun Peng and Kincho H. Law. September 2003.

PEER 2003/01 *Shake Table Tests and Analytical Studies on the Gravity Load Collapse of Reinforced Concrete Frames.* Kenneth John Elwood and Jack P. Moehle. November 2003.

PEER 2002/24 *Performance of Beam to Column Bridge Joints Subjected to a Large Velocity Pulse.* Natalie Gibson, André Filiatrault, and Scott A. Ashford. April 2002.

PEER 2002/23 *Effects of Large Velocity Pulses on Reinforced Concrete Bridge Columns.* Greg L. Orozco and Scott A. Ashford. April 2002.

PEER 2002/22 *Characterization of Large Velocity Pulses for Laboratory Testing.* Kenneth E. Cox and Scott A. Ashford. April 2002.

PEER 2002/21 *Fourth U.S.-Japan Workshop on Performance-Based Earthquake Engineering Methodology for Reinforced Concrete Building Structures*. December 2002.

PEER 2002/20 *Barriers to Adoption and Implementation of PBEE Innovations.* Peter J. May. August 2002.

PEER 2002/19 *Economic-Engineered Integrated Models for Earthquakes: Socioeconomic Impacts.* Peter Gordon, James E. Moore II, and Harry W. Richardson. July 2002.

PEER 2002/18 *Assessment of Reinforced Concrete Building Exterior Joints with Substandard Details.* Chris P. Pantelides, Jon Hansen, Justin Nadauld, and Lawrence D. Reaveley. May 2002.

PEER 2002/17 *Structural Characterization and Seismic Response Analysis of a Highway Overcrossing Equipped with Elastomeric Bearings and Fluid Dampers: A Case Study*. Nicos Makris and Jian Zhang. November 2002.

PEER 2002/16 *Estimation of Uncertainty in Geotechnical Properties for Performance-Based Earthquake Engineering*. Allen L. Jones, Steven L. Kramer, and Pedro Arduino. December 2002.

PEER 2002/15 *Seismic Behavior of Bridge Columns Subjected to Various Loading Patterns*. Asadollah Esmaeily-Gh. and Yan Xiao. December 2002.

PEER 2002/14 *Inelastic Seismic Response of Extended Pile Shaft Supported Bridge Structures.* T.C. Hutchinson, R.W. Boulanger, Y.H. Chai, and I.M. Idriss. December 2002.

PEER 2002/13 *Probabilistic Models and Fragility Estimates for Bridge Components and Systems.* Paolo Gardoni, Armen Der Kiureghian, and Khalid M. Mosalam. June 2002.

PEER 2002/12 *Effects of Fault Dip and Slip Rake on Near-Source Ground Motions: Why Chi-Chi Was a Relatively Mild M7.6 Earthquake*. Brad T. Aagaard, John F. Hall, and Thomas H. Heaton. December 2002.

PEER 2002/11 *Analytical and Experimental Study of Fiber-Reinforced Strip Isolators*. James M. Kelly and Shakhzod M. Takhirov. September 2002.

PEER 2002/10 *Centrifuge Modeling of Settlement and Lateral Spreading with Comparisons to Numerical Analyses***.** Sivapalan Gajan and Bruce L. Kutter. January 2003.

PEER 2002/09 *Documentation and Analysis of Field Case Histories of Seismic Compression during the 1994 Northridge, California, Earthquake*. Jonathan P. Stewart, Patrick M. Smith, Daniel H. Whang, and Jonathan D. Bray. October 2002.

PEER 2002/08 *Component Testing, Stability Analysis and Characterization of Buckling-Restrained Unbonded Braces^{TM}*. Cameron Black, Nicos Makris, and Ian Aiken. September 2002.

PEER 2002/07 *Seismic Performance of Pile-Wharf Connections.* Charles W. Roeder, Robert Graff, Jennifer Soderstrom, and Jun Han Yoo. December 2001.

PEER 2002/06 *The Use of Benefit-Cost Analysis for Evaluation of Performance-Based Earthquake Engineering Decisions*. Richard O. Zerbe and Anthony Falit-Baiamonte. September 2001.

PEER 2002/05 *Guidelines, Specifications, and Seismic Performance Characterization of Nonstructural Building Components and Equipment*. André Filiatrault, Constantin Christopoulos, and Christopher Stearns. September 2001.

PEER 2002/04 *Consortium of Organizations for Strong-Motion Observation Systems and the Pacific Earthquake Engineering Research Center Lifelines Program: Invited Workshop on Archiving and Web Dissemination of Geotechnical Data, 4–5 October 2001*. September 2002.

PEER 2002/03 *Investigation of Sensitivity of Building Loss Estimates to Major Uncertain Variables for the Van Nuys Testbed.* Keith A. Porter, James L. Beck, and Rustem V. Shaikhutdinov. August 2002.

PEER 2002/02 *The Third U.S.-Japan Workshop on Performance-Based Earthquake Engineering Methodology for Reinforced Concrete Building Structures*. July 2002.

PEER 2002/01 *Nonstructural Loss Estimation: The UC Berkeley Case Study.* Mary C. Comerio and John C. Stallmeyer. December 2001.

PEER 2001/16 *Statistics of SDF-System Estimate of Roof Displacement for Pushover Analysis of Buildings.* Anil K. Chopra, Rakesh K. Goel, and Chatpan Chintanapakdee. December 2001.

PEER 2001/15 *Damage to Bridges during the 2001 Nisqually Earthquake.* R. Tyler Ranf, Marc O. Eberhard, and Michael P. Berry. November 2001.

PEER 2001/14 *Rocking Response of Equipment Anchored to a Base Foundation.* Nicos Makris and Cameron J. Black. September 2001.

PEER 2001/13 *Modeling Soil Liquefaction Hazards for Performance-Based Earthquake Engineering*. Steven L. Kramer and Ahmed-W. Elgamal. February 2001.

PEER 2001/12 *Development of Geotechnical Capabilities in OpenSees*. Boris Jeremić. September 2001.

PEER 2001/11 *Analytical and Experimental Study of Fiber-Reinforced Elastomeric Isolators*. James M. Kelly and Shakhzod M. Takhirov. September 2001.

PEER 2001/10 *Amplification Factors for Spectral Acceleration in Active Regions.* Jonathan P. Stewart, Andrew H. Liu, Yoojoong Choi, and Mehmet B. Baturay. December 2001.

PEER 2001/09 *Ground Motion Evaluation Procedures for Performance-Based Design.* Jonathan P. Stewart, Shyh-Jeng Chiou, Jonathan D. Bray, Robert W. Graves, Paul G. Somerville, and Norman A. Abrahamson. September 2001.

PEER 2001/08 *Experimental and Computational Evaluation of Reinforced Concrete Bridge Beam-Column Connections for Seismic Performance*. Clay J. Naito, Jack P. Moehle, and Khalid M. Mosalam. November 2001.

PEER 2001/07 *The Rocking Spectrum and the Shortcomings of Design Guidelines.* Nicos Makris and Dimitrios Konstantinidis. August 2001.

PEER 2001/06 *Development of an Electrical Substation Equipment Performance Database for Evaluation of Equipment Fragilities*. Thalia Agnanos. April 1999.

PEER 2001/05 *Stiffness Analysis of Fiber-Reinforced Elastomeric Isolators.* Hsiang-Chuan Tsai and James M. Kelly. May 2001.

PEER 2001/04 *Organizational and Societal Considerations for Performance-Based Earthquake Engineering*. Peter J. May. April 2001.

PEER 2001/03 *A Modal Pushover Analysis Procedure to Estimate Seismic Demands for Buildings: Theory and Preliminary Evaluation*. Anil K. Chopra and Rakesh K. Goel. January 2001.

PEER 2001/02 *Seismic Response Analysis of Highway Overcrossings Including Soil-Structure Interaction*. Jian Zhang and Nicos Makris. March 2001.

PEER 2001/01 *Experimental Study of Large Seismic Steel Beam-to-Column Connections.* Egor P. Popov and Shakhzod M. Takhirov. November 2000.

PEER 2000/10 *The Second U.S.-Japan Workshop on Performance-Based Earthquake Engineering Methodology for Reinforced Concrete Building Structures*. March 2000.

PEER 2000/09 *Structural Engineering Reconnaissance of the August 17, 1999 Earthquake: Kocaeli (Izmit), Turkey.* Halil Sezen, Kenneth J. Elwood, Andrew S. Whittaker, Khalid Mosalam, John J. Wallace, and John F. Stanton. December 2000.

PEER 2000/08 *Behavior of Reinforced Concrete Bridge Columns Having Varying Aspect Ratios and Varying Lengths of Confinement*. Anthony J. Calderone, Dawn E. Lehman, and Jack P. Moehle. January 2001.

PEER 2000/07 *Cover-Plate and Flange-Plate Reinforced Steel Moment-Resisting Connections.* Taejin Kim, Andrew S. Whittaker, Amir S. Gilani, Vitelmo V. Bertero, and Shakhzod M. Takhirov. September 2000.

PEER 2000/06 *Seismic Evaluation and Analysis of 230-kV Disconnect Switches.* Amir S. J. Gilani, Andrew S. Whittaker, Gregory L. Fenves, Chun-Hao Chen, Henry Ho, and Eric Fujisaki. July 2000.

PEER 2000/05 *Performance-Based Evaluation of Exterior Reinforced Concrete Building Joints for Seismic Excitation*. Chandra Clyde, Chris P. Pantelides, and Lawrence D. Reaveley. July 2000.

PEER 2000/04 *An Evaluation of Seismic Energy Demand: An Attenuation Approach*. Chung-Che Chou and Chia-Ming Uang. July 1999.

PEER 2000/03 *Framing Earthquake Retrofitting Decisions: The Case of Hillside Homes in Los Angeles.* Detlof von Winterfeldt, Nels Roselund, and Alicia Kitsuse. March 2000.

PEER 2000/02 *U.S.-Japan Workshop on the Effects of Near-Field Earthquake Shaking*. Andrew Whittaker, Editor. July 2000.

PEER 2000/01 *Further Studies on Seismic Interaction in Interconnected Electrical Substation Equipment.* Armen Der Kiureghian, Kee-Jeung Hong, and Jerome L. Sackman. November 1999.

PEER 1999/14 *Seismic Evaluation and Retrofit of 230-kV Porcelain Transformer Bushings*. Amir S. Gilani, Andrew S. Whittaker, Gregory L. Fenves, and Eric Fujisaki. December 1999.

PEER 1999/13 *Building Vulnerability Studies: Modeling and Evaluation of Tilt-up and Steel Reinforced Concrete Buildings*. John W. Wallace, Jonathan P. Stewart, and Andrew S. Whittaker, Editors. December 1999.

PEER 1999/12 *Rehabilitation of Nonductile RC Frame Building Using Encasement Plates and Energy-Dissipating Devices*. Mehrdad Sasani, Vitelmo V. Bertero, James C. Anderson. December 1999.

PEER 1999/11 *Performance Evaluation Database for Concrete Bridge Components and Systems under Simulated Seismic Loads*. Yael D. Hose and Frieder Seible. November 1999.

PEER 1999/10 *U.S.-Japan Workshop on Performance-Based Earthquake Engineering Methodology for Reinforced Concrete Building Structures*. December 1999.

PEER 1999/09 *Performance Improvement of Long Period Building Structures Subjected to Severe Pulse-Type Ground Motions*. James C. Anderson, Vitelmo V. Bertero, and Raul Bertero. October 1999.

PEER 1999/08 *Envelopes for Seismic Response Vectors.* Charles Menun and Armen Der Kiureghian. July 1999.

PEER 1999/07 *Documentation of Strengths and Weaknesses of Current Computer Analysis Methods for Seismic Performance of Reinforced Concrete Members*. William F. Cofer. November 1999.

PEER 1999/06 *Rocking Response and Overturning of Anchored Equipment under Seismic Excitations*. Nicos Makris and Jian Zhang. November 1999.

PEER 1999/05 *Seismic Evaluation of 550 kV Porcelain Transformer Bushings.* Amir S. Gilani, Andrew S. Whittaker, Gregory L. Fenves, and Eric Fujisaki. October 1999.

PEER 1999/04 *Adoption and Enforcement of Earthquake Risk-Reduction Measures.* Peter J. May, Raymond J. Burby, T. Jens Feeley, and Robert Wood. August 1999.

PEER 1999/03 *Task 3 Characterization of Site Response General Site Categories*. Adrian Rodriguez-Marek, Jonathan D. Bray and Norman Abrahamson. February 1999.

PEER 1999/02 *Capacity-Demand-Diagram Methods for Estimating Seismic Deformation of Inelastic Structures: SDF Systems*. Anil K. Chopra and Rakesh Goel. April 1999.

PEER 1999/01 *Interaction in Interconnected Electrical Substation Equipment Subjected to Earthquake Ground Motions*. Armen Der Kiureghian, Jerome L. Sackman, and Kee-Jeung Hong. February 1999.

PEER 1998/08 *Behavior and Failure Analysis of a Multiple-Frame Highway Bridge in the 1994 Northridge Earthquake*. Gregory L. Fenves and Michael Ellery. December 1998.

PEER 1998/07 *Empirical Evaluation of Inertial Soil-Structure Interaction Effects.* Jonathan P. Stewart, Raymond B. Seed, and Gregory L. Fenves. November 1998.

PEER 1998/06 *Effect of Damping Mechanisms on the Response of Seismic Isolated Structures*. Nicos Makris and Shih-Po Chang. November 1998.

PEER 1998/05 *Rocking Response and Overturning of Equipment under Horizontal Pulse-Type Motions*. Nicos Makris and Yiannis Roussos. October 1998.

PEER 1998/04 *Pacific Earthquake Engineering Research Invitational Workshop Proceedings, May 14–15, 1998: Defining the Links between Planning, Policy Analysis, Economics and Earthquake Engineering*. Mary Comerio and Peter Gordon. September 1998.

PEER 1998/03 *Repair/Upgrade Procedures for Welded Beam to Column Connections*. James C. Anderson and Xiaojing Duan. May 1998.

PEER 1998/02 *Seismic Evaluation of 196 kV Porcelain Transformer Bushings.* Amir S. Gilani, Juan W. Chavez, Gregory L. Fenves, and Andrew S. Whittaker. May 1998.

PEER 1998/01 *Seismic Performance of Well-Confined Concrete Bridge Columns.* Dawn E. Lehman and Jack P. Moehle. December 2000.

PEER REPORTS: ONE HUNDRED SERIES

PEER 2012/103	*Performance-Based Seismic Demand Assessment of Concentrically Braced Steel Frame Buildings.* Chui-Hsin Chen and Stephen A. Mahin. December 2012.
PEER 2012/102	*Procedure to Restart an Interrupted Hybrid Simulation: Addendum to PEER Report 2010/103.* Vesna Terzic and Bozidar Stojadinovic. October 2012.
PEER 2012/101	*Mechanics of Fiber Reinforced Bearings.* James M. Kelly and Andrea Calabrese. February 2012.
PEER 2011/107	*Nonlinear Site Response and Seismic Compression at Vertical Array Strongly Shaken by 2007 Niigata-ken Chuetsu-oki Earthquake.* Eric Yee, Jonathan P. Stewart, and Kohji Tokimatsu. December 2011.
PEER 2011/106	*Self Compacting Hybrid Fiber Reinforced Concrete Composites for Bridge Columns.* Pardeep Kumar, Gabriel Jen, William Trono, Marios Panagiotou, and Claudia Ostertag. September 2011.
PEER 2011/105	*Stochastic Dynamic Analysis of Bridges Subjected to Spacially Varying Ground Motions.* Katerina Konakli and Armen Der Kiureghian. August 2011.
PEER 2011/104	*Design and Instrumentation of the 2010 E-Defense Four-Story Reinforced Concrete and Post-Tensioned Concrete Buildings.* Takuya Nagae, Kenichi Tahara, Taizo Matsumori, Hitoshi Shiohara, Toshimi Kabeyasawa, Susumu Kono, Minehiro Nishiyama (Japanese Research Team) and John Wallace, Wassim Ghannoum, Jack Moehle, Richard Sause, Wesley Keller, Zeynep Tuna (U.S. Research Team). June 2011.
PEER 2011/103	*In-Situ Monitoring of the Force Output of Fluid Dampers: Experimental Investigation.* Dimitrios Konstantinidis, James M. Kelly, and Nicos Makris. April 2011.
PEER 2011/102	*Ground-Motion Prediction Equations 1964–2010.* John Douglas. April 2011.
PEER 2011/101	*Report of the Eighth Planning Meeting of NEES/E-Defense Collaborative Research on Earthquake Engineering.* Convened by the Hyogo Earthquake Engineering Research Center (NIED), NEES Consortium, Inc. February 2011.
PEER 2010/111	*Modeling and Acceptance Criteria for Seismic Design and Analysis of Tall Buildings.* Task 7 Report for the Tall Buildings Initiative - Published jointly by the Applied Technology Council. October 2010.
PEER 2010/110	*Seismic Performance Assessment and Probabilistic Repair Cost Analysis of Precast Concrete Cladding Systems for Multistory Buildlings.* Jeffrey P. Hunt and Božidar Stojadinovic. November 2010.
PEER 2010/109	*Report of the Seventh Joint Planning Meeting of NEES/E-Defense Collaboration on Earthquake Engineering. Held at the E-Defense, Miki, and Shin-Kobe, Japan, September 18–19, 2009.* August 2010.
PEER 2010/108	*Probabilistic Tsunami Hazard in California.* Hong Kie Thio, Paul Somerville, and Jascha Polet, preparers. October 2010.
PEER 2010/107	*Performance and Reliability of Exposed Column Base Plate Connections for Steel Moment-Resisting Frames.* Ady Aviram, Božidar Stojadinovic, and Armen Der Kiureghian. August 2010.
PEER 2010/106	*Verification of Probabilistic Seismic Hazard Analysis Computer Programs.* Patricia Thomas, Ivan Wong, and Norman Abrahamson. May 2010.
PEER 2010/105	*Structural Engineering Reconnaissance of the April 6, 2009, Abruzzo, Italy, Earthquake, and Lessons Learned.* M. Selim Günay and Khalid M. Mosalam. April 2010.
PEER 2010/104	*Simulating the Inelastic Seismic Behavior of Steel Braced Frames, Including the Effects of Low-Cycle Fatigue.* Yuli Huang and Stephen A. Mahin. April 2010.
PEER 2010/103	*Post-Earthquake Traffic Capacity of Modern Bridges in California.* Vesna Terzic and Božidar Stojadinović. March 2010.
PEER 2010/102	*Analysis of Cumulative Absolute Velocity (CAV) and JMA Instrumental Seismic Intensity (I_{JMA}) Using the PEER–NGA Strong Motion Database.* Kenneth W. Campbell and Yousef Bozorgnia. February 2010.
PEER 2010/101	*Rocking Response of Bridges on Shallow Foundations.* Jose A. Ugalde, Bruce L. Kutter, and Boris Jeremic. April 2010.
PEER 2009/109	*Simulation and Performance-Based Earthquake Engineering Assessment of Self-Centering Post-Tensioned Concrete Bridge Systems.* Won K. Lee and Sarah L. Billington. December 2009.

PEER 2009/108 *PEER Lifelines Geotechnical Virtual Data Center.* J. Carl Stepp, Daniel J. Ponti, Loren L. Turner, Jennifer N. Swift, Sean Devlin, Yang Zhu, Jean Benoit, and John Bobbitt. September 2009.

PEER 2009/107 *Experimental and Computational Evaluation of Current and Innovative In-Span Hinge Details in Reinforced Concrete Box-Girder Bridges: Part 2: Post-Test Analysis and Design Recommendations.* Matias A. Hube and Khalid M. Mosalam. December 2009.

PEER 2009/106 *Shear Strength Models of Exterior Beam-Column Joints without Transverse Reinforcement.* Sangjoon Park and Khalid M. Mosalam. November 2009.

PEER 2009/105 *Reduced Uncertainty of Ground Motion Prediction Equations through Bayesian Variance Analysis.* Robb Eric S. Moss. November 2009.

PEER 2009/104 *Advanced Implementation of Hybrid Simulation.* Andreas H. Schellenberg, Stephen A. Mahin, Gregory L. Fenves. November 2009.

PEER 2009/103 *Performance Evaluation of Innovative Steel Braced Frames.* T. Y. Yang, Jack P. Moehle, and Božidar Stojadinovic. August 2009.

PEER 2009/102 *Reinvestigation of Liquefaction and Nonliquefaction Case Histories from the 1976 Tangshan Earthquake.* Robb Eric Moss, Robert E. Kayen, Liyuan Tong, Songyu Liu, Guojun Cai, and Jiaer Wu. August 2009.

PEER 2009/101 *Report of the First Joint Planning Meeting for the Second Phase of NEES/E-Defense Collaborative Research on Earthquake Engineering.* Stephen A. Mahin et al. July 2009.

PEER 2008/104 *Experimental and Analytical Study of the Seismic Performance of Retaining Structures.* Linda Al Atik and Nicholas Sitar. January 2009.

PEER 2008/103 *Experimental and Computational Evaluation of Current and Innovative In-Span Hinge Details in Reinforced Concrete Box-Girder Bridges. Part 1: Experimental Findings and Pre-Test Analysis*. Matias A. Hube and Khalid M. Mosalam. January 2009.

PEER 2008/102 *Modeling of Unreinforced Masonry Infill Walls Considering In-Plane and Out-of-Plane Interaction.* Stephen Kadysiewski and Khalid M. Mosalam. January 2009.

PEER 2008/101 *Seismic Performance Objectives for Tall Buildings.* William T. Holmes, Charles Kircher, William Petak, and Nabih Youssef. August 2008.

PEER 2007/101 *Generalized Hybrid Simulation Framework for Structural Systems Subjected to Seismic Loading*. Tarek Elkhoraibi and Khalid M. Mosalam. July 2007.

PEER 2007/100 *Seismic Evaluation of Reinforced Concrete Buildings Including Effects of Masonry Infill Walls*. Alidad Hashemi and Khalid M. Mosalam. July 2007.

The Pacific Earthquake Engineering Research Center (PEER) is a multi-institutional research and education center with headquarters at the University of California, Berkeley. Investigators from over 20 universities, several consulting companies, and researchers at various state and federal government agencies contribute to research programs focused on performance-based earthquake engineering.

These research programs aim to identify and reduce the risks from major earthquakes to life safety and to the economy by including research in a wide variety of disciplines including structural and geotechnical engineering, geology/seismology, lifelines, transportation, architecture, economics, risk management, and public policy.

PEER is supported by federal, state, local, and regional agencies, together with industry partners.

PEER Core Institutions

University of California, Berkeley (Lead Institution)
California Institute of Technology
Oregon State University
Stanford University
University of California, Davis
University of California, Irvine
University of California, Los Angeles
University of California, San Diego
University of Nevada, Reno
University of Southern California
University of Washington

PEER reports can be ordered at https://peer.berkeley.edu/peer-reports or by contacting

Pacific Earthquake Engineering Research Center
University of California, Berkeley
325 Davis Hall, Mail Code 1792
Berkeley, CA 94720-1792
Tel: 510-642-3437
Email: peer_center@berkeley.edu

ISSN 2770-8314
https://doi.org10.55461/SSXE9861